The Dissertation Committee for Ashish Sharma
certifies that this is the approved version of the following dissertation:

Computational modeling of high pressure plasmas for plasma assisted combustion, liquid reforming and thermal breakdown applications

Committee:

Laxminarayan L. Raja, Supervisor

Philip L. Varghese

David B. Goldstein

Fabrizio Bisetti

Gary A. Hallock

Computational modeling of high pressure plasmas for plasma assisted combustion, liquid reforming and thermal breakdown applications

by

Ashish Sharma

DISSERTATION

Presented to the Faculty of the Graduate School of
The University of Texas at Austin
in Partial Fulfillment
of the Requirements
for the Degree of

DOCTOR OF PHILOSOPHY

THE UNIVERSITY OF TEXAS AT AUSTIN
December 2018

Dedicated to my family.

Acknowledgments

I wish to thank the multitudes of people who helped and guided me through this long journey. First and foremost I thank my mom Kaushalya Sharma, my dad Sitaram Sharma and my dear sister Sneha Sharma for motivating me to follow my dreams and supporting me at every step of my Ph.D. I thank my advisor, Dr. Laxminarayan L. Raja for his support and encouragement throughout my graduate studies. Dr. Raja inspired me, taught me all that I know about plasmas and gave me the freedom to explore topics that deeply interested me. I acknowledge my collaborators Dr. Dmitry Levko, Dr. Min Suk Cha and Dr. Ahmad Hamdan for working alongside me to accomplish my research endeavors. I thank my committee members Dr. David Goldstein, Dr. Philip Varghese, Dr. Fabrizio Bisetti and Dr. Gary Hallock for providing invaluable suggestions and improvements to my doctoral research work. I thank my colleague and my best friend Prem for being my mentor and for sitting with me through countless hours of debugging. I thank my colleagues Miles, Dylan, Yunho, Vivek, Michael, Evrim, Young-Jun, Anand, Chris, Doug, Konstantinos and Daiju who also became my close friends over the course of the last 5 years. I will definitely miss the endless debate sessions, the long coffee break discussions and the basketball games with you guys. Thank you all for answering my countless questions and helping me become a good researcher, a good orator and a good friend. I also want to thank my dear friends Janaki, Sriram and Mahesh, who also played an important role in this journey.

Lastly I acknowledge Scott Messec for helping me fix my computer three times over the course of the last five years, without which this work would not have been possible.

Computational modeling of high pressure plasmas for plasma assisted combustion, liquid reforming and thermal breakdown applications

Publication No. ________________

Ashish Sharma, Ph.D.
The University of Texas at Austin, 2018

Supervisor: Laxminarayan L. Raja

The goal of the present work is to study high pressure non-equilibrium plasma discharges in chemically reactive systems. In this work, we present coupled computational studies of high pressure nanosecond pulsed plasmas for multiphysics applications ranging from plasma assisted combustion ignition, large gap thermal breakdown, to electric discharge in liquids for fuel reforming and biomedical applications.

In the first part of the work, we report the results of a computational study which explores argon surface streamers as a low-voltage mechanism for thermal breakdown of large interelectrode gaps and investigate the effect of impurities (molecular oxygen) on the development of continuous surface streamer channels under atmospheric-pressure conditions. In pure argon, a continuous conductive streamer successfully bridges the gap between two electrodes indicating high probability of transition to arc. Presence of oxygen impurities in small concentrations (less than 5%) is found to be conducive to streamer induced thermal breakdown as it reduces the threshold voltage of streamer formation and minimizes unwanted streamer branching effects while maintaining a high probability of streamer to arc transition. Higher oxygen impurity levels $> 5\%$ are found to significantly deteriorate the continuous conductivity of streamer channel and lead to a much lower probability for transition to thermal arcs.

In the second part of the work, we present a computational study of nanosecond streamer discharges in helium gas (He) bubbles suspended in distilled water (H_2O) for liquid reforming applications. The model takes into account the presence of water vapor in the gas bubble for an accurate description of the discharge kinetics. The objective is to study the kinetics and dynamics of streamer evolution and maximize active species production within the gas bubbles which is the quantity of interest for plasma processing of liquids. We investigate two parameters, namely a) trigger voltage polarity and b) the presence of multiple bubbles, which are found to significantly influence the characteristics of the discharge in gas bubbles. A substantial difference is observed in initiation, transition and evolution stages of streamer discharge for positive and negative trigger voltages. The volumetric distribution of species in the streamer channel is more uniform for negative trigger voltages on account of the formation of multiple streamers. In case of the presence of more than one gas bubble, we see the phenomenon of streamer hopping between bubbles where the high electric field in the sheath of the first bubble triggers the streamer discharge in the adjacent bubble. The presence of multiple immersed bubbles reduces the breakdown voltage of the plasma discharge and results in more uniform generation of active species. It is concluded that a negative pin trigger with multiple immersed gas bubbles maximizes the active species generation which is conducive to plasma assisted liquid reforming applications.

In the final part of the work, a coupled two-dimensional computational model of nanosecond pulsed plasma induced flame ignition and combustion for a lean H_2−air mixture in a high pressure environment is described. The model provides a full fidelity description of plasma formation, combustion ignition, and flame development. We study the effect of three important plasma properties that influence combustion ignition and flame propagation, namely a) plasma gas temperature, b) plasma-produced primary combustion radicals $\mathrm{O, OH, and\, H}$ densities, and c) plasma-generated charged and electronically excited radical densities. Preliminary zero-dimensional studies indicate that plasma generated trace quantities of $\mathrm{O, OH\, and\, H}$ radicals drastically reduces the ignition delay of the H_2−air mixture and becomes especially important for high pressure lean conditions. Multi-dimensional simulations are performed for a lean H_2−air mixture (ϕ=0.3) at 1 and 3.3 atm and a range of initial temperature from 1000 - 5000 K. The plasma is accompanied by fast gas heating due to N_2 metastable quenching that results in uniform volumetric heating in the interelectrode gap. The spatial extent of the high temperature region generated by the plasma is a key parameter in influencing ignition; a larger

high temperature region being more effective at initiating combustion ignition. Plasma generation of even trace quantities ($\sim 0.1\%$) of primary combustion radicals, along with plasma gas heating, results in a further fifteen-fold reduction in the ignition delay. The radical densities alone did not ignite the H_2-air mixture. The generation of other plasma specific species results only in a slight $\sim 10\ \%$ improvement in the ignition delay characteristics over the effect of primary combustion radicals, with the slow decaying ions $({H_2}^+, {O_2}^-, O^-)$ and oxygen metastable species $({O_2}^{a1}, {O_2}^{b1}, {O_2}^*)$ primarily contributing to combustion enhancement. These species influence the ignition delay, directly by power deposition due to quenching, attachment and recombination reactions, and indirectly by enhancing production of primary combustion radicals.

Table of Contents

List of Tables

List of Figures

Chapter 1

Introduction

Non-equilibrium plasma discharges finds application in wide range of areas such as fuel reforming [10], combustion ignition [11], semiconductor processing [12], display panels [13], plasma medicine [14], nanomaterials and nanoparticle synthesis [15, 16], water purification [17] and thermal breakdown applications [18]. Non-equilibrium plasmas are characterized by ionization fractions of $\sim 10^{-6} - 10^{-3}$ and can be operated in low pressure and high pressure regimes. In low pressure chambers, these plasmas are highly diffused and have a characteristic glow on account of the large mean free path of the species in the rarefied medium. These plasmas are referred to as glow discharges and characterized by small currents ($\sim \mu$A) and develop over microsecond timescales. In high pressure chambers, these plasmas acquire a filamentary nature and are also termed as streamers. Streamer discharges are characterized by moderate currents ($\sim$ mA) and usually develop over faster nanosecond timescales. Non-equilibrium plasmas are typically operated using direct-current (DC), nanosecond pulsed, radio-frequency, inductively-coupled, microwave and other sources. Under most operating conditions (currents $<$ 100 mA) these discharges are not in thermal equilibrium since the temperature of the electrons ($\sim$ 1-10 eV) far exceeds the temperature of the ions and neutral species ($\sim$ 300-3000 K). This is primarily on account of the small characteristic timescales of these discharges ($\sim$ ns) and extremely low energy transfer efficiency of electrons via collisions over these short timescales. They are hence referred to as non-thermal or "cold" plasmas. At higher pressures, streamers can typically transition into thermal plasmas or arcs if the streamer channel maintains sufficient conductivity over longer timescales which allow the electron to reach thermal equilibrium with the heavy species and reach a common temperature of $\sim$ 1 eV. Arcs are thermal plasmas characterized by large discharge currents $>$ 100 mA and typically formed over microsecond timescales. The present work will focus on non-equilibrium plasmas formed under high pressure conditions over millimeter length scales and nanosecond timescales.

Direct current discharges are typically generated by applying a large potential difference between two parallel electrodes. If the applied voltage, exceeds a threshold value known as the 'breakdown' voltage, a self-sustained plasma is established between the electrodes. The threshold voltage is a function of the operating pressure, gas composition and the interelectrode gap. The bulk of the plasma is quasi-neutral, i.e. net space charge in this region is zero, except in the region near solid and liquid surfaces which are typically electrodes or dielectric surfaces. In case of solid surfaces, a thin non-neutral region known as the sheath is formed. The primary function of the sheath is to maintain overall current continuity in the discharge by arresting the flux of highly mobile electrons to the electrode surfaces, resulting in a potential profile that accelerates positive ions towards the electrodes. The thickness of sheath is $\sim \mu m$ and constrained by the debye length of the electrons. In case of liquid surfaces, an electrostatic debye layer is formed which functions similar to a sheath and limits the transport of highly mobile electrons into the liquid medium. The thickness of the electrostatic debye layer is $\sim nm$ and typically constrained by the diffusion length scales of solvated electrons in the liquid. When the positive ions impact the electrodes, secondary electrons are emitted from the metal surface and these electrons rapidly gain energy in the sheath sufficient to cause further ionization of the gas at the sheath edge. Hence, secondary electron emission is a key mechanism that helps establish a self-sustaining plasma for non-equilibrium direct-current discharges. A streamer channel usually comprises of a thin long filament with considerable space-charge concentration at the head of the filament and quasi-neutral plasma distribution in the rest of the channel. Nanosecond pulsing is a common approach to generate streamers while preventing their transition to thermal plasmas. The underlying principle is that a higher-than-threshold voltage applied over short nanosecond timescales is sufficient for formation of transient filamentary streamers but insufficient for thermalization of these streamer channels which require longer microsecond timescales.

Surface streamers (i.e streamers creeping along the surface of the dielectric) find importance is their use as an intermediate stage to initiate thermal breakdown at relatively lower voltages [19, 20, 21, 22, 23]. This depends on the ability of the streamer channel to maintain high conductivity as it bridges the interelectrode gap which can be greatly influenced by the presence of gas impurities [24, 25]. This is the focus of the first part of the present work which models argon (Ar) surface streamers as a low-voltage mechanism for initiating thermal breakdown in large interelectrode gaps and investigates the effect of oxygen (O_2) impurities on the dynamics of this transition process.

Plasmas generated by electrical discharges in liquids or in the immediate vicinity of liquids have attracted attention in the field of clean energy based liquid fuel reforming [10, 26, 27, 28, 29, 30, 31, 32, 33] and plasma medicine [14]. In the field of liquid fuel reforming, active species and radicals generated by plasma discharges in liquids are used to facilitate reforming, which is the process of breaking down larger hydrocarbons into smaller ones. These simpler hydrocarbons burn more cleanly and are commercially more important. In the area of plasma medicine, 'cold' plasma torches have shown great potential towards wound healing and tissue repairs [14]. A common approach for initiating plasmas in liquids is to introduce gas bubbles into the liquid medium and initiate plasma discharge into these immersed gas bubbles [34]. The active species in the plasma discharge formed in these immersed gas bubbles migrate to the liquid surface where they diffuse, solvate and react with the surrounding liquid medium or tissues serving their main purpose in the application. Hence, plasma generated active species and excited radicals are the quantity of interest for these multiphysics applications. The second part of the present work focuses on high-fidelity simulations of plasma discharges generated in Helium (He) bubbles introduced in distilled water to gain insight into the parameters influencing kinetics and dynamics of the plasma active species. Preliminary studies are also conducted to model plasma penetration into the liquid medium using a multiphase-plasma fluid model to resolve the active liquid layer and electrostatic debye layer in the liquid medium.

In the last decade, there has been an increased interest in utilizing non-equilibrium plasma discharges for combustion ignition applications [35, 11, 36]. Studies have shown that non-equilibrium plasma generated active radicals and reaction species can significantly influence the combustion efficiency, reduce NO_x emission and enables ignition at low initial temperatures. Obtaining an understanding into the complex spatio-temporal dynamics governing this multiphysics process would require a fully coupled high-fidelity computational model that can simultaneously resolve the plasma and combustion kernel in multiple (2D or higher) dimensions, seamlessly transitioning from the former to the latter as the plasma discharge begins to quench. This is the focus of the final part of the present work where we develop a coupled plasma combustion solver and perform high fidelity simulations to resolve plasma formation, combustion ignition, and flame development stages in lean H_2-air under high pressure conditions.

1.1 Surface streamer based thermal breakdown

1.1.1 Review

Surface streamers that bridge a large interelectrode gap can serve as the initial conducting channel from which an arc discharge can develop in an interelectrode region under high pressure conditions [19, 20, 21, 22, 23]. Fig. 1.1 shows the transition of the initial streamer channel into a thermal plasma as observed in the experimental studies by Pachuilo et al. [1]. The key features of streamer-to-arc transition are a) nanosecond timescales for streamer formation as compared to microsecond timescales for direct arc discharge and b) lower electrode voltage for surface streamer breakdown ~ 1 kV as compared to ~ 100 kV required for millimeter to centimeter gap breakdown as dictated by the Paschen breakdown mechanism [37, 12]. As a result, arcs can be ignited much faster and at lower voltages through the use of surface streamers as an intermediate stage. Arcs initiated by surface streamers have found application in a wide range of areas including but not limited to aerodynamic applications [38, 39, 40, 41], magneto-hydrodynamic control of hypersonic flows [42], plasma assisted combustion and ignition [43, 44],plasma actuators [45, 13], atmospheric-pressure dielectric barrier discharge [43, 13] etc.

The success of the streamer in bridging the gap largely depends on the continuous conductivity of the streamer channel throughout the length of the interelectrode gap [24, 25] as well as the time-scale for which this conductivity can be maintained [46] long enough to allow transition to arcs. Gas impurities play an important role in determining the conductivity of the medium because they act as the source or sink of electrons. Also, impurities can significantly influence the plasma chemical reactions in the streamer channel. The dynamic characteristics of the streamer discharge in inert gases are quite different from those in air and pure nitrogen. This is due to the differences

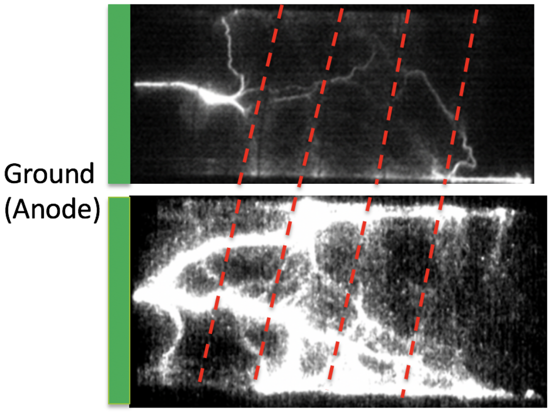

Figure 1.1: Long exposure images of streamer formation (top image) and streamer to arc transition (bottom image) in experiments done by [1]. The red dotted lines are the helically would copper wires embedded in the quartz tube(which forms the plasma chamber).

in the electron mean free path in these three mediums. Moreover, impurities of electronegative gases (e.g. O_2, SF_6) are important as they have electron-attachment reactions and thus these impurities can bring a significant change in the conductivity and the breakdown voltage of the discharge.

1.1.2 Objectives

The goal of the first part of this study is to use computational models to gain physical insight into the kinetics and dynamics of argon surface streamers. The aim of this work is to investigate the use of surface streamers as a low-voltage mechanism for thermal breakdown in large interelectrode gaps. Since the presence of impurities is common for most of these applications, we further aim to study the effect of impurities (molecular oxygen) on the development of continuous surface streamer channels under atmospheric-pressure conditions. In particular, we aim to analyze the influence of the oxygen impurities on the breakdown voltage, streamer induction time, streamer velocity and the physical properties of the streamer channel. To model the spatio-temporal dynamics associated with streamer to arc transition, it is necessary to incorporate finite-rate reaction mechanisms for argon gas for varying concentrations of oxygen impurities. Hence, we aim to develop and validate a finite rate plasma chemistry mechanism of $\mathrm{Ar-O_2}$ mixture for high pressure conditions.

1.2 Plasma discharges in liquids

1.2.1 Review

The use of non-equilibrium plasmas for liquid reforming and biomedical applications has attracted significant attention in recent years [10, 26, 27, 28, 29, 30, 31, 32, 14]. This approach is motivated by the ability of non-equilibrium plasmas to generate a highly reactive medium at room temperatures which is otherwise difficult to achieve. These discharges have been found to be effective in the production of reactive species and radicals that drive chemical reactions in the liquids for a number of applications [47]. The work of Lu et al. [14] provides an in-depth review of reactive species generation through non-equilibrium atmospheric-pressure plasma jets and their interaction with tissue cells for wound healing and treatment. In particular, non-equilibrium nanosecond plasma discharges have the advantage of coupling most of the input electrical energy to the electrons with negligible gas heating. These discharges also make it possible to achieve efficient and non-uniform spatial production of active chemical species if one can exercise some measure of control on the direction of streamer propagation.

Non-equilibrium plasmas are readily generated in gaseous environment, but their extension to generation of ionized species in a liquid medium requires extremely high electric fields [48]. This is on account of the high liquid densities which are three orders of magnitude larger than gas densities [49, 50]. For example, breakdown electric fields for distilled water under atmospheric pressure conditions is of the order of 0.1 - 0.4 MV/cm while the breakdown fields in argon is around 0.3 kV/cm [51, 34]. To circumvent this issue, one can generate plasmas near or in-contact with liquid [49]. Thus, discharges can be generated in the gas phase in the immediate vicinity of the liquid or in bubbles immersed within the liquid. These bubbles can be generated inside the liquid due to electrostriction effect [50], electrolysis [52], underwater spark discharges [53, 54] or can be introduced into the liquid using external gas source [10, 55]. The high voltage requirement ($\sim$ 100 kV) for bubble generation through electrostriction and additional energy for electrolysis means that the introduction of gas bubbles provides perhaps the best option for large industrial scale liquid fuel reforming using plasma technology.

Discharges in gas bubbles have been can be generated using both DC [56, 33, 57] and Microwaves sources [58]. Fig. 1.2 show the experimental setup used by Miotk et al. [2] for microwave plasma based reforming of mixture of

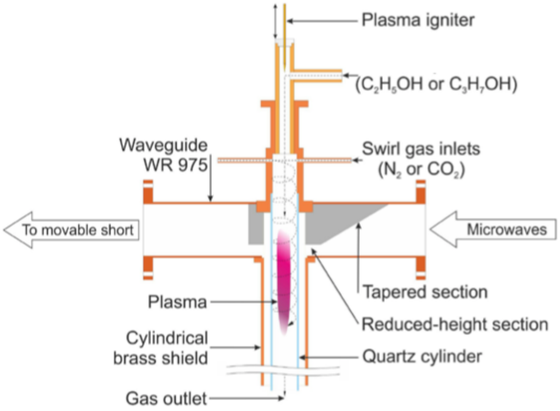

Figure 1.2: Experimental studies by [2] on reforming of ethanol and propanol mixture using microwave plasmas.

$C_2H_5OH-C_3H_7OH$. The mixture is introduced from the top and a wave guide setup is used to generate microwave plasmas. Pure hydrogen gas is produced as a result of the reforming process which is extracted from the bottom of the setup. Figure 1.3 shows the schematic of the setup used by Hirst et al. [3] for treatment of tumors. Gas flow is ignited by high voltage applied across ring electrodes. The core plasma propagates from the end of the tube and is applied into a bulk tumor, causing DNA damage through the formation of reactive oxygen and nitrogen species.

Sommers et al. [59] showed that oscillations of deformed gas bubbles could result in significant electric field enhancement at the bubble surface which can be used as a tool to facilitate plasma breakdown in gas bubbles immersed in liquids. The method of injection of bubbles into liquids and generation of plasma within these gas bubbles has been studied extensively both

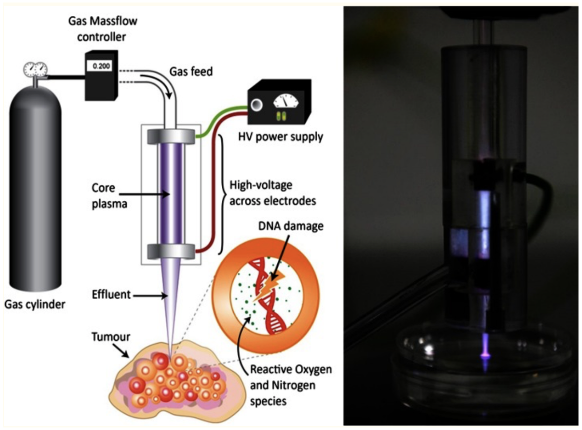

Figure 1.3: Schematic representation (left) of low temperature plasma formation and application for treatment of tumors, cold plasma jet observed in experiments (right). [3]

experimentally [59, 60, 61, 8, 62] and computationally [63, 64, 65, 66, 67, 68, 69] this past decade. Several groups have also conducted experiments to study the fundamentals of discharge in a single bubble immersed in liquids [59, 60, 61, 8]. Discharges at atmospheric-pressure and over-voltage conditions are seen to evolve through streamers where the liquid dielectric constant, liquid conductivity and voltage can be chosen in such a way so as to control the direction of the streamer propagation [63] and make it move along the bubble axis or along its surface. This results in selective and non-uniform generation of the active chemically reactive species in the trail of the streamer. For liquids with a reasonably high vapor pressures, the gas bubble can be saturated with the liquid vapor which can have a strong influence on the bubble plasma kinetics. Other important features of plasmas generated within bubbles are: (1) well-defined plasma–liquid interface and large surface-to-volume ratio; (2) possibility to control plasma chemical reactions and gas component content using different buffer gases (e.g. air, noble gases, etc) for better plasma processing; (3) capability of both direct-current (DC) and alternating current operating modes.

1.2.2 Objectives

This goal of the second part of this work is to perform high-fidelity simulations of nanosecond pulsed plasmas generated in helium bubbles immersed in distilled water under atmospheric pressure conditions. The objective of the study is to obtain physical insight into the discharge structure, chemical kinetics and spatio-temporal dynamics in order to maximize active species production within the gas bubbles, as the active specie and plasma radicals are our quantity of interest. To resolve the chemical kinetics processes governing the generation of active species and plasma radicals in the immersed gas bubbles, we aim to formulate $He-H_2O$ plasma chemistry for atmospheric pressure conditions by compiling relevant reactions from existing literature. The presence of water vapor in the gas bubble is taken into account for a more accurate description of the plasma discharge kinetics. This study aims to investigate two main parameters namely a) trigger voltage polarity and b) the presence of multiple bubbles, which have been proposed to significantly influence the dynamics of the plasma discharge in the suspended gas bubbles. To model plasma penetration inside the liquid, we also propose to develop and implement a multi-phase plasma fluid model to simulate the transport,

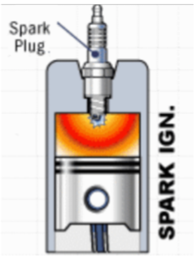

Figure 1.4: Schematic of spark ignition process in internal combustion engines, take from [4].

solvation and reaction of plasma species in the liquid medium. Owing to large disparity in the length scales in the gas and the liquid medium (three orders of magnitude) for resolving the plasma processes, our goal (with regards to the plasma penetration in liquids) is to perform 1D simulations to gain qualitative insight into the formation of active liquid layer and electrostatic debye layer in the liquid medium.

1.3 Plasma assisted combustion ignition

1.3.1 Review

Traditional internal combustion (IC) engines utilize spark plugs (Fig. 1.4) that initiate a combustion kernel by depositing a large amount of energy into a small volume within the fuel-air mixture. The spark channel expands to redistribute this energy generating a complex reactive flow field, through a series of compression waves and shocks, before eventually transitioning into a combustion kernel.

Major disadvantages of spark ignition include increased ignition misfires under lean combustion and high-pressure conditions. To improve upon these limitations, new combustion engine technologies [70, 71] have been developed to operate at high pressures and lower temperatures. However, they face significant challenges in the field of ignition timing control and flame stability. A recent interest in supersonic transportation has also highlighted these challenges for supersonic operation, where there is not enough time for the fuel to auto-ignite since the flow timescales are smaller than the spark discharge based combustion timescales [72]. In industrial power generation applications, ultra-lean HHC (high hydrogen content) is one of the preferred approaches to reduce NO_x and CO_2 emission but this encounters obstacles in the form of combustion instability and flame flashbacks [73]. Thus there is a need for new combustion ignition technologies that can address the issues of ignition tunability, flame stability, low temperature combustion, combustion enhancement and emission reduction in a wide range of conditions. Non-equilibrium plasma based ignition offers significant potential to achieve success in several different areas.

Non-equilibrium plasmas generate active radicals and reactive species that significantly modify reaction pathways and considerably enhance combustion efficiency, enabling ignition at lower initial temperatures. This also makes them quite suitable for NO_x emission reduction. These discharges also have extremely small timescales $\sim$ ns making them attractive from an ignition timing control perspective. In last the two decades, non-thermal plasmas have been investigated as a promising technique for ignition, flame stabilization,

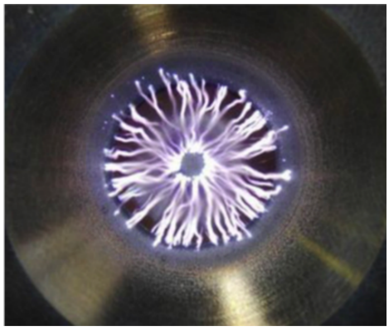

Figure 1.5: Nanosecond pulsed plasma based igniter used for ultra-lean combustion in high pressure methane air mixture [5].

combustion enhancement, and emission reduction [11, 35, 36, 74, 75, 76, 77]. The nanosecond pulsed plasma igniter shown in Fig. 1.5 has been used for experimental studies of ignition of CH_4−air mixtures by nanosecond pulsed plasmas. Studies were conducted on the development of a pulsed high-voltage nanosecond discharge in a series of plasmatrons [5] for ultra-lean mixture ignition . These plasmatrons have been used by Nikipelov et al. [5] to ignite ultra-lean ($\phi = 0.06 - 0.3$) flames across a wide range of equivalence ratios and temperatures for methane and diesel vapor at a pressure of 1 bar.

Fig. 1.6 shows the experimental studies on stabilization of methane-air mixture using non-equilibrium plasma discharge [7]. Experimental studies have shown that nanosecond discharges can lower the ignition delays in IC engines [44] and pulsed detonation engines [78, 79, 80]. Recent experimental studies in the field of supersonic propulsion (Fig. 1.7) have shown that various forms of non-thermal pulsed plasma discharges can improve fuel/air mixing, enhance ignition, and induce flame stabilization [6, 81, 82].

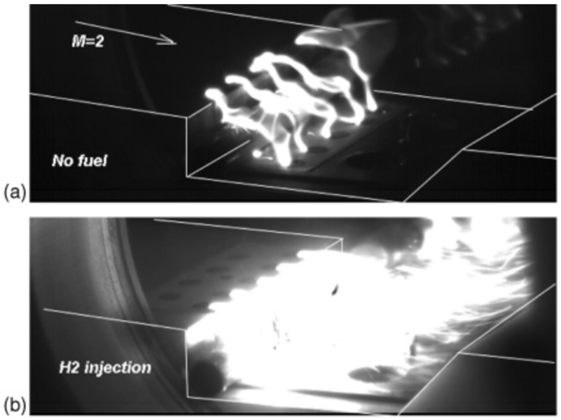

Figure 1.6: Observations of nanosecond pulsed plasma assisted combustion in supersonic flows taken from [6](a) Formation of non-equilibrium plasma kernel in absence of H_2 (fuel) (b) Ignition of H_2 by the non-equilibrium plasma kernel.

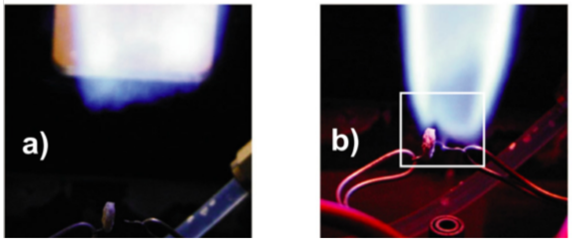

Figure 1.7: Observations of discharge enhanced flame stabilization. (a) Without discharge and (b) with discharge. (a) and (b) are taken from [7].

Non-thermal plasma-based ignition and combustion has been successfully demonstrated in IC engines using corona and nanosecond pulsed discharges [44, 83, 84]. It has also been shown that non-thermal discharges can effectively lower the emission of unburned hydrocarbons and reduce NO_x and SO_x emissions [85, 86, 87, 88]. Several experimental studies have been performed to obtain an improved understanding of the thermal and kinetic processes governing non-thermal plasma assisted combustion. It has been found that atomic oxygen (O) production of by electron impact reactions with O_2, excited nitrogen species and ions [89, 90, 36] are the major pathways that facilitate combustion at low temperatures. Studies have also shown that increased concentration of atomic hydrogen (H), hydroxyl (OH) radicals and gas heating effects during the formation of nanosecond pulsed discharge lower the ignition temperature by 200 K [91]. Although these experiments provide insights into the physio-chemical processes underlying plasma-driven combustion enhancement, the number of measurable quantities remain limited and many conclusions are indirectly inferred.

To bridge this gap, several computational studies have been carried out to obtain a deeper understanding of the mechanisms responsible for plasma assisted combustion. The underlying physics governing the formation of the initial plasma kernel can be accurately captured by existing plasma models [92, 93]. This has motivated several studies that investigate the dynamics of a plasma discharge in a premixed fuel-air mixture[93, 94] and study the influence of oxygen on the plasma kernel formation [18]. However, numerical modeling of plasma-assisted ignition and combustion appears to be limited, primarily due to the range of scales involved. Most modeling studies of ignition by a nanosecond discharge are zero-dimensional (0D) [95, 96, 97] due to the computational complexity associated with simultaneously resolving disparate spatio-temporal scales in multiple dimensions. Zero-dimensional (0D) studies [96] have demonstrated that metastable species produced by non-equilibrium plasmas reduce ignition delay of fuel/air mixtures. Low pressure studies by Yang et al. [98] identified the need for higher dimensional simulations to resolve the underlying physics and outlined strategies for simplified coupling in one dimension (1D). Other work, performed at low or atmospheric pressures include studies of DBD based ignition using simplified 1D models [99], non-thermal plasma based ignition of n-heptane [100], and H_2-O_2 [101] mixtures. Atmospheric pressure studies have also been conducted to resolve the hydrodynamic expansion following a nanosecond pulsed discharge [102] in higher dimensions, neglecting the combustion kinetics. A recent two-dimensional (2D) study [103] considered an initial plasma kernel distribution, approximated the plasma generated gas heating by time integrating the energy released over the discharge duration and then used this temperature kernel to ignite a fuel-air mixture. While these studies provide significant insight into the kinetic mechanisms through which non-equilibrium plasmas enhance ignition, a more complete understanding of the complex spatio-temporal dynamics underlying plasma-assisted combustion was missing. Obtaining this understanding would require a fully coupled high-fidelity computational model that can simultaneously resolve the plasma and combustion kernel in multiple (2D or higher) dimensions, seamlessly transitioning from the former to the latter as the plasma discharge begins to quench.

1.3.2 Objectives

The goal of the final part of this work is to obtain physical insight into the discharge structure, chemical kinetics and spatio-temporal dynamics of nanosecond pulse plasma induced flame ignition and combustion in a lean premixed H_2-air mixture under high pressure conditions. The objective is to simulate the formation of an initial plasma kernel and investigate its influence on the ignition of a combustion kernel using a fully coupled multi-dimensional computational framework. Hence, we aim to develop a computational model to resolve the complex spatio-temporal dynamics of this highly coupled multiphysics problem. The model must be able to provide full fidelity description of plasma formation, combustion ignition, and flame development stages. The plasma and combustion length scales are highly disparate and the coupled framework must account for the disparate length scales governing these process to a) resolve individual processes of plasma and combustion stages accurately b) optimize computational performance by choosing the appropriate length scale for modeling each stage. Next, to model plasma assisted combustion ignition phenomenon, there is a need for formulating reaction mechanisms that are capable of representing all important chemical effects in both non-equilibrium plasma and combustion. The chemical kinetics governing these processes are dissimilar, since both these processes are inherently different physical phenomenon with largely disparate characteristic length scales and time scales. Hence, we aim to develop and validate a separate plasma and combustion chemistry mechanisms for lean H_2-air mixture under high pressure conditions.

Chapter 2

Computational Model

In this chapter, the computational models for non-equilibrium plasmas and combustion are discussed in detail. The plasma model has been under development as a group effort since 2003 [104, 105, 106, 107, 108, 109, 110, 111], while the combustion model has been developed, by coupling the non-equilibrium plasma model with a compressible flow solver [111] with necessary additions to resolve the combustion process. The combustion solver adds significant new capability to the computational tool set that our group possesses. Both plasma and combustion models use the same underlying mesh infrastructure and can be used in a standalone fashion or a fully coupled manner based on the application.

2.1 Non-equilibrium plasma model

2.1.1 Assumptions

1. A continuum fluid approach is used to model non-thermal plasmas at atmospheric pressure conditions or higher used in the present study. This assumption is reasonable if the mean free path of the species is smaller than the characteristic dimensions of the discharge which is usually valid for operating pressures greater than 10 Torr for millimeter

scale dimensions. The continuum assumption is questionable near the cathode sheath region where the electric fields are strong and the electron kinetic effects are important. Nevertheless, past studies have shown that the fluid model predicts the plasma properties fairly accurately for millimeter-scale plasmas [112, 113].

2. A two-temperature model is used in this work with a common temperature for all heavy species and a separate temperature for electrons. Thermal equilibrium amongst heavy species is valid if the energy transfer mean free path between ions and neutrals is smaller than the characteristic dimensions of the plasma which is true for pressures greater than 10 Torr, and hence valid for the current work.
3. A local mean energy approximation (LMEA) is used to evaluate the transport and rate coefficients in this work . The LMEA approximation stipulates that the rate coefficients and electron transport coefficients are a function of the local mean electron energy and this approximation is accurate at high pressure conditions used in the current work. [18, 92],
4. Drift-diffusion approximation is used to approximate the species momentum equation. This simplification of the momentum equation assumes that collisional processes are dominant, while the inertial terms and time variations of species momentum are negligible. This assumption is reasonable for operating pressures $>$ 0.1 Torr and millimeter scale dimensions where the plasma is highly collisional and the mean free path of

the species is much smaller than the characteristics length scales.

5. The ion Joule heating effect is neglected due to the relatively low drift velocities of the ions in the bulk of the discharge compared to the electrons. The ion Joule heating term is significant within the sheath, owing to the large sheath electric fields. However, since the dimensions of the sheath are comparable to the mean free path for ion-background gas collisions, it is assumed that the ions are unable to transfer the kinetic energy gained from the electric field to the background gas due to insufficient number of collisions [113].

2.1.2 Governing equations

The non-equilibrium plasma model is based on a self-consistent multi-species continuum based formulation with finite rate chemistry. The governing equations are derived by taking the moments of the species Boltzmann equation, with the first three moments yielding the continuity, momentum and energy conservation equations respectively. These equations are described below.

Species Continuity

The number densities of constituent species in plasma is determined by solving the species continuity equation

$$\frac{\partial}{\partial t}(n_k) + \vec{\nabla} \cdot (\vec{\Gamma}_k) = \dot{G}_k + \dot{G}_{ph}. \tag{2.1}$$

Here, k is the index of individual species, n_k denotes the number density and $\vec{\Gamma}_k$ denotes the species flux. The first source term $\dot{G}_k$ in the continuity equation denotes the chemical production rate of species k and is computed using the rate coefficients associated with the production and/or consumption of the appropriate species. These rate coefficients are formulated as a function of the mean electron energy by solving the zero−dimensional electron Boltzmann equation solver BOLSIG+ [114]. The second source term $\dot{G}_{ph}$ in the continuity equation incorporates the effect of photo-ionization and becomes important for plasma discharges in air. Details of the Air photo-ionization model are provided is section 2.1.2. The above equation is solved for all constituent species in the plasma except the dominant background gas. The density of the background gas is calculated based on the total pressure and is given by

$$p = n_e k_B T_e + k_B T_g \sum_{k \neq k_e} n_k \tag{2.2}$$

Here p is the total gas pressure in plasma domain, n_e is electron number density, T_e is electron temperature, T_g is heavy species or gas temperature and k_B is the Boltzmann constant.

Species Number Flux

The species number flux ($\vec{\Gamma}_k$) is obtained using the drift-diffusion approximation given by

$$\vec{\Gamma}_k = -z_k \mu_k n_k \vec{\nabla}\phi - D_k \vec{\nabla} n_k \tag{2.3}$$

where z_k denotes the species charge number, μ_k and D_k denotes the mobility and diffusion coefficient respectively of the individual species k . The drift diffusion approximation is a simplification of the species momentum equation for a collisional plasma and is valid in cases where the species mean free path is significantly smaller than the characteristic length scale of the problem [115, 116, 108]. This is true for atmospheric pressures conditions and millimeters length scale problems considered in this study and hence usage of the assumption is justified. Electron transport properties μ_e, D_e are computed as a function of electron temperature T_e (Local Mean Energy Approximation) using the zero-dimensional Boltzmann equation solver BOLSIG+ [114] while the ion transport properties are referred using experimental data.

Electrostatic Potential Equation

The discharge in the present work is categorized as weakly ionized ($< 0.1\%$ ionization) plasma and characterized by small current densities and negligible magnetic fields. Thus the Maxwell's equations are reduced to solving a single Poisson's equation for evolving the electrostatic potential ϕ in the plasma domain

$$-\vec{\nabla} \cdot (\epsilon_r \vec{\nabla}\phi) = \frac{e}{\epsilon_o} \sum_{k=1}^{N} Z_k n_k \tag{2.4}$$

where ϕ is the electrostatic potential, e is the elementary charge, Z_k is the charge of the k^{th} species, ϵ_r is the dielectric constant and ϵ_o is the permittivity of free space. The source term of Eq. 2.4 represents the the net space charge density due to all charged species in the plasma.

Species Energy Equation

The two-temperature treatment of the plasma results in separate energy balance equations for the electrons and the heavy species. The mean electron energy e_e is defined in terms of the electron temperature as

$$e_e = \frac{3}{2} n_e k_B T_e \tag{2.5}$$

and is obtained by solving the complete electron energy conservation equation given by

$$\frac{\partial}{\partial t} e_e + \vec{\nabla} \cdot \left((\frac{5}{3} \mu_e \vec{\nabla} \phi + \vec{V}) e_e - \frac{5}{3} D_e \vec{\nabla} e_e \right) = e \vec{\Gamma}_e \cdot \vec{\nabla} \phi + \Lambda_{e,elastic} + \Lambda_{e,inelastic} \tag{2.6}$$

where $\vec{V}$ is the bulk velocity (= 0 for a stationary plasma), μ_e is the electron mobility and D_e is the electron diffusion coefficient. The first source term ($e\vec{\Gamma}_e \cdot \vec{\nabla}\phi$) of Eq. 2.6 is the electron Joule heating term while the second ($\Lambda_{e,elastic}$) and third terms ($\Lambda_{e,inelastic}$) indicate the losses due to elastic and inelastic collisions respectively. The collisional loss term for elastic and inelastic collisions are given by

$$\Lambda_{e,elastic} = -\frac{3}{2}k_B n_e \frac{2m_e}{m_{k_b}}(T_e - T_g)\bar{\nu}_{e,k_b}, \tag{2.7}$$

$$\Lambda_{e,inelastic} = -e\sum_{i=1}^{I_g} \Delta E_i^e r_i \tag{2.8}$$

In Eq. 2.7 and Eq. 2.8, m_e and m_{k_b} are the molecular weights of electron and dominant background gas species respectively, $\bar{\nu}_{e,k_b}$ is the electron momentum transfer collision frequency with the background gas, ΔE_i^e is the energy lost per electron (in eV) in an inelastic collision event represented by the gas phase reaction i, r_i is the rate of progress of reaction i, and I_g is the total number of gas-phase reactions involving electrons. The heavy species (ions and neutral) are assumed to have a common temperature T_g which is determined by solving the heavy species energy equation given by

$$\begin{aligned}\frac{\partial}{\partial t}\left(\sum_{k\neq k_e} n_k C_{v_k} T_g\right) + \vec{\nabla}\cdot\left(\sum_{k\neq k_e} C_{p_k} T_g \vec{\Gamma}_k - \sum_{k\neq k_e}\kappa_k \vec{\nabla} T_g\right) \\ = \alpha\left(\sum_{k\neq k_e} e z_k \vec{\Gamma}_k \cdot \vec{\nabla}\phi\right) + \Lambda_{g,collisions}\end{aligned} \tag{2.9}$$

$$\Lambda_{g,collisions} = \frac{3}{2}k_B n_e \frac{2m_e}{m_{k_b}}(T_e - T_g)\bar{\nu}_{e,k_b} - e\sum_{j=1}^{I_g} \Delta E_j^g r \tag{2.10}$$

In Eq. 2.9, summation in each term is over all the species in the plasma except electron. C_{v_k}, C_{p_k} and κ_k are the specific heat capacities and the thermal diffusivities of the heavy species k. The source term of this equation comprises of the ion Joule heating term and the collisional heating terms. The multiplier α to the ion Joule heating term represents the fraction of ion kinetic energy that is thermalized with the neutral gas. Consequently the factor $(1-\alpha)$ is the fraction of the ion energy lost to the wall surface. If the ion mean free path is comparable to the sheath thickness, the ions fail to thermalize with the neutrals and lose all their energy to the wall surface. This is the case for conditions employed in the present work, and hence the energy factor α is set to zero. The collisional source term $\Lambda_{g,collisions}$ in equation Eq.2.10 comprises of (a) heating due elastic collisions (of heavy species with electrons) and (b) inelastic collisions losses due to heavy species reactions. $e\sum_{j=1}^{I_g} \Delta E_j^g r_j$ is the energy lost / gained by heavy species in the j^{th} inelastic collision reaction (in eV). The elastic collision source term in Eq. 2.10 is equal in magnitude but opposite in sign to the elastic collision source term in electron energy Eq. 2.7 as energy lost by electrons due to elastic collisions directly results in energy gained by the heavy species.

Photoionization

In case of gas mixtures containing air, an additional source term appears in the electron species continuity equation Eq. 2.1 to account for the additional production of seed electrons due to ionization of O_2 molecules by photons emitted from de-excitation of N_2 excited states (${N_2}^* \longrightarrow N_2 + h\nu$). This process of ionization by impact with energetic photons is termed as photoionization and the entire process can be expressed as a single reaction ($O_2 + h\nu \longrightarrow E + {O_2}^+$) whose rate appears as the photoionization source term (G_{ph}) for Eq. 2.1. For this study, a three−term version of the Helmholtz model formulated by Breden et al. [109] based on the works of Bourdon et al. [117] is chosen along with relevant fit parameters for air. The three-term Helmholtz model is an approximation of the classical integral model developed in the 1980s by Zheleznyak et al. [118]. In the classical integral model, photoionization source term at a point in space $\vec{r'}$ is expressed as an integral over the domain of interest.

$$G_{ph}(\vec{r}) = \int_V \frac{I(\vec{r'})g(R)}{4\pi R^2} dV \tag{2.11}$$

where $R = |\vec{r} - \vec{r'}|$ is the distance between the location of the photon absorbing species O_2 and emitter ${N_2}^*$ excited species. $I(\vec{r'})$ is an emission function characterizing the intensity of radiation emitted by ${N_2}^*$ during de-excitation.

$$I(\vec{r'}) = \frac{P_q}{P + P_q} \xi G_i(\vec{r'}) \tag{2.12}$$

where production of photons is assumed to be proportional to the rate of ionization $G_i(\vec{r'})$ of the emitted species (N_2), $\xi = 0.02$ is the photoionizaiton efficiency, $\frac{P_q}{P+P_q}$ is a quenching factor, P is the total discharge pressure and P_q is derived from experiments to be about 30-60 Torr. The kernel function $g(R)$ in Eq. 2.11 represents the transport of radiation and determines the absorption of photons by O_2 molecules and is given by

$$\frac{g(R)}{P_{O_2}} = \frac{\exp^{-\chi_{min} P_{O_2} R} - \exp^{-\chi_{max} P_{O_2} R}}{P_{O_2} R \ln(\frac{\chi_{max}}{\chi_{min}})} \tag{2.13}$$

where $-\chi_{min} = 0.035 Torr^{-1} cm^{-1}$, $-\chi_{max} = 2 Torr^{-1} cm^{-}1$ are derived through experiments [117] and P_{O_2} is the partial pressure of molecular oxygen (= 150 Torr at 1 atm)

In the three-term Helmholtz model used in the present study, the calculation of the complete integral in Eq. 2.11 is replaced with a solution of a set of Helmholtz differential equations with three (or more terms)

$$G_{ph}(\vec{r}) = \sum_j G^j_{ph}(\vec{r}) \tag{2.14}$$

with terms on the RHS

$$G^j_{ph}(\vec{r}) = \int_V \frac{I(\vec{r})}{4\pi R} A_j P^2_{O_2} \exp^{-\lambda_j P_{O_2} R} dV \tag{2.15}$$

satisfying the Helmholtz differential equations

$$\nabla^2 G_{ph}^{j}(\vec{r}) - (\lambda_j P_{O_2})^2 G_{ph}^{j}(\vec{r}) = -A_j P_{O_2}^2 I(\vec{r}) \tag{2.16}$$

Comparing Eq. 2.15 and Eq. 2.11, it can be seen that for the solutions of these equations to be identical it is necessary to approximate the absorption function $\frac{g(R)}{P_{O_2}}$ in Eq. 2.13 by a series of exponentially decaying functions given by

$$\frac{g(R)}{P_{O_2}} = P_{O_2} R \sum_j A_j \exp^{-\lambda_j P_{O_2} R} \tag{2.17}$$

The parameters λ_j and A_j are obtained by fitting [117, 109] the experimental data from the original absorption function in air to the approximate absorption function $\frac{g(R)}{P_{O_2}}$ in Eq. 2.17.

2.1.3 Constitutive relations

The transport properties of plasma species namely mobility (μ_k) and diffusion coefficients (D_k) and the species thermal conductivity (κ_k) are derived using a hard sphere collision model. Collision cross-sections (σ) obtained from literature are used to compute the collision frequency of species k with the background gas n_b using the relation

$$\bar{\nu}_{k,b} = n_b \bar{g} \sigma \tag{2.18}$$

Where k is the species index, n_b is the total background density, $\bar{g}$ is the mean thermal velocity, and σ is the total momentum transfer collision cross section of species with the background. Using the collision frequency, the transport coefficients and thermal conductivity are evaluated using the following relations,

$$\mu_k = \frac{eZ_k}{m_k \bar{\nu}_{k,b}} \tag{2.19}$$

$$D_k = \frac{k_B T_k}{m_k \bar{\nu}_{k,b}} \tag{2.20}$$

$$\kappa_k = \frac{5}{2} n_k k_B D_k \tag{2.21}$$

Where m_k is the mass of the species k and T_k is the temperature of the heavy species and n_k is the species number density. As an alternative to the hard sphere model, the transport coefficients can be derived from experimentally available data on mobility and diffusion coefficients. Once the mobility is known, the diffusion coefficient can be calculated using Einstein's relation $D_k = \frac{k_B T_k \mu_k}{e}$ and vice-versa.

For electrons, the zero-dimensional Boltzmann solver BOLSIG+ [114] is used to compute the transport coefficients as a function of reduced electric field $\frac{E}{N}$ or mean electron energy e_e. Under the hood, BOLSIG+ [114] uses the collision cross-sections to compute velocity distribution functions, which are then used to evaluate the transport coefficients and thermal conductivity.

2.1.4 Boundary conditions

Species Continuity

For solid surfaces, the electrons are assumed to be in equilibrium with the wall surface at a temperature T_e. The total flux of the electrons from the discharge to the wall surface comprises of Maxwellian flux and secondary electron emission flux components, and is expressed as

$$\vec{\Gamma}_e \cdot \hat{n}_s = \frac{1}{4} n_e \Big(\frac{8 k_B T_e}{\pi m_e} \Big)^{1/2} - \sum_k \gamma_k (\vec{\Gamma}_k \cdot \hat{n}_s) \tag{2.22}$$

where $\hat{n}_s$ is the unit vector normal to surface of wall, γ_k is the secondary electron emission coefficient associated with species k and Γ_k is the flux of all species k directed towards the wall surface. The first term is Eq. 2.22 is the Maxwellian flux of electrons to the surface and the second term denotes secondary electron emission flux from the dielectric/metal surface into the discharge. Secondary electron emission (SEE) coefficient is typically a function of the material work function, the applied electric field and background gas density and is determined experimentally. For ions, the number flux comprises of Maxwellian flux component and mobility limited flux component,

$$\vec{\Gamma}_i \cdot \hat{n}_s = \frac{1}{4} n_i \Big(\frac{8 k_B T_g}{\pi m_i} \Big)^{1/2} + n_i max(0, -\mu_i \vec{\nabla} \phi \cdot \hat{n}_s) \tag{2.23}$$

Here, the first term on the RHS is the Maxwellian flux component while the second term denotes mobility limited flux. When the electric field is directed towards the wall, the mobility limited flux component is positive for positive ions (as they drift towards the wall surface) and zero for negative ions (as the negative ions are repelled by the surface). A Maxwellian flux condition is imposed for all the neutral species given by

$$\vec{\Gamma}_n \cdot \hat{n}_s = \frac{1}{4} n_n \Big(\frac{8 k_B T_g}{\pi m_i} \Big)^{1/2} \tag{2.24}$$

The plasma model also takes surface reactions into account and the species flux for ions and neutrals is appropriately modified to include the effect of wall surface kinetics. For boundaries representing the edges of the computational domain or boundaries along the plane of symmetry, the flux of species k normal to this boundary is set to zero.

Species Energy

Electron energy can be lost due to electron flux to the wall or gained on account of secondary electron emissions from the wall surface. The energy flux of electrons towards a solid surface is given by

$$\vec{Q}_e \cdot \hat{n}_s = \epsilon_{se}\left(\frac{1}{4}n_e\left(\frac{8k_BT_e}{\pi m_e}\right)^{1/2}\right) - e\Delta E_{se}^{e}\sum_{k}\gamma_k(\vec{\Gamma}_k \cdot \hat{n}_s) \tag{2.25}$$

Here, the first term denotes energy lost by a single electron to the surface on account of electron species flux to the wall and the second term is the energy added to the discharge by electrons emitted from the surface due to secondary electron emission. $\epsilon_{se} = 2k_BT_e$ is the energy content of each electron as it approaches the wall surface which can be derived assuming a Maxwellian distribution function for electrons near the surface which follows from Eq. 2.22. ΔE_{se}^{e} is the energy content of a each electron as it enters the discharge domain due to secondary electron emission and mainly depends on the work function of the material surface. For surfaces denoting the edges of the computational domain, a fixed temperature Dirichlet boundary condition is specified where the temperature is fixed to the constant value.

Electrostatic Poisson's equation

At electrode surfaces, the electrostatic potential is usually specified as a constant or evaluated based on an external circuit if present. In either case, equation 2.4 is given a Dirichlet boundary condition. The impact of the charged species with the dielectric surface results in charging of dielectric surface due to accumulation of charged particles which in turn alters the potential near these surfaces. This boundary surface charge density is evolved by solving an ordinary differential equation,

$$\frac{\partial \rho_s}{\partial t} = \sum_k e z_k \vec{\Gamma}_k \cdot \hat{n}_s \tag{2.26}$$

Here the term on the RHS is the total space charge accumulation at the wall due to charged species flux $\vec{\Gamma}_k$, ρ_s is the surface charge density, z_k is charge number associated with species k and $\hat{n}_s$ is the unit vector normal to the wall surface. After the evaluation of ρ_s, the surface potential is found analytically using Gauss's law given by ($\vec{D}_{dielectric} - \vec{D}_{plasma} = \rho_s$) where $\vec{D} = -\epsilon\vec{\nabla}\phi$ is the electrostatic flux density.

2.2 Combustion model

A combustion solver in the present work is developed to model flame ignition and combustion induced by a nanosecond pulsed plasma discharge. The combustion model is derived by coupling the non-equilibrium plasma model with the compressible flow solver [111] with necessary additions to resolve the combustion process. This section discuss the governing equations for the combustion model.

2.2.1 Assumptions

1. Reactive compressible Euler equations are used to model the combustion process.
2. The species velocity is assumed to be equal for all species in the combustion model. This description is justified on account of presence of

high pressure conditions in the current study which ensures sufficient collisionality between individual species.

3. Electrons are assumed to be in thermal equilibrium with the heavy species. This assumption is reasonable, as the electrons (generated before the combustion stage) quickly thermalize with the background in absence of external electric field and presence of high pressure conditions (1 atm or greater) which ensures high collisionality to achieve thermal equilibrium.

4. Wall viscous effects and thermal conduction to the wall is neglected. This assumption is reasonable for high pressure reactive flow problems, as the contribution of collisional heating to the combustion dynamics is much higher than wall losses due viscous dissipation and thermal conduction. In addition, for small timescales associated with ignition, the viscous and thermal conduction effects are not important.

5. Hirschfelder and Curtis approximation [119] is used to derive the multi-species diffusion coefficient for combustion species. The approximation is valid for sufficiently diluted flames which is the case in air when Y_{N_2} is sufficiently large, which is also true for the present studies.

2.2.2 Governing equations

The dynamics and thermodynamics of chemically reacting flows involved during the combustion process are governed by global conservation laws of mass, momentum, energy and continuity equations for individual species. The combustion process in the present work is modeled using reactive compressible Euler equations. The equation system consists of separate continuity equations for the densities of individual species and a global system of conservation equation for density, velocity and gas temperature. The equations are cast in a conservative form and described below.

Individual species continuity

The number densities of individual species, except the dominant background species N_2, is determined by solving a continuity equation for individual species and given as

$$\frac{\partial}{\partial t}(\rho_k) + \vec{\nabla} \cdot (\rho_k \vec{V} + D_k \vec{\nabla} \rho_k) = \dot{G}_k \tag{2.27}$$

Here, ρ_k and $\vec{V}$ represent the species density and species velocity associated with a combustion species k respectively. D_k is the species mixture averaged diffusion coefficient which differs from the kinetic diffusion coefficient used for plasma species in the non-equilibrium plasma model. The source term $\dot{G}_k$ in the continuity equation denotes the chemical production rate of species k during the combustion process and is computed using the rate coefficients associated with the production and/or consumption of the appropriate species. The species modeled during combustion include all the species generated in the plasma kernel as well as additional species produced as a result of long time scale combustion kinetics.

Global continuity

The global continuity equation governing the evolution of total density is,

$$\frac{\partial}{\partial t}(\rho) + \vec{\nabla} \cdot (\rho \vec{V}) = 0 \tag{2.28}$$

Here ρ is the total density and $\vec{V}$ is the species velocity. The net species density is given by $\rho = \sum_k \rho_k$. The species velocity is the same for all species during combustion and this description is justified on account of presence of high pressure conditions in the current study which ensures sufficient collisionality between individual species. In the current model, mass conservation is imposed by solving the individual species density equations Eq. 2.27 for all the species except the background gas N_2 and solving for global density using Eq. 2.28. The N_2 number density is then obtained from the global mass density as follows,

$$\rho_{N_2} = \rho - \sum_{k \neq N_2} \rho_k \tag{2.29}$$

This couples equations Eq.2.27 and Eq. 2.28 consistently to ensure mass conservation and prevents redundancy in computation of species densities.

Global momentum

The global conservation equation for momentum, neglecting viscous effects, is given as

$$\frac{\partial}{\partial t}(\rho\vec{v}) + \vec{\nabla}\cdot(\rho\vec{V}\vec{V} + p) = 0 \tag{2.30}$$

Here p is the total species pressure. The total species pressure is given by $p = \sum_k n_k k_B T_g$, where $n_k = \rho_k/M_k$ is the species number density in the combustion system indexed using the subscript k, M_k denotes the molecular mass of species k, k_B is the Boltzmann constant and T is the species temperature.

Global energy

The global conservation equation for energy is given by,

$$\frac{\partial}{\partial t}\left(\rho\left(e + \frac{\vec{V}\cdot\vec{V}}{2}\right)\right) + \vec{\nabla}\cdot\left(\left(\rho\left(e + \frac{\vec{V}\cdot\vec{V}}{2}\right) + p\right)\vec{V}\right) = \dot{E} \tag{2.31}$$

Here e represents the total internal energy and T denotes the species temperature. The species temperature is the same for all species during combustion. For the combustion mixture, the internal energy is given by,

$$e = \sum_u \frac{\rho_u e_u}{\rho} \tag{2.32}$$

Where e_u is the internal energy associated with combustion species u. Under high pressure conditions, the contribution of collisional heating to the gas energy equation is much larger than wall losses due viscous dissipation and thermal conduction. This is due to the smaller timescales associated with ignition compared to the viscous dissipation and thermal conduction timescales. Hence in the current combustion model, the source term on the RHS of Eq. 2.31 only comprises of collisional heating term arising from elastic and inelastic collision and thermal and viscous wall losses are neglected. The collisional term is given by,

$$\dot{E}_h = \frac{3}{2} k_B n_e \frac{2m_e}{m_{k_b}} (T_e - T_g) \nu_{e,k_b} - e \sum_{k=1}^{I_g} \Delta E_k^g r_k \tag{2.33}$$

The first term in Eq. 2.33 denotes the energy gained by the heavy species on account of elastic collisions between electrons and heavy species. Similar to Eq. 2.10, this term is positive here since all the energy lost by the electrons due to elastic collision with the heavy species goes into heating the background gas. The second term in Eq. 2.33 is the energy change due to inelastic collisions between heavy species, where r_k rate of progress of the combustion reactions.

The reactive compressible Euler equations outlined are solved in the following manner. First, the combustion species densities ($\rho_k(k \neq N_2)$) are updated using the individual species continuity equations 2.27 taking into account the chemical reactions for species production and consumption and the convective and diffusive fluxes. These densities are used to evaluate the collisional heating source terms 2.33 which are the the dominant power deposition term in the global energy equation during the small ignition timescales. Next, the global system of conservations equations 2.28,2.30 and 2.31 are solved to update the macroscopic properties ρ, $\vec{V}$ and p. These terms are then used to update the species density of N_2 ($\rho_{N_2} = \rho - \sum_k (k \neq N_2)\rho_k$) in order to impose mass continuity, gas temperature $T_g = \frac{p}{\sum_k \frac{\rho_k k_B}{m_k}}$, mixture averaged transport coefficients D_k and the flux and source terms for reactive species continuity equations 2.27. In this way, the combustion process is decoupled and modeled using a reactive continuum formulation to update individual reactive species densities and a global compressible Euler formulation to update the macroscopic combustion properties, while consistently coupling these two formulations to resolve the ignition process.

2.2.3 Constitutive relations

The transport properties for the individual species diffusion D_k are derived using a mixture-averaged formulation. The mixture average diffusion coefficient is different from the kinetic diffusion coefficient used in the non-equilibrium plasma model and takes into account the effect of neighbouring species on the transport properties of individual species. The effect of neighbouring species in D_k is incorporated using the binary diffusion coefficient D_{kj} given by,

$$D_{kj} = \frac{2.1415 \times 10^{-15} T_g^2}{P \pi \sigma_{kj}^2 \sqrt{T_g M_{kj}} \Omega_D} \tag{2.34}$$

Here D_{kj} is the binary diffusion coefficient of species k in species j in $m^2 s^{-1}$,

T_g is the gas temperature in K, P is the total pressure in Pa, M_{kj} is the reduced molecular weights given by $M_{kj} = \frac{M_j M_k}{M_j + M_k}$, Ω_D is the collision integral, σ_{kj} is the Lennard Jones force constant and Ω_D is the collision integral. The Leonard-Jones force constant for the binary mixture σ_{kj} is derived using a hard sphere collision model based on the relation,

$$\sigma_{kj} = \frac{\sigma_k + \sigma_j}{2} \tag{2.35}$$

Here σ_k and σ_j are Leonard Jones collision diameter for the respective species. The collision integral Ω_D for non-polar gases have been fitted (Monchich and Mason to excellent accuracy [119]) and given by

$$\Omega_D = \frac{1.069}{(T^*)^{0.15610}} + \frac{0.3445}{e^{0.6537T^*}} + \frac{1.556}{e^{-2.099T^*}} + \frac{1.967}{e^{-6.488T^*}} \tag{2.36}$$

$$T^{=\frac{k_B T}{\epsilon_{okj}}}(2.37)$$

$$\epsilon_{okj} = \sqrt{\epsilon_{ok}\epsilon_{oj}} \tag{2.38}$$

Here k_B is the Boltzmann gas constant and ϵ_{ok} and ϵ_{oj} are the the Leonard Jones well-depth associated with the respective species. The multi-species diffusion coefficient D_k of species k can be related to the binary diffusion coefficients of species k with all other species using Hirschfelder and Curtis approximation [119] and are given by,

$$D_k = \frac{1 - Y_k}{\sum_{j \neq k} \frac{X_j}{D_{kj}}} \tag{2.39}$$

Where D_k is the multi-species diffusion coefficient of the species in the mixture also termed as mixture averaged diffusion coefficient of the species k, Y_k mass fraction of the species k, X_j is the mole-fraction of neighbouring species indexed by j and D_{kj} is the binary diffusion coefficient of species k in species j given by equation Eq.2.34. The summation is taken over all species except the species k whose D_k is to be computed. The Hirschfelder and Curtis approximation is valid for sufficiently diluted flames which is the case in air when Y_{N_2} is sufficiently large.

2.2.4 Boundary conditions

The number flux of individual combustion species at the wall surface are analogous to species number flux for the plasma species in the non-equilibrium plasma model. The Eq. 2.22 is used to describe the number flux for electrons at solid surfaces in the combustion model and includes both Maxwellian and secondary electron emission components. The electric field in domain is negligible during the combustion process and hence the flux of ions and neutrals at the solid surfaces is described by their Maxwellian flux at the wall surface given by Eq.2.24. The charged and the excited neutral are assumed to undergo quenching at the wall surface which also modifies the flux terms for these species at the wall boundary. For the global conservation system, the gas temperature of the wall surfaces and domain edges are specified using a constant temperature based Dirichlet boundary condition, supersonic outflow boundary condition is used for all outflow boundaries and an inviscid wall boundary condition is specified for wall surfaces.

2.3 Fully coupled plasma combustion model

The computational coupling framework is developed with the goal of consistently resolving nanosecond pulsed plasma induced combustion ignition of a premixed fuel – air mixture under high pressure conditions. In order to achieve this, the model first needs to resolve the plasma kernel characterized by strong electric fields over sub-micrometer length scales and ionization processes that take place over nanosecond timescales. The framework must also include the ability to resolve the plasma induced ignition kernel characterized by combustion species production/transport over millimeter length scales and microsecond timescales. Incorporating the species generated by the plasma kernel as initial conditions for the ignition kernel couples the plasma and combustion stages, generating one consistent simulation.

2.3.1 Coupled formulation

The first step in the coupled formulation involves solving the governing equations for the non-equilibrium plasma model. This constitutes solving the following governing equations outlined in section 2.1.2 : a) electrostatic potential Eq. 2.4, b) plasma species continuity Eq. 2.1 for all plasma species,

c) electron energy Eq. 2.5 and d) gas energy Eq. 2.9. The length scales for the plasma model are constrained by the sheath dynamics ($\sim \mu m$) and the time scales for the plasma formation are dependent on the chemical kinetics ($\sim ns$). The transport properties for the individual plasma species are evaluated as describe in section 2.1.3. The plasma equations are time-integrated with a time-step of 5×10^{-13}. After the plasma evolution stage is complete, the external nanosecond pulse is switched off. The afterglow stage, when the external power switched off, lasts for a couple of nanoseconds. At the end of the after-glow stage, the electrostatic potential in the inter-electrode gap reaches negligible values and the sheath effects disappear. Due to absence of external power, the electron rapidly thermalize with the background gas so that $T_e = T$ at the end of the afterglow stage.

In the next step, the plasma parameters at the end of the after-glow stage are incorporated as initial conditions for the combustion model. The combustion model constitutes solving the following equations outlined in section 2.2.2 namely : a) Individual species continuity Eq. 2.27 b) Electron energy Eq. 2.5 c) Global continuity Eq. 2.28 d) Global momentum Eq. 2.30 and e) Global energy Eq. 2.31 equations. Even though the plasma species are present at the start of the combustion simulation, the electrostatic potential is negligible in the inter-electrode gap at the end of the afterglow stage. Hence the electrostatic potential equation is not solved in the combustion model. Also, at the end of the afterglow stage, the electrons thermalize with the background gas. Thus, the electron temperature is obtained directly from the gas temperature rather than solving the complete electron energy equation during the combustion process. The transport properties in the combustion model are evaluated as outlined in section 2.2.3 and mainly governed by the diffusion process.

Due to the absence of sheath effects around the electrode surfaces during the combustion process, the computational domain for the combustion model does not require fine mesh elements around the electrode surfaces. Hence, the combustion kernel simulations are performed using a coarser computational mesh than that used to resolve the plasma kernel. However, since the computational mesh for the ignition and plasma simulations are different, an interpolation scheme needs to be employed to initialize the combustion simulation from the plasma mesh.

A schematic describing the centroid based interpolation method is shown in Fig. 6.4. The interpolation is performed in two steps. First, for each cell in the plasma kernel mesh an interpolated cell is found in the combustion mesh. 6.4 shows a schematic of cells in the plasma mesh (with red points as centroids) mapped to a given cell in the combustion mesh (red boundary). This generates a unique one-to-one mapping where every cell in the plasma mesh is mapped to a unique cell in the combustion mesh. In the second step of the interpolation, the variable at a combustion mesh cell is obtained by volume averaging the variable over the corresponding cells in the plasma mesh as,

$$\beta_i = \frac{\sum_k \beta_k \Omega_k}{\sum_k \Omega_k} \tag{2.40}$$

At the end of the interpolation step, all the cells in the combustion kernel mesh are initialized . The combustion simulations are time-integrated with a time step of 1 ns which is significantly smaller than the time steps needed for the plasma model.

Chapter 3

Numerical Methodology

This chapter describes the numerical techniques used to discretize the governing equations discussed in the previous chapter. The non-equilibrium plasma model and the combustion model are simulate physical phenomenon with largely disparate length scales and timescales. This warrants a different numerical methodology suitable for each model. The first half of the chapter describes the numerical framework used to solve plasma governing equations which were outlined in section 2.1.2, while the second half of the chapter outlines the numerical approach for the combustion model outlined in section 2.2.2.

3.1 Non-equilibrium plasma model: Numerical approach

The governing equations of the plasma model, namely plasma species continuity Eq. 2.1, electrostatic potential Eq. 2.4, electron energy Eq. 2.6 and gas energy Eq. 2.9 are first cast as transient convection-diffusion source conservation equations. The governing equations are then solved by integrating them over the plasma computational domain. The integral form of the conservation equations over a control volume V can be written as

$$\iiint\limits_{\Omega} \frac{\partial \varphi}{\partial t} d\Omega + \iint\limits_{\partial\Omega} (\vec{c}_{\varphi}\varphi - D_{\varphi}\vec{\nabla}\varphi) \cdot d\vec{S} = \iiint\limits_{\Omega} S_{\varphi} d\Omega \tag{3.1}$$

Here φ is the plasma solution variable, $\vec{c}_{\varphi}$ and D_{φ} are the transport coefficients associated with convection and diffusion for variable φ, S_{φ} is the volumetric source term which accounts for the net production/consumption of φ in the control volume Ω and $\partial\Omega$ represents the boundary of the control volume Ω.

3.1.1 Spatial discretization

The conservation equations are discretized using a cell centered finite volume approach over a generalized unstructured mesh framework. The finite volume approach represents the conservative variable φ and volumetric source terms S_{φ} by their mean averaged values over that cell, and approximates the convective and diffusive fluxes using the mean averaged values over each face of that cell. The discretization of Eq. 3.1 for each cell c in the computational domain yields,

$$\left(\frac{\partial \varphi}{\partial t}\right)_c \Omega_c + \sum_{f=1}^{N_f} (\vec{c}_{\varphi}\varphi - D_{\varphi}\vec{\nabla}\varphi)_f \cdot \vec{A}_f = (S_{\varphi})_c \Omega_c \tag{3.2}$$

Here the convective $\vec{c}_{\varphi}\varphi$ and diffusive fluxes $D_{\varphi}\vec{\nabla}\varphi$ are summed over all the faces N_f of a cell c to compute the net flux entering/leaving the cell. A_f represents the area of the individual faces and Ω_c represents of the volume of the cell. Eq. 3.2. Spatial discretization of the face fluxes $(\vec{c}_{\varphi}\varphi - D_{\varphi}\vec{\nabla}\varphi)_f$ is performed using the Scharfetter-Gummel exponential scheme [120] where the face fluxes are estimated using the analytical solution of a steady convection diffusion equation. Details of the formulation can be found in Patankar [121]. The potential equation Eq. 2.4 is a specialized form of Eq. 3.2 with the time-derivative and convective terms set to zero. The evaluation of Electric field $E = -\vec{\nabla}\phi$ from cell-centered potential values ϕ is non-trivial. For this, Green-Gauss gradient reconstruction is used to compute the gradients of cell centered solution variables based on their cell averaged values. The gradient is constructed by applying the Green-Gauss theorem to individual volumes in the mesh using the relation

$$\vec{E} = -(\vec{\nabla}\phi)_c = -\frac{1}{\Omega_c}\sum_f \phi_f \vec{A}_f \tag{3.3}$$

Here ϕ_f is electrostatic potential at the face center which is obtained by a simple average of the potential ϕ_c at the neighboring cell centers. On structured mesh implementations, a typical approach for evaluating the Joule heating source term is using multi-dimensional averaging. However, while dealing with unstructured meshes in the present work, this approach leads to spurious results since the orientation of the face normals of the grid cells is arbitrary and does not align with the Cartesian coordinate directions. A special flux reconstruction approach developed previously in our research group [122] is used to evaluate the Joule heating source terms in electron energy Eq. 2.5 and heavy species energy equation Eq. 2.9.

3.1.2 Temporal discretization

The plasma governing equations are discretized using a first order backward Euler scheme to obtain the following

$$\frac{\varphi^{n+1}-\varphi^{n}}{\Delta t}+\frac{1}{\Omega_c}\sum_{f=1}^{N_f}\vec{\Gamma}_f(c^n_\varphi, D^n_\varphi, \varphi^{n+1}, \nabla\varphi^{n+1})\cdot\vec{A_f} = -S_A(\varphi^{n+1})+S_B(\varphi^{n}) \quad (3.4)$$

Where the face flux $\vec{\Gamma}_f$ is given as

$$\vec{\Gamma}_f(c^n_\varphi, D^n_\varphi, \varphi^{n+1}, \nabla\varphi^{n+1}) = \sum_{f=1}^{N_f}(\vec{c}^n_\varphi\varphi^{n+1} - D^n_\varphi\vec{\nabla}\varphi^{n+1})_f \quad (3.5)$$

Here superscript n denotes the previous time-integration step while $n+1$ denotes the current time-integration step. The terms in Eq. 3.4 evaluated at the $(n+1)^{th}$ time-step are termed as implicit terms while those evaluated at $(n)^{th}$ time step are termed as explicit terms. The above equation can be cast as an $Ax = b$ system for all cell center solution variables φ. In order to solve Eq. 3.4, the implicit terms, which usually comprise of unknown variables, are moved to the left while all the explicit terms or known quantities are moved to the right. The flux term in Eq. 3.5 is expressed as a function of the neighboring cell center solutions using the Scharfetter-Gummel exponential scheme [120] with the transport coefficients lagged and evaluated at the n^{th} time step. The source term in Eq. 3.6 is expressed as sum of explicit and implicit terms. Rearranging Eq. 3.4 as mentioned above yields

$$\frac{1}{\Delta t}\varphi^{n+1} + \frac{1}{\Omega_c}\sum_{f=1}^{N_f}\vec{\Gamma}_f(c_\varphi^n, D_\varphi^n, \varphi^{n+1}, \nabla\varphi^{n+1}) \cdot \vec{A}_f + S_A(\varphi^{n+1}) = \frac{1}{\Delta t}\varphi^n + S_B(\varphi^n) \tag{3.6}$$

The coefficients of the solution variable φ^{n+1} on LHS form the entries of the A matrix, while the source terms on the RHS of the above equation fill the corresponding entires of the b vector.

Due to the stiffness associated with the governing equations in the plasma model, a time-splitting approach is used to solve them. The conservation equations are solved sequentially in the following order: 1) electrostatic potential 2) electron number density 3) electron energy 4) heavy species number density 5) gas energy. As each equation is solved, the updated solution variable is used to solve all the subsequent equations. For individual species continuity, Eq. 2.1, $\varphi = n_k$, the general linear system $Ax = b$ given by Eq. 3.6 can be written as

$$\frac{1}{\Delta t}n_k^{n+1} + \frac{1}{\Omega_c}\sum_{f=1}^{N_f}\vec{\Gamma}_f(\mu_k^n, \vec{\nabla}\phi^{n+1}, D_k^n, n_k^{n+1}, \nabla n_k^{n+1}) \cdot \vec{A}_f + \dot{S}_{dest}(n_k^{n+1}) = \frac{1}{\Delta t}\varphi^n + \dot{S}_{prod}(n_k^n) \tag{3.7}$$

and the face flux $\vec{\Gamma}_f$ is given by

$$\vec{\Gamma}_f(\mu_k^n, \vec{\nabla}\phi^{n+1}, D_k^n, n_k^{n+1}, \nabla n_k^{n+1}) = \sum_{f=1}^{N_f}(-Z_k\mu_k^n\vec{\nabla}\phi^{n+1}n_k^{n+1} - D_k^n\vec{\nabla}n_k^{n+1})_f \tag{3.8}$$

In Eq. 3.9, the source term for the species continuity (Eq. 2.1) $\dot{G}_k$ is expressed as a sum of species production term $\dot{S}_{prod}$ and a species destruction term $-S_{dest}$. The species destruction source term is negative and treating it implicitly $-\dot{S}_{dest}(n_k^{n+1})$ improves the diagonal dominance of the matrix as this term is moved to the left in Eq. 3.9 during linear solving step and adds to the diagonal component of matrix A associated with cell. In case of electron energy equation, Eq. 2.6 , $\varphi = \epsilon_e$ and the linear system $Ax = b$ becomes

$$\frac{1}{\Delta t} e_e^{n+1} + \frac{1}{\Omega_c} \sum_{f=1}^{N_f} \vec{\Gamma}_f(\mu_e^n, \vec{\nabla}\phi^{n+1}, D_e^n, e_e^{n+1}, \vec{\nabla} e_e^{n+1}) \cdot \vec{A_f} = \frac{1}{\Delta t} e_e^n + S_{Joule}^{n+1} + S_{coll}^n \tag{3.9}$$

and the electron energy face flux $\vec{\Gamma}_f$ is given by

$$\vec{\Gamma}_f(\mu_e^n, \vec{\nabla}\phi^{n+1}, D_e^n, e_e^{n+1}, \vec{\nabla} e_e^{n+1}) = \sum_{f=1}^{N_f} (\frac{5}{3}\mu_e^n \vec{\nabla}\phi^{n+1} e_e^{n+1} - \frac{5}{3} D_e^n \vec{\nabla} e_e^{n+1})_f \tag{3.10}$$

Where S_{Joule}^{n+1} is the electron Joule heating in Eq. 2.6 and S_{coll}^n is the heating due to elastic and inelastic collisions given by Eq. 2.7. The electron Joule heating term S_{Joule}^{n+1} is not directly dependent on the electron energy e_e^{n+1}, but only depends on the electrostatic potential gradient $\vec{\nabla}\phi^{n+1}$ and n_e^{n+1}. As the governing equations are solved sequentially, both these variables are already known at the current time step since the electron density and potential equation solve precedes the electron energy solve. Thus, the value of Joule heating term at the current time step S_{Joule}^{n+1} is a known quantity and hence treated explicitly while solving the electron energy equation. The collisional heating term S_{coll}^{n} is evaluated using the rate of progress of reactions at the previous time-step, evaluated using $T_e(e_e^n)$, while the species number densities n_k^{n+1} are considered at the current time-step (as they have already been evaluated). The linear system for the heavy species energy equation closely resembles that for the electron energy equation.

The electrostatic potential Poisson's equation given by Eq. 2.4 is a specialized form of Eq. 3.1 where the time-derivative terms as well as the convective flux terms are absent. Thus, the Poisson's equation is inherently a steady state equation and does not require a time-integration scheme. However, the electrostatic potential ϕ is strongly influenced by the space charge distribution in the plasma, which in turn strongly depends on the species number densities and species energies. Thus, the discretization scheme for solving the Poisson's equation, is loosely termed as implicit if the number densities and species energies used to compute the space charge of the Poisson's equation (Eq. 2.4) are evaluated at the current time step $(n + 1)$. Similarly, the discretization scheme for Poisson's equation is termed as explicit if the space charge distribution is computed using species properties at the previous time step (n).

A purely explicit discretization of Poisson's equation is infeasible in the plasma model as it leads to stringent time-step restrictions for time-integration of electron number density Eq. 2.1 and mean electron energy equations Eq.

2.6. This time-step constraint arises due to the presence of $\vec{\nabla}\phi$ potential gradient in the flux term for the electron continuity equation and the Joule heating source term for the electron energy equation. In the explicit method, the characteristic timescale for coupling between the charged species densities and potential equation is governed by the dielectric relaxation time-step $\Delta t_d = \frac{\epsilon_0}{\sigma}$, where σ is the plasma conductivity. This time-step restriction is significantly smaller than the CFL restriction $(min(\frac{\Delta x}{\mu_e \nabla\phi}, \frac{\Delta x^2}{D_e}))$. Using a purely implicit discretization would remove these stringent time-step restrictions. However, a fully implicit discretization would involve simultaneously solving the Poisson's equations with electron species density and electron energy equations, together as a single system of equations. This requires the determination of analytical Jacobians, and for a tightly coupled system such as the one in the present work, derivation of Jacobians and implementation of fully implicit discretization system is a tedious and time-consuming numerical strategy.

To overcome the limitations of the explicit Poisson's while alleviating the time-step restrictions imposed by it, a semi-implicit formulation for the Poisson's equation is introduced [108]. The semi-implicit discretization of the Poisson's equation can be written as

$$-\vec{\nabla}\cdot(\epsilon_r\vec{\nabla}\phi^{n+1}) = \frac{e}{\epsilon_o}\left(\sum_i Z_i n_i^n - n_e^{m+1}\right), \tag{3.11}$$

Here index i is used to denote the ions. The semi-implicit formulation uses a electron number density predictor at the current 'pseudo' time step (indexed by (m+1)) to evaluate the potential equation at the current time step (n+1). The current 'pseudo' time-step and the current time-step are not necessarily identical. In Eq. 3.11, $\vec{\nabla}\phi^{n+1}$ denotes the potential at the current time step (n+1) and n_e^{m+1} is the 'predicted' electron number density at the current 'pseudo' time step. The predicted electron number density is different from the actual electron number density at the current time step which is referred as n_e^{n+1} and evaluated by solving the electron species density equation. The electron predictor term is estimated using the electron continuity equation

$$n_e^{m+1} = n_e^n - \Delta t \vec{\nabla} \cdot \left[(-D_e \vec{\nabla} n_e)^n - (\mu_e n_e)^n \vec{\nabla} \phi^{n+1} \right] + \Delta t G_e^n. \tag{3.12}$$

All the terms in the electron predictor except $\vec{\nabla}\phi$ are treated explicitly and evaluated using the number densities at the previous time step n. Substituting the electron predictor term in the Poisson's equation Eq. 3.11 yields the modified Poisson's equation

$$-\vec{\nabla} \cdot \left(\left[\epsilon_r - \frac{e}{\epsilon_0} (\mu_e n_e)^n \Delta t \right] \vec{\nabla} \phi^{n+1} \right) = \frac{e}{\epsilon_o} \left(\sum_i Z_i n_i^n - n_e^n \right) + \frac{e}{\epsilon_o} \Delta t \left((-D_e \vec{\nabla} n_e)^n - G_e^n \right) \tag{3.13}$$

The electron number density predictor increases the diffusion coefficient from ϵ_r to $\epsilon_r - \frac{e}{\epsilon_0}(\mu_e n_e)^n \Delta t$ as the electron mobility term is negative. With this formulation, the time-step for the Poisson's equation can be several orders of magnitude larger than the time step given by the dielectric relaxation constraint. To explain this, it is important to understand the cause of the time-step constraint. In the absence of electron predictor term, small perturbations in the species density cause an equivalent perturbation in the potential. The characteristic timescales of these perturbations/numerical instabilities are governed by the dielectric relaxation time step $\Delta t_d = \frac{\epsilon_0}{Z_e \mu_e n_e}$. Since the potential directly influences charged species transport, instabilities in the potential further amplify the perturbations in the species number density. The role of the diffusion coefficient in the potential equation is to dampen and smoothen out these perturbations. However, the diffusion coefficient ϵ_r is not sufficient to damped these perturbations. The increased diffusion coefficient in the modified Poisson's equation Eq. 3.13 (from ϵ_r to $\epsilon_r - \frac{e}{\epsilon_0}(\mu_e n_e)^n \Delta t$) is able to smoothen out the perturbations in the potential induced by the species number densities. This allows larger time-steps for the simulations while maintaining stability of the numerical scheme.

The semi-implicit Poisson's formulation with an electron predictor works well for simulating plasma discharges with low to moderate number densities (upto $10^{22} m^{-3}$). However, for simulating high pressure discharges, it imposes severe time step restrictions. This is the case for simulations dealing with plasma assisted combustion ignition which deal with plasma species densities of about $10^{23} m^{-3}$ or higher and pressures as high as 10 atm. Thus, in order to further increase the smoothing property of the diffusion coefficient, the semi-implicit formulation in Eq. 3.11 can be reformulated [111] to incorporate ion predictor term in addition to the electron predictor term . Thus the new semi-implicit formulation is expressed as

$$-\vec{\nabla} \cdot (\epsilon_r \vec{\nabla} \phi^{n+1}) = \frac{e}{\epsilon_o} \bigg(\sum_i Z_i n_i^{m+1} - n_e^{m+1} \bigg). \tag{3.14}$$

Where both the ion and electron predictor terms are used to predict the space charge source term. The ion predictor term n_i^{m+1} is given as

$$n_i^{m+1} = n_i^n - \Delta t \vec{\nabla} \cdot [-(\mu_i n_i)^n \vec{\nabla} \phi^{n+1}] + \Delta t G_e^n, \tag{3.15}$$

The electron predictor term used previously in Eq. 3.12 is also modified and given as

$$n_e^{m+1} = n_e^n - \Delta t \vec{\nabla} \cdot [-(\mu_e n_e)^n \vec{\nabla} \phi^{n+1}] + \Delta t G_i^n. \tag{3.16}$$

The diffusion components in both the electron predictor and the ion predictor are not included in this formulation. This is because an explicit evaluation of the diffusion term $(-D_k \vec{\nabla} n_k)^n$ in the species predictor equation imposes a strong time step constraint in the regions of fine sheaths governed by the CFL number $(\frac{\Delta x^2}{D_e})$. The mesh element sizes needed to resolve the sheaths for high pressure reduces significantly and hence this explicit treatment of diffusion in the species predictor term starts constraining the time step only at higher pressures. Further details of this discussion can be found here [111]. Substituting this in Eq. 3.14 results in the new modified Poisson's equation as

$$-\vec{\nabla}\cdot\left(\left[\epsilon_r-\frac{e}{\epsilon_0}(\mu_e n_e)^n\Delta t+\frac{e}{\epsilon_0}\sum_i Z_i\mu_i^n n_i^n\Delta t\right]\vec{\nabla}\phi^{n+1}\right)=\frac{e}{\epsilon_o}\left(\sum_i Z_i n_i^n-n_e^n\right) \tag{3.17}$$

3.1.3 Solution to linear system

The discretized equations for the non-equilibrium plasma model are non-dimensionalized and the sparse linear system $Ax = b$ is constructed for solution variables ϕ, n_k, e_e and T_g. Each governing equation forms a linear system which must be solved at each time step. The model has been parallelized [108] using Message Passing Interface (MPI) and the key components of the parallel framework include a) Domain decomposition using METIS Library [123] b) Data communication between the partitions after each time-step c) Parallel Linear solve using scalable solvers. Owing to their high scalability, Krylov Subspace (KSP) solvers from Portable Scientific Toolkit for Scientific Computing (PETSC) [124] are used to solve the sparse linear system, specifically Generalized Minimal Residual (GMRES) algorithm is used with Block-Jacobi (BJ), Incomplete LU (ILU) or Geometric Algebraic Multi-grid (GAMG) Preconditioning

3.2 Combustion model: Numerical approach

This section describes the numerical methods employed to solve the governing equations in the combustion model namely individual species continuity 2.27 and a global conservation system of mass (2.28), momentum (2.30) and gas energy (2.31) equations. The individual species continuity equation are solved using an equation time-splitting approach similar to the non-equilibrium plasma governing equations using a implicit backward Euler time-integration scheme while the global conservation equations are solved as a single system using explicit forward Euler time-integration scheme.

The governing equations are cast into the template of a transient convection-diffusion conservation equation and solved by integrating them over the computational domain, where the integral form of the conservation equations is given by Eq. 3.1.

3.2.1 Spatial discretization

The conservation equations are discretized using a cell centered finite volume approach over a generalized unstructured mesh framework. The conservation equations for combustion are solved on the same generalized grid framework as the plasma model described in the previous section.

Individual species continuity

For solving the individual species continuity equations, the discretization approach is similar to the approach followed for solving the non-equilibrium plasma governing equations. Individual species continuity equations is solved for each species over all the cells in the computational domain. The discretization of Eq. 3.1 for combustion species k with a species density ρ_k at cell c in the computational domain yields,

$$\left(\frac{\partial \rho_k}{\partial t}\right)_c \Omega_c + \sum_{f=1}^{N_f} (\rho_k \vec{V} + D_k \vec{\nabla} \rho_k)_f \cdot \vec{A_f} = (\dot{S}_k)_c \Omega_c. \tag{3.18}$$

Here the fluxes are summed over all the faces N_f of a cell c to compute the net flux entering/leaving the cell. A_f represents the area of the individual faces and Ω_c represents of the volume of the cell, $\vec{V}$ is species velocity associated with a combustion species k respectively and D_k is the species mixture averaged diffusion coefficient which differs from the kinetic diffusion coefficient used for plasma species in the non-equilibrium plasma model. Since the total flux consists of both convective and diffusive components, the spatial discretization of the face fluxes $(\rho_k \vec{v} + D_k \vec{\nabla} \rho_k)_f$ is performed using the Scharfetter-Gummel exponential scheme [120]. In this scheme, the face fluxes are expressed in terms of the neighbouring cell averaged values using the analytical solution of a steady convection diffusion equation, similar to the non-equilibrium plasma model.

Global conservation system

The global system of compressible Euler equations are solved as a single system separate from the individual species continuity equation. The work is based on the previous work in our research group [111]. The global system can expressed in the conservation form as

$$\frac{\partial \boldsymbol{U}}{\partial t} + \vec{\nabla} \cdot \boldsymbol{F}_{convective} = \boldsymbol{S} \tag{3.19}$$

Here $\boldsymbol{U}$ represents the vector of global conservative variables, $\boldsymbol{F}_{convective}$ denotes the vector of conservative face fluxes and $\boldsymbol{S}$ denotes the vector of source terms.

$$\boldsymbol{U} = \begin{bmatrix} \rho \\ \rho u \\ \rho v \\ \rho(e + \frac{|\vec{V}|^2}{2}) \end{bmatrix} \tag{3.20}$$

$$\boldsymbol{F} = \begin{bmatrix} \rho u \\ \rho u^2 + p \\ \rho uv \\ (\rho(e + \frac{|\vec{V}|^2}{2}) + p)u \end{bmatrix} \hat{i} + \begin{bmatrix} \rho v \\ \rho uv \\ \rho v^2 + p \\ (\rho(e + \frac{|\vec{V}|^2}{2}) + p)v \end{bmatrix} \hat{j} \tag{3.21}$$

$$\boldsymbol{S} = \begin{bmatrix} 0 \\ 0 \\ 0 \\ \dot{E}_h \end{bmatrix} \tag{3.22}$$

Here u and v are the components of the species velocity $\vec{V}$ along x and y directions ($\vec{V} = u\hat{i} + v\hat{j}$), ρ is the total gas density given by $\rho = \sum_k \rho_k$, p is the total species pressure, e is the internal energy of the gas given as $e = \frac{p}{(\gamma-1)\rho}$, γ is the ratio of specific heats of the gas. Thermal and viscous terms are neglected and $\dot{E}_h$ is the collisional heating term given by Eq. 2.33. The governing equations are non-dimensionalized and then spatially discretized using cell-centered finite volume methods. The discretized form can be written as

$$\frac{\partial \boldsymbol{U}_c}{\partial t}\Omega_c + \sum_{f=1}^{N_f} (\boldsymbol{F}_{convective})_f \cdot \hat{A}_f = \boldsymbol{S}_c \Omega_c \tag{3.23}$$

The convective face fluxes are discretized using a using a local Lax-Friedrichs method [125]. The details of the flux schemes are not presented here for the sake of brevity and for more details the reader is requested to refer the previous works in our group [111].

3.2.2 Temporal discretization

Different time-integration schemes are used for the solving the individual species continuity equation and the global system of conservation equation.

Global conservation system

The global system is discretized is using an explicit forward Euler scheme as it lacks the diffusion operator which imposes stringent CFL time-step constraints. At each time step, first, the global conservation system is solved to update the vector of conservative variables $\boldsymbol{U}$ given by

$$\frac{\boldsymbol{U}_c^{n+1} - \boldsymbol{U}_c^{n}}{\Delta t} + \frac{1}{\Omega_c} \sum_{f=1}^{N_f} (\boldsymbol{F}^n_{convective})_f (\boldsymbol{U}^n, p^n, \rho^n) = \boldsymbol{S}(\rho_k^n, p^n) \tag{3.24}$$

The components of the $\boldsymbol{F}$ are expressed as a function of the conservative variables $\boldsymbol{U}$ and the species pressure p, while the source terms $\boldsymbol{S}$ are expressed as a function of the individual species densities ρ_k and species pressure p. Specifically, the collisional heating term in the global energy equation $\dot{E}_h$ (which is the only non-zero source term of $\boldsymbol{S}$) is evaluated using the updated individual species density ρ_k and the gas temperature T_g obtained from solving the individual species continuity equation. For the first time step, this term is computed using the species density and temperature interpolated from the non-equilibrium plasma model or initialized explicitly. The explicit terms are moved to the right and a set of algebraic equations are solved to compute the updated $\boldsymbol{U}$. Rearranging Eq. 3.25 to yield the final form

$$\frac{1}{\Delta t}\boldsymbol{U}_c^{n+1} = \frac{1}{\Delta t}\boldsymbol{U}_c^{n} - \frac{1}{\Omega_c}\sum_{f=1}^{N_f}(\boldsymbol{F}^n_{convective})_f(\boldsymbol{U}^n, p^n, \rho^n) + \boldsymbol{S}(\rho_k^n, p^n,) \tag{3.25}$$

Here the species densities ρ_k and T_g are initialized from the non-equilibrium plasma model using the interpolation scheme described in Fig 6.4. Once $\boldsymbol{U}$ is updated, the species velocity $\vec{V}^{n+1}$ at the current time step is evaluated using the relation $\vec{V} = \frac{\rho(u\hat{i}+v\hat{j})}{\rho}$. The species pressure p^{n+1} is updated using the conservative variable $\rho(e + \frac{\vec{V}\cdot\vec{V}}{2})$, where ρ^{n+1} and $\vec{V}^{n+1}$ are known and $e = \frac{p}{(\gamma-1)\rho}$, using the relation

$$p^{n+1} = (\gamma - 1)\rho^{n+1}\left(\frac{(\rho[e + \frac{|\vec{V}|^2}{2}])^{n+1}}{\rho^{n+1}} - \frac{(|V|^{n+1})^2}{2}\right) \tag{3.26}$$

At the end of the global system time step, the updated values of ρ, p, and $\vec{V}$ are obtained. The next step is to solve the individual species continuity equation. The time step used for the explicit flow solve is about 1 ns.

Individual species continuity

The individual species continuity equation is solved next to update the species density ρ_k, the gas temperature T_g and the background density ρ_{N_2}. The updated values of species velocity $\vec{V}^{n+1}$, total density ρ^{n+1} and total pressure p^{n+1} are available at the current time-step from the global system solve. The presence of a diffusion operator in the individual species continuity equation introduces numerical stiffness and imposes severe time-step restrictions due to the CFL constraint $(\Delta x^2/D_k)$. To overcome this limitations, an implicit backward Euler time-integration method is employed to discretize individual species continuity equations. The time-discretization for updating the individual species density ρ_k for species k ($k \neq \mathrm{N}_2$) can be written as

$$\frac{\rho_k^{n+1} - \rho_k^n}{\Delta t} + \frac{1}{\Omega_c} \sum_{f=1}^{N_f} \vec{\Gamma}_f(\vec{V}^{n+1}, D_k^n, \rho_k^{n+1}, \nabla \rho_k^{n+1}) \cdot \vec{A}_f = -S_{dest}(\rho_k^{n+1}) + S_{prod}(\rho_k^n) \tag{3.27}$$

Where the flux term $\vec{\Gamma}_f$ is given by

$$\vec{\Gamma}_f(\vec{V}^{n+1}, D_k^n, \rho_k^{n+1}, \nabla \rho_k^{n+1})) = \sum_{f=1}^{N_f} (\rho_k^{n+1} \vec{V}^{n+1} + D_k^n \vec{\nabla} \rho_k^{n+1})_f \tag{3.28}$$

Similar to non-equilibrium plasma species continuity equations, the species destruction source term in Eq. 3.27 $-\dot{S}_{dest}(n_k^{n+1})$ is treated implicitly to improves the diagonal dominance of the matrix A. Rearranging the terms in Eq. 3.27 yields the linear system $Ax = b$ given as

$$\frac{1}{\Delta t}\rho_k^{n+1}+\frac{1}{\Omega_c}\sum_{f=1}^{N_f}\vec{\Gamma}_f(\vec{V}^{n+1}, D_k^n, \rho_k^{n+1}, \nabla\rho_k^{n+1})\cdot\vec{A}_f+S_{dest}(\rho_k^{n+1}) = \frac{1}{\Delta t}\rho_k^n+S_{prod}(\rho_k^n) \tag{3.29}$$

This equation yields the individual species densities ρ_k^{n+1} at the current time-step. The gas temperature T_g^{n+1} and the N_2 species density $\rho_{N_2}^{n+1}$ are updated using the relations

$$\rho_{N_2}^{n+1} = \rho^{n+1} - \sum_{k\neq N_2} \rho_k \tag{3.30}$$

$$T_g^{n+1} = \frac{p^{n+1}}{\sum \frac{\rho_k^{n+1}}{m_k} k_B} \tag{3.31}$$

The updated species densities ρ^k, T_g and N_2 density are passed to the global conservation system and used to compute the collisional heating term $\dot{E}_h$ in the $\boldsymbol{S}$. The time step used for solving the individual species density is constrained by the reaction kinetics and is the same as the time step for the global conservation system.

3.2.3 Solution to linear system

The discretized equations for the combustion model are non-dimensionalized before solving them. The explicit global conservation system forms a set of algebraic equations which are solved directly to update the conservation variables at each time step. However, in case of the implicit species density equations, governing equation for each individual species $k, (k \neq N_2)$ forms a sparse linear system $Ax = b$ which must be solved at each time step. The sparse linear system is solved using Generalized Minimal Residual (GMRES) algorithm with Block-Jacobi (BJ), Incomplete LU (ILU) or Geometric Algebraic Multigrid (GAMG) Preconditioning from Portable Scientific Toolkit for Scientific Computing (PETSC) [124].

Algorithm 1 Algorithm for Combustion model

```
Interpolate plasma variables into combustion model
Initialize combustion variables ($\rho_k, T_e, T_g, \rho, \rho\vec{V}, \rho(e + (\vec{V} \cdot \vec{V})/2)$)
Update pressure using the relation $p = \sum_k n_k k_B T_g$
while $t < t_{combustion_{end}}$ ($O(\mu s)$) do
    Update transport coefficients for all species (Eq. 2.2.3)
    Update $T_e$ using $T_e = T_g$
    Update Collisional heating $\dot{E}_h$ using $\rho_k$,$T_g$
    Explicit step: Solve global system (Eq. 2.28 to Eq. 2.31)
    Update $\rho$,$\vec{V}$ and $p$, pass to individual species continuity
    Implicit step: Solve individual species continuity (Eq. 2.27 for $k \neq k_{N_2}$)
    Update $\rho_k$,$T_g$ and $\rho_{N_2}$, pass to global system
end while
exit
```

Chapter 4

Modeling surface streamer assisted large gap thermal breakdown

Surface streamers[1] that bridge a large interelectrode gap can serve as the initial conducting channel from which an arc discharge can develop in an interelectrode space at high pressure conditions [19, 20]. The key features of streamer-to-arc transition are a) nanosecond timescales for streamers as compared to microsecond timescales for direct arc discharge and b) lower electrode voltage for surface streamer breakdown $\sim$ 1 kV as compared to $\sim$ 100 kV required for gap breakdown as dictated by the Paschen breakdown mechanism [37, 12]. As a result, arcs can be ignited much faster and at lower voltages through the use of surface streamers as an intermediate stage. Arcs initiated by surface streamers have found application in the range of areas including but not limited to aerodynamic applications [38, 39, 40, 41], magneto-hydrodynamic control of hypersonic flows [42], plasma assisted combustion and ignition [43, 44], plasma actuators [45, 13], atmospheric-pressure dielectric barrier discharge [43, 13] etc.

---

[1] Portions of this chapter were previously published as '"Effect of oxygen impurities on atmospheric-pressure surface streamer discharge in argon for large gap arc breakdown,"[18] in Physics of Plasmas. All writing and figures included in this chapter are the original work of the author, with editing by Dr. Laxminarayan L. Raja

4.1 Problem description

In the present work, argon surface streamers are modeled as a low-voltage mechanism for thermal breakdown in large interelectrode gaps [126, 18]. The non-equilibrium plasma model used in the present study has been described in section 3.1. The study also investigates the effect of impurities (molecular oxygen) on the development of continuous surface streamer channels under atmospheric-pressure conditions. The conductivity of the streamer channel in the presence of oxygen impurities is used as a governing parameter to estimate the probability of streamer-to-arc transition. The study analyzes the influence of the oxygen impurities on the breakdown voltage, streamer induction time, streamer velocity and the physical properties of the streamer channel.

4.2 Experimental overview

The physical problem is motivated by the experimental work by Pachuilo et al. [1] which focused on development of plasma sources for high-density surface streamers in argon for large gap thermal breakdown. The experimental setup [1] is shown in figure 4.1. The plasma chamber, shown in Fig. 4.2 consists of a quartz tube with an inner diameter of 5 cm and length 10 cm. The quartz tube is capped on both ends by ‘main’ electrodes. The voltage drop across the gap between main electrodes is 1-3 kV.

The breakdown of the arc is achieved using a non-intrusive ‘fuse’ that connects the main electrode during the arc breakdown stage. This ‘fuse’ is es-

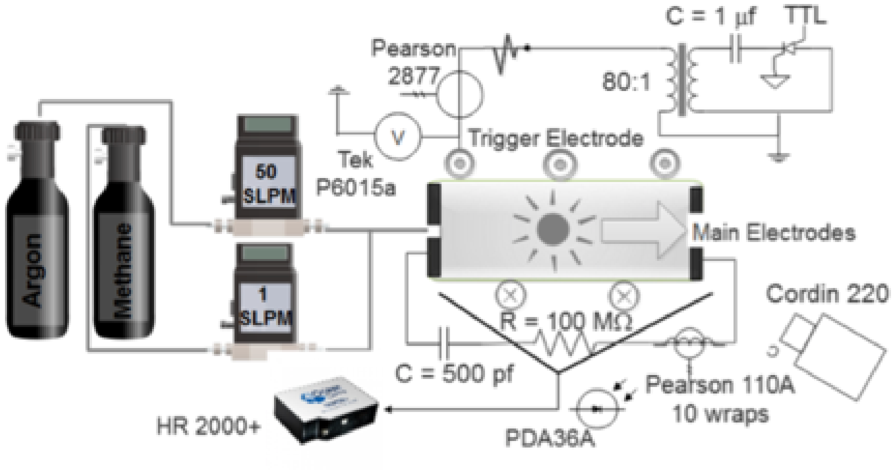

Figure 4.1: Experimental setup from Pachuilo et al. [1]

sentially a conductive channel between the main electrodes formed by a surface streamer that bridges the main electrode gap. The streamer itself is formed by applying a fast-negative voltage ($\sim$ 10 kV) on a ‘trigger’ electrode that comprises a copper wire that is wrapped around the quartz tube. The streamer is initiated on the grounded main electrode and propagates towards the trigger electrode where it encounters the dielectric tube wall as seen in figure 4.3. The streamer then quickly transitions into a surface hugging discharge and propagates along the tube inner surface until it reaches the opposite main electrode. If the streamer maintains its integrity and creates a continuous conducting channel between the main electrodes, a successful ‘fuse’ is realized and the arc breakdown is triggered.

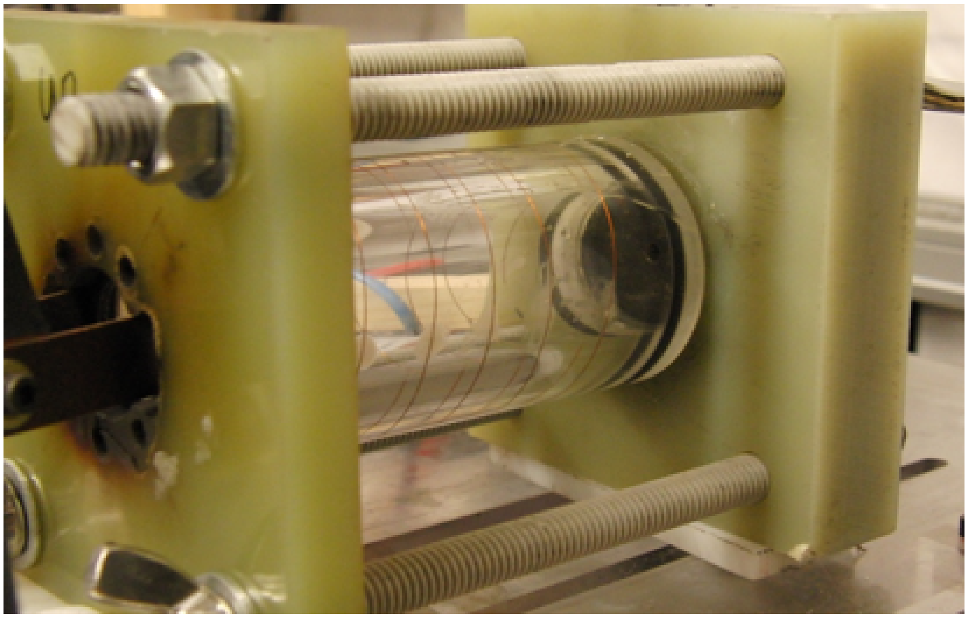

Figure 4.2: Plasma chamber [1] consisting of a quartz tube surrounded by helically wound copper wires.

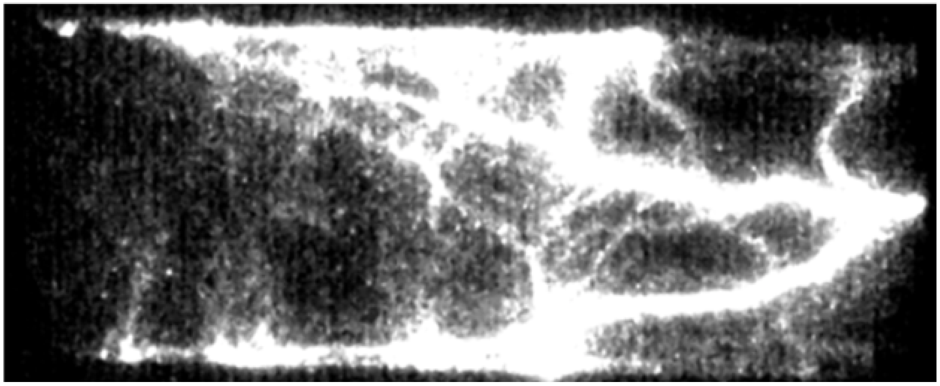

Figure 4.3: Long exposure image of the entire trigger electrode pulse (300 μs) in argon. A constricted streamer filament emerges from the anode and propagates in the regions of the helically wound trigger electrode until completely bridging the main inter-electrode gap.

Table 4.1: Species present in plasma model of $Ar-O_2$ mixture

Charged	$e, Ar^+, {Ar_2}^+, O^+, {O_2}^+, O^-, {O_2}^-$
Neutral	$Ar^*, {Ar_2}^*, O$
Background	Ar, O_2

4.3 Discussion of chemistry: Argon-oxygen($Ar-O_2$)

The gas chemistry is this work is derived for an $Ar-O_2$ mixture with O_2 impurity concentration in the range 1-10%. The mechanism consists of 12 species and 45 reactions (Appendix A). Table 4.1 lists the species in the plasma finite-rate chemistry mechanism for $Ar-O_2$ mixture. The species considered include: electrons (e), atomic argon ion (Ar^+), argon dimer ion (${Ar_2}^+$), metastable atomic argon (Ar^*), metastable argon dimer (${Ar_2}^*$), atomic oxygen (O), atomic oxygen ion (O^+), oxygen dimer ion (${O_2}^+$), atomic oxygen negative ion (O^-), oxygen dimer negative ion (${O_2}^-$) and the background species, i.e. argon atoms (Ar) and diatomic oxygen atoms (O_2). The dimer ions and metastables are important owing to the presence of high-pressure conditions. The importance of negative oxygen ions comes from the significantly low electron temperature in the streamer body where electron attachment kinetics dominate. Dimer argon species, i.e. ${Ar_2}^+$,${Ar_2}^*$ are also included due to atmospheric-pressure conditions. The list of reactions considered in the present study is given in Appendix A. Rate coefficients of the individual reactions are computed as a function of T_e by solving the electron Boltzmann equation in the two-term approximation [114] using the electron-neutral collision cross sections taken from [127, 128]. Vibrational excitation (reactions

10-11 in Appendix A) and electronic excitation reactions for O_2 (reactions 12-14 Appendix A) are taken into account only in the electron energy balance equation and do not lead to the production of new species. Electron impact reactions with atomic oxygen are not taken into consideration because their rates are small. This is primarily due to the orders of magnitude lower number density of atomic oxygen generated in the discharge compared to the number densities of background species Ar and O_2. The scheme of reactions also does not include the atom-atom reactions such as O^+O because their rates are much smaller in comparison with the rates of O+Ar and O+O_2 reactions. This is primarily due to considerably higher number density of background species Ar and O_2, causing the probability of reaction of type O+O to be significantly lower.

4.4 Geometry and computational domain

Our focus here is to model the streamer formation phase and resolve the branching effects observed in the experiments. Figure 4.4 shows an inset of a smaller domain (compared to the experiment) that is the subject of this study. Streamer initiation from the main electrode on the left and the subsequent propagation of the streamer on the tube wall is simulated. We do not simulate the entire streamer propagation event, i.e. streamer bridging of the main electrode gap, in order to limit the computational problem size. Also, the main features of the streamer dynamics in the problem and the impact of impurities on the working noble gas Ar is reasonably well described in spite of

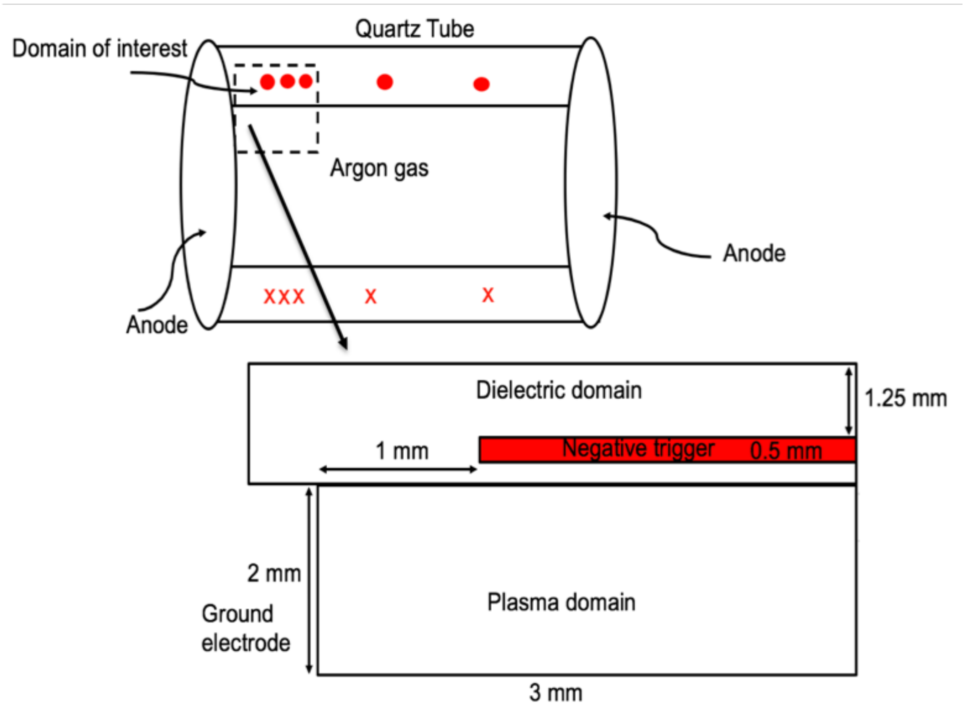

Figure 4.4: Schematic of the experimental domain (top) and the computational domain (bottom) chosen in this study.

this limited domain size.

The inset in Fig. 4.4 is represented by a computational mesh that is shown in Fig. 4.5. A couple of strands of the trigger electrode wire in the experiments is modeled as a continuous electrode that is embedded within a dielectric as shown in the figure 4.4. The grounded main electrode is located to the left of the plasma domain and shares a boundary with the dielectric tube. The trigger electrode is embedded in the dielectric medium at a distance of 0.25 mm from the plasma-dielectric interface and is located at an offset of 1 mm away from the grounded electrode. The thickness of the trigger electrode for the present investigations is 0.5 mm. The dielectric is assumed to be quartz with $\epsilon_r = 3.8$. A two-dimensional unstructured mesh for the computational domain is generated using a commercial two-dimensional mesher VizMesh [129]. The mesh consists of fine quadrilateral cells in the plasma subdomain immediately abutting the plasma-dielectric interface, in the region where the streamer tends to remain confined. Triangular cells are used to fill in the remaining part of the plasma subdomain that are further away in the plasma-dielectric boundary. The remaining parts of the domain, i.e. the dielectric, are meshed with triangles. Size functions in the meshing operation are used to minimize the total cell count in the problem. The quadrilateral cell sizes close to the plasma-dielectric is chosen to be of the order of the Debye length in order to accurately resolve the sheath physics at the electrode and dielectric surface. This is necessary to accurately capture the propagating streamer dynamics. The total number of mesh cells in the domain is 500,000 and the minimum mesh size is 2 μm.

4.5 Results and discussion

4.5.1 Threshold trigger voltage

The first part of our study focuses on the prediction of the threshold trigger voltage and the effect of applied electric field on the streamer propagation dynamics. We investigate the streamer formation and propagation for pure argon and with 1% by volume of oxygen (O_2) in argon. In all the fol-

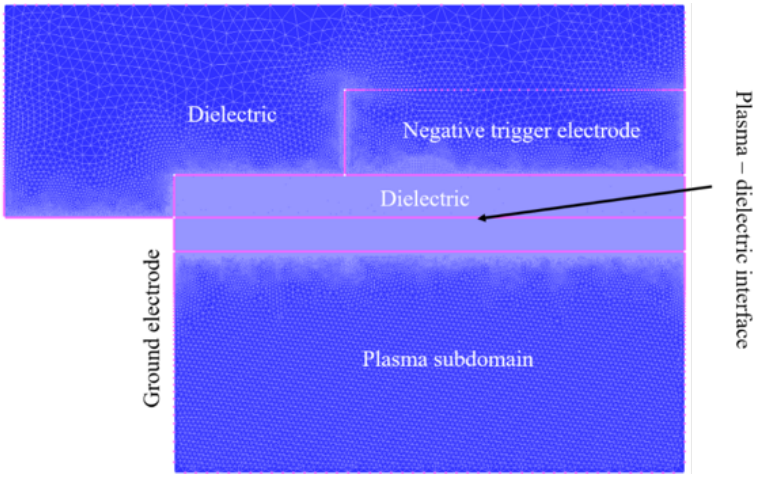

Figure 4.5: Computational mesh employed with fine mesh elements in the vicinity of dielectric-plasma interface to capture surface streamer characteristics and resolve sheath dynamics.

lowing studies, it is found that the streamer tends to remain confined in the immediate vicinity of the plasma-dielectric interface. Therefore all streamer results presented below will focus on a 0.4 mm domain in the y-direction (from y = 1.6 mm to 2 mm).

The threshold for streamer initiation is determined by performing a series of simulation runs starting with a low trigger voltage and increasing it incrementally until streamer phenomenon is observed. The minimum voltage for streamer initiation is termed as the ‘threshold voltage’ (V_{th}). The streamer initiation is also characterized by an ‘induction time’, i.e. a time delay between the application of the voltage on the trigger electrode and the observation of the streamer. Figures 4.6 and 4.7 illustrate the salient features of the discharge phenomena below the threshold voltage and at the threshold voltage, respec-

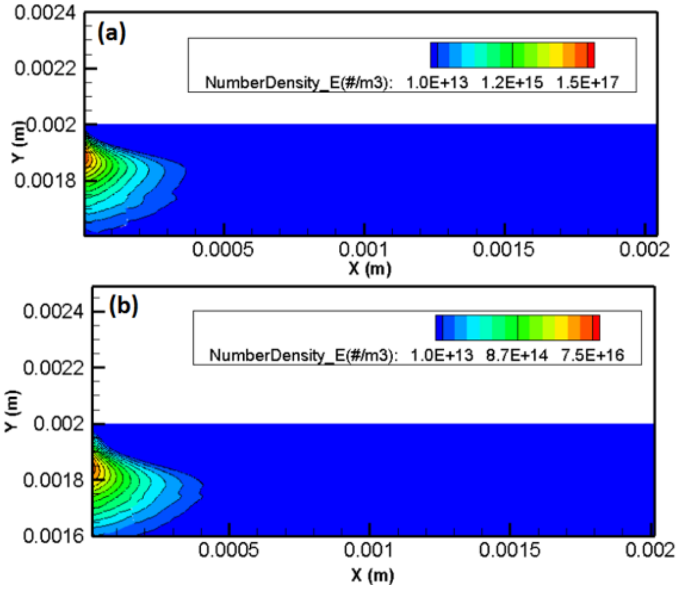

Figure 4.6: Electron number density in pure argon below threshold voltage (V = -3.5 kV) at (a) 2 ns and (b) 3 ns.

tively. Here the working gas is pure argon and the threshold voltage is V_{th} = -4 kV.

Figure 4.6 shows that below threshold voltage at V = -3.5 kV, a relatively weak and diffuse corona-like discharge is observed near the corner of the grounded main electrode and the upper dielectric surface. This corona can transform into a streamer only if the electric field at the streamer head matches the applied electric field or,

$$\frac{e}{R^2}\exp(\alpha(E_0) \times d) \sim E_0 \tag{4.1}$$

Here, R is the curvature radius of the corona, α is the Townsend ionization coefficient, d is the gap between the cathode and corona, and E_0 is the electric field at the head of corona from its cathode side. One can see from Eq. 4.1 that the breakdown electric field is sensitive to the ionization coefficient, i.e. the type of gas and electron temperature, as well as the curvature of the corona.

As seen in Fig. 4.6(a), the electron number density in the discharge increases during the first 2 ns and reaches the peak value of $\sim 1.5{\times}10^{17} m^{-3}$. At larger times, it follows from Fig. 4.6(b) that electron number density decreases. This indicates that the discharge is not self-sustaining and corona is unable to transform to a positive streamer, i.e. condition 4.1 is not satisfied. For the threshold voltage of V_{th} = -4 kV and higher, the corona-like discharge rapidly transits into a volume streamer which propagates to the right as shown in Fig.

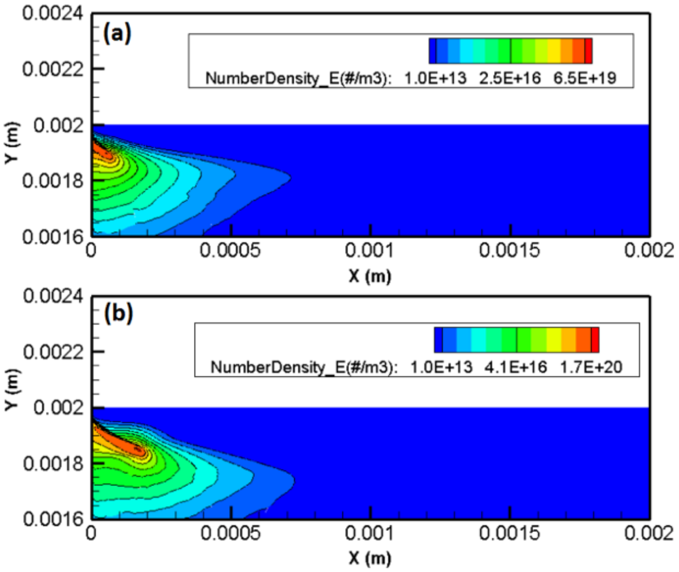

Figure 4.7: Electron number density in argon for the threshold voltage V_{th} = -4 kV at (a) 2 ns and (b) 3 ns.

4.7. This confirms the self-sustaining nature of the discharge at the breakdown voltage. The streamer propagates to the cathode due to the acceleration of electrons present in front of the streamer head. These electrons generate new electron-ion pairs before the streamer head promoting its propagation [37].

Thus, the key feature which describes the threshold voltage is the peak electron density in the corona-like discharge. For trigger voltages at or above V_{th}, the peak electron density in the corona-like discharge is high enough to generate self-consistent local electric field which distorts the external electric field. The self-consistent field then leads to the formation of a propagating streamer. Below threshold voltage, the electron density in the corona is not high enough and the corona eventually decays owing to charged species losses

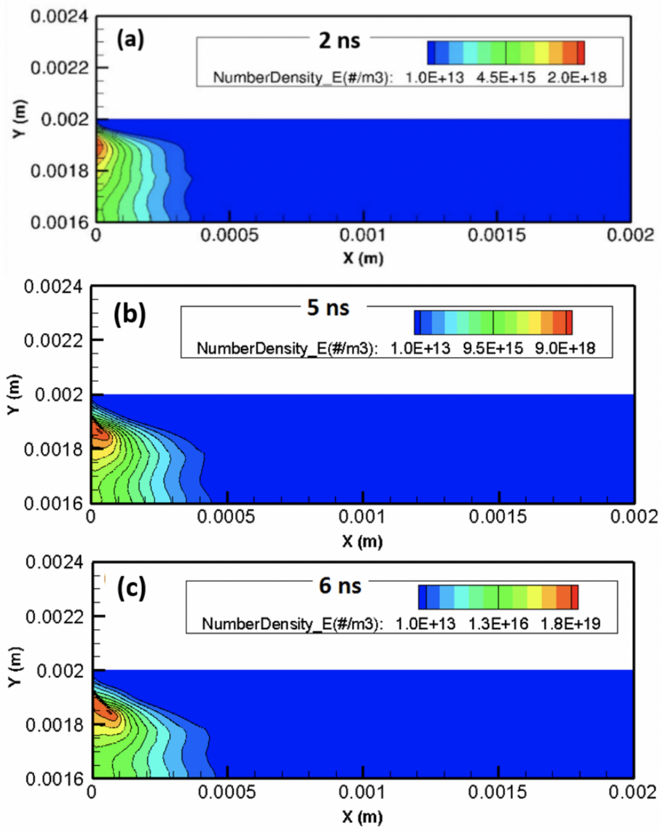

Figure 4.8: Electron number density in $Ar-O_2$ mixture with 1 % of O_2 at (a) 2 ns, (b) 5 ns and (c) 6 ns.

through wall quenching and volume recombination.

Our simulation results have shown $V_{th} \sim$ -3.5 kV for $Ar-O_2$ mixture with 1% of O_2, i.e. lower value than in pure argon. For these conditions, the formation of a successfully propagating streamer is shown in Fig. 4.8. To explain the lower threshold voltage due to addition of tiny amounts of oxygen we look closely at the variation of Townsend ionization coefficients of the Ar$-$O$_2$ mixture with mean electron energy, as shown in Fig. 4.9 (a). These figures were created using the Boltzmann equation solver Bolsig+ [114]. Let us assume that the length d in the Meek's criterion 4.1 does not depend on the mixture. This assumption is in rather good agreement with our results shown in Figs. 4.6 - 4.8. Then, we conclude that the value of $\alpha(E_0)$ is constant for all mixtures.

Our simulation results have shown that in pure argon, electron temperature (T_e) during the initial stage of breakdown is $\sim$ 6 eV. The addition of O$_2$ to Ar leads to the decrease of the electron temperature due to the electron energy losses to excitation of electronic and vibrational states of O$_2$. However, as we conclude from Fig. 4.9(a) for different mixtures, the decrease in T_e from 6 to 4.5 eV does not change α. This means that in Ar$-$O$_2$ mixture with 1% of O$_2$ impurity the same value of α is obtained at lower T_e.

Figure 4.9(b) shows that in pure Ar, 6 eV corresponds to the reduced electric field $\sim$ 50 Td, 5.5 eV in Ar$-$O$_2$ mixture with 1% of O$_2$ corresponds to $\sim$40 Td, and 5.0 eV in Ar$-$O$_2$ mixture with 5% of O2 corresponds to $\sim$ 45 Td. This explains the non-linear dependence of the breakdown electric field on the O$_2$ density obtained in our studies. Also, it is important to note that for 1% of O$_2$ impurity concentration, electron attachment is not efficient. But with further increase of O$_2$ attachment starts playing an important role which reduces the density of seed electrons.

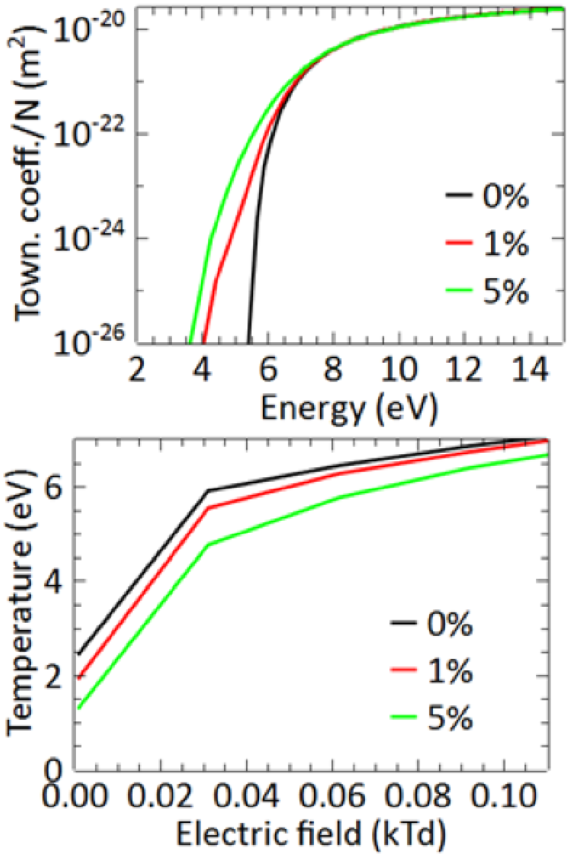

Figure 4.9: (a) Townsend ionization coefficient of Ar$-$O$_2$ mixture as a function of T_e, (b) mean electron energy as a function of E/N for Ar$-$O$_2$ mixture.

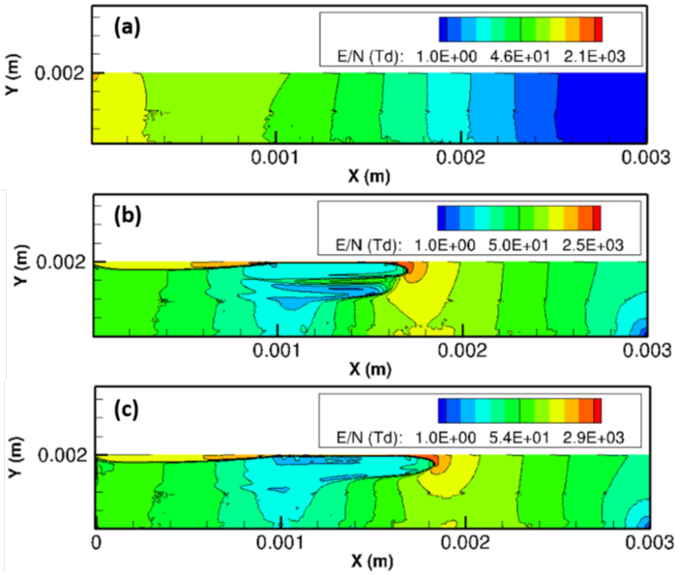

Figure 4.10: Distribution of the electric field in (a) vacuum, (b) pure Ar and (c) Ar$-$O$_2$ mixture for -5.0 kV at t = 2.7 ns.

4.5.2 Dynamic characteristics of the streamer discharge

Figure 4.10 shows the electric field distribution in the plasma subdomain in the plasma-free space (vacuum), pure Ar streamer case, and Ar$-$O$_2$ mixture (1% of O$_2$) streamer case for the trigger voltage of -5 kV at time t = 2.7 ns after the start of simulation. The electric field in vacuum decreases uniformly as we move away from the grounded anode along the x axis [Fig. 4.10(a)] with no localized electric field enhancement. The latter is due to the absence of the space charge. Here, the peak value of $E/N \sim 900$ Td is observed in the small region in the vicinity of the dielectric-anode boundary (x $\sim$ 0 and y $\sim$ 0.002 m).

When the streamer is present in the interelectrode space, the plasma-induced electric field enhancement is obtained at the streamer head [see Figs. 4.10(b) and (c)] due to its small tip radius. The reduced electric field E/N at the streamer head is $\sim$ 103 Td while in the streamer body it is $\sim$1 Td. The comparison between Figs. 4.10(a), (b) and (c) shows that the peak value of electric field in the gap with plasma is higher than that in vacuum. This is explained by the presence of the streamer in the domain whose space charge and small tip radius induce high electric field. Comparing Figs. 4.10(b) and (c) we find higher field peak values of electric field for $\mathrm{Ar-O_2}$ mixture which is due to the smaller and sharper tip of the streamer head in Fig. 4.10(c) compared to Fig. 4.10(b). The electric field enhancement at the streamer head enables the self-consistent streamer propagation forward into the region with smaller electric field because high electric field at the streamer head leads to high electron production rates at the head of the streamer. Low E/N in the streamer body is explained by the quasi-neutrality and high density of plasma. Small electric field and frequent electron-neutral collisions result in small T_e in the streamer body. High value of E/N is also seen along the plasma-dielectric interface resulting from the charge deposited on the interface as the streamer propagates along this boundary.

Snapshots of the electron temperature profile obtained in the pure Ar and in the $\mathrm{Ar-O_2}$ mixture at 2.7 ns are shown in Fig. 4.11. The electron temperature is seen to be maximum at the streamer head in both gases with the peak value $\sim$ 11 eV in the pure Ar and $\sim$ 18 eV in the $\mathrm{Ar-O_2}$ mixture.

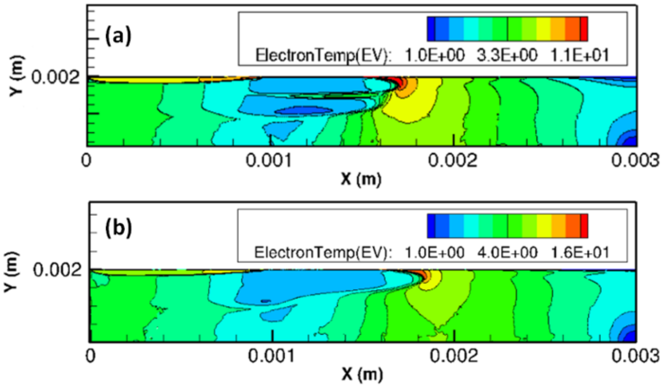

Figure 4.11: Distribution of the electron temperature for -5.0 kV at t = 2.7 ns in (a) pure Ar and (b) Ar$-$O$_2$ mixture.

Thus, T_e at the streamer head in pure Ar is smaller than that in Ar$-$O$_2$ mixture which is explained by the larger electric field in the latter case [compare Figs. 4.10(b) and (c)].

In the streamer body, the electron temperature for both cases are comparable and $\sim$ 1 eV. The electric field within the streamer body is below the breakdown threshold and hence the streamer body can be thought as the discharge afterglow. Here T_e drops rapidly and active species quench/recombine through volume processes as well as loss processes to the adjacent plasma-dielectric interface.

An important feature of the streamer structure is the streamer branching that occurs at a distance of about 1 mm from the left electrode (see Fig. 4.12). Here the streamer splits into a surface branch that propagates along the dielectric surface and a volume branch that separates from the surface streamer but continues to propagate parallel to the surface streamer. The 1 mm distance where the branching occurs coincides with the start of the trigger electrode embedded within the dielectric (Fig. 4.4). The streamer branching is clearly evident in Fig. 4.12 that shows snapshots of the electron densities for the pure Ar and Ar$-$O$_2$ mixture at t = 2.7 ns. The surface and volume streamer components are distinguishable in the pure Ar as seen in Fig. 4.12(a). In the Ar$-$O$_2$ mixture, the life-time of the volume streamer is short and it quickly ceases to propagate leaving behind only the surface streamer component for the rest of the transient [see Fig. 4.12(b)]. The latter is explained by the destruction of electrons due to their attachment to O$_2$ (see Table I, reactions # 17-20) in the streamer body. This is an important observation for applications, where only surface streamer discharges are required. One can conclude from Fig. 4.12 that this can be achieved by adding tiny amounts ($\sim$ 1%) of electronegative gases such as O$_2$ to the noble gases.

4.5.3 Conductivity of streamer trail and transition to arc

In the arcs initiated by streamers, the integrity of the streamer channel and a continuous conductivity of the channel is essential. The streamer body is where the plasma is essentially quenching and hence most vulnerable to loss of conductivity. The electrical conductivity of such plasma is defined by the electron component due to much larger electron mobility and by the electron-neutral momentum transfer collisions [37]

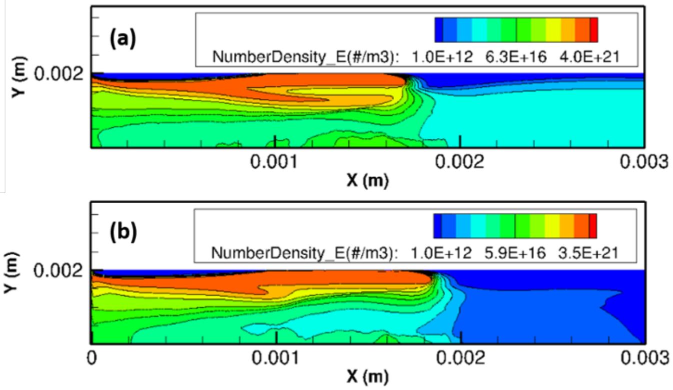

Figure 4.12: Electron number density for -5 kV at t = 2.7 ns for (a) pure Ar and (b) Ar$-$O$_2$ mixture. Streamer branching is visible for the pure Argon case and completely eliminated by addition of oxygen impurities.

$$\sigma = \frac{e^2 N_e}{m_e \nu_m}. \tag{4.2}$$

Here ν_m is the electron-neutral momentum transfer frequency. Below, we analyze the conductivity for the trigger voltage -5.0 kV in Ar gas with the oxygen impurities in the range 1-10%.

It is seen from Figs. 4.13 and 4.14 that the local conductivity in the cathode-anode gap in both pure Ar and Ar$-$O$_2$ mixture peaks at the head and the tail end of the streamer to the values of about 500 S/m . This is in accordance with Eq. 4.2 due to the largest electron density there. For the pure Ar, a relatively high electrical conductivity ~ 200 S/m is maintained throughout the streamer channel indicating the integrity of the streamer which is necessary for the arc breakdown applications.

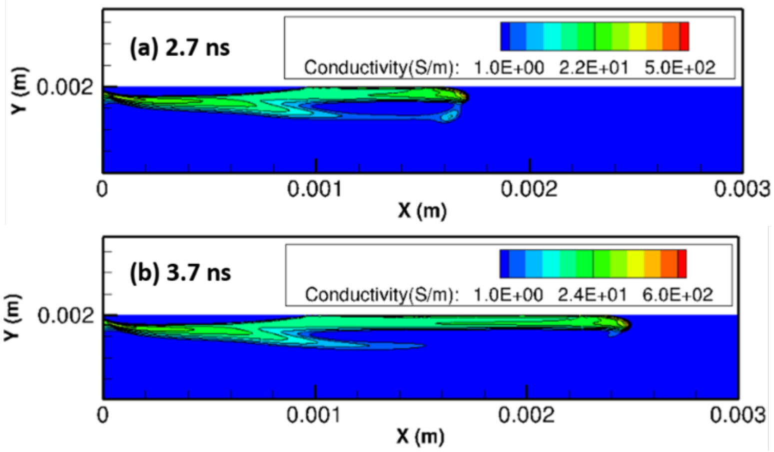

Figure 4.13: Distribution of the conductivity in the streamer channel in pure Ar for -5.0 kV obtained at (a) t = 2.7 ns and (b) t = 3.7 ns.

The presence of oxygen has a strong effect on the continuous conductivity of the streamer channel. An admixture of O_2 leads to the nonlinear decrease of the local conductivity in the streamer channel (Fig. 4.14). For small oxygen concentrations ($< 5\%$), a continuous conductivity of the streamer column is preserved throughout the transient time considered with a small loss of channel conductivity for increasing oxygen concentration and the conductivity in the entire body of the streamer is similar to the pure Ar case even at t = 3.7 ns when the steamer has crossed 90% of the entire computational domain [Fig. 4.14(a)]. However, further increase in the oxygen concentration ($> 5\%$) results in a dramatic change in the continuous conductivity of the channel. For example, at 10% of O_2 there is nearly complete loss of electrical conductivity in the middle of the streamer channel at 2.7 ns. One can see from Fig. 4.14(c) that at 10% of O_2 the conductivity of the streamer channel is 0.5-0.8 S/m, which

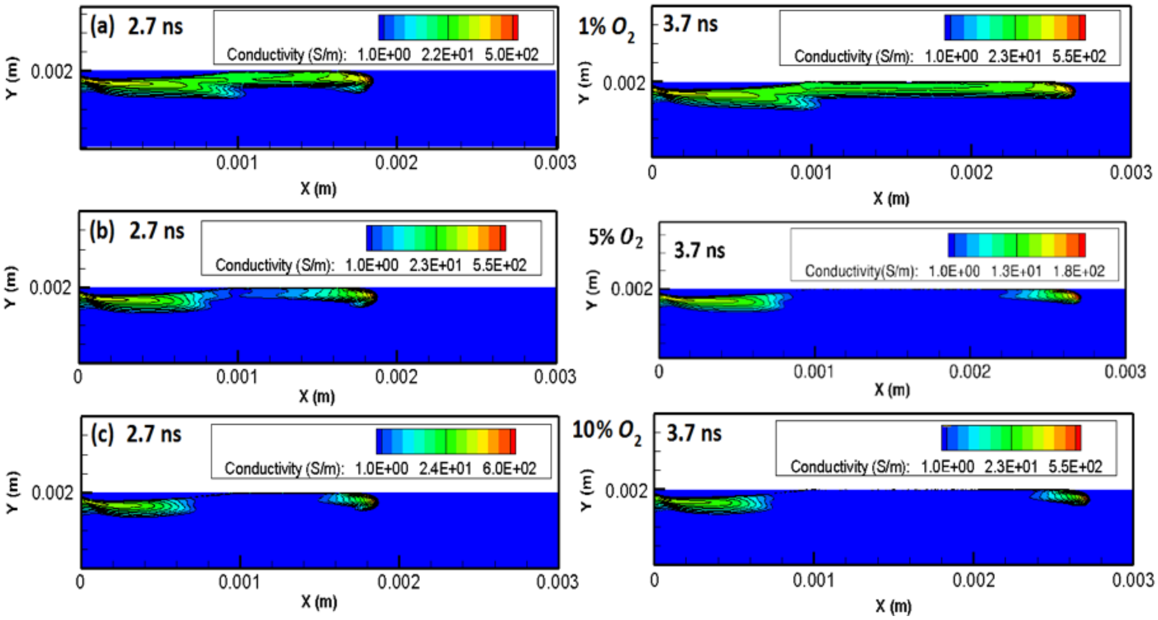

Figure 4.14: Distribution of the conductivity of the streamer channel obtained at t = 2.7 ns (left) and t = 3.7 ns (right) for (a) 1% of O_2, (b) 5% of O_2, and (c) 10% of O_2.

is 40-50 times lower than the streamer conductivity in pure Ar. Essentially, the electrical conductivity of the streamer is significant only at the head and in the tail regions of the streamer.

It is also important to note that the decrease in the conductivity from t = 2.7 ns to 3.7 ns due to addition of oxygen $>$ 5% is much faster (i.e $\sim$ 1 ns) even though the timescale of the attachment reactions for oxygen (17) and (19) is $\sim$ 100 ns. This is explained as follows: the addition of O_2 causes the reduction of electron temperature in the streamer channel. This results in the higher rate coefficients of the recombination reactions (e.g. $e + Ar^+ \longrightarrow Ar$)

which have timescales of ~ 2 ns for $T_e = 1$ eV and $\mathrm{N_{Ar}} \sim 10^{21} m^{-3}$. In addition, the electron diffusion coefficient is $D_e \sim 0.5 m^2 s{-}1$ at 1 eV and we have seen before that the streamer diameter is larger for Ar$-$O$_2$ mixture R $\sim 100\ \mu m$ [Fig. 4.10 (c)]. This results in much smaller diffusion timescales $\tau \sim \frac{R^2}{D_e} \sim$ 2.5 ns compared to pure Ar medium, which results in faster diffusion of the electrons to the wall. Thus, addition of oxygen in proportions $> 5\%$ causes the reduction in electron temperature which stimulates recombination reactions as well as increases the diffusion of the electrons (in the streamer channel) to the dielectric wall. These results show that the addition of electronegative gas such as O$_2$ in proportions $> 5\%$ causes the streamer channel to lose its conductivity as the streamer head passes through the domain.

Thus, the probability of the streamer-to-arc transition decreases in Ar$-$O$_2$ mixtures if the impurity of O$_2$ exceeds 5%. It is however important to note that the local conductivity in the head and the tail end (i.e. the place where the streamer is in contact with the grounded electrode) of the streamer channel remains high [Fig. 4.14(a-c)] in Ar$-$O$_2$ mixture even at O$_2$ concentrations as high as 10%. This is explained by the highest electron density in the streamer head.

4.6 Chemical kinetics dimensional reduction: Recursive Principal Component Analysis (RPCA)

Chemical complexity of non-equilibrium plasma poses a challenge towards plasma modeling. The number of species and the corresponding chemical reactions can become large for complex gases. The plasma models treat the species as a continuum and require solving the continuity equation for all the species to accurately capture underlying physics. This is computationally expensive for large reaction chemistries due to the stiff nature of the system. Principal Component Analysis (PCA) is a statistical technique which reduces the number of species equations by identifying the correlation between different species in the higher dimensional chemical space and defining new uncorrelated variables, which are a linear combination of the original variables in a lower dimensional space. PCA has been used rigorously in the area of combustion modeling and turbulent flame modeling to identify a low dimensional manifold which governs the evolution of the entire system [130, 131]. All the species under consideration in the above area are primarily neutrals. Recently Peerenboom et.al [132] implemented the technique for a a CO_2 plasma kinetic model. The major focus still remained on tracking the density of neutral species, and excited states.

Dimensional reduction algorithms using PCA typically compute the principal components at the start of the simulation and assumes them to be valid during the course of the transient simulation. This assumption is invalid for plasma based reactive systems when the charged and excited species are present due to their highly non-linear rates. The approach derived in this work uses a recursive approach to update these components dynamically during the transient simulation.

In this section, a Recursive Principal Component Analysis (RPCA) al-

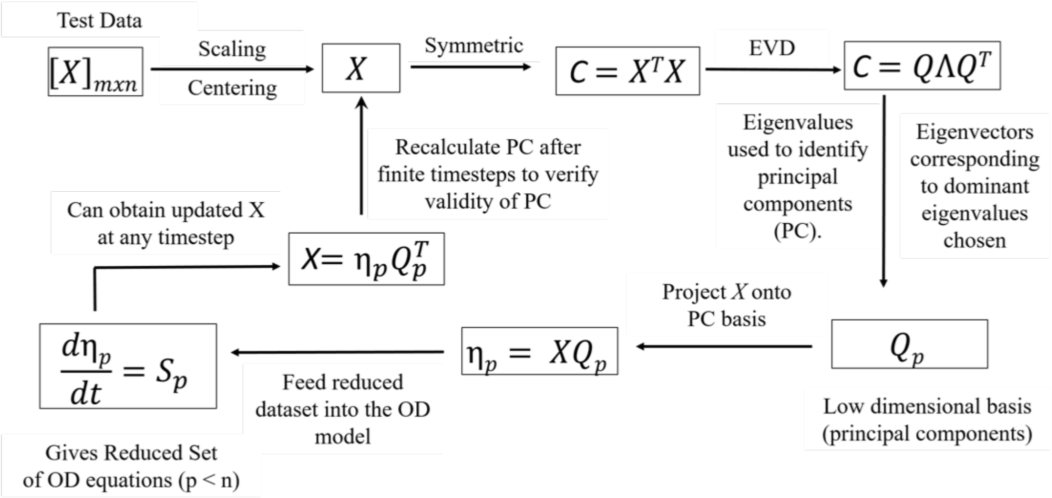

Figure 4.15: Recursive principal component analysis algorithm

gorithm is formulated for a Zero-Dimensional (0D) plasma model towards reduction of chemical complexity primarily on account of the presence of charged species. The 0D model is constructed from the non-equilibrium plasma model described in section 2.1.2 by neglecting the flux terms and consists of ODE's for species continuity and electron energy equations. A constant power source to estimate Joule heating is the electron energy equation.

To test the chemical kinetics reduction formulation, we have considered Ar$-$O$_2$ gas with 1% Oxygen impurity for studies in this section. However the formulation is general and can be applied to gas chemistry of all sizes. The Ar$-$O$_2$ chemistry consists of 12 species (4.1) and 46 reactions (Appendix A) and has been described in section 4.3. The background pressure P = 1 atm and background temperature is held constant at T = 300K.

The algorithm is described in Fig. 4.15. First the 0D model is solved for 'n' time steps in order to generate the training data for the algorithm. The matrix X, consists of transient species number densities of 'm' species over 'n' time steps. The data matrix X is scaled, centered and multiplied by its transpose in order to make it symmetric. Next we perform eigen-value decomposition to generate the eigen value spectrum associated with the eigen vectors. Based on a predefined threshold (λ_{th}), all the eigen vectors with eigen values lower than the threshold value λ_{th} are neglected. The eigen spectrum for the Ar$-$O$_2$ used for the present study is shown in Figure 4.16. The p selected eigen vectors are termed as principal components (Q_p) and form the lower dimensional basis. The original dataset X and the source terms in the original ODE's are projected onto this lower dimensional principal component basis $\eta_p = XQ_p, S_p = SQ_p$ to obtain the initial conditions in this new basis η_p, S_p. The system of ODE's are solved in this new lower dimensional basis which only consists of p ODE's where $p < m$. The species density in the original higher dimension can be obtained at any time-step from the lower dimensional basis via a linear transformation $X = \eta_p Q_P^T$. The reaction rates and the number density of the dominant species can change drastically during the course of a simulation, which will, in turn, cause a substantial change in the dominant principal components. Thus, to ensure that the selected principal components are accurate throughout the course of the simulation, the principal components are recalculated after finite number of time-steps to check the validity of these principal components with time. Hence this algorithm is named Recursive

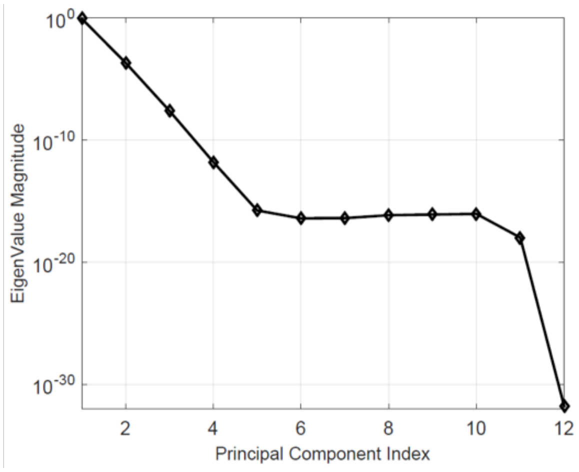

Figure 4.16: Eigen spectrum for a Ar$-$O$_2$ mixture

Principal Component Analysis (RPCA)

Figure 4.17 shows the evolution of species densities in the global plasma model using two principal components. The principal components are chosen by using $\lambda_{th} = 9 \times 10^{-6}$. The number of principal component mentioned in Fig. 4.17 is the value which persists for a major portion of the test run, as the value changes over the course of the simulation. It is seen that, using only two principal components, RPCA reduced model predicts the number densities of all species in close agreement with the actual solution. This is due to the fact that the first two eigen values account for almost 98-99% of the total variance as seen in Fig. 4.16.

To optimize performance, simulations are conducted to find the limiting values of the Training Data Set Size (TDS) and Interval of Recursion (IOR) for the RPCA algorithm. The Training Data Set Size is the number of time steps

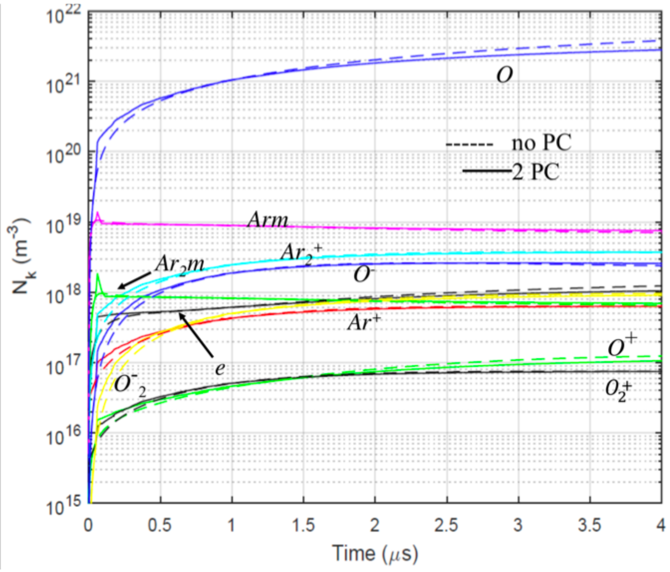

Figure 4.17: Comparison of evolution of species number densities in the global plasma model using 2 PC vs the complete global plasma model

for which the global model is solved to collect data before performing PCA to identify the principal components. The Interval of Recursion (IOR) is the interval after which the principal components are recalculated and updated over the course of the simulation.

It is seen from 4.18, that Intervals > 6000 time steps cause the solution to diverge, as the information about PC's has changed significantly during this time. An optimum interval of 4000 time steps is identified to optimize computation while maintaining accuracy. It is also seen from 4.19 that datasets smaller than 200 time steps are unable to provide complete information about the underlying physics and dominant principal components. They introduced substantial errors in the transient simulations as seen in Fig. 4.19. An op-

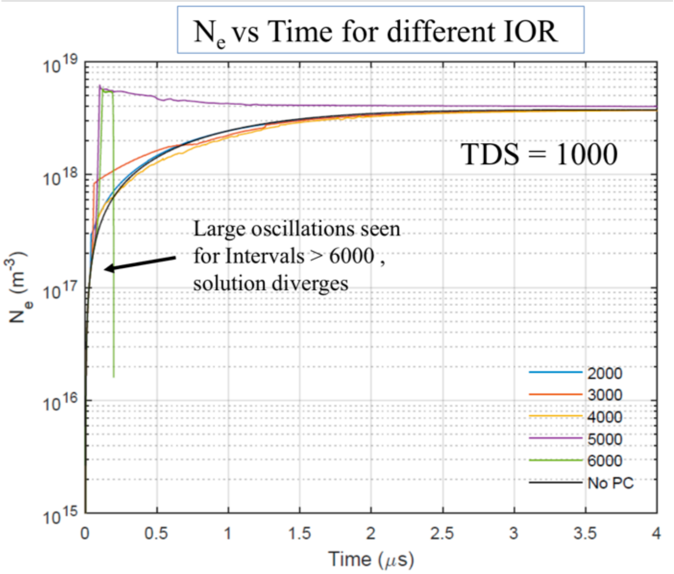

Figure 4.18: Transient evolution of electron density for various Interval of Recursion (IOR) for a fixed Training dataset size of 1000

timum TDS of 1000 is chosen to optimize computation while maintaining accuracy.

The algorithm reduces the computation time for the global plasma model by 30% when two principal components are chosen for the simulations while maintaining the accuracy of the transient solution.

4.7 Conclusions

The effect of oxygen impurities on the positive streamer initiation and propagation through the atmospheric-pressure argon was studied by the self-consistent fluid simulations.

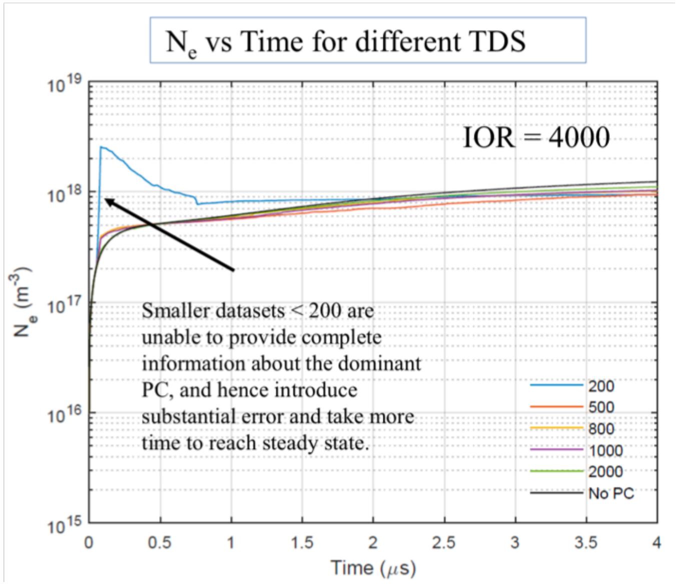

Figure 4.19: Transient evolution of electron density for various Training Data Set Sizes (TDS) for a fixed Interval of Recursion of 4000

It was found that the admixture of oxygen to argon causes profound changes in the dynamic characteristics of the streamer discharge. Namely, threshold voltage of the discharge decreased by a few hundreds of volts due to the addition of tiny amounts of O_2 ($\sim 1\%$). On the other hand, peak electron temperature obtained in the streamer head, increased after the addition of small quantities of O_2.

It was observed that the streamer channel in pure argon maintained its spatial conductivity during the streamer propagation throughout the cathode-anode gap. Addition of the oxygen gas with concentration lower than 5% did not considerably affect the conductivity of the streamer channel. Also, small impurity of oxygen decreased the breakdown voltage of the medium, and the streamer successfully bridged the gap at even lower trigger voltages. Surface streamer branching effects are also minimized by addition of tiny amounts of O_2 due to suppression of volumetric streamer channels by the attachment reaction.

When the mole fraction of O_2 exceeded 5%, the conductivity of the streamer channel deteriorates significantly and the probability of the streamer-to-arc transition decreased considerably. We obtain a strong dependence of the conductivity of the streamer channel on the mole fraction of oxygen. This is due to the reduction in electron temperature on account of addition of oxygen which increases recombination reaction rates and speeds up the diffusion of the electrons (in the streamer channel) to the dielectric wall.

Lastly a dimensional reduction algorithm is formulated using Recursive

PCA and validated for Ar$-$O$_2$ chemistry. The recursive framework (RPCA) is devised to dynamically update the principal components during the transient simulation which is vital due to the highly non-linear reaction coefficients associated with the charged species in the plasma.

Chapter 5

Modeling plasma discharges in bubbles suspended in liquids

Plasmas generated by electrical discharges in liquids[1] or in the immediate vicinity of liquids have attracted attention in the field of clean energy based liquid fuel reforming [10, 26, 27, 28, 29, 30, 31, 32] and plasma medicine [14]. Non-equilibrium plasma discharges are particularly effective in the production of highly reactive chemical species that drive chemical reaction in the liquids for a number of applications [47]. These discharges also make it possible to achieve efficient and non-uniform spatial production of active chemical species if one can exercise some measure of control on the direction of streamer propagation. Direct plasma discharge in liquids is highly infeasible as it require much higher breakdown electric fields [49, 50]. A more feasible approach is to initiate plasma discharge in immersed gas bubbles suspended in liquids, and utilize the active species generated for processing the liquid medium. Thus, a deeper understanding into the parameters governing the plasma evolution

---

[1] Portions of this chapter were previously published as "Kinetics and dynamics of nanosecond streamer discharge in atmospheric-pressure gas bubble suspended in distilled water under saturated vapor pressure conditions,"[92] in the Journal of Physics D: Applied Physics. All writing and figures included in this chapter are the original work of the author, with editing by Dr. Laxminarayan L. Raja

in immersed gas bubbles is crucial in understanding the dynamics of active species generation, which is the quantity of interest for plasma processing applications in liquids.

5.1 Problem description

This study focuses on computational studies of nanosecond streamer discharges generated in helium bubbles immersed in distilled water under atmospheric pressure conditions [92]. The objective of this study is to maximize the active species generation inside the gas bubbles and we investigate the effect of two parameters a) trigger voltage and b) presence of multiple bubble on the dynamic characteristics of discharge. The non-equilibrium plasma model described in 2.1.2 is used for modeling the discharge. The study takes into account the presence of water vapor in the gas bubble for an accurate description of the discharge kinetics. The work investigates the effect of water vapor on the breakdown voltage and studies the evolution of streamers in the gas bubbles for a range of positive and negative trigger voltages. The work also discusses the spatial and temporal distribution of dominant species and compares the distribution of these species for positive and negative trigger voltages. Preliminary studies are also conducted to model plasma penetration into the liquid medium using a multiphase-plasma fluid model to resolve the active liquid layer and electrostatic debye layer in the liquid medium.

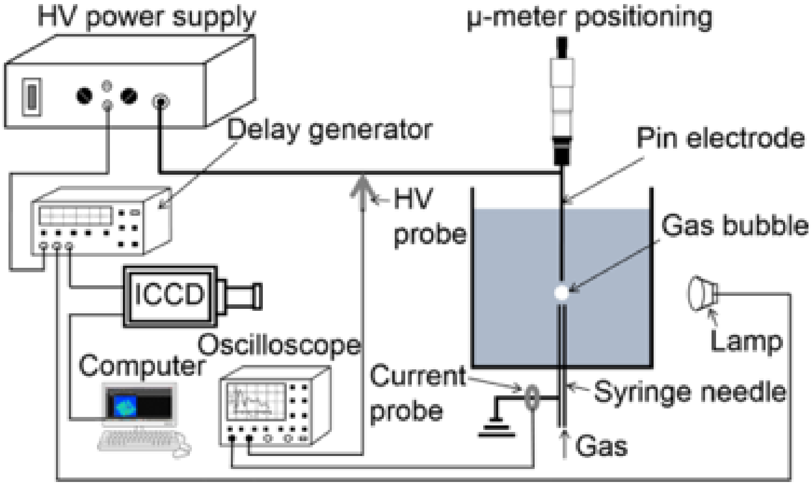

Figure 5.1: Experimental setup used by Hamdan et al [8].

5.2 Experimental overview and motivation

The physical problem relevant to this study is motivated by the experimental work by Hamdan et al. [8] which focused on the experimental study of plasma discharge in He gas bubbles immersed in distilled under atmospheric pressure conditions.

Fig. 5.1 shows the experimental setup of the problem under consideration. Helium gas is bubbled in through the hollow electrode located at the bottom with the pin electrode on the top acting as a trigger electrode. The electrodes are immersed in distilled water and separated by a gap width of 1 to 2 mm. Helium gas is bubbled at a low mass flow rate so that timescales of motion of the bubble in the liquid are negligible compared to the nanosecond timescales of the trigger voltage. Figure 5.2 (left image) shows the long

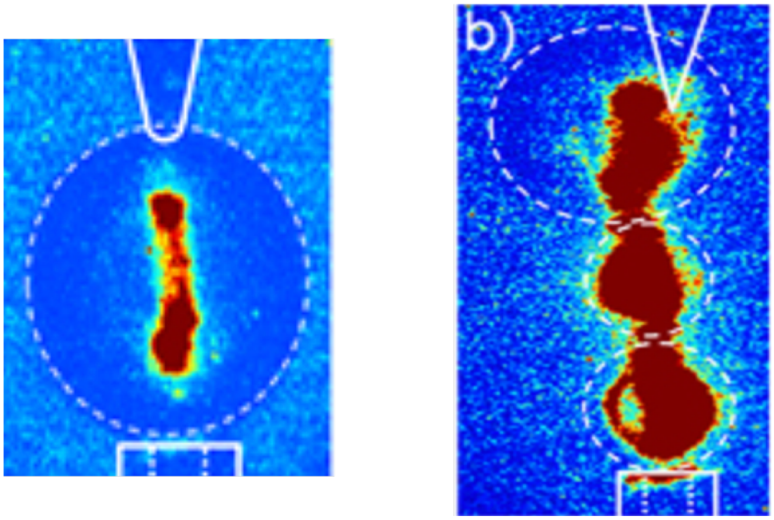

Figure 5.2: Long exposure images of streamers formed in single bubble 1 mm interelectrode gap (left) and multiple bubble 2 mm interelectrode gap (right).

exposure image for a single bubble discharge in the above configuration where an axial streamer bridges the gap in the gas bubble. They also see that the presence of multiple bubbles (Fig. 5.2(right)) allows streamer hopping from one bubble in order to bridge the gap. The streamer formed in multiple bubble configuration is thicker, highly diffused with more uniform species distribution inside the bubble volume to the single bubble configuration. The goal of the present work is to gain insight into the kinetics and dynamics of nanosecond streamer discharge in atmospheric-pressure gas bubbles and gain a qualitative comparison with the experimental observations.

Table 5.1: Species present in plasma model of $He-H_2O$ mixture

Charged	$e, He^+, He_2{}^+, HeH^+, H^+, H^-, H_2{}^+, O^+, O^-, O_2{}^+, OH^+, OH^-, H_2O^+, H_3O^+, H_4O_2{}^+, H_5O_2{}^+, H_7O_3{}^+, H_9O_4{}^+, H_{11}O_5{}^+, H_{13}O_6{}^+, H_2O_2{}^-, H_3O_2-, H_5O_3{}^-$
Neutral	$H, He^*, H^*, He_2{}^*, O, O(^1D), H_2, O_2, O_2(a), O_2(b)$ $O_3, OH, OH(A), HO_2, H_2O_2$
Background	He, H_2O

5.3 Discussion of chemistry: Helium-Water($He-H_2O$)

This section describes the chemistry formulation for the gas bubble filled with Helium and water vapor mixture($He-H_2O$). The chemical kinetic pathways due to presence of H_2O vapor in the gas bubble are taken into consideration for a more accurate description of gas phase discharge. The H_2O vapor concentration is computed using saturated vapor pressure conditions at an initial pressure of 1 atm. The finite-rate reaction chemistry mechanism is derived from the work of Bruggemann et al. [133] and consists of 40 species (Table 5.1) and 143 reactions (Appendix B).

In the present model, the reactions are assumed to occur only in the gas-phase (within the bubble). The transport, solvation effects and interactions of plasma species with the liquid medium are neglected (see, for instance, discussion in [68]). In general, these processes can affect the plasma component content because species such as OH, HO_2 and H_2O_2 have high Henry's constants and easily dissolve in water. However, on the time scale of the streamer propagation through the bubble, which is $\sim$ nanoseconds, fluxes of heavy species to the bubble wall are negligible and solvation of species does not play a significant role on the active species production/consumption in the gas bubble and on the streamer dynamics in the gas phase. The main pathways incorporated for electron impact reactions comprises of electron impact ionization, excitation, dissociative excitation, dissociative ionization, dissociation, de-excitation, attachment and recombination reactions. The electron impact reaction rate coefficients are calculated offline using zero-dimensional Boltzmann solver BOLSIG+ [114] using reaction cross-section data from literature [134]. The reactions between heavy species such as ions and neutrals are modeled to include ion-ion recombination reactions, quenching reactions for excited states of ion-neutral and ion-metastable impact reactions. The surface quenching reactions for charged and excited neutral species are also taken into consideration in the current study.

5.4 Simulation approach

The objective of the present work is to model the plasma discharge in gas bubbles immersed in distilled water to maximize active species densities and investigate the influence of the trigger voltage polarity and presence of multiple bubbles on the dynamics of the discharge.

Single bubble configuration

The computational domain (figure 5.3) for a single bubble configuration consists of an axisymmetric spherical bubble with diameter of 1 mm surrounded by distilled water (acting as the dielectric) with a relative permittivity (ϵ_r) of 80.4. A pin-to-hollow tube geometry is employed in the current work

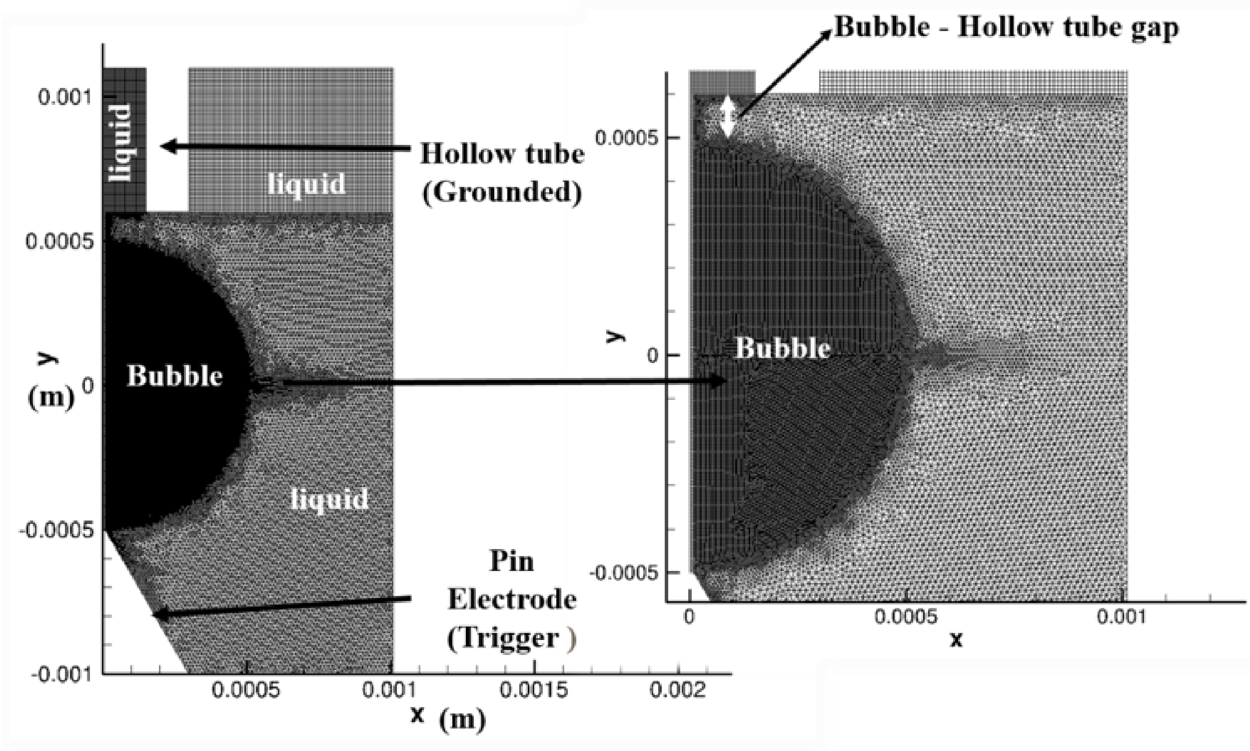

Figure 5.3: Geometry of the gas bubble-liquid problem and the computational domain.

similar to the configuration in the experiments. The trigger electrode is pin shaped with flat tip of 1 μm and a base length of 0.6 mm, while the ground electrode is a hollow tube with a flat base and the inner and outer diameter of 0.3 mm and 0.6 mm, respectively. Both the electrodes are completely immersed in the dielectric, with the flat pin electrode off from the surface of the gas bubble by 0.01 mm and the tube electrode off from the surface of the gas bubble by 0.12 mm. The choice of these parameters is similar to the experiments reported in [8] and described in section 5.2.

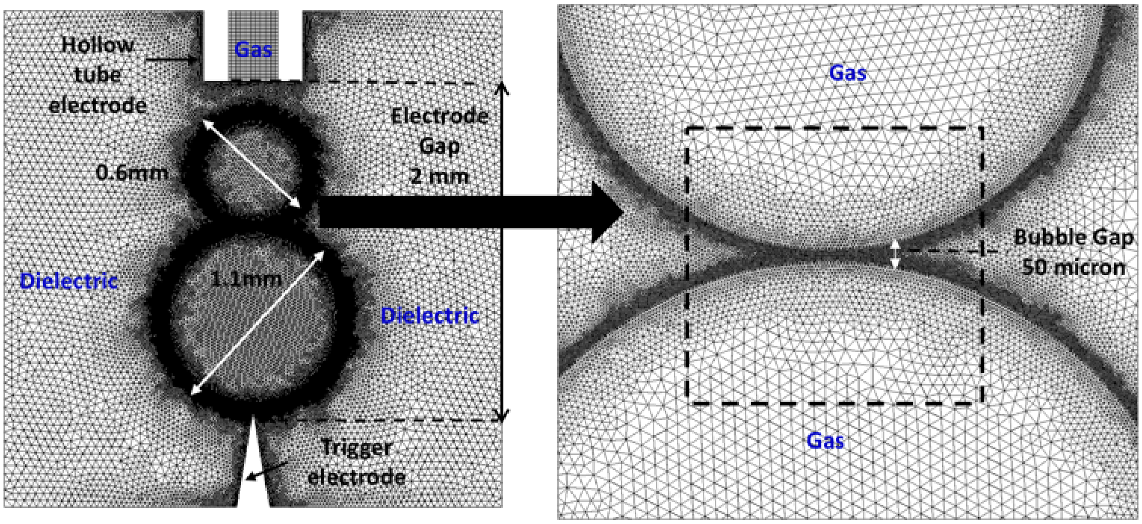

Figure 5.4: Computational domain of the gas bubble-liquid problem consisting of two bubbles and the computational domain.

The numerical grid comprises an unstructured mesh with highly refined regions near the electrodes and the bubble surface to capture the sheath effects. The mesh consists of approximately 60,000 cell elements of which 36,000 cells are located inside the gas bubble. The smallest mesh size in the current simulations is 2 μm and constrained by the sheath thickness which is a function of the debye length.

Multiple bubble configuration

A computational domain for a multiple-bubble study (Fig. 5.4) consists of a 2D planar geometry with two spherical bubbles located symmetrically along the electrode axis. The inter-electrode gap is increased from 1 mm to 2 mm in accordance with the experimental studies. The domain (Fig.

5.4) consists of two bubbles located along the axis of the electrodes with pin electrode acting as the trigger electrode/anode and the hollow tube electrode grounded. The diameter for the smaller bubble is 0.6 mm while the diameter of the larger bubble is 1.1 mm and the gap between the two bubbles is chosen as 50 microns. Figure 5.4(right) also shows as inset of the mesh refinement in the region between the two bubbles. The mesh is particularly fine along the surfaces of both bubbles and the region between the two bubbles to resolve the sheath at the plasma-liquid boundary. The mesh consists of 135,000 cells, with a minimum mesh size of 1 μm constrained by the sheath thickness.

Simulation setup

The gas bubble is filled with the helium and water vapor mixture ($He-H_2O$) at a constant pressure of one atmosphere and a constant bulk temperature of 300 K. Simulations were conducted for direct-current trigger voltage of both positive and negative polarity of the pin electrode. For the majority of the investigations, the molar concentration of water vapor in the helium bubble is 3% (saturated $He-H_2O$) computed using the saturated vapor pressure of water at atmospheric-pressure conditions [135]. The bubble was initially seeded with a plasma (electrons and He^+ ions) of density $10^{12}m^{-3}$ while the density of other species (ions and radicals) is 10^9m^{-3}. The influence of the non-homogeneous distribution of the initial plasma kernel on the discharge dynamics was also investigated. For initial seed plasma densities $< 10^{12}m^{-3}$, the influence of initial plasma density on the discharge characteristics was negligible. The dielectric used in the present studies is distilled water similar to previous numerical studies [68, 64, 65, 66, 63, 67]. Helium gas is bubbled at a low mass flow rate so that timescale of bubble movement in the liquid are negligible compared to the nanosecond timescales of the trigger voltage and thus the gas bubble is considered stationary during the duration of the duration of the simulation.

5.5 Breakdown voltage studies

The breakdown voltage in the $He-H_2O$ mixture is found to be $\sim$ 1.5 kV for the positive trigger voltage studies and is $\sim$ - 1.5 kV for the negative trigger voltage (i.e. $|E_{app}| \sim 1.5\ MV/m$) studies. Figure 5.5 shows the dynamic characteristics of the discharge at the breakdown voltage (1.5 kV) for positive trigger studies. We find that the breakdown voltage also remains constant for the water vapor density in the range 0-10 %, i.e. from pure helium case (0%) to highly over saturated $He-H_2O$ mixture (10 %). This indicates that the breakdown voltage is unaffected by the low density of water vapor present in the bubble at the atmospheric-pressure conditions and is primarily defined by the dominant He species. From [12], the breakdown voltage can be estimated using Eq. 5.1

$$V_b = \frac{Bpd}{\ln(Apd) - \ln[\ln[1 + \frac{1}{\gamma_{se}}]]} \tag{5.1}$$

Where, V_b is the breakdown voltage in Volts, p is the pressure in Torr, d is the distance between electrodes in cm, γ_{se} is the secondary electron emission

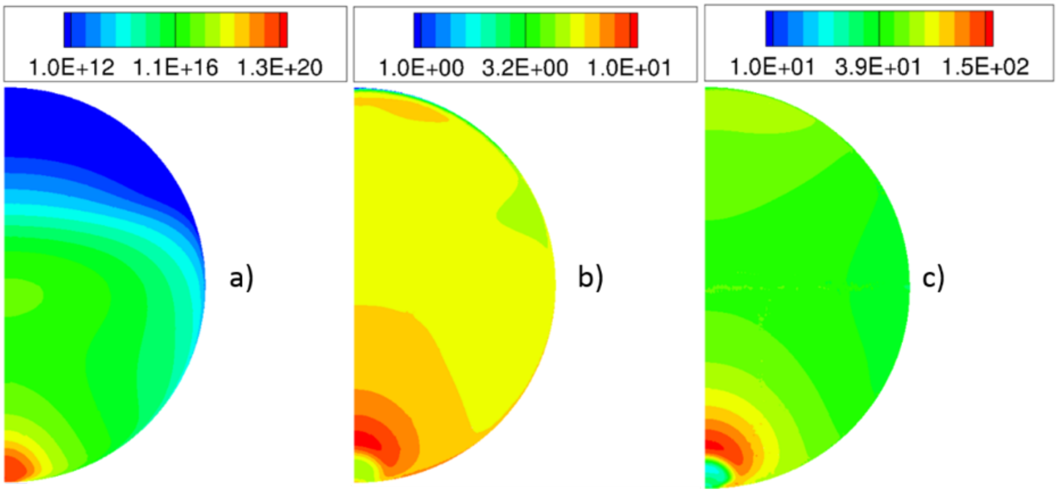

Figure 5.5: (a) Electron number density (in m^{-3}), (b) electron temperature (in eV) and (c) reduced electric field (in Td) distribution at the breakdown voltage for positive trigger i.e. 1.5 kV at t = 3 ns.

coefficient due to ion impact, and A and B are experimentally determined coefficients. For helium, these coefficients are roughly constant for electric fields in the range 30 to 250 Td [12]. For p = 760 Torr, d = 1.1 cm and $\gamma_{se} = 0.01$ used in our study, the Eq. 5.1 gives $V_b = 1.52$ kV which agrees with the breakdown voltage obtained in the present work. The trigger voltage is slightly lower for the breakdown in the bubble compared to the parallel plate configuration due to the large local electric field at the tip of the pin electrode and electric field enhancement at the surface of the bubble.

Depending on the electrode polarity, the streamer stage of discharge is preceded by the avalanche growth at the pin electrode or in the cathode-anode gap [37]. This is confirmed in Fig. 5.5(a) where we observe electron number density $\sim 10^{20} m^{-3}$ (high enough to indicate avalanche formation) near the pin electrode at $V_{br} = 1.5$ kV for positive polarity. Peak electron temperatures of ~ 10 eV are observed at the head of the corona while the electron temperature in the body drops to ~ 3.2 eV (Fig. 5.5(b)). Quantitatively, the avalanche-to-streamer transition is described by the Meek's criterion [37] which for parallel plate configuration is given as

$$\alpha(E_{app})x \sim 18 \tag{5.2}$$

Here E_{app} is the applied electric in V/cm, x is the distance from the cathode in cm and α is the Townsend ionization coefficient of the helium in cm^{-1}. Assuming x is the bubble diameter, we get the value of α to be in the range of $180 - 210 cm^{-1}$. Using the relation between Townsend ionization coefficient and applied electric field (E_{app}) for He determined experimentally by two different sources, Chanin et al. [136] and Davis et al. [137], we get $E_{app} = 1.6$ to 2.1 MV/m. Though Meek's criterion 5.2 was derived for parallel plate configuration, the value of electric field for avalanche-to-streamer transition agrees quite well with the conditions for the present configuration.

5.6 Trigger voltage polarity studies

5.6.1 Positive trigger streamer characteristics

For the positive trigger voltage, the simulation results have shown that in the beginning the electron/ion avalanche (also termed as corona) [41] grows

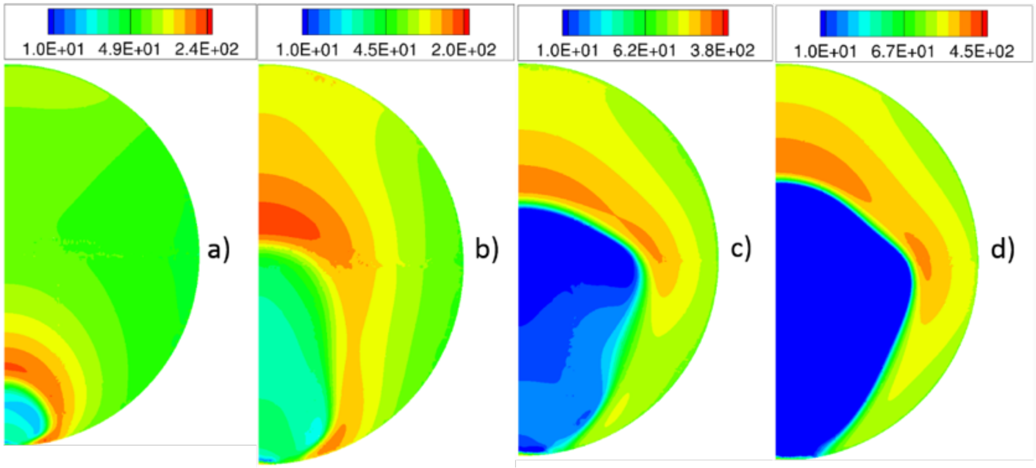

Figure 5.6: Transient evolution of the reduced electric field ($(E/N)_{br}$) distribution (Td) for 2 kV at (a) t = 2 ns, (b) t = 2.5 ns, (c) t = 3 ns, (d) t = 3.5 ns.

near the pin electrode as seen in Fig. 5.5(a). The electric field enhancement is observed at the streamer head as seen in Fig. 5.5(c) with the peak value of E/N reaching $\sim$ 150 Td. We identify this as the breakdown reduced electric field $(E/N)_{br}$ necessary for the streamer formation in the atmospheric pressure He gas bubble of 1 mm diameter immersed in water. Later, when the Meek's criterion Eq. 5.2 is satisfied this corona transforms to the cathode-directed streamer (i.e. negative streamer). The streamer propagates toward the cathode aided by the acceleration of background electrons present ahead of the streamer head.

We carried out the simulations for the positive trigger voltage in the range 1.5 - 15 kV. It was found that the discharge evolves through two completely different modes depending on the magnitude of the applied voltage. For the positive trigger voltage in the range 1.5 to 3 kV, the discharge is initiated through a corona phase at the bubble-anode interface. Once the Meek's criterion (Eq. 5.2) is satisfied, the corona transforms into a filamentary streamer as seen in Fig. 5.6(b)). The streamer moves primarily along the axis of the bubble till it reaches the center of the bubble (Fig. 5.6(b)). This is due to the fact that as the applied voltage is close to the breakdown voltage the inclined electric field lines from the pin anode have magnitude lower than the breakdown voltage, i.e. the electric field exceeds $(E/N)_{br}$ only near the axis of the bubble. This prevents the streamer deviation from the axis. We also see from figures 5.6(a) and (b) that the electric field at the head of the streamer decreases during its axial motion. This is because of the decreasing influence of the bubble wall on the electric field at the streamer head as it approaches the bubble center. From Eq. 5.3, it is seen that this results in a decrease in the net electric field at the streamer head. The radius of the streamer remains almost constant during this axial propagation phase of the discharge and is very close to the thickness of the base of the pin electrode. This indicates axial mode dominance during the initial stages of the discharge and agrees with the experimental results of Hamdan and Cha [8].

$$E_{head} = E_{applied} + E_{induced} \tag{5.3}$$

The streamer head has a convex shape with radius of curvature R. Therefore, the electric field of the space charge at the streamer head can be defined by

$$E_{induced} = \frac{eN_e}{R^2}, Ne = \exp(\alpha x) \tag{5.4}$$

Hence we conclude that, while the increase in the radius decreases the space charge field (Eq. 5.4), the applied external electric field increases much more at the head due to its proximity to the cathode. This more than compensates for the space charge field reduction and results in a substantial increase in the electric field at the streamer head once it crosses the center of the bubble as seen in figure 5.6 (c,d).

For higher applied voltages (> 8 kV), the streamer, once again, evolves through a corona formed at the bubble-anode interface. In this case, however, the streamer moves both along the surface and the axis of the bubble during the initial stage of the discharge (see figure 5.7(a)). This is due to the fact that the electric field lines originating from the pin anode are inclined at an angle to the axis owing to the shape of the anode. Thus, the region where electric field exceeds $(E/N)_{br}$ expands for increasing trigger voltages and is enough to deviate the streamer from the bubble axis. Figure 5.7(b) shows that the streamer hugs the surface of the bubble during the initial stage of the discharge. Once the streamer head moves further away from the anode the axial component of electric field, once again, becomes dominant, pulling the streamer to move along the bubble axis as seen in figure 5.7(c). As the streamer approaches the cathode the refracted electric field lines cause the expansion of the streamer head similar to the low voltage case (compare figures 5.6(d) and 5.7(d)).

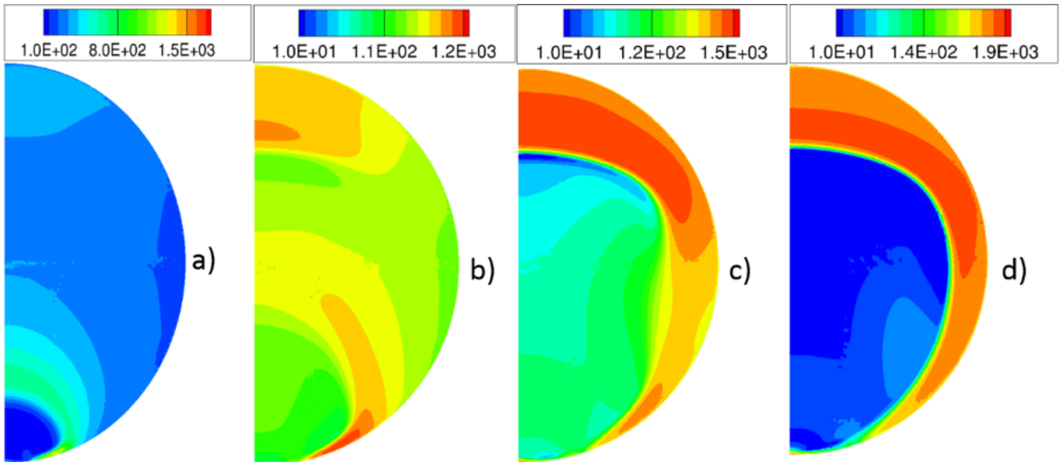

Figure 5.7: Transient evolution of the reduced electric field distribution (in Td) for 8 kV at a) t = 0.2 ns, b) t = 0.25 ns, c) t = 0.3 ns, d) t = 0.35 ns.

Figure 5.8 shows the transient evolution of the electron number density (n_e) and electron temperature (T_e) for low voltage studies (2 kV). We see that the region of high electron density is mainly concentrated near the bubble axis and consists primarily of low-energy electrons with temperature ($\sim$ 4 eV) much lower than the temperature at the streamer head ($\sim$ 15 eV). The electron temperature (T_e) at the head decreases slightly during the initial stage of the discharge (Fig. 5.8(a) and (b)) due to decrease in the net electric field at the streamer head (Fig. 5.6) and increases after the streamer head crosses the bubble center due to the increased proximity of the streamer head to the cathode.

At a higher voltage (8 kV) we see from figure 5.9 that the axial region consisting of high electron density is longer and wider than this region for

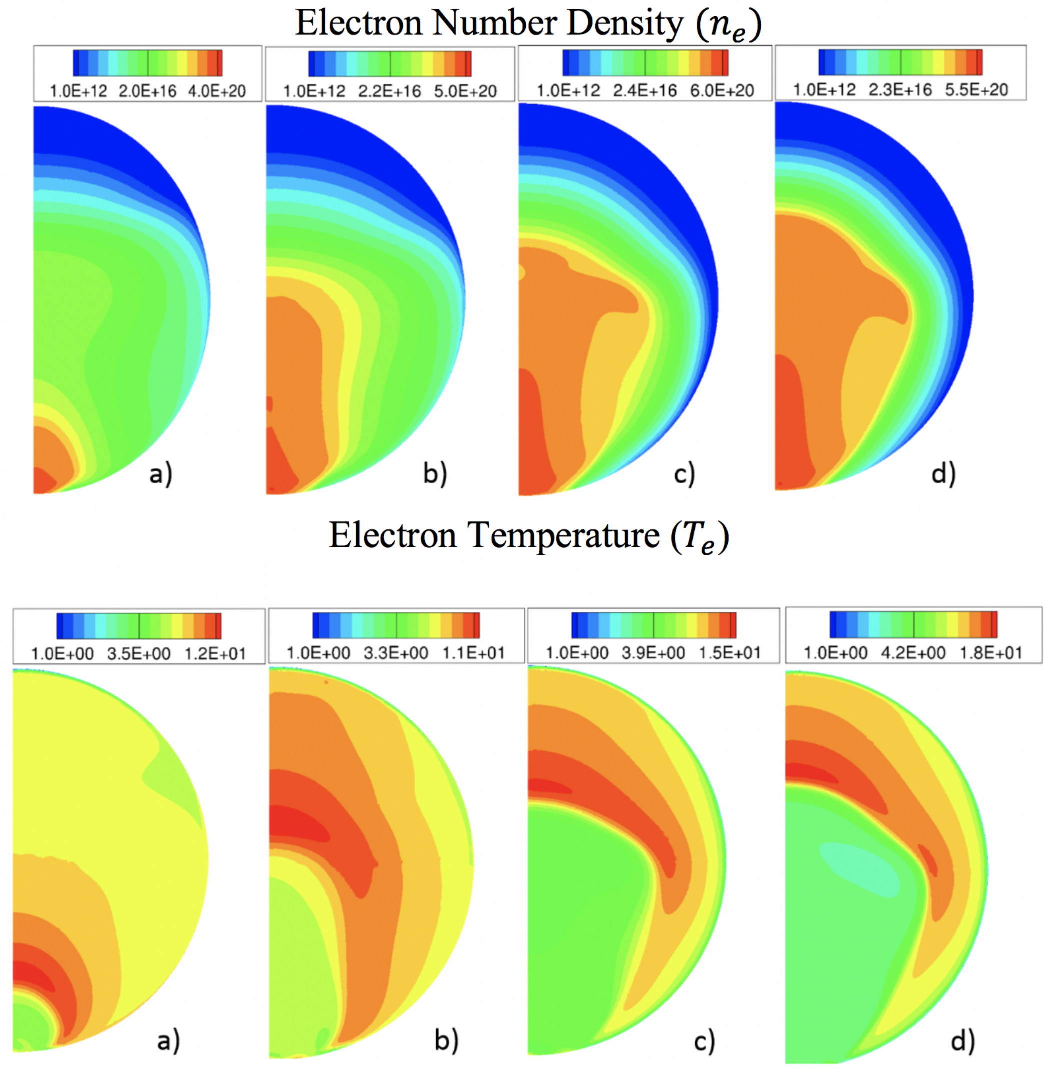

Figure 5.8: Transient evolution of the reduced electric field distribution (in Td) for 8 kV at a) t = 0.2 ns, b) t = 0.25 ns, c) t = 0.3 ns, d) t = 0.35 ns.

2 kV. The high electron temperature in the spherical ionization wave front is concentrated near the bubble surface as seen in Fig. 5.9(b), which is opposite to the case shown in Fig. 5.8. This clearly demonstrates the surface propagation mode during the initial stages of the discharge for higher voltage. However, a closer observation of the results indicate that the streamer does not necessarily propagate along the bubble surface, as was obtained for instance in [28], but in close vicinity to the surface. This can be explained by faster streamer propagation under the conditions in our study so that the dielectric has no time to be charged and to attract the streamer.

We find that, for 2 kV studies, the dominant positive ions are He^+, $\mathrm{H_2O^+}, \mathrm{OH^+}\,\mathrm{and}\,\mathrm{H^+}$ (figures 5.10, 5.11) with the density of He^+ being an order of magnitude higher than the densities of other positive ions. The production of helium positive ions is high both at the streamer head and in the axial region in its tail. The latter is, in spite of the low electron temperature near the streamer axis, due to the high electron density in this region. This results in a net high electron energy ($\alpha\ n_e T_e$) near the axis as compared to the streamer head. Since the dominant production reaction of these ions is the electron impact ionization $\mathrm{e} + \mathrm{He} \longrightarrow \mathrm{He}^+ + 2\,\mathrm{e}$, we conclude that a high net electron energy near the axis results in a high ion density near the discharge axis and not at the streamer head.

Our simulation results have shown that at the considered conditions, the dominant active neutral species are O, H and OH (figure 5.12). The densities of both $\mathrm{H}\,\mathrm{and}\,\mathrm{OH}$ are comparable since the dominant reaction for pro-

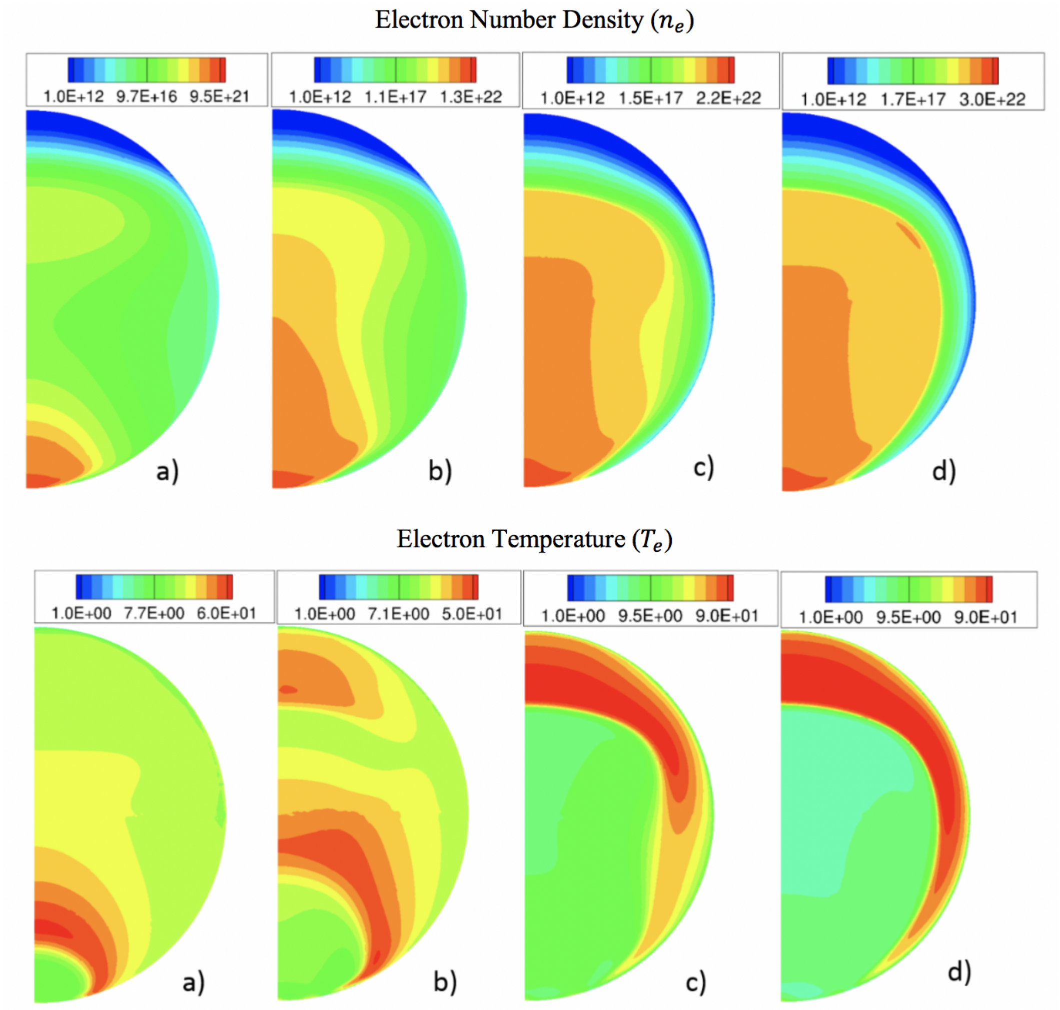

Figure 5.9: Transient evolution of electron number density, top half (in m^{-3}) and electron temperature, bottom half (in eV) for 8 kV at a) t = 0.2 ns, b) t = 0.25 ns, c) t = 0.3 ns, d) t = 0.35 ns.

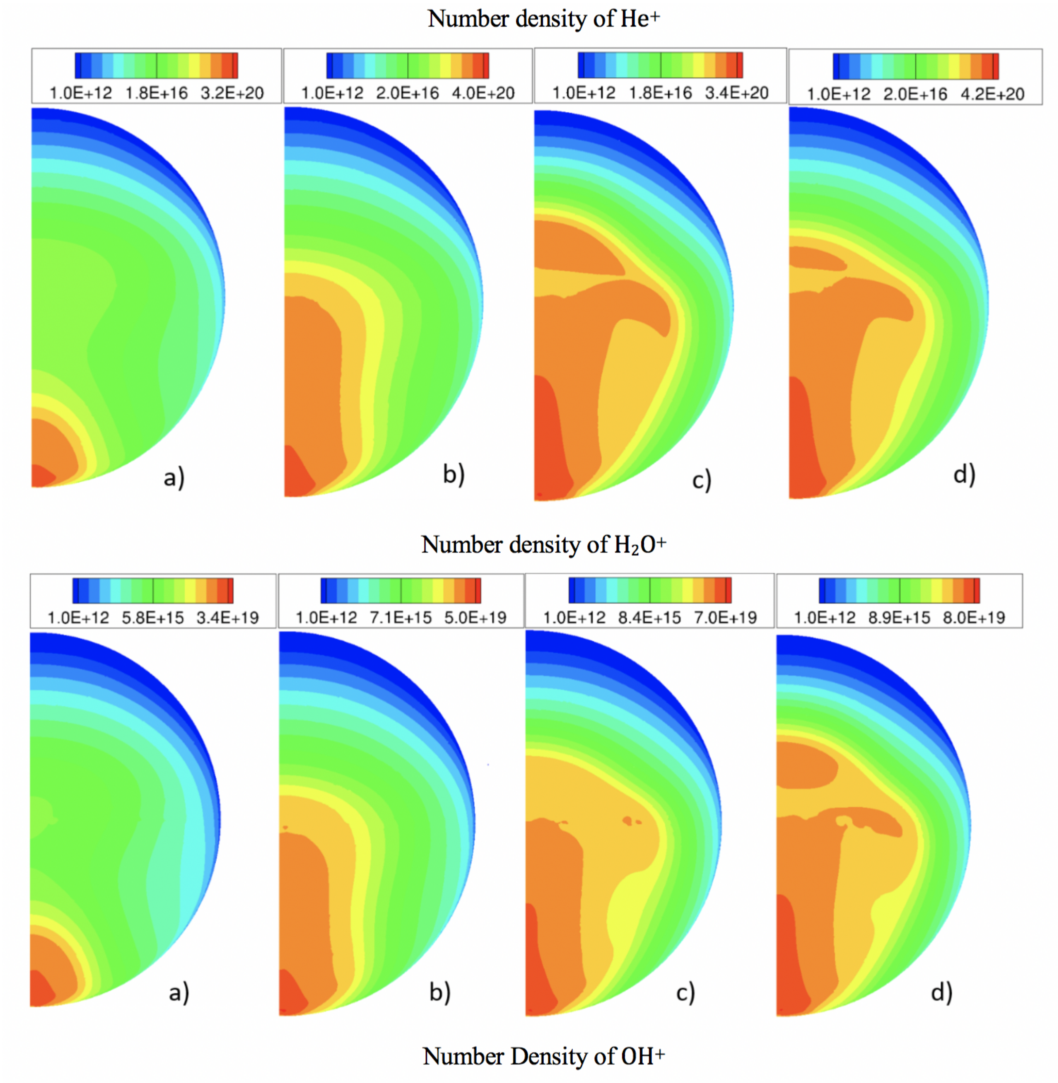

Figure 5.10: Transient number densities of He^+ and H_2O^+ ions at a) t = 2 ns, b) t = 2.5 ns, c) t = 3 ns, d) t = 3.5 ns.

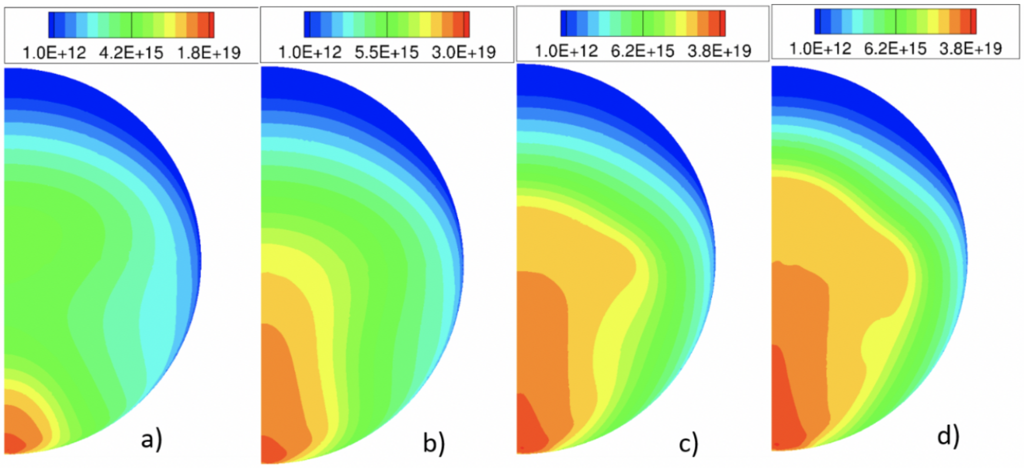

Number Density of H+

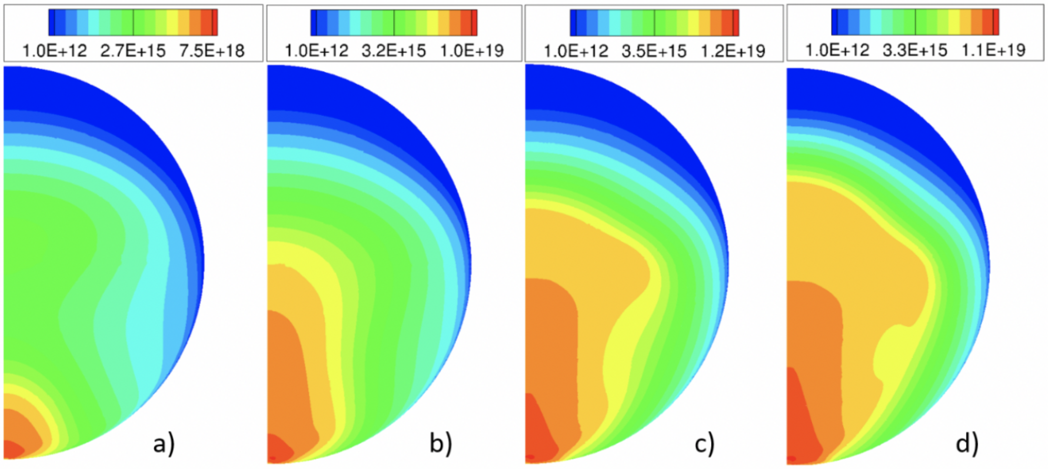

Figure 5.11: Transient number densities of OH^+ and H^+ ions at a) t = 2 ns, b) t = 2.5 ns, c) t = 3 ns, d) t = 3.5 ns.

duction of these species is the electron impact dissociation of water

Figure 5.13 shows the flux of the dominant species to the bubble wall for 2 kV. The largest flux is obtained for He^+ (not shown). Also, the flux of H^+ is one order of magnitude smaller than that of H_2O^+. This is explained by much smaller number density of H^+ compared to the number density of H_2O^+ (Fig. 5.10). The flux of H radicals is comparable with that of OH radicals and therefore not shown here. Flux of O radicals is $\sim$ 2 orders of magnitude lower than the flux of OH radicals and thus not significant for positive trigger voltages.

The dominant water complex species for conditions of our study are $H_{11}O_5{}^+$, $H_9O_4{}^+$ and $H_{13}O_6{}^+$ with the peak number density of these species reaching the values $\sim 10^{19} m^{-3}$ after 3.5 ns. It is interesting to note that the dominant negative ion found in the current work is the heavier water complex anion $H_5O_3{}^-$ with the density an order of magnitude higher than the density of other major negative ion OH^-. This is due to the fact that hydroxyl anions undergo rapid attachment to form $H_5O_3{}^-$ through the two step three-body recombination reactions:

$$\mathrm{OH^- + H_2O + M \longrightarrow H_3O_2{}^- + M} \tag{5.5}$$

$$\mathrm{H_3O_2{}^- + H_2O + M \longrightarrow H_5O_3{}^- + M} \tag{5.6}$$

Here M = He. The rate coefficients of both reactions are of the order of

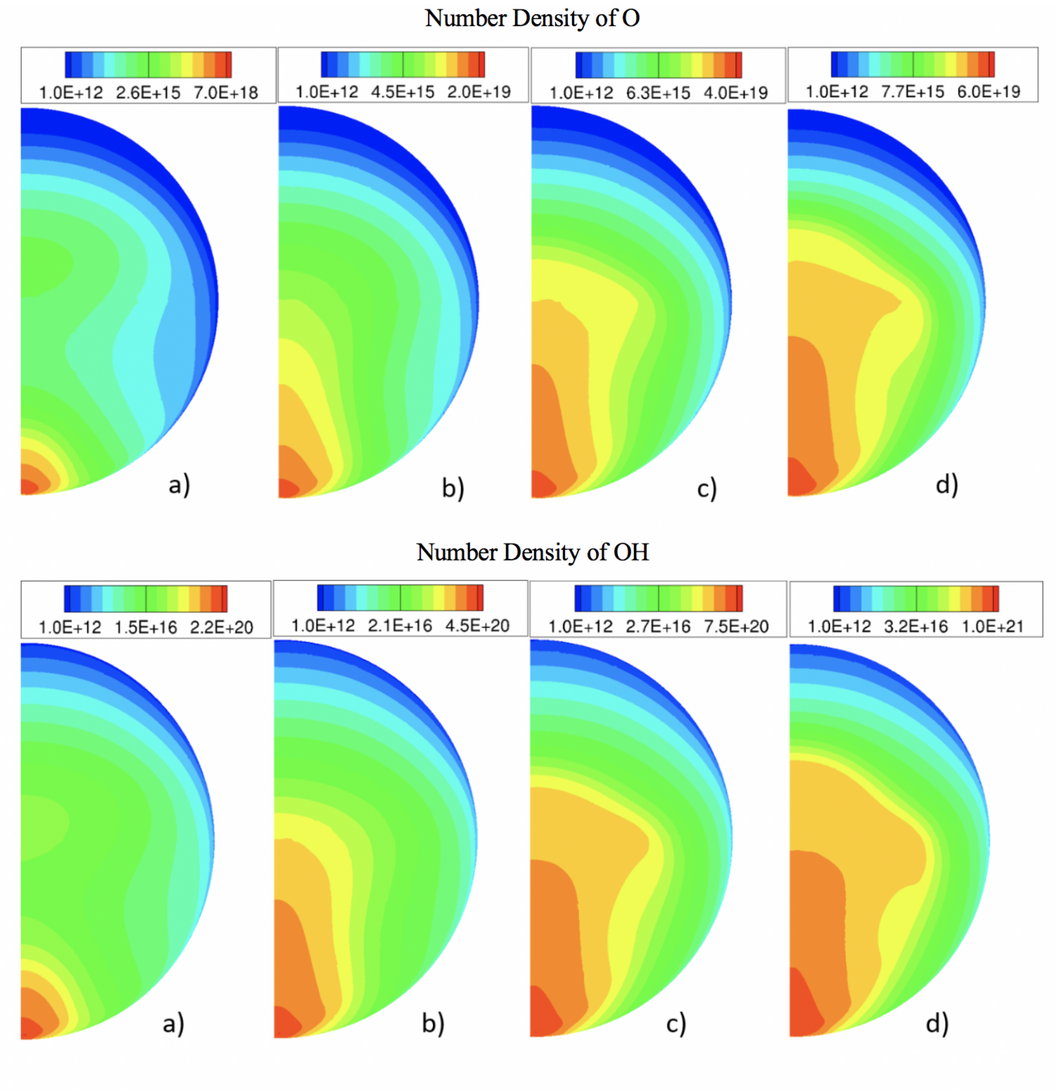

Figure 5.12: Transient number densities of OH and O radicals at a) t = 2 ns, b) t = 2.5 ns, c) t = 3 ns, d) t = 3.5 ns.

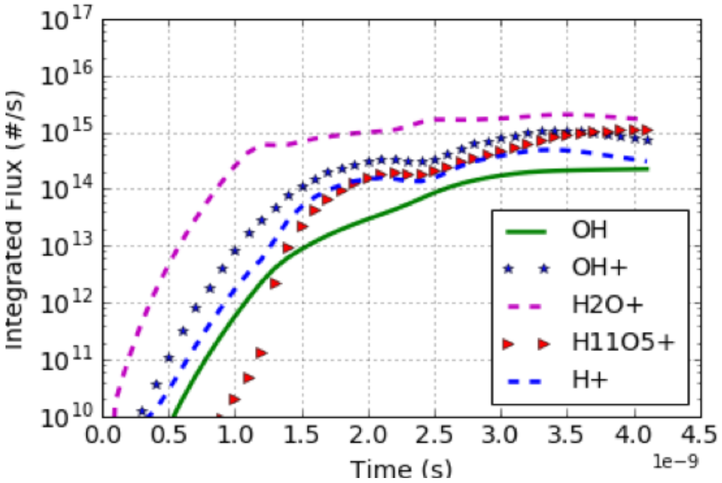

Figure 5.13: Time evolution of the integrated flux of the dominant species to the surface of the bubble at 2 kV.

$10^{-28} m^3 s^{-1}$ (Table 2). Substituting the densities of He and H_2O we estimate the rates of both reactions as $\sim 10^{40}-10^{41} m^{-3} s^{-1}$. For comparison, the rates of ion-ion recombination reactions (e.g. He^+ and OH^-) are $\sim 10^{37} - 10^{38} m^{-3} s^{-1}$ which is much smaller than the rate of ion conversion reactions shown above.

5.6.2 Negative trigger streamer characteristics

In this section, we present results of studies conducted by reversing the polarity of the pin electrode. The negative trigger voltage in the range -1.5 kV to -15 kV is applied to the pin electrode. We find that the discharge evolves through completely different modes as compared to the positive trigger voltage discussed in the previous section.

For the low voltage studies, we see the formation of the electron/ion

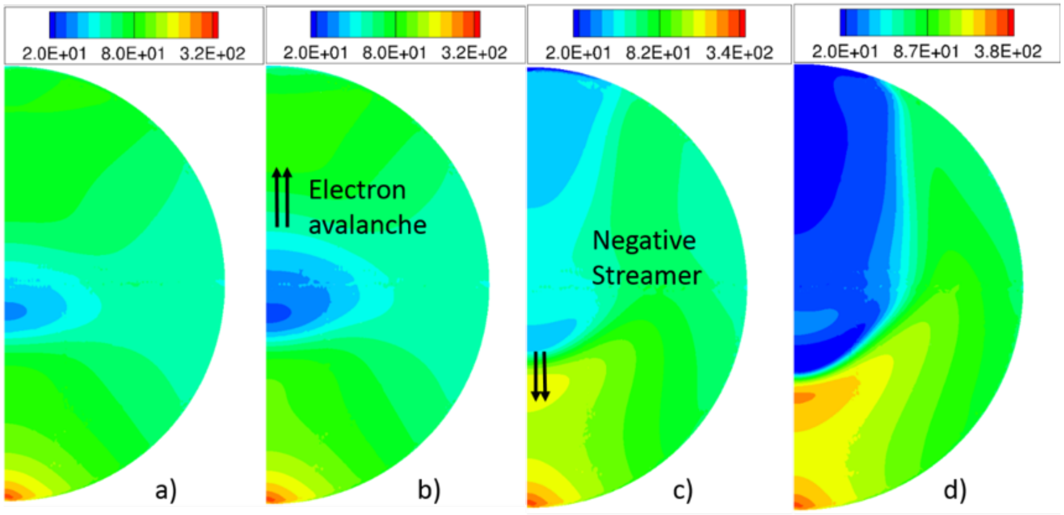

Figure 5.14: Transient evolution of the reduced electric field distribution (in Td) for -2 kV at a) t = 2 ns, b) t = 2.2 ns, c) t = 2.7 ns, d) t = 3 ns from left to right.

avalanche on the axis of the bubble at a finite distance from the pin cathode (see Fig. 5.14(a) and Fig. 5.16(a)). This avalanche moves toward the anode along the bubble axis. The avalanche is not transformed into a streamer owing to the low plasma densities. As a consequence, there is no self-consistent mechanism for the propagation of the avalanche to the anode and the avalanche propagates due to the plasma generation by the electrons which are being accelerated in the high electric field present between the avalanche and the anode. The plasma density in the avalanche is enough to marginally screen the applied electric field but not enough to cause the local enhancement of electric field. One can see from figure 5.14(a) the high-voltage sheath between the cathode and the avalanche because the electrons need to travel some distance

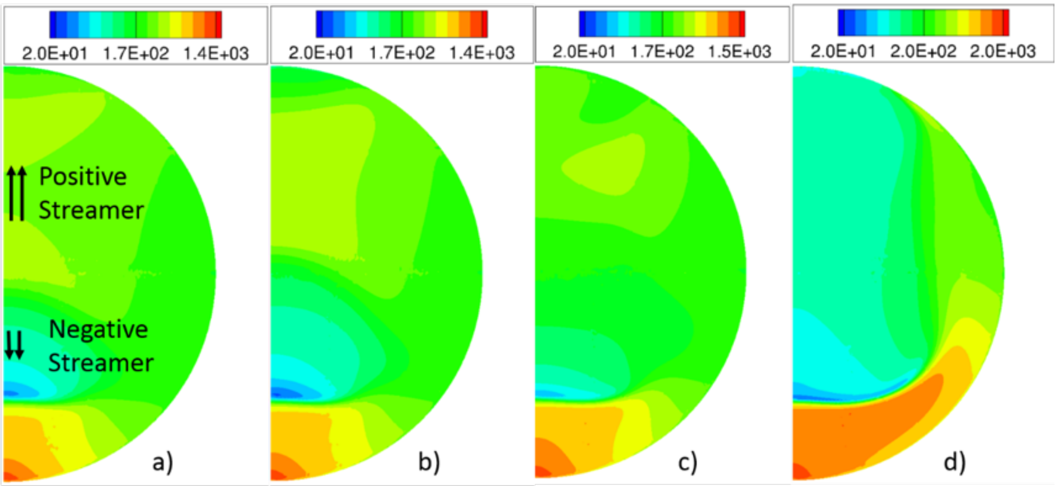

Figure 5.15: Transient evolution of the reduced electric field distribution (Td) for -8 kV at a) t = 0.2 ns, b) t = 0.22 ns, c) t = 0.25 ns, d) t = 0.3 ns.

to gain the energy and form a rather dense plasma to screen the applied electric field.

Figure 5.15 shows the electric field profile obtained for -8 kV. We conclude from Fig. 5.15(a) that a dense avalanche is formed on the axis of the bubble and closer to the cathode which is explained by shorter distance necessary for seeded electrons to generate dense plasma. Figure 5.17(a) shows that this avalanche transforms into an anode-directed streamer (positive streamer). This implies that the Meek's criterion (Eq. 5.2) is satisfied for this avalanche.

One observes from figure 5.16, the formation of the cathode-directed streamer for both trigger voltages. The mechanism of this streamer formation is analogous to that described in section 5.6.1. The anode-directed streamer (positive streamer) moves much faster as compared to its counterpart cathode-directed one, i.e. negative streamer (Fig. 5.17). The anode-directed streamer propagates primarily along the axis of the bubble due to the shape of the anode with the radius of the anode-directed streamer comparable to the anode radius, while the cathode-directed streamer spreads as it moves towards the anode due to the influence of the inclined electric field lines originating from the pin shaped cathode (figure 5.17(c)).

Figure 5.16 shows the transient evolution of the electron density and the electron temperature for the trigger voltage -2 kV. The comparison between figures 5.16(a) and (d) allows us to conclude that the most efficient plasma generation occurs during the propagation of the cathode-directed streamer. This is explained by the electric field distortion caused by the streamer (see figure 5.14,5.16). Namely, one can see from figure 5.14 that during the stage shown in figures 5.16(a) and (b), the largest electric field is obtained in the vicinity of the cathode (figures 5.14(a) and (b)) where electron density is small. The electric field in the bubble does not exceed 80 Td. Figures 5.14(c) and (d) show high electric field at the head of the cathode-directed streamer ($\sim$ 200 Td) which explains higher rate of plasma generation during the streamer stage of discharge. Figures 5.16(c) and (d) show that the region of high electron density is mainly concentrated near the bubble axis. It is also observed that the axial discharge consists primarily of low-energy electrons with the energy $\sim$ 3-4 eV (refer Fig. 5.16) which is much lower than the energy at the streamer head ($\sim$ 12-15 eV) (see discussion in section 5.6.1).

Our simulation results also showed that the avalanche propagating to-

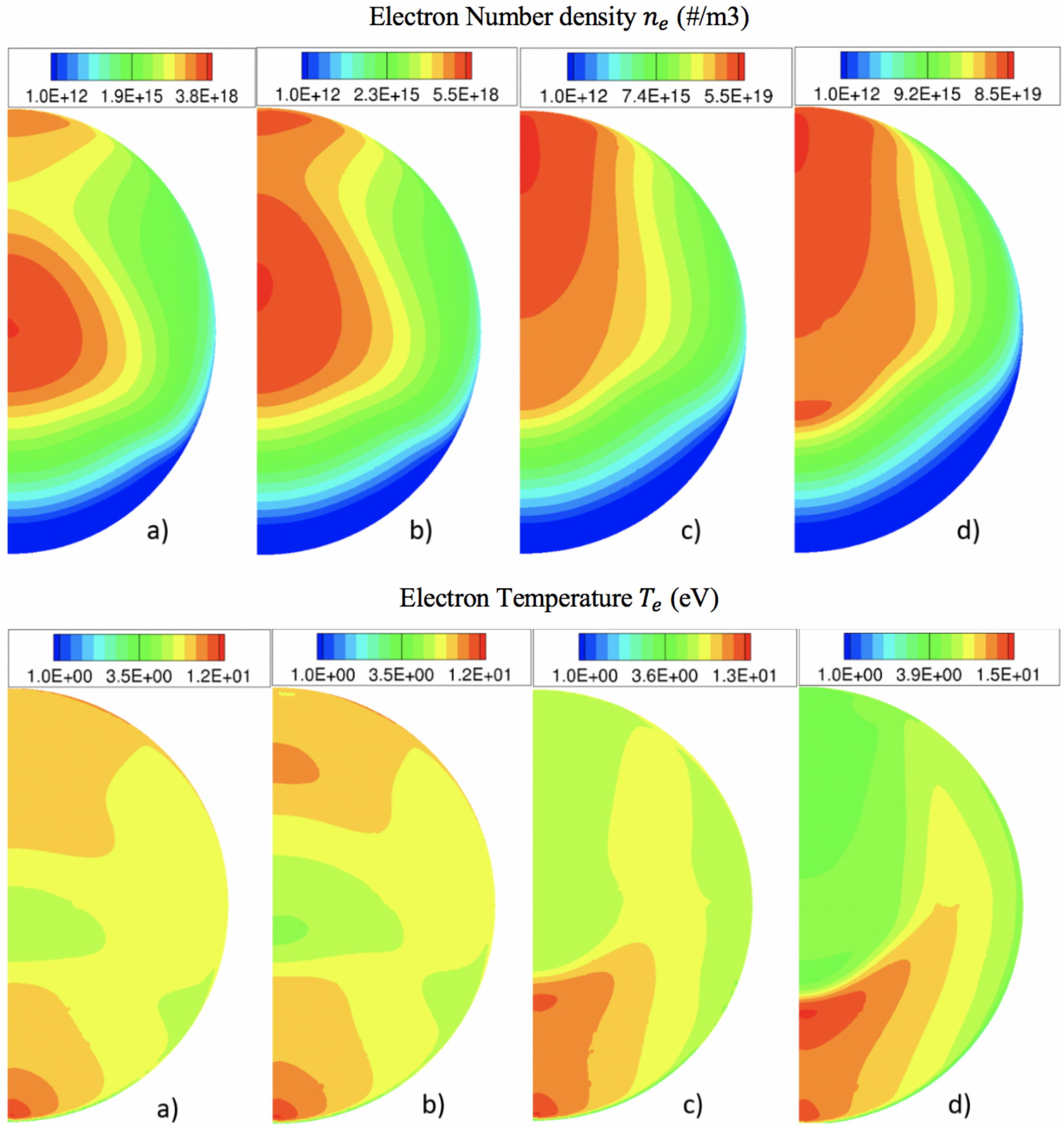

Figure 5.16: Transient evolution of the electron number density(in m^{-3}), and electron temperature (in eV) for -2 kV at a) t = 2 ns, b) t = 2.2 ns, c) t = 2.5 ns, d) t = 3 ns from left to right.

ward the anode promotes the formation of the cathode-directed streamer for low trigger voltages. Namely, the avalanche pre-ionizes the bubble increasing the electron number density before the head of the cathode-directed streamer. Also, the electric field between the avalanche and the anode corona increases when the distance between them decreases. This means that the Meek's criterion 5.2 is satisfied at an earlier time. Moreover, we conclude from figures 5.16(b) and (c) that the cathode-directed streamer does not start until the avalanche reaches the anode.

The increase in the trigger voltage results in the increase of the electric field in the bubble. As a consequence, the streamer dynamics and plasma parameters change (figure 5.17). Figure 5.17(a) shows faster growth of the anode corona which transforms to the streamer earlier than in the case of -2 kV (figure 5.16). On one hand, this is caused by the larger applied electric field. On the other hand, the formation and propagation of the anode-directed streamer changes the electric field in the bubble drastically. Namely, anode-directed streamer can be considered as the moving pin. Then, the electric field between the anode corona and this streamer increases with time which means the earlier satisfaction of Meek's criterion 5.2. Figures 5.17 (a) - (b) allow us to conclude that the anode-directed streamer promotes the cathode-directed streamer formation only through the electric field distortion. Since the cathode-directed streamer is formed when the anode-directed one is still far from the anode (figure 5.15(a) and 5.17(a)), we conclude that there is no promotion of the cathode-directed streamer formation through pre-ionization

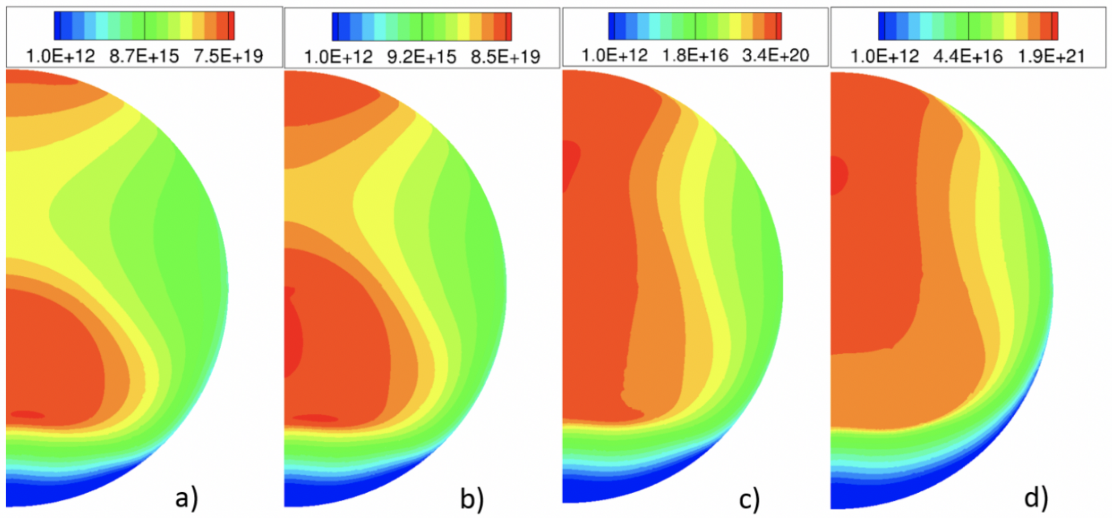
Electron Number density n_e (#/m3)

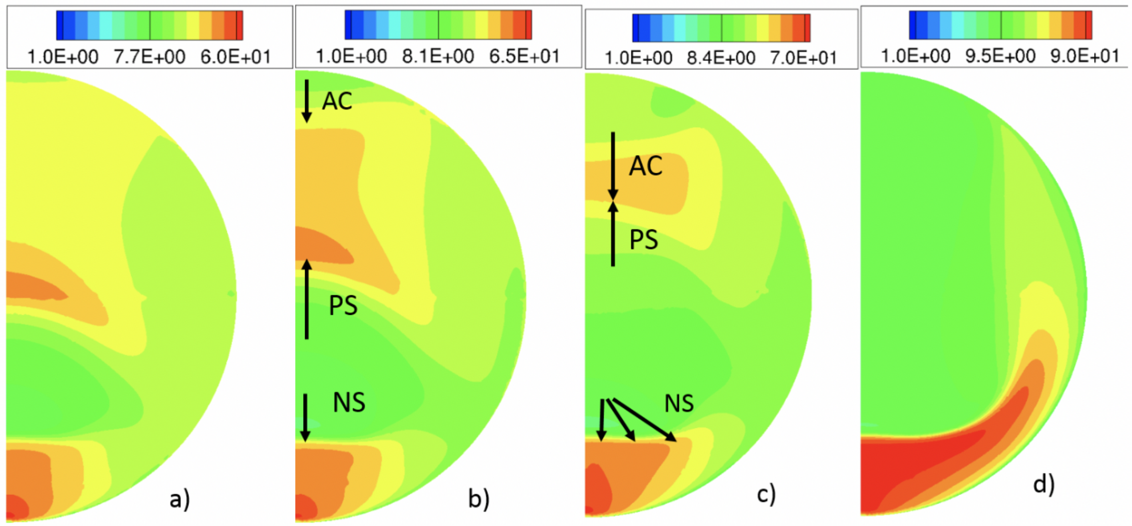
Electron Temperature T_e (eV)

Figure 5.17: Transient evolution of the electron number density, (in m^{-3}), and electron temperature (in eV) for -8 kV at a) t = 0.2 ns, b) t = 0.22 ns, c) t = 0.25 ns, d) t = 0.3 ns. Here 'AC' refers to Anode Corona. 'PS' refers to positive streamer and 'NS' refers to Negative Streamer.

by the anode directed streamer.

The anode directed streamer (positive streamer) merges with the corona originating at the anode as seen in figure 5.17(c). When the streamer and corona merge, we do not obtain any streamer in the bubble. However, the merging of streamers leads to the fast redistribution of the electric field in the bubble (figure 5.15(c)) and, as a consequence, leads to the penetration of high electric field in the bodies of both streamer and corona. This electric field heats electrons and leads to the fast generation of plasma whose density is $\sim 10^{21} m{-}3$. This plasma screens the applied electric field leading to its concentration only in the sheath around the bubble. One can conclude from figure 5.17(c) that the peak electron density is obtained in the position where the streamer and the corona merged. In this location we obtained the largest electric field and, as a consequence, the largest T_e and n_e.

It is also important to note that, for all negative trigger voltage (-1.5 kV to -15 kV), we did not observe any surface hugging mode of the streamers (see figure 5.16(a) and figure 5.17(a)), whereas, for larger positive trigger voltages (8 kV to 15 kV), we spotted the cathode directed streamer hugging the bubble wall during the initial stage of the discharge (figure 5.9 (a)).

We find that the dominant positive ions for the negative trigger voltage studies are the same as those observed for the positive trigger voltage studies, i.e. $\mathrm{He}^+, \mathrm{H_2O}^+, \mathrm{OH}^+ \,\mathrm{and}\, \mathrm{H}^+$. The comparison between their spatial profiles (figure 5.18 and Fig. 5.19) shows that the distribution is quite similar for all positive ions with the density being highest along the axis of the streamer tail,

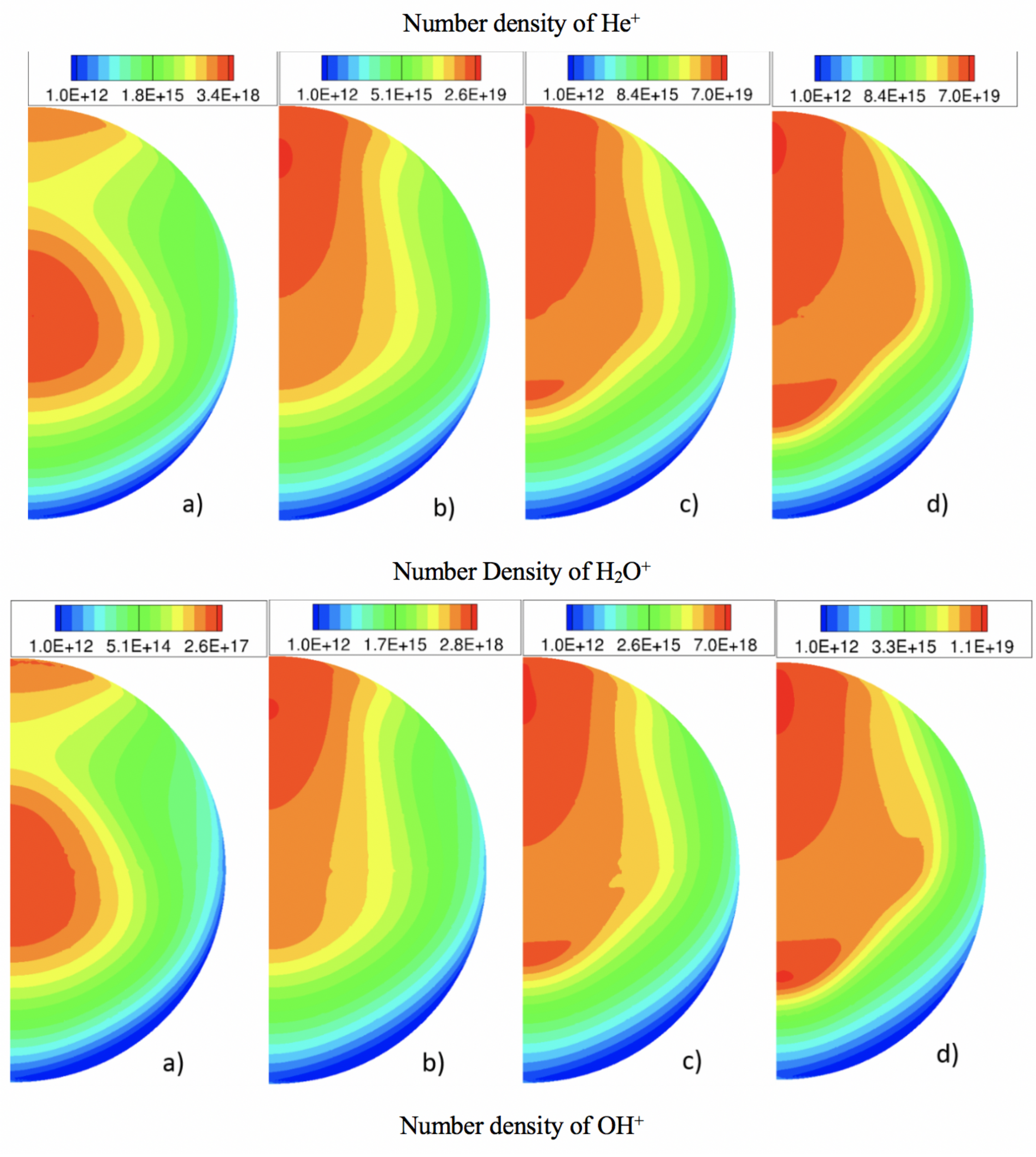

Number density of He^+

Number Density of H_2O^+

Number density of OH^+

Figure 5.18: Transient evolution of He^+ and H_2O^+ from top to bottom) for -2 kV at a) t = 2 ns, b) t = 2.5 ns, c) t = 3 ns, d) t = 3.5 ns from left to right.

similar to the results observed previously for low positive voltage (see section 5.6.1). However, figures 5.18 and 5.19 (c) - (d), show two peaks of ions densities which is not observed for the positive trigger voltage (compare with figure 5.10, 5.12). Moreover, the plasma density is more uniform in the streamer body. This is due to the fact that the entire structure of streamer discharge for negative voltage studies is very different from that of positive voltage. Namely, for the negative voltage, we see either avalanche and streamer or two streamers moving in the opposite directions rather than just one streamer moving toward the cathode (which was observed for the positive voltage studies). We conclude from figures 5.18 to 5.20 that the main contribution to the plasma is by the cathode-directed streamer. For the positive trigger voltage this anode directed avalanche propagates through the gas seeded with the electrons having density $\sim 10^{12} m^{-3}$. For the negative trigger voltage, anode-directed streamer propagates through the gas ionized by the avalanche moving toward the anode having density $\sim 10^{18} m^{-3}$. Therefore, more electrons participate in the cathode-directed streamer propagation.

The dominant excited neutrals for the negative trigger voltage are $\mathrm{OH, H\, and\, O}$ radicals with the density of $\mathrm{OH\, and\, H}$ radicals exceeding that of O by an order of magnitude (Fig. 5.20). This is explained by the fact that OH radicals are generated directly from the primary species H_2O by the electron impact ($\mathrm{H_2O + e \longrightarrow OH + H + e}$), while O is generated from OH in dissociation reaction $\mathrm{OH + e \longrightarrow O + e}$. The rate of the latter reaction is much smaller than the rate of water dissociation reaction due to much smaller

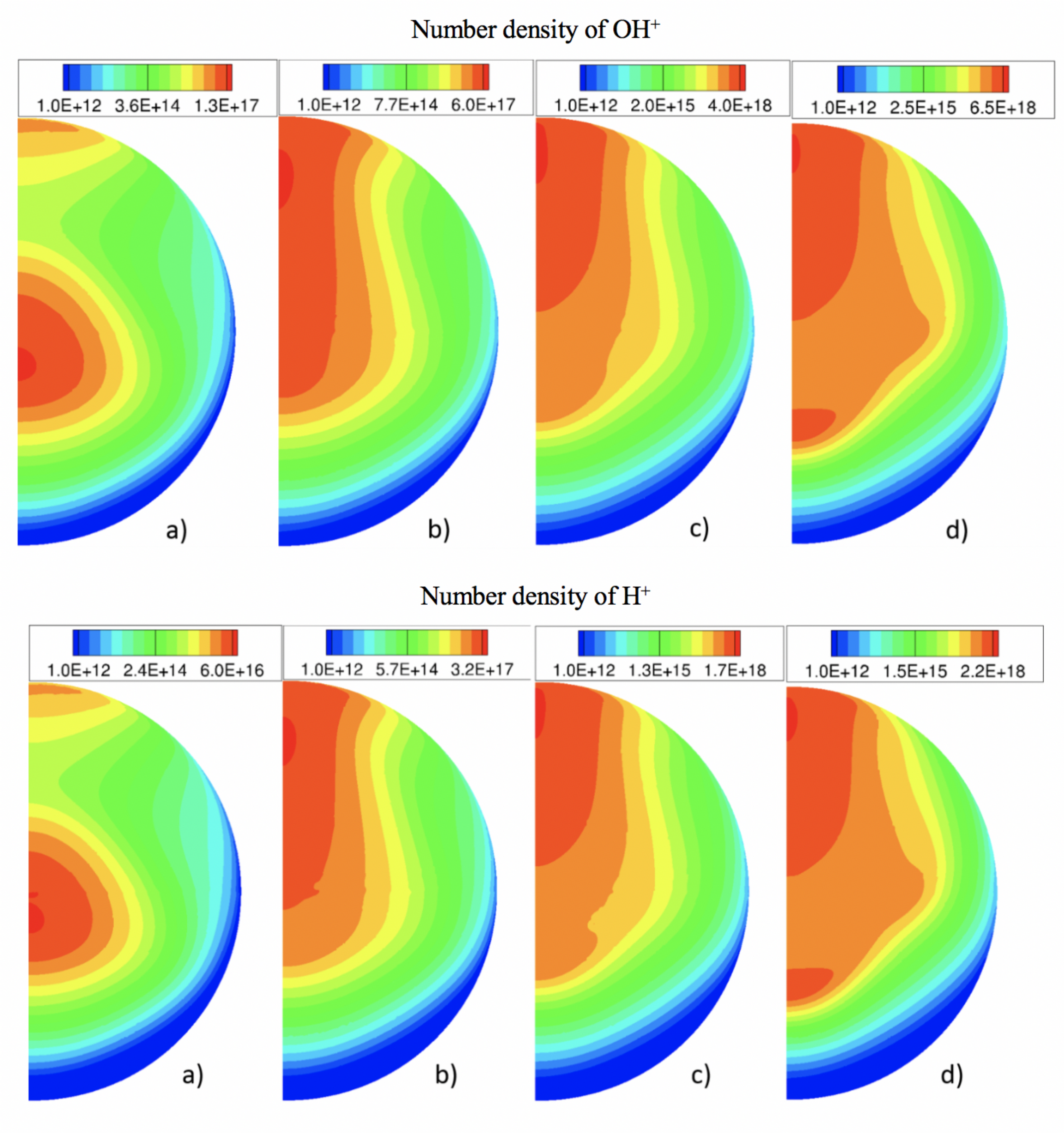

Figure 5.19: Transient evolution of OH$^+$ and H$^+$ from top to bottom) for -2 kV at a) t = 2 ns, b) t = 2.5 ns, c) t = 3 ns, d) t = 3.5 ns from left to right.

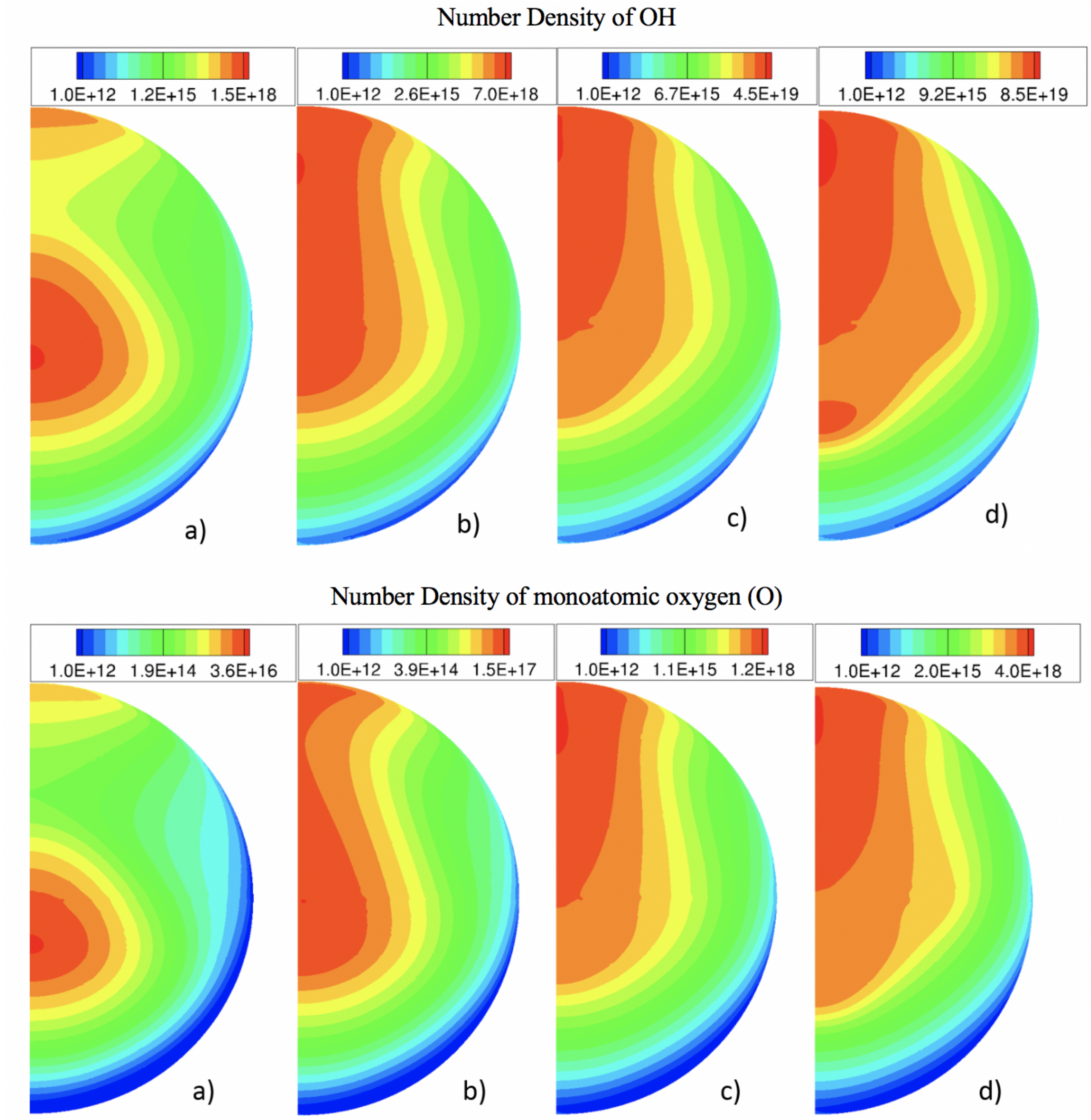

Figure 5.20: Transient evolution of OH and O radicals for -2 kV at a) t = 2 ns, b) t = 2.5 ns, c) t = 3 ns, d) t = 3.5 ns from left to right.

density of OH than the density of H_2O.

As compared to the positive trigger voltage of 2 kV, we find that the density of OH radicals is ~ 2 orders of magnitude smaller for negative trigger voltage (compare figures 5.19(a) and 5.11(a)). OH radicals are mainly generated in reaction (5), (see Appendix B) whose rate for a fixed density of H_2O depends on n_e and T_e. The comparison between figures 5.16(b) and 5.8(b) shows smaller T_e in the streamer body for the negative trigger voltage which is due to different structure of the electric field in the body of the streamers originated at the pin and flat electrodes. The rate coefficients of the electron impact ionization and dissociation reactions of He and H_2O increase exponentially for $T_e < 10$ eV. Therefore, even small changes in T_e result in the drastic changes in the rate coefficients of the electron impact reactions. This explains the significant difference of OH density obtained for two polarities of the pin electrode.

The dominant water complex species found for the negative trigger voltage are the heavier species $H_9O_4{}^+, H_{11}O_5{}^+$ and $H_{13}O_6{}^+$ with the number density of these species reaching values $\sim 10^{18} m{-3}$ after 3.5 ns. These values are an order of magnitude smaller than those obtained for the positive trigger voltage. These species are generated from H_2O^+ whose density is ~ 1 order of magnitude smaller for the negative trigger voltage (compare figures and 5.10 and 5.18).

The dominant negative ions are $H_5O_3{}^-$ with the density an order of magnitude higher than that of OH^-. The densities of negative ions are much

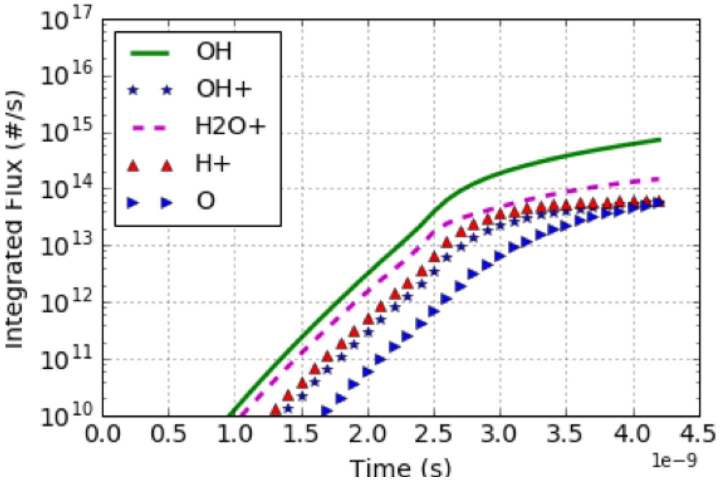

Figure 5.21: Transient integrated flux of the dominant species to the surface of the bubble at -2 kV.

smaller than the densities of positive ions. The presence of these ions does not affect the streamer dynamics and hence is not shown here.

5.7 Streamer discharge in multiple bubbles

Next, we investigate the influence of presence of multiple bubbles on the characteristics of the streamer discharge. The computational domain for a two-bubble streamer discharge problem is shown in the figure 5.4. A positive trigger voltage is used for the applied to the pin electrode and the streamer dynamics in this configuration are investigated.

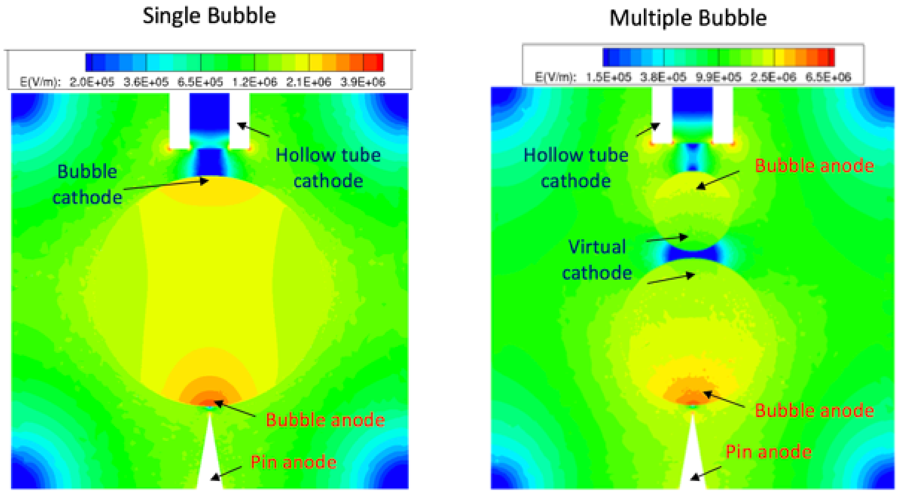
Single Bubble

Multiple Bubble

Figure 5.22: Transient evolution of reduced electric field for single bubble (left) and multiple bubble (right) discharge configurations for 2 mm interelectrode gap..

5.7.1 E-field distribution comparison

Analyzing the electric field distributions in Fig. 5.22 we note that the electric field in both single bubble and two bubble configurations is enhanced more at the poles of the bubble compared to its equatorial region. The peak value of electric field for both the configurations lies at the bubble surface close to the pin trigger electrode, with the electric field magnitude for the two bubble configurations being twice as high as the electric field in the single bubble configuration. It is also interesting to note that the physical anode and cathode coincide with the bubble anode and cathode for the single bubble configuration. However, for the two bubble configuration, a virtual cathode is formed in the gap between the two bubbles switching the polarity of the electric field for the smaller bubble. Thus, for the two bubble configuration, the physical anode acts as the anode for the lower bubble, however the physical cathode also acts as the anode for the top bubble and the region between the two bubbles acts as a virtual cathode for both top and bottom bubbles.

5.7.2 Breakdown voltage comparison

Figure 5.23 shows the transient evolutions of reduced electric field (E/N) for single bubble configuration on the left and multiple bubble configuration on the right. Here the interelectrode gap between single and multiple-bubble configurations is equal and set as 2 mm. For the same interelectrode gap, we find that the breakdown voltage (V_br) for multiple bubble configuration is 2 kV as compared to 3 kV for the single bubble configurations. This reduction in breakdown E-field is due to a decrease in the radius of curvature at the bubble-liquid interface near the pin-electrode for the multiple-bubble configuration, due to the presence of smaller bubble. This results in a larger field enhancement at the lower pole for the multiple bubble configuration for the same magnitude of applied E-field, which can be seen in Fig. 5.22.

Fig. 5.24 shows the spatial electron number density distribution for single and multiple bubble configuration. We see that the streamer discharge in the single bubble is preceded by a corona (near the pin electrode) and evolves into a thin axial streamer which bridges the gap in 3 ns (Fig. 5.22). For the multiple bubble configuration, at the breakdown voltage, we observe the streamer discharge only in the lower bubble and with no breakdown observed

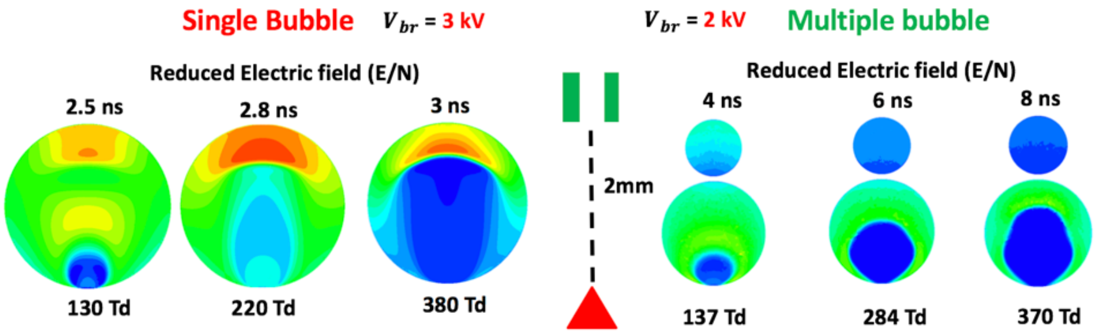

Figure 5.23: Transient evolution of reduced electric field for single bubble (left) and multiple bubble discharge configurations for 2 mm interelectrode gap.

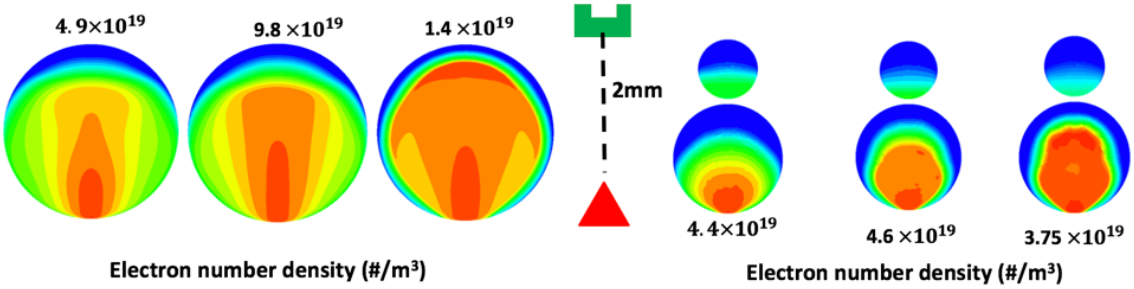

Figure 5.24: Transient evolution of electron number density for single bubble (left) and multiple bubble discharge configurations for 2 mm interelectrode gap.

in the top bubble. The streamer observed is thicker and more diffused and bridges the gap in 6 ns. Thus the streamer velocity in the multiple-bubble configuration is much slower and more diffused and thus expands volumetrically as it moves along the axis. This is in excellent agreement with the results obtained in the experimental work [45] shown in Fig. 5.2. Thus, breakdown voltage is found be lower by introduction of multiple bubbles, but the induction time of the discharge increases from 3 to 6 ns.

5.7.3 Streamer hopping between bubbles

At a trigger voltage of 4 kV or higher, it is observed that the streamer discharge, initiated in the lower bubble, jumps to the adjacent bubble and continues to propagate in the this bubble until the gap is bridged. This phenomenon is termed as streamer hopping and was observed in the experimental work [45] shown in Fig. 5.2. The axial streamer in the lower bubble has a larger diameter and engulfs the entire volume of the bubble, while the surface streamer in the top bubble has a wider base and transitions into a conical shaped axial streamer with a small radius at the head of the streamer. As the axial streamer in the lower bubble moves closer to the upper bubble, the electric field in the sheath region of the lower bubble reaches a peak value of 1565 Td at 3 ns. This strong electric field initiates breakdown in the adjacent bubble as seen in Fig. 5.25 and Fig. 5.26. Thus, the strong E-field in the sheath of lower bubble acts as the trigger electrode for the adjacent (upper) bubble and initiates gas breakdown and subsequent streamer discharge. This

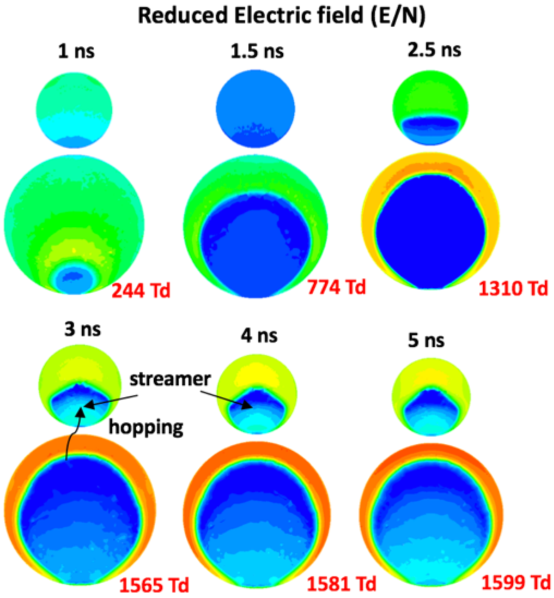

Figure 5.25: Transient reduced electric field at 4 kV at six different time instances

allows the streamer discharge to 'hop' from one bubble to another and continue its motion in the upper bubble, until it bridges the gap.

The shape of the streamer channel is inherently different in both gas bubbles. The streamer in the lower bubble has the smallest area at the initiation point (near the pin anode bubble surface) and is completely volumetric in nature. However, the streamer in the adjacent (upper) bubble has the largest area at the initiation phase (which is at the interface between the two bubbles). This is because, a concentrated external field at the point pin electrode causes breakdown in the lower bubble. However, in case of the upper bubble, a slowly developing electric field in the sheath (of the lower bubble) needs to

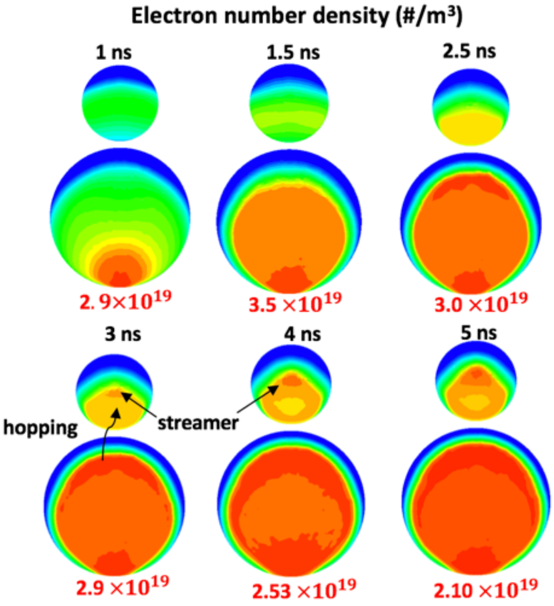

Figure 5.26: Transient evolution of electron number density for 4 kV at six different instances.

reach a critical value for the breakdown to commence in the upper bubble. This cause the electron density and the space charge in the upper bubble to evolve along the surface of the bubble [Fig. 5.26 at 2.5 ns] as this region is the closest to the lower bubble surface and has the highest electric field influence from the lower bubble. This is also confirmed by the reduced electric field distribution [Fig. 5.25 at 2.5 ns] where we see strong space charge accumulating near the lower surface of the upper bubble. As soon as the electric field reaches a threshold value in the sheath of the lower bubble, the streamer in the upper bubble starts propagating axially in a conical shape with a wider base and a thin tip.

5.8 Plasma evolution in liquids

In the current work, we have neglected the evolution of plasma and reactive species inside the liquid medium. The bubble liquid surface is considered as a solid boundary with the species reaching the liquid surface quenching at the wall or accumulating on the surface. The next step towards completion of this problem is modeling the evolution the plasma generated reactive species into the liquid medium and to resolve the resulting changes in the liquid composition due to diffusion, solvation and interaction of active species. This is the principle governing plasma based liquid fuel reforming where the plasma species generated in the gas phase are used to bring out desirable changes in the liquid.

Here, we provide a brief overview of the multiphase plasma fluid model and preliminary 1D investigations of plasma evolution in the liquid phase [138]. The computational model for plasma discharge in liquid is analogous to the non-equilibrium plasma model described in section 2.1.2 and referred from previous works [139, 68]. The model is constructed on the same mesh framework as non-equilibrium plasma model. The multiphase model solves plasma fluid equations in both gas and the liquid medium simultaneously so as to resolve plasma formation, the reactive species transport into the liquid medium and the resulting changes in the liquid composition. The governing equations solved in the liquid phase include solvated species continuity equation 2.1, electrostatic Poisson's equation 2.4 and drift diffusion approximation 2.3. A single temperature description of the plasma is assumed in the liquids owing to the high collision frequencies due to three orders of magnitude higher background densities in the liquid phase (compared to gas phase). The length scales associated with species transport in the liquid medium are three orders of magnitude smaller than the plasma length scales in the gas phase. Owing to microsecond to millisecond timescales associated with the complete evolution of reactive species in the liquid phase, multi-dimensional simulations of the active species evolution in the liquid phase are extremely expensive.

Due to the time-constraints owing to largely disparate length scales, we only present 1D studies of plasma evolution in the liquids during the nanosecond timescales associated with the gas phase discharge. The goal is to resolve the formation of plasma activation layer and electrostatic debye layer formed at the gas-liquid boundary and identified by experimental studies [140].

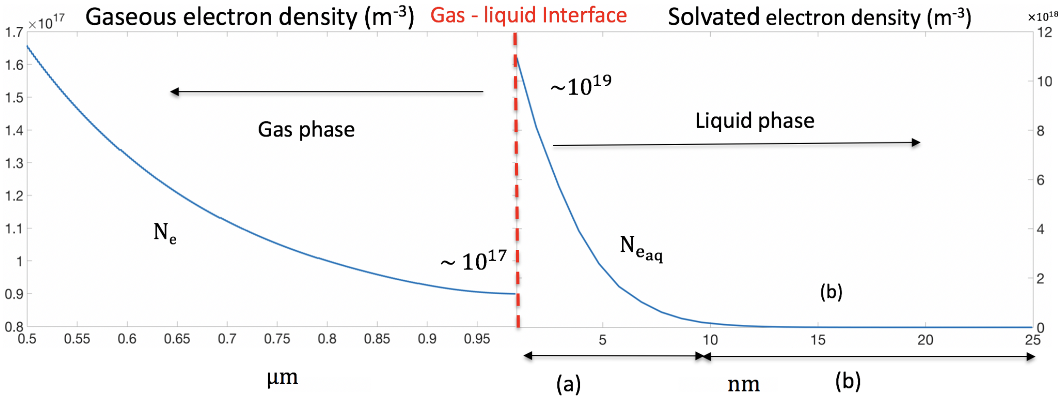

Figure 5.27: Electron number densities across the gas-liquid interface at time instance of t = 10 ns and V = 2 kV. Here a) denotes the interface layer and b) denotes the bulk liquid layer

For the 1D studies, the gas and liquid mixtures comprise of an air-water admixture. This air-water mixture composition is chosen due to the absence of detailed reaction kinetics of Helium gas in aqueous medium. The chemical kinetic pathways in the gas and liquid phase are based on the works of [68, 139]. The 1D computational domain consists of a parallel plate configuration with an inter-electrode gap of 1 mm. The aqueous liquid layer is located at one end of the configuration and has a width of 25 nm. The gas and the liquid phase are in direct contact with each other. A DC voltage of 2 KV is applied to the anode which is immersed in the liquid medium while the cathode is grounded. The minimum mesh size in the gas phase is 1 μm while the minimum mesh size in the liquid phase in 1 nm.

Figure 5.27 shows a snapshot of electron species density across the gas-liquid interface at a time instance of t = 10 ns. There exists a large

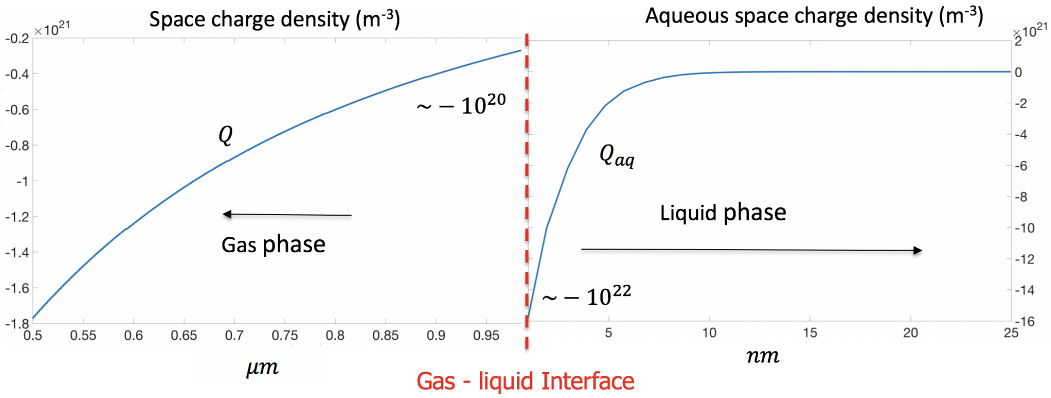

Figure 5.28: Net space charge density across the gas-liquid interface at time instance of t = 10 ns and V = 2 kV

discontinuity in the electron number density across the gas-liquid interface with the solvated electron densities in the liquid phase observed to be ∼ 10^2 times the electron number densities in the gas phase. We also observe formation of a double layer at the interface of the gas and liquid phase. The double layer consists of an interface layer/ active liquid layer and a bulk layer. The accumulation of active species and electrons take place in the interface layer and hence the liquid phase reaction pathways are highly dominant in this layer due to higher concentration of active species. The thickness of the active liquid layer in the liquid medium is observed to be ∼ nm in accordance with the experimental studies [140]. The densities of species in the bulk liquid layer remains unaffected by the transport of gas phase species from the interface over nanosecond timescales.

Figure 5.28 shows a snapshot of total space charge density across the gas-liquid interface at a time instance of t = 10 ns. It is observed that an electrostatic debye layer is formed at the gas liquid interface due to a net accumulation of space-charge density near the interface. This was also predicted in the experiments [140]. The debye layer has a net negative polarity and in turn shields the transport of negatively charged species into the liquids. Thus the formation of electrostatic debye layer in the liquids is analogous to the formation of sheaths at the gas-solid surfaces. The net negative polarity is due to the faster accumulation of solvated electrons in the liquids on account of their lower mass and larger diffusivity.

5.9 Conclusions

The plasma dynamics and chemical kinetics of streamers generated in the atmospheric-pressure helium bubbles suspended in the distilled water is studied using a non-equilibrium plasma model. This work was primarily motivated by the experiments reported in [8]. All the studies were conducted at saturated vapor pressure conditions, noting that the results were not sensitive for water vapor mole fractions in the range 0 to 10%.

We find that, for positive trigger voltages, the streamer discharge evolves axially at low voltages but prefers surface propagation mode at high voltages, while no surface propagation mode was found for negative trigger voltages. The polarity of the trigger voltages substantially changes the dynamic characteristics of the discharge. For a positive trigger voltage, the discharge progresses through a single cathode-directed streamer from the point of origin in the vicinity of the pin anode. For a negative trigger voltage of the pin electrode, the discharge evolves through either an avalanche and streamer mode or two streamers propagating opposite to each other. The regime depends on the value of the applied negative voltage. A comparison between active species generated for the negative and positive trigger voltage showed larger number densities of active species in the latter case but more uniform distribution of active species in the former case. We also observe that the presence of water vapor in the bubble leads to water complex ions dominating the concentration of negative ions and OH radicals dominating the concentration of excited neutrals.

It is found that, the presence of multiple bubbles reduces the breakdown voltage and results in thicker and more uniform streamers compared to single bubble configuration which is highly desirable for liquid reforming applications. We also find that the streamer hops from one bubble to another to bridge the gap between the electrode at voltages above the breakdown voltage. Thus streamer discharge through multiple bubbles is not-only feasible but also results in thicker discharge and more uniform generation of active species inside the gas bubble.

From 1D preliminary multi-phase studies, it is found that a double layer is formed in the liquid medium over nanosecond timescales. It is also observed that an electrostatic debye layer is formed at the interface with a net negative polarity which shields the transport of negatively charged species into the liquid medium.

Chapter 6

Fully coupled modeling of plasma assisted combustion ignition

Internal combustion (IC) engines utilize spark plugs to initiate combustion. Major disadvantages of spark ignition include increased ignition misfire under lean combustion and high-pressure conditions[1]. In the aerospace industry, applications such as supersonic combustion and scram jet engines are also challenged by combustion ignition and flame holding problems owing to extremely small flow time scales that are comparable or even smaller than the plasma time scales [72]. In industrial power generation applications, ultra-lean HHC (high hydrogen content) combustion is one of the preferred approaches to reduce NO_x and CO_2 emission but encounters obstacles in the form of combustion instability and flame flashbacks [73]. In the last the two decades, non-thermal plasmas have been investigated as a promising technique for ignition, flame stabilization, combustion enhancement, and emission reduction [11, 35, 36, 74, 75, 76, 77]. However, obtaining a complete understanding of the complex spatio-temporal dynamics underlying plasma-assisted combustion

---

[1] Portions of this chapter were previously published as "Fully coupled modeling of nanosecond pulsed plasma assisted combustion ignition,"[9] in the Journal of Physics D: Applied Physics,2019. All writing and figures included in this chapter are the original work of the author, with editing by Dr. Laxminarayan L. Raja

requires a fully coupled high-fidelity computational model that can simultaneously resolve the plasma and combustion kernel in multiple (2D or higher) dimensions, seamlessly transitioning from the former to the latter as the plasma discharge begins to quench. This work has been done in collaboration with members in our research group [9, 141].

6.1 Problem description

The goal of the present study is to model nanosecond pulse plasma induced flame ignition and combustion in a lean premixed H_2−air mixture under high pressure conditions [9]. The objective is to simulate the formation of an initial plasma kernel and investigate its influence on the ignition of a combustion kernel using a consistent multi-dimensional coupling framework. A coupled computational model is developed for this study and described in section 2.3. The model provides full fidelity description of plasma formation, combustion ignition, and flame development. Preliminary zero-dimensional studies indicate that plasma generated trace quantities of primary combustion radicals $\mathrm{O}, \mathrm{OH}\,\mathrm{and}\,\mathrm{H}$ drastically reduces the ignition delay of the H_2−air mixture and becomes especially important for high pressure lean conditions. Multi-dimensional simulations are performed for a lean H_2−air mixture ($\phi = 0.3$) at 3.3 atm and an initial temperature of 1000 K. The model accounts for the disparate length scales governing the plasma and combustion processes and incorporates the chemical reaction pathways governing the kinetics of both these processes. The work investigates three main parameters of the non-equilibrium plasma kernel that influence the combustion kernel, namely a) gas temperature, b) primary combustion radicals O, OH and H and c) other plasma species such as ions and electronically excited radicals. Selectively incorporating these features from the plasma discharge into the combustion kernel enables a parametric study to assess the relative importance of these combustion enhancing plasma parameters.

6.2 Discussion of chemistry: Hydrogen-air ($H_2-O_2-N_2$)

This section briefly describes the chemistry formulation for coupled plasma-combustion ignition studies. The chemical kinetics and reaction pathways for the non-equilibrium plasma model are inherently different from reaction kinetics for the combustion model. This is because the two models are inherently modeling fundamentally different physical processes with largely disparate timescales. The plasma formation process is a non-thermal phenomenon which is characterized by nanosecond timescale reaction kinetics and involves resolving both charged and neutral species formation and transport. The combustion process, however, is thermal in nature, characterized by reaction kinetics over microsecond timescales and mainly involves neutral species transport and formation over these long timescales.

6.2.1 Non-equilibrium plasma kinetics

The gas chemistry mechanism in this work is derived for a H_2-air mixture and consists of 25 species (Table 6.1) and 106 reactions (Appendix C).

The mechanism has been developed from previous studies [92, 43, 96, 142, 93] on plasma discharges in CH_4-air, H_2-O_2 mixtures and the work of Bourdon et al. [94] on H_2-air discharges at atmospheric pressure condition. The species modeled in the plasma discharge are tabulated in table 6.1. The mechanism incorporates the dominant pathways necessary for formation of primary combustion radicals (O, OH, H) and includes the effect of fast-gas heating reactions caused by the quenching of N_2 and O_2 excited states. The main pathways incorporated for electron impact reactions consists of electron impact ionization, excitation, dissociative excitation, dissociative ionization, dissociation, de-excitation, attachment and recombination reactions. The electron impact reaction rate coefficients are calculated offline using zero-dimensional Boltzmann solver (BOLSIG+) [114] using reaction cross-section data from literature [96, 142]. The reactions between heavy species such as ions and neutrals are modeled to include ion-ion recombination reactions, quenching reactions for excited states of N_2 and O_2, ion-neutral and ion-metastable impact reactions. The excited states of N_2, O_2 and H_2 due to vibrational/rotational excitation are not tracked explicitly, but are lumped as a single species in the ground state with the energetics of these excited states accounted for in the reaction mechanism. Electron impact reactions with atomic oxygen are not taken into consideration because their rates are small. This is primarily due to the orders of magnitude lower number density of atomic oxygen generated in the discharge compared to the number densities of background species N_2, H_2 and O_2.

Table 6.1: Species present in plasma model of H_2−air mixture

Charged	$e, O^+, H^+, H_2^+, N_2^+, O_2^+, N_4^+, O_4^+, O_2^+N_2, O_2^-, O^-$
Neutral	$O, H, OH, O_2^{a1}, O_2^{b1}, O_2^*, N_2^A, N_2^B, N_2^C, N_2^{a1}, O^1D$
Background	N_2, H_2, O_2

6.2.2 Combustion kinetics

The combustion chemistry consists of 28 species (Table 6.2) and 135 reactions (Appendix D) and includes all the reactions from the gas plasma chemistry and additional reactions from GRI-Mech 3.0 [143] for CH_4−air combustion by excluding reactions involving carbon and nitrogen. The species modeled in the combustion model are tabulated in table 6.2. The plasma based reactions are included in combustion kinetics to maintain consistency between plasma and combustion stages and incorporate the effects of plasma species relaxation and quenching, especially heating due to quenching of N_2 and O_2 excited states, on the flame kernel formation.

Table 6.2: Species present in combustion model of H_2−air mixture

Charged	$e, O^+, H^+, H_2^+, N_2^+, O_2^+, N_4^+, O_4^+, O_2^+N_2, O_2^-, O^-$
Neutral	$O, H, OH, O_2^{a1}, O_2^{b1}, O_2^*, N_2^A, N_2^B, N_2^C, N_2^{a1}, O^1D$ H_2O, HO_2, H_2O_2
Background	N_2, H_2, O_2

6.3 Simulation approach

The simulation approach is as follows. First, the plasma discharge generated by applying a high-voltage sigmoid pulse across a cylindrical electrode configuration pre filled with a H_2−air mixture is modeled. Once the voltage

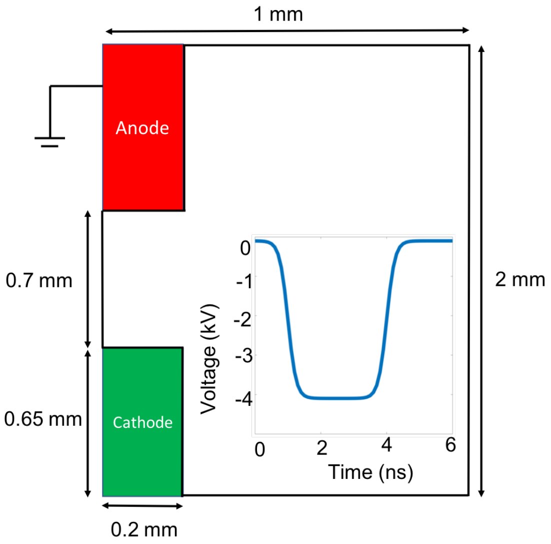

Figure 6.1: Schematic of simulation domain indicating electrode and domain dimensions. (inset) Time trace of sigmoid voltage pulse applied on the cathode surface.

pulse is fully ramped down, the gas temperature and species generated by the discharge are assumed to be the initial conditions for the ignition kernel. Following this, a combustion simulation is performed to further evolve the plasma and newly generated combustion species over longer combustion timescales.

6.3.1 Plasma kernel

The axisymmetric simulation domain used for this study is shown in Fig. 6.1. It consists of cylindrical electrodes 0.2 mm in radius and 0.65 mm long separated axially by 0.7 mm. The anode is grounded and a negative trigger sigmoid voltage pulse is applied to the cathode, as shown in the inset in Fig. 6.1. The duration of the pulse is 6 ns and voltage pulse is formed by

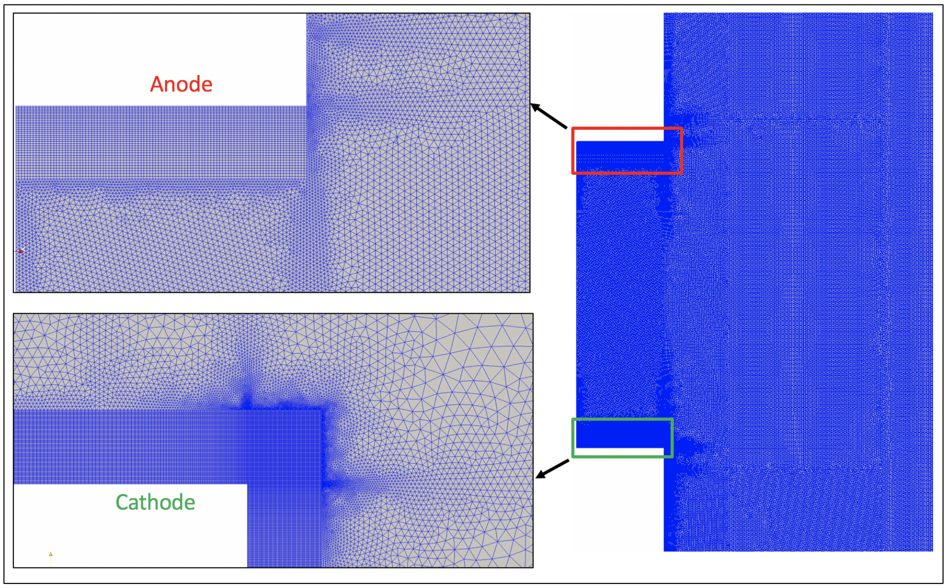

Figure 6.2: Computational mesh employed to resolve the plasma kernel with fine mesh elements in the vicinity of electrode surfaces to resolve sheath dynamics.

superimposition of sigmoid functions and is given by

$$V(t) = V_0 + V_{max}[\eta(t - \delta, \lambda) + \eta(t - \delta - T_p - T_r, -\lambda) - 1] \tag{6.1}$$

Where η is given by

$$\eta(t, \lambda) = \frac{1}{1 + \exp(-\lambda t)} \tag{6.2}$$

Here, V_0 = -10 V, is the minimum voltage during the duration of the pulse,

V_{max} = - 4000 V is the maximum voltage chosen as the breakdown voltage for the gas mixture, $T_p = 2$ ns is the pulse width, $T_r = 1$ ns is the rise time of the pulse, $\delta = 1$ ns and $\lambda = \frac{8}{T_r}$ are function parameters.

The domain is initialized with a H_2−air mixture at an equivalence ratio (ϕ) of 0.3, an initial pressure (P) of 3.3 atm, and an initial temperature (T_g) of 1000 K. The high-pressure conditions lead to the generation of cathode/anode sheaths with sub-micrometer length scales. The computational mesh is shown in Fig. 6.2 with an enlarged view of the fine elements in the vicinity of the anode and cathode surfaces needed to resolves the sheaths. The mesh contains $\sim 250,000$ elements with minimum mesh size of 0.1 μm near the cathode. The simulations described here are performed using a time step of 5×10^{-13} s. As the sigmoid voltage pulse enters the ramp-down phase, the electric field within the discharge also starts to decrease and reaches a negligibly small value towards the end of the pulse. On ramp-down, electrons rapidly lose energy and equilibrate with the background gas resulting in a single-temperature system. The charged species also begin to quench, predominantly though recombination reactions, eliminating the need to resolve the fine sheath structure at the electrodes.

6.3.2 Combustion kernel

Once the sigmoid voltage pulse is fully ramped down ($t > 6$ ns), all the species generated by the plasma kernel are further evolved using the combustion model. The combustion simulations are time integrated using a sig-

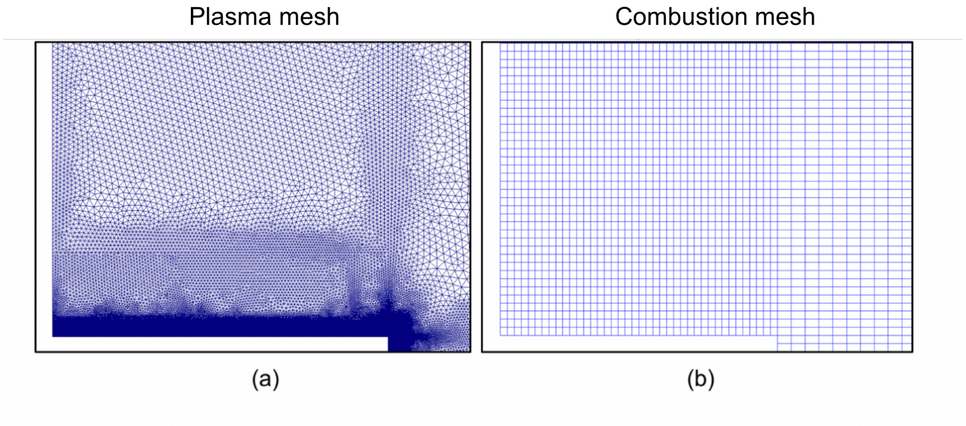

Figure 6.3: Enlarged view of computational mesh employed to resolve (a) plasma kernel (b) combustion kernel near the the cathode surface.

nificantly larger time step of 1 ns compared to the plasma simulation. The combustion phenomenon is characterized by much larger length scales and hence a much coarser mesh is sufficient. The physical domain extents, however, remain the same as those used in Fig. 6.2. Figure 6.3 compares the meshes used to simulate the plasma kernel and the combustion kernel. The combustion kernel mesh is uniformly refined to capture the combustion process characterized by flow driven transport and inter-species diffusion using a mesh resolution of 5 μm. The combustion mesh has about $\sim$ 25,000 elements, a factor of 10 smaller than the plasma mesh.

6.3.3 Coupling plasma and combustion simulations

The parameters in the combustion model are initialized using the species number densities and species temperature obtained at the end of the of the

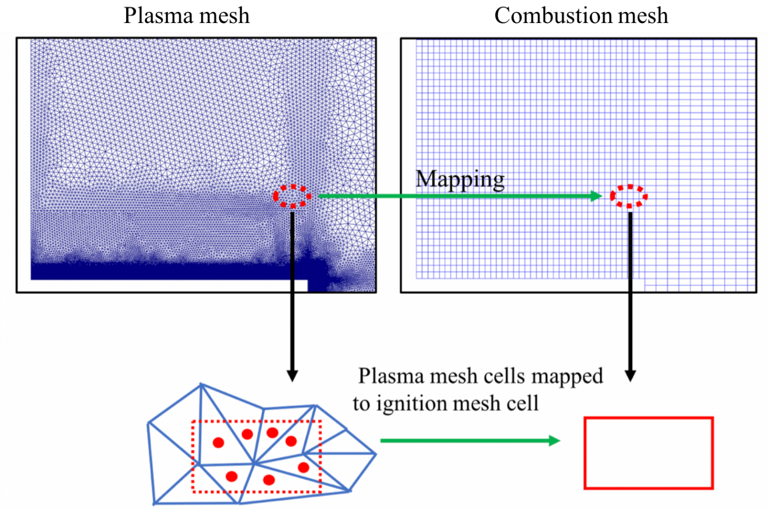

Figure 6.4: Illustration of centroid based mapping employed to interpolate solution variables from plasma kernel mesh to combustion kernel mesh. Centroids of plasma mesh cells that fall within the ignition mesh cell shown using red points.

plasma kernel simulation (t = 6 ns). However, since the computational mesh for the combustion and plasma simulations are different, an interpolation scheme needs to be employed to initialize the combustion simulation from the plasma mesh (Fig. 6.2). A schematic describing the centroid based interpolation method has been outlined before and is given by Eq. 2.40. For each cell in the plasma kernel mesh an interpolated cell is found in the combustion mesh. Figure 6.4 shows a schematic of cells in the plasma mesh (with red points as centroids) mapped to a given cell in the combustion mesh (red boundary). This generates a unique one-to-one mapping where every cell in the plasma mesh is mapped to a unique cell in the combustion mesh. Once the mapping is generated, the variable at a combustion mesh cell is obtained by volume averaging the variable over the corresponding cells in the plasma mesh given by Eq. 2.40.

6.4 Results and discussion

6.4.1 Chemical kinetics effects of plasma kernel on combustion ignition

It is important to establish the advantages of a plasma initiated ignition process from a chemical kinetics standpoint before moving on to computationally expensive, multi-dimensional simulations. Hence, as a first step in our studies, we establish the accuracy of the developed combustion kinetics mechanism (including the plasma species) using a zero-dimensional global reactor model [144]. Here coupled ordinary differential equations for species concen-

Table 6.3: Mixture A,B and C composition for 0D studies

Mixture A	H_2, O_2, N_2 at $\phi = 0.3, 1$ $H, O, OH, HO_2, H_2O_2, H_2O$ at seed density $10^{12} m^{-3}$
Mixture B	Mixture A + $0.1\%(O, OH, H)$
Mixture C	Mixture B + $< 0.01\%(e, O^+, H^+, {H_2}^+, {N_2}^+, {O_2}^+, {N_4}^+, {O_4}^+, {O_2}^+,$ ${O_2}^+N_2, {O_2}^-, O^-, {O_2}^{a1}, {O_2}^{b1}, {O_2}^*, {N_2}^{\mathrm{A}}, {N_2}^{\mathrm{B}}, {N_2}^{\mathrm{C}}, {N_2}^{a1}, O^1D)$

tration evolution in time are solved subject to specified initial conditions for species concentration with H_2-air mixture for an equivalence ratio (ϕ) of 1 and 0.3, initial temperature (T) ranging from 1000 K to 5000 K, at two constant pressures (P) of 1 and 3.3 atm. The pressure is fixed in these simulations since it has been shown that constant pressure isobaric conditions in a 0D setting are the closest to replicating real (multi-dimensional) combustion conditions without taking flow and transport effects into consideration.

Three different gas mixture composition variations are considered as shown in Table 6.3. Mixture A is initialized with a H_2-air mixture at $\phi = 0.3, 1$ and consists of the following species: H_2,O_2,N_2, H, O, OH, HO_2, H_2O_2, H_2O, which are part of the H_2-O_2 sub-mechanism in GRI-Mech 3.0 [64]. All non-background species (in mixture A) are initialized with a seed density of $10^{12} m^{-3}$. Mixture B contains, in addition to species in mixture A, a 0.1% trace concentration of primary combustion radicals O, OH and H. The radical concentrations are typical of those generated by a nanosecond pulsed plasma discharge. Mixture C contains, in addition to species and their concentrations in mixture B, all the plasma species generated by the discharge, including

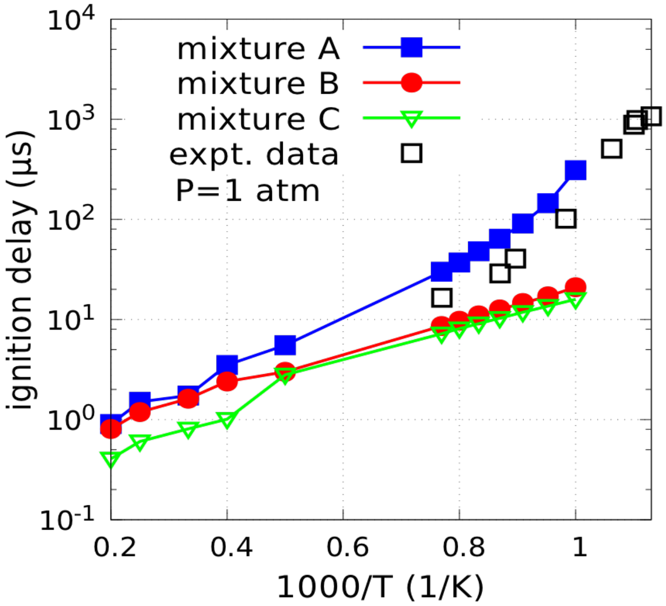

Figure 6.5: Ignition delay characteristics as a function of the initial temperature for mixture A (consisting of H_2-air mixture at $\phi = 1$), mixture B (consisting of all species in combustion mixture A with O, OH and H number densities initialized from plasma kernel), mixture C (consisting of all species densities initialized from the plasma kernel).

metastables (${O_2}^{a1}, {O_2}^{b1}, {O_2}^{*}, {N_2}^{A}, {N_2}^{B}, {N_2}^{C}, {N_2}^{a1}, O^1D$), ions ($O^+, H^+, {H_2}^+, {N_2}^+, {O_2}^+, {N_4}^+, {O_4}^+, {O_2}^+N_2, {O_2}^-, O^-$) and electrons. Here, the plasma species are initialized using their mean bulk densities from the 2D plasma kernel.

The ignition delay characteristics are compared for the three mixtures at P = 1 and 3.3 atm in Fig. 6.5. The ignition delay trends for autoignition mixture A closely agree with the experimental ignition delay measurements [145] at P = 1 atm, establishing the validity of the mechanism used 6.5(a). The original GRI-Mech 3.0 sub mechanism used has been optimized for combustion over a temperature range of 1000 K to 2500 K and a pressure range of 10 Torr to 10 atm [143]. However, the plasma simulations in this work predict peak temperatures $\sim$ 4400 K. It is assumed that the mechanism continues to remain valid at these conditions. In Fig. 6.5, the ignition delay is calculated for initial temperatures upto 5000 K.

For temperatures in the range of 1000K to 1300 K, the ignition delay for mixture B is significantly lower than the ignition delay for mixture A, by approximately a factor of 50 at 1000 K. For mixture C, where all plasma species are included, the ignition delay is found to be slightly lower ($\sim$ 33%) but of the same order of magnitude as mixture B. As the initial gas temperature is increased, the ignition delay for mixtures B and C approach the value for mixture A indicating the plasma assist is increasingly ineffective at high initial gas temperatures.

Previous studies have established that the combustion kinetics are strongly dependent on the initial gas temperature and the densities of primary combustion radicals O, OH and H [96]. In the mixture A, it takes a finite amount of time to generate sufficient concentration of these radicals necessary for activating the dominant reaction pathways responsible for ignition. This results in relatively large ignition delays. Presence of small initial concentrations of O, OH and H ($\sim$ 0.1% of background) activates these pathways at significantly earlier times, greatly reducing ignition delay. In mixture C, due to the incorporation of all the species produced by the plasma kernel, the combustion stage is governed by additional reaction pathways generated by the plasma chemistry.

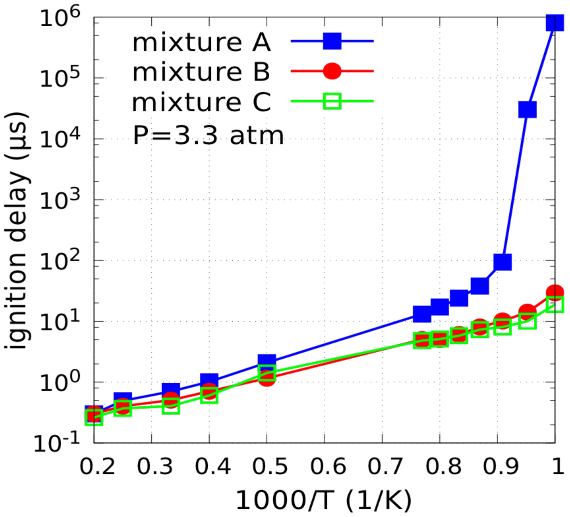

Figure 6.6: Ignition delay characteristics as a function of the initial temperature at P = 3.3 atm for mixtures A, B, and C (with an initial lean composition of $\phi = 0.3$) [9].

These pathways, primarily driven by quenching of N_2 and O_2 excited states, recombination reactions and electron attachment reactions, generate additional gas heating effects and contribute to the production of primary combustion radicals. This results in a further reduction in the ignition delay of mixture C below that of mixture B, outlining the importance of incorporating plasma species/reaction kinetics within the combustion stage.

Figure 6.6 shows the ignition delay characteristics for a higher initial pressure (P = 3.3 atm) H_2−air admixture at lean conditions of $\phi = 0.3$. Compared to the 1 atm pressure $\phi = 1$ case (Fig. 6.5, it is seen that at high pressure lean conditions, the ignition delay of mixture A increases exponentially for the lowest initial temperatures < 1100 K. The presence of an initial plasma ker-

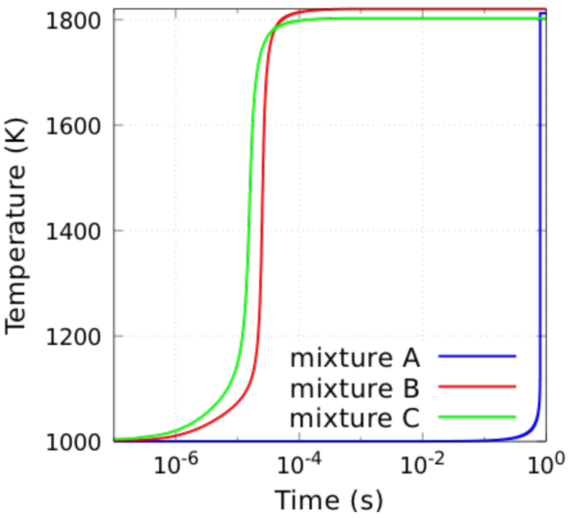

Figure 6.7: Transient evolution of flame kernel temperature for mixture A, B and C [9].

nel results in a decrease in the ignition delay over the mixture A conditions, but this effect is most significant for the lowest initial gas temperatures. The ignition delay for mixtures B and C is lower than that of mixture A by four orders of magnitude at 1000 K, underlining a significant advantage of plasma assisted ignition at higher pressure lean conditions.

The transient evolution of the flame kernel temperature for mixture A, B and C is shown in Fig. 6.7. The initial enthalpy is different for mixtures A, B and C which results is slightly different final temperature of these mixtures in steady state. It is seen that the flame temperature for mixture C is slightly lower than flame temperature of mixture B by ∼ 5-10 K. This is due to the presence of slightly higher number densities of H, OH and O as well as presence of stable plasma species in the steady state of mixture C. This difference in mixture composition results in a redistribution of the heating over a slightly higher background density reducing the steady state temperature of mixture C.

6.4.2 2D plasma kernel dynamics

We study plasma discharge in a 2D axisymmetric interelectrode gap containing a H_2-air admixture at an initial pressure of 3.3 atm, temperature of 1000 K and $\phi = 0.3$. As noted in Fig. 6.6, this condition does not lead to auto ignition in the times scales of interest in this study. Transient snapshots of electron number densities at equally spaced time instances during the nanosecond pulse are shown in Fig. 6.8(a-c). Ionization fronts originate in the vicinity of both cathode and anode surfaces, as seen in Fig. 6.8(a), and propagate axially towards each other to bridge the interelectrode gap.

The thickness of sheath near the cathode is $\sim 7\ \mu m$ (Fig. 6.8(d)) and the peak electron densities reach $4.8 \times 10^{22} m^{-3}$. During the relaxation stage (from t = 3.5 ns to 6 ns), the nanosecond pulse ramps down to -10 V and is maintained at -10 V until the electric field in the entire spark gap reaches negligible values. The spatial distribution of gas temperature at the end of the relaxation stage i.e. t = 6 ns is shown in Fig. 6.8(a). High temperature hotspots are formed near the cathode corner just outside the sheath, with peak values of gas temperature reaching $\sim$ 4400 K as seen in Fig. 6.8(b). This is due to the presence of high electron number densities in this region which results

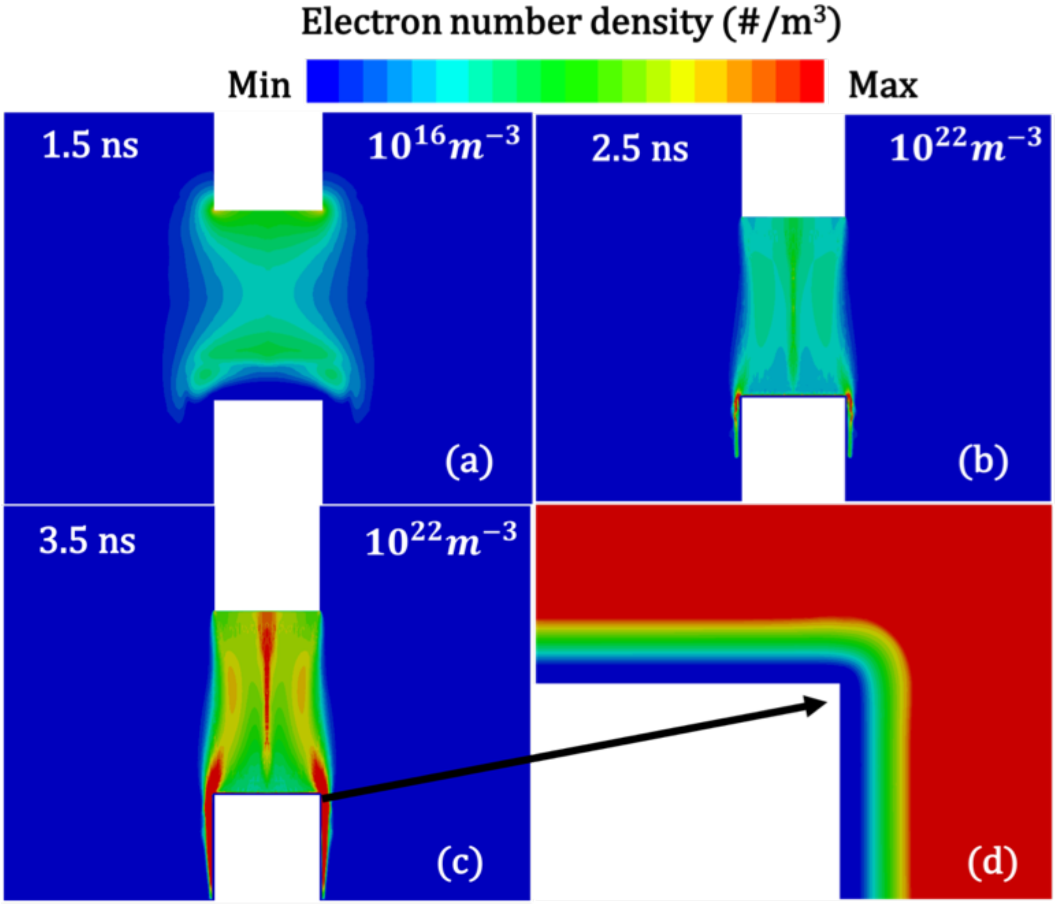

Figure 6.8: Electron number density ($\#/m^3$) transients during the nanosecond pulse at (a) t = 1.5 ns (b) t = 2.5 ns and (c) t = 3.5 ns (d) Inset of the sheath resolution at the cathode edge. The peak values of the electron densities are mentioned in figures ($a - c$).

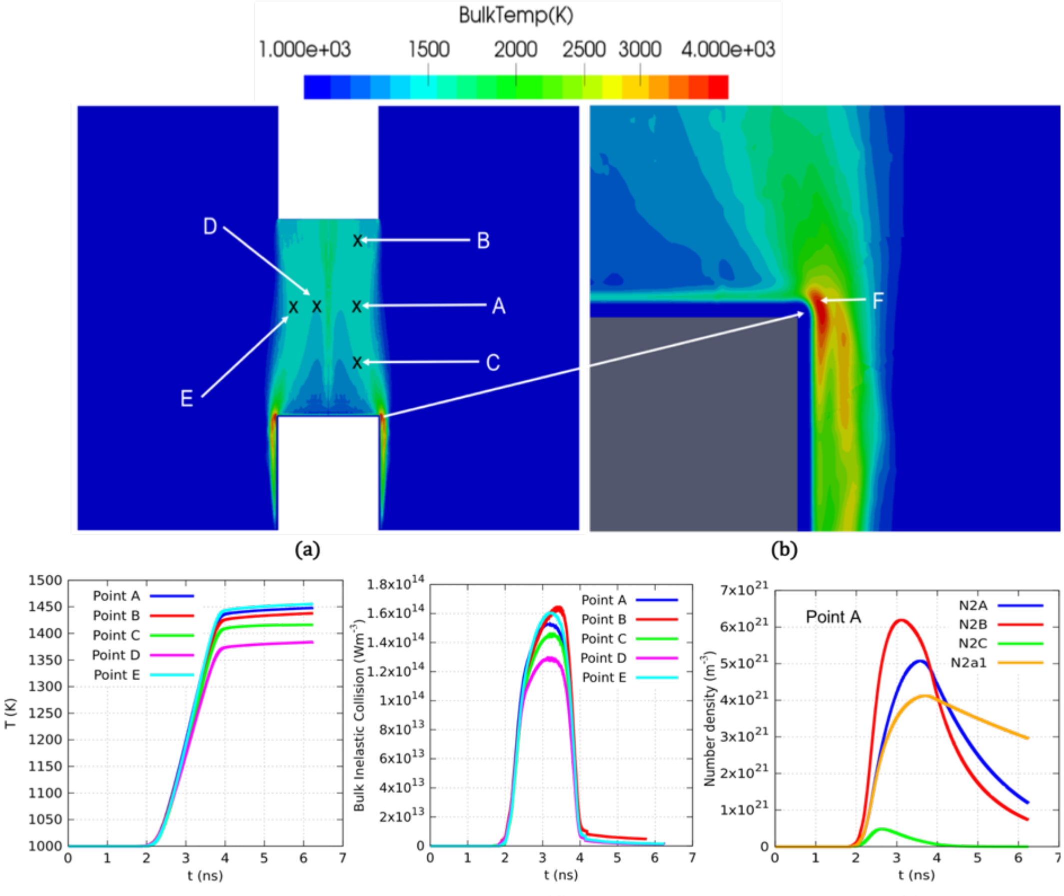

(a) (b)

(c) (d) (e)

Figure 6.9: (a) Gas temperature (T) spatial distribution at t = 6 ns. (b) Inset of the gas temperature hotspot at point A, near the cathode corner outside the sheath region (c) Transient variation of gas temperature (T) as randomly selected points A, B, C, D, E in the inter-electrode gap. (d) Gas temperature inelastic collision heating term at point A (e) Transient variation of N_2 electronically excited species densities at point A.

in significantly higher production of N_2 excited states i.e ${N_2}^{A}, {N_2}^{B}, {N_2}^{C}, {N_2}^{a1}$ as seen in Fig. 6.9(a-c). The N_2 excited states begin to quench as the pulse is ramped down and contribute to the majority of heating via fast gas heating reactions.

The average gas temperature in the interelectrode gap at the end of the nanosecond pulse is 1400 to 1500 K as seen in Fig. 6.9. The transient variation of T during the nanosecond pulse is analogous across the five randomly chosen points (points A to E) in the interelectrode gap as shown in Fig. 6.9(c), indicating a nearly uniform volumetric heating across the spatial region through the duration of the nanosecond pulse. The gas temperature remains unchanged during the ramp up phase of the nanosecond pulse (from t = 0.5 ns to 1.5 ns) and also during the first quarter of the voltage plateau (from t = 1.5 ns to t = 2 ns when the applied voltage V = -4 kV). From t = 2 ns to t = 4 ns the gas temperature rises sharply by about 400 K throughout the interelectrode gap as seen in Fig. 6.9(c). This can be attributed to the substantial increase in the power deposition by inelastic collisions during this time interval as seen in Fig. 6.9(d). The rise in the inelastic collision heating is in turn strongly dependent on the rates of fast gas heating based quenching reactions for N_2 excited states (see their evolution in Fig. 6.9(e)) as these are the dominant reaction pathways to realize gas heating in N_2 containing mixtures over nanosecond time scales.

The dominant excited species in the plasma at the end of relaxation stage (t = 6 ns) are ${N_2}^{A}, {N_2}^{B}, {N_2}^{a1}$ as shown in Fig. 6.10. ${N_2}^{C}$ quickly decays

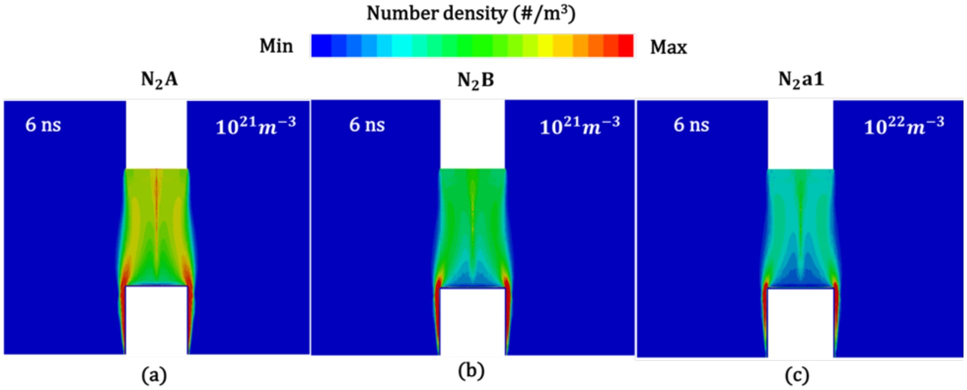

Figure 6.10: Number densities of N_2 electronically excited species (a) ${N_2}^{A}$,(b) ${N_2}^{B}$,(c) ${N_2}^{a1}$ at time t = 6 ns. The peak values of the species densities are specified in Figures (a-c).

during the afterglow stages to less than $10^{18} m^{-3}$ as seen in Fig. 6.9(e) while ${N_2}^{A}, {N_2}^{B}, {N_2}^{a1}$ maintain high number densities $\sim 10^{21} - 10^{22} m^{-3}$ in the afterglow stage (t = 4 ns to 6 ns) and thus cannot be neglected. These longer-lived species play a direct role in the combustion kernel formation.

The spatial distribution of primary combustion radicals $\mathrm{H, OH, and\, O}$ at the end of the nanosecond pulse (t = 6 ns) is shown in Fig. 6.11(a-c). The primary pathways for production of combustion radicals $\mathrm{O, OH, and\, H}$ are electron impact dissociation, electron impact dissociative ionization and metastable quenching reactions. Thus the spatial distribution of these species is strongly influenced by the spatial distribution of electrons and the excited species. From Fig. 6.11(a-c) it is seen that the peak values of $\mathrm{O, OH, and\, H}$ number densities are obtained near the cathode sheath edge. This is on account of the high electron densities (Fig. 6.8(c)) and high excited species number

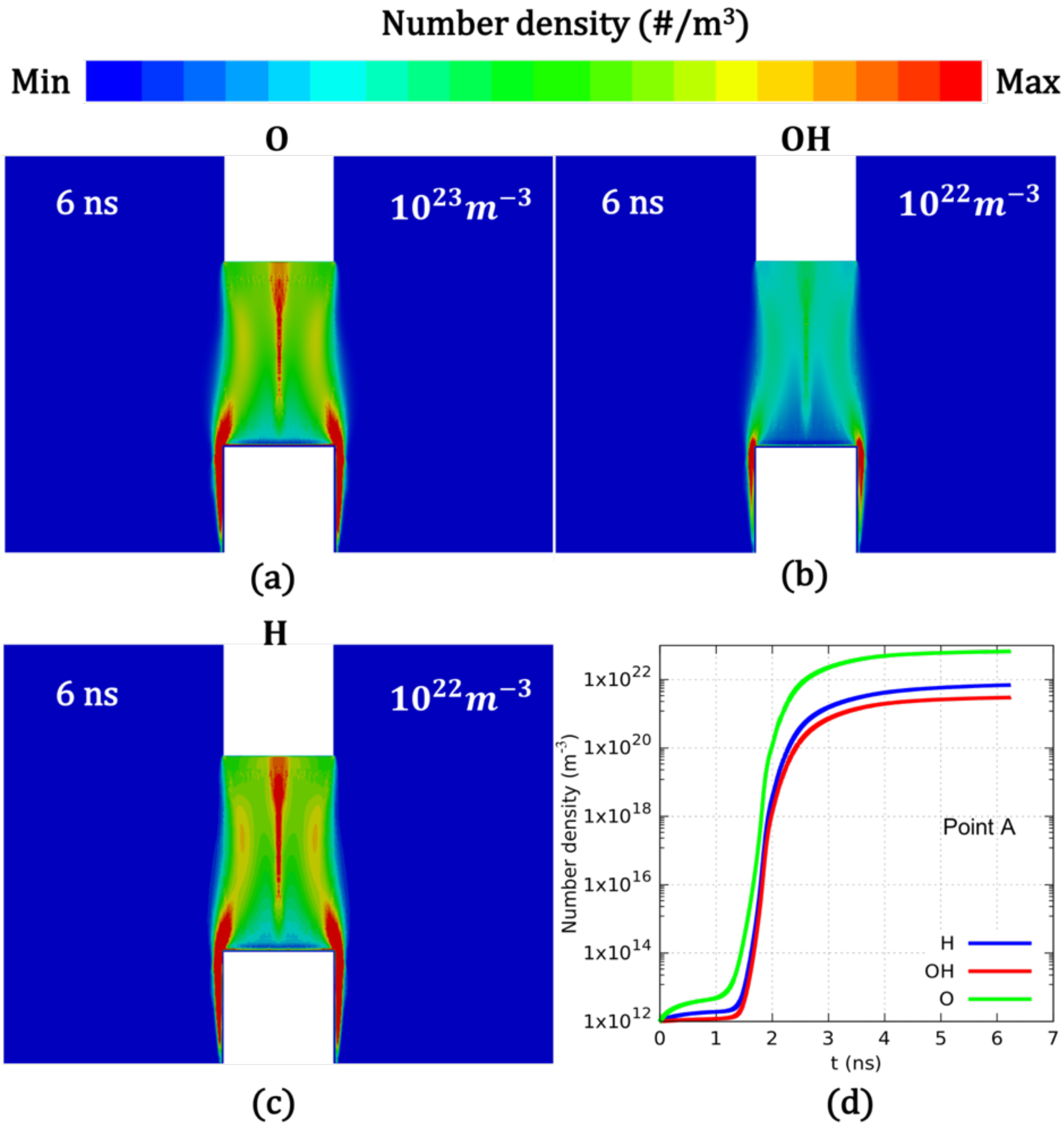

Figure 6.11: Number densities of the primary combustion radicals (a) O, (b) OH and (c) H after the end of the nanosecond pulse at t = 6 ns and (d) transient variation of densities of O, OH and H at point A. The peak values of the species densities are specified in Figures (a-c).

densities (Fig. 6.10) in this region which facilitates higher production rates of primary combustion radicals in this region. The number densities of these species (O, OH and H) is mostly uniform in the interelectrode gap with values $\sim 10^{22} m^{-3}$ (about 0.1% of background density), which is the radical number densities identified in the 0D studies discussed in section 6.4.1. Thus, the non-equilibrium plasma kernel is able to generate the required concentration of active species and radicals necessary for combustion enhancement. The radical number densities saturate during the afterglow stage (t = 4 to 6 ns) as seen in Fig. 6.11(d) and are directly used to initialize the densities of these species in the combustion simulations.

6.4.3 2D combustion kernel dynamics

The plasma discharge influences the flame kernel through at least three pathways that can be simultaneously active. First, during the plasma production phase, the discharge heats up the H_2-air mixture predominantly through fast-gas heating reactions. This generates local hotspots with favorable ignition conditions. Second, the discharge generates primary combustion radicals that are an integral part of key reaction pathways associated with the combustion mechanism. For the H_2-air mixture considered here, these are the atomic hydrogen (H), atomic oxygen (O) and hydroxyl (OH) radicals. The effect of these radicals on reducing ignition delay has already been shown in Sec. 6.4.1. Similar to the combustion enhancing effect of temperature hotspots, the mixture can selectively ignite in the regions of high radical concentration. Finally, the charged and excited species generated by the discharge also influence flame kernel evolution. The excited species in the plasma comprising of nitrogen ($N_2^A, N_2^B, N_2^C, N_2^{a1}$) and oxygen ($O_2^{a1}, O_2^{b1}, O_2^*$) along with the charged species in the plasma (H_2^+, O_2^+, O_2^-, O^-) are generated by electron impact reactions during the discharge formation phase (0-6 ns). Although the production time scales for these species is of the order of few nanoseconds, their quenching time scales ranging from 100's of nanoseconds to few microseconds, are comparable to the combustion time scales. As the excited species begin to quench, the energy released by these quench reactions can contribute to lowering ignition delay.

To understand the relative importance of these plasma based combustion enhancing pathways, namely the temperature hotspots, primary combustion radicals, and plasma species, a parametric study is performed. Selectively interpolating solution variables obtained at the end of the plasma discharge simulations into the initial conditions of the combustion simulation forms the basis of this study. First, the effect of temperature hotspots is investigated by only interpolating the gas temperature from the plasma kernel. Second, both the gas temperature and the densities of primary combustion radicals (H, O, OH) are interpolated to study the added benefits of including these species. Finally, all the solution variables including the gas temperature, primary combustion radicals, and plasma species including charged and excited species are interpolated to study the combined effect of all plasma based combustion enhancing parameters.

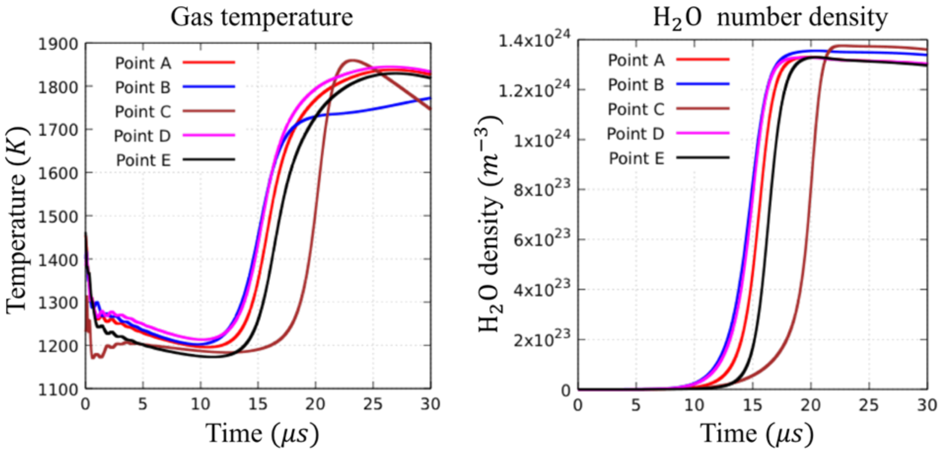

Figure 6.12: (Left) Temporal trace of gas temperature at sampled points (right) temporal trace of H2O number density at sampled points.

Gas temperature effects

We first discuss the case when the gas temperature alone is interpolated from the plasma solution. Solution variables at five trace points (same as Fig. 6.8) within the axisymmetric domain are tracked over the duration of the simulation. The time-trace of gas temperature and H_2O number density at these points is shown in Fig. 6.12. It can be concluded from the gas temperature trace that ignition occurs between 12-15 μs based on the sharp rise in gas temperature which saturates to a constant value at approximately 22 μs. It is seen that points A, B and D situated the center and top of the gap experience a faster temperature rise compared to points C and E situated at the bottom and radially outer edge of the gap. The temperature rise at point C (located near the cathode) lags by ~ 3 μs, indicating delayed ignition near

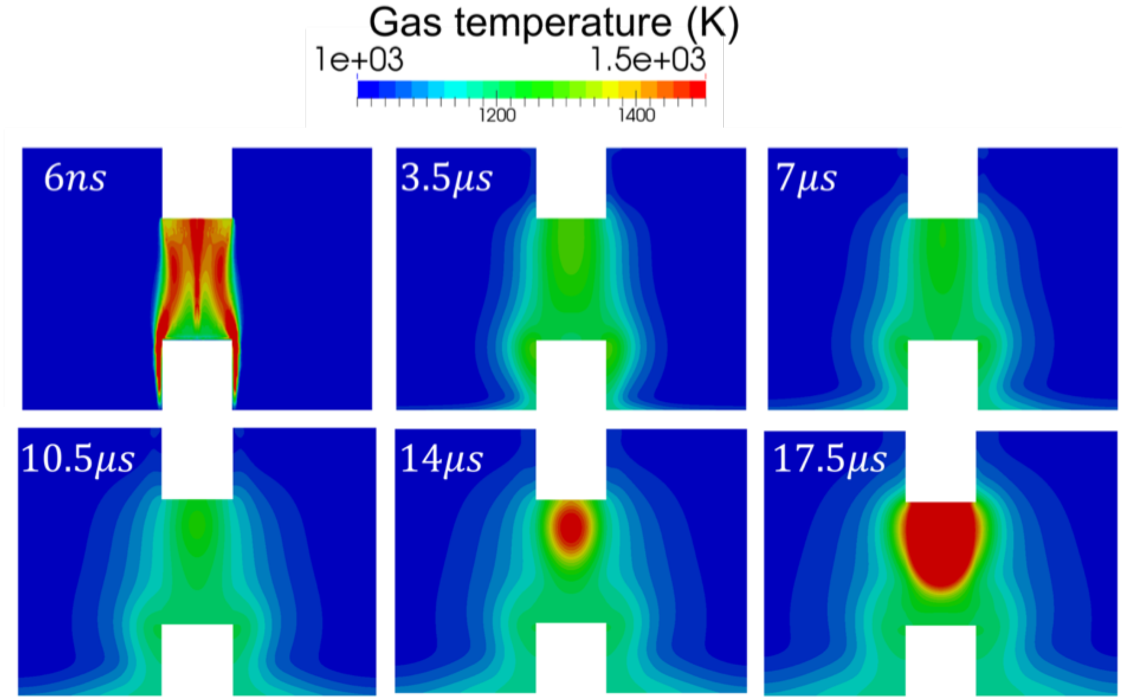

Figure 6.13: Spatial distribution of gas temperature within the domain at time instances 3.5 μs apart leading up to ignition.

the cathode. The number density of H_2O at all the sampled points also shows an exponential increase to $\sim 10^{24}\ m^{-3}$, confirming successful ignition.

To elucidate the mechanism by which plasma-generated gas heating affects combustion ignition, the dynamics leading up to ignition is analyzed. Figure 6.13 shows the snapshots of gas temperature at time instances 3.5 μs apart, starting from 6 ns when the combustion simulation is started to 17.5 μs when the flame kernel starts to bridge the interelectrode gap. The 6 ns snapshot shows a non-uniformly heated plasma kernel with local hotspots in regions

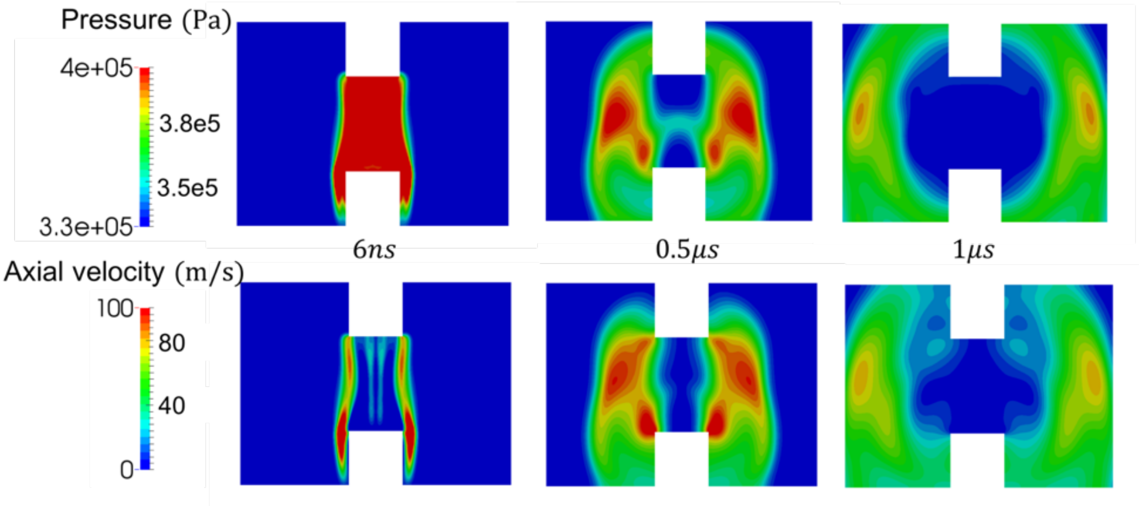

Figure 6.14: Spatial distribution of pressure (top panel) and axial velocity (bottom panel) at 6 ns (left) 0.5 μs (center) and 1 μs (right) during the hydrodynamic relaxation phase.

close to the cathode sheath and near the anode. High temperatures within the hotspots are predominantly achieved through fast gas heating/recombination and attachment reactions being activated as the sigmoid pulse ramps down.

The gas heating effects also substantially increase the pressure within the gap. Since the nanosecond timescales associated with the discharge are significantly smaller than the microsecond acoustic timescales, gas heating is effectively an isochoric process. Consequently, the pressure within the gap rises rapidly within the nanosecond plasma timescales as pressure relief brought about by hydrodynamic expansion is essentially inactive during the lifetime of the discharge. However, on the microsecond timescales associated with combustion, the hydrodynamic effects start to kick in and the pressure/temperature within gap begins to decrease. The top panel in Fig. 6.13 and the point transients in Fig. 6.12 indicate that the gas temperature decreases, sharply at first until about 1 μs and comparatively slowly at later times (1 - 11 μs) until the mixture ignites at between 12-15 μs.

Figure 6.14 shows the pressure (top panel) and axial velocity (bottom panel) at time instances 0.5 μs apart during the initial hydrodynamic relaxation phase. As the sigmoid pulse ramps down, the pressure in the plasma sustaining region rises by approximately $\sim$ 1 atm, as shown in the 6 ns snapshot (Fig. 6.14 top left), with peak values of 5.9 atm attained at the electrode corners. The high pressure plasma core generates a precursor shock that propagates radially outwards as seen at 0.5 μs and 1 μs. As the shock moves past the interelectrode region, the pressure in the interelectrode gap falls back to the initial value of approximately 3.3 atm. The pressure relief in the wake of the precursor shock is responsible for the sharp decrease in gas temperature in the gap upto about 1 μs. After the initial precursor shock, comparatively weaker compression waves are generated to smooth out smaller scale pressure variations between different regions in the gap. This explains the oscillatory, (Fig. 6.12) slower temperature decrease at the sampled trace points between 1 and 11 μs.

After 1 μs, there are two regions with locally high temperatures. The centrally located anode temperature kernel formed near the anode surface and the cathode temperature kernel formed at the cathode corner. The cathode kernel contains higher peak temperatures distributed over a smaller volume

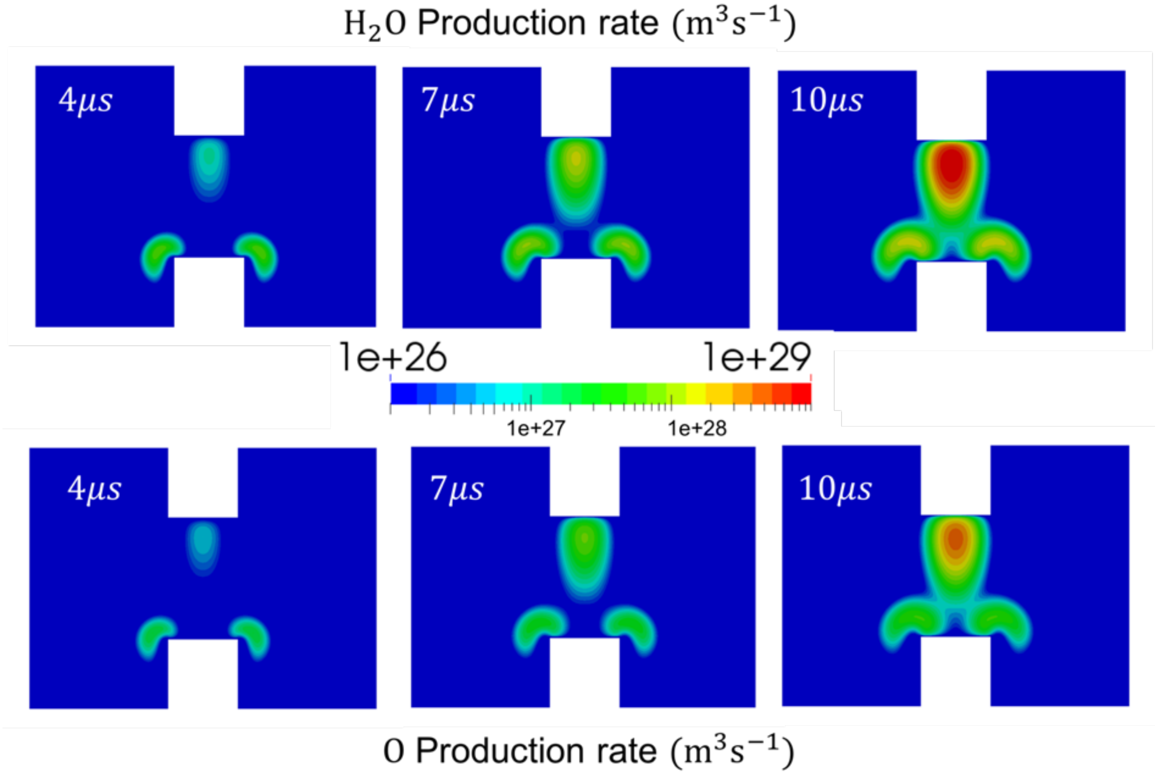

Figure 6.15: H_2O (top panel) and O radical (bottom panel) production rate at select time instances before ignition, 4 μs (left) 7 μs (center) and 10 μs (right).

while the anode kernel is characterized by lower peak temperatures spread over a much larger volume. The two temperature kernels essentially represent locations with significantly higher gas heating during the plasma discharge phase and maintain a higher temperature than the surrounding regions even after the pressure relief following the precursor shock. The anode and cathode temperature kernels display locally higher reaction rates throughout the 1-11 μs slow temperature decay phase. Although the gas temperature within the two hotspots decays with time, the temperature decay time scales are slow enough that combustion ignition reactions are activated to ignite the fuel-air mixture. Figure 6.15 shows the production rates of H_2O (top panel) and O radical (bottom panel) during the temperature decay phase at 4, 7 and 10 μs. H_2O is a by-product of combustion and the O radical is generated as an intermediate species in several reactions which take place during the ignition process. Together, the production rates of these species serve as good indicators of the rate at which the fuel-air mixture proceeds to ignition conditions.

The cathode kernel is initially (4 μs) seen to have a higher production rate for both species, consistent with the relative temperature distributions between the cathode and anode kernels. However, at later times (7 and 10 μs) it is seen that the volumetric extent of temperature activation is more important from a combustion perspective as the production rates in the anode kernel match and further exceed those in the cathode kernel. By 10 μs the reaction rates in the anode kernel start to surpass that in the cathode. In fact, the mixture ignites first in the anode kernel, strongly suggesting that a high

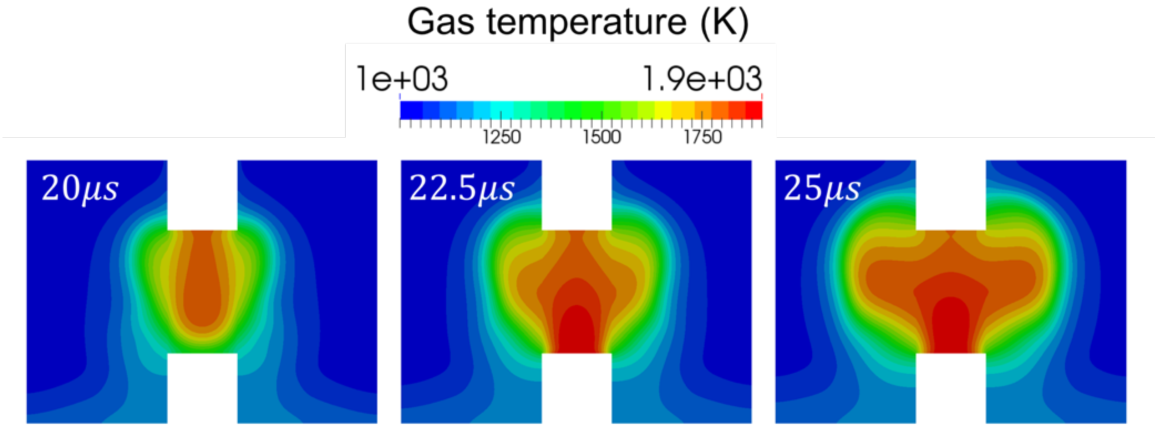

Figure 6.16: Spatial distribution of gas temperature within the domain at times following ignition, 20 μs (left), 22.5 μs (center) and 25 μs (right)

volume temperature kernel is most beneficial from an combustion ignitability. Fig. 6.16 shows snapshots of the spatial distribution of gas temperature as the flame propagates post-ignition. The 20 μs snapshot shows the mixture igniting at the anode kernel, before moving to bridge the electrode gap at 22.5 μs and then finally expanding radially outward beyond the gap at 25 μs.

Primary combustion radicals

In the second part of the parametric study, both the gas temperature and densities of primary combustion radicals $(\mathrm{H}, \mathrm{O}, \mathrm{OH})$ from the plasma solution are interpolated to investigate the added benefit of including these radicals.

The time-trace of gas temperature and H_2O density (Fig. 6.17) at the trace points shows that ignition within the interelectrode gap starts at around

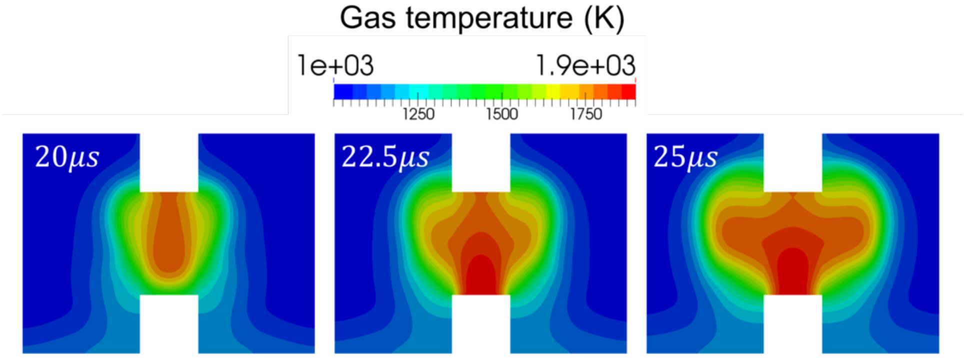

Figure 6.17: (Left) Schematic of axisymmetric simulation domain indicating sampled points (center) Temporal trace of gas temperature at sampled points (right) temporal trace of H_2O number density at sampled points.

1 μs. Comparing this to the previous study where only the gas temperature was interpolated from the discharge (Fig 6.12), it is observed that the inclusion of plasma generated primary combustion radicals results in a further fifteen-fold decrease in ignition delay from 15 μs to 1 μs.

To understand the beneficial effect of including these radicals, their spatial distribution is examined at the time instant just preceding ignition. For the case where plasma generated radicals are included, this time corresponds to 1 μs, while for gas temperature only interpolation case, it is approximately 15 μs.

Figure 6.18 compares the pre-ignition radical densities when (top panel) both radicals and gas temperature are interpolated and (bottom panel) when only gas temperature is interpolated. Comparing these two cases, it is seen that for all three radicals, a critical radical number density ($\sim 10^{22}$ to $10^{23} m^{-3}$)

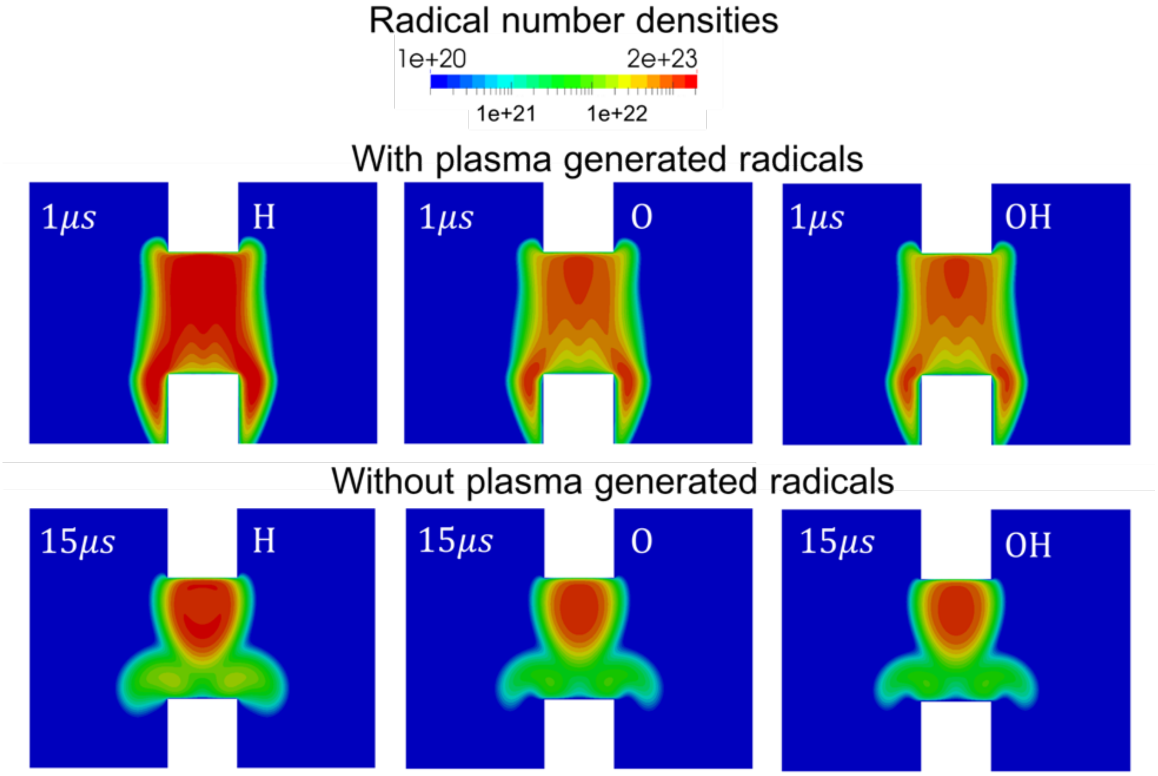

Figure 6.18: Spatial distribution of H (left), O (center) and OH (right) number densities at 1 μs (top panel) when gas temperature and plasma generated radicals are incorporated and 15 μs (bottom) when only gas temperature effects are considered. Both these times correspond to pre-ignition conditions, just prior to the ignition event.

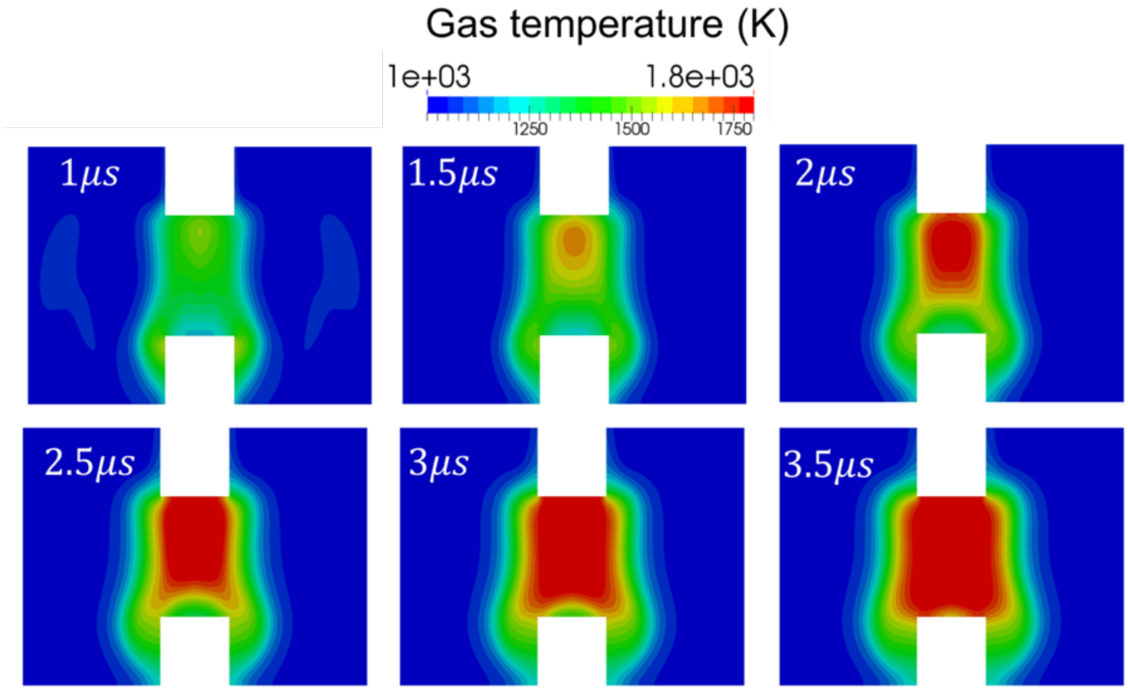

Figure 6.19: Spatial distribution of temperature at time instances 0.5 μs as the mixture in the gap begins to ignite.

is necessary for successful ignition. When the plasma contribution is not taken into account, the radical densities increase from zero to ignition critical values of $\sim 10^{22}$ to $10^{23} m^{-3}$. This process takes around 15 μs and is facilitated by the anode temperature kernel.

However, if primary combustion radicals generated by the plasma discharge are included, it is observed that (Fig. 6.18) their densities reach this critical value by the time the sigmoid pulse fully ramps down (t = 6 ns). Hence, the initial conditions for the combustion simulations already contain sufficient radical densities necessary for ignition. The 15 μs 'burn-in' time necessary for the mixture to ignite via the plasma temperature kernel is completely eliminated. This is confirmed by looking at the time trace in Fig. 6.17 which shows that H_2O production starts as soon as the combustion simulation is initiated. Although the gas temperature trace in Fig. 6.17 displays a 1 μs lag for the temperature to start rising, this is mainly due to the precursor shock. As the precursor shock exits the gap and the pressure drops to the ambient value of approximately 3.3 atm, the effects of ignition immediately result in the temperature rise.

Figure 6.19 shows the spatial distribution of gas temperature from 1 μs to 3.5 μs in intervals of 0.5 μs. This corresponds to the time interval where the gas temperature at the trace points shown in Fig. 6.17 starts to rise. Similar to temperature hotspots, the plasma kernel also generates regions containing locally higher radical number densities. The regions that were classified as the anode and cathode temperature kernels are also the regions with locally higher radical number densities. The anode kernel displays a low peak density high-volume radical distribution as compared to a high peak density low-volume distribution in the cathode kernel. The presence of critical radical number densities within these kernels adds to the already favorable ignition conditions within these regions. From an ignitability perspective, it is again observed that a high-volume radical kernel is preferable since, as shown in Fig. 6.19, the mixture first ignites at the anode kernel before bridging the gap (bottom panel) and moving radially outward. Although the cathode kernel has higher temperatures (Fig. 6.19) and higher radical densities (Fig. 6.18) it fails to sustain reaction rates over a sufficiently large volumetric region, necessary for successful ignition.

Effect of combined gas temperature, combustion radicals, and plasma species

For the last part of this parametric study, all the species generated by the plasma discharge namely, the metastables, ions, electrons, and primary combustion radicals are interpolated and tracked within the combustion simulation. As was the case with the previous parametric studies, the gas temperature is also interpolated. Figure 6.20 shows the gas temperature at all the sampled points and the number density of various plasma species at the centrally located trace point through the course of the combustion simulation. The gas temperature time trace indicates that ignition starts at 1 μs, approximately the same ignition delay observed when plasma generated primary combustion radicals were incorporated.

Based on their characteristic decay time, the plasma species can be classified into two distinct categories. First are the fast decaying species namely the fast decaying ions $(\mathrm{O_2}^+, \mathrm{O}^+, \mathrm{O_4}^+, \mathrm{O_2}^+\,\mathrm{N_2})$ shown in Fig. 6.20(b) and the fast decaying nitrogen metastable species $(\mathrm{N_2}^{\mathrm{A}}, \mathrm{N_2}^{\mathrm{B}}, \mathrm{N_2}^{\mathrm{C}}, \mathrm{N_2}^{a1})$ shown in Fig. 6.20(c). As the external voltage pulse that drives their production is switched off, the densities of these species rapidly decays ($\sim$ 0.2 - 0.3 μs) at a rate faster than the time taken for the precursor shock to exit the gap ($\sim$ 1 μs). Hence, the energy released from the de-excitation reactions responsi-

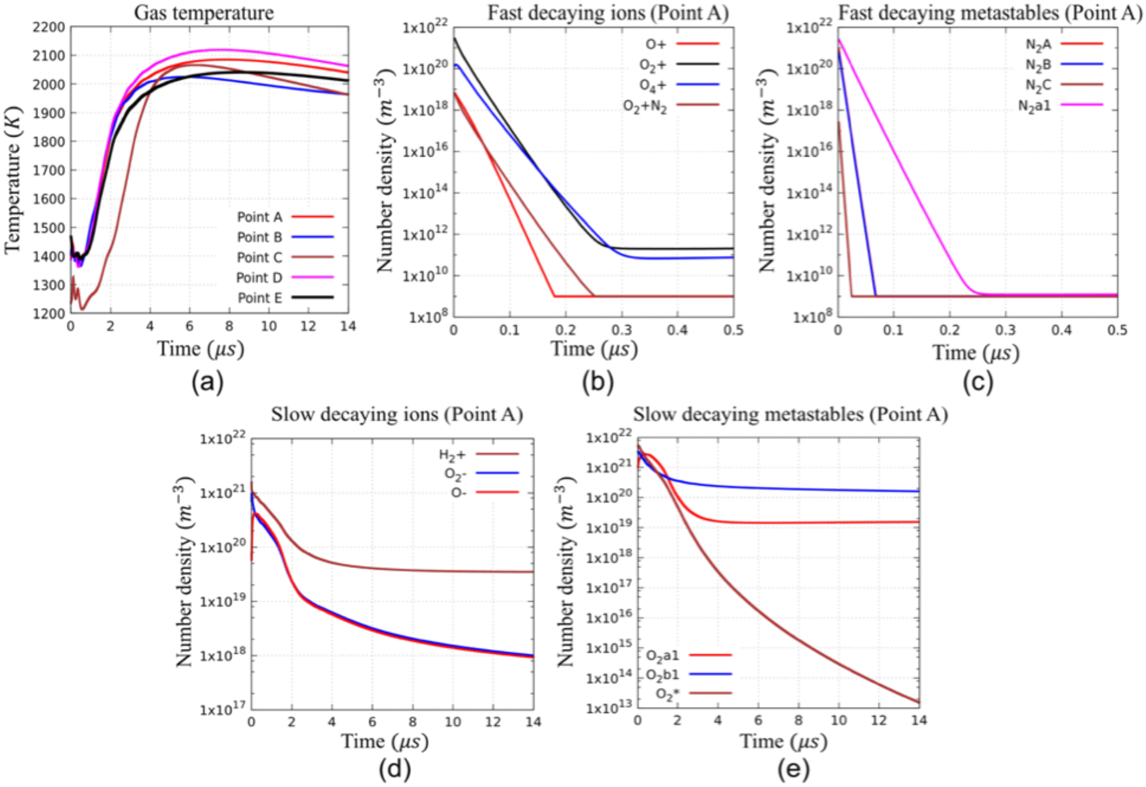

Figure 6.20: Time variation of (a) gas temperature at trace points (b) fast decaying ions (note scale is 0.5 μs) (c) fast decaying metastables (note scale is 0.5 μs) (d) Slow decaying ions and (e) slow decaying metastable species at the centrally located trace point.

ble for quenching these species has a negligible effect on the ignition delay. This can be seen in Fig. 6.20(b) where the temperature dip associated with the precursor shock is unaffected by the quenching of fast decaying plasma species. The second category is the slow decaying species, the slow decaying ions (${H_2}^+, {O_2}^-, O^-$) shown in Fig. 6.20(d) and the slow decaying oxygen metastable species (${O_2}^{a1}, {O_2}^{b1}, {O_2}^*$) shown in Fig. 6.20(e). These species maintain a sufficiently high density even after the precursor shock has processed the interelectrode gap and have the ability to influence ignition.

To study the influence of the slow decaying plasma species on the combustion process, the gas temperature at the sampled points is compared to the parametric study where the primary combustion radicals are the only species incorporated from the plasma discharge. Figure 6.21(a)-(c) compares the gas temperature transients at the points A, B and C for the two cases, one where all the plasma species are tracked (all species) and other where only the primary combustion radicals (primary radicals) are interpolated from the discharge. The incorporation of additional plasma species is observed to reduce the ignition delay by approximately 0.1 μs ($\sim 10\%$) at all the sampled points. The slow decaying plasma species enhance ignition through two dominant mechanisms. First, the quenching reactions that consume these species are predominantly exothermic, resulting in additional heating of the gas mixture during the course of ignition. Figure 6.20(e) and (f) shows the maximum decrease in the number density of slow decaying species occurring at times when the temperature (Fig. 6.21(b)) at the sampled points starts to rise, suggesting significant quenching during the ignition phase. Second, the quenching reactions also enhance the production of primary combustion radicals. Figure 6.21(d)-(f) shows the concentration of primary combustion radicals at point A, located at the interelectrode midpoint. At times preceding ignition, it is seen that for all three radicals, a slightly higher concentration is achieved when all the plasma species are incorporated. Hence, the quenching of excited plasma species provides an additional source of primary combustion radicals allowing the mixture to achieve critical radical concentrations necessary for ignition at a faster rate. However, since the concentration of slow decaying plasma species is a relatively low fraction ($\sim 0.01\%$) of the fuel/oxidizer concentration, the contribution of these quenching reactions is relatively small as compared to the effects induced by gas temperature and primary combustion radicals.

Effect of combustion radicals alone

We also performed simulations with only the primary combustion radical densities (O, OH and H) from the plasma results as initial conditions for the combustion simulations, i.e. starting with a uniform gas temperature of 1000 K and no other plasma species. In this case, no ignition was observed for reasonable time scales of milliseconds confirming that high gas temperatures from the plasma kernel play a key role in nanosecond pulsed plasma-assisted combustion ignition phenomena.

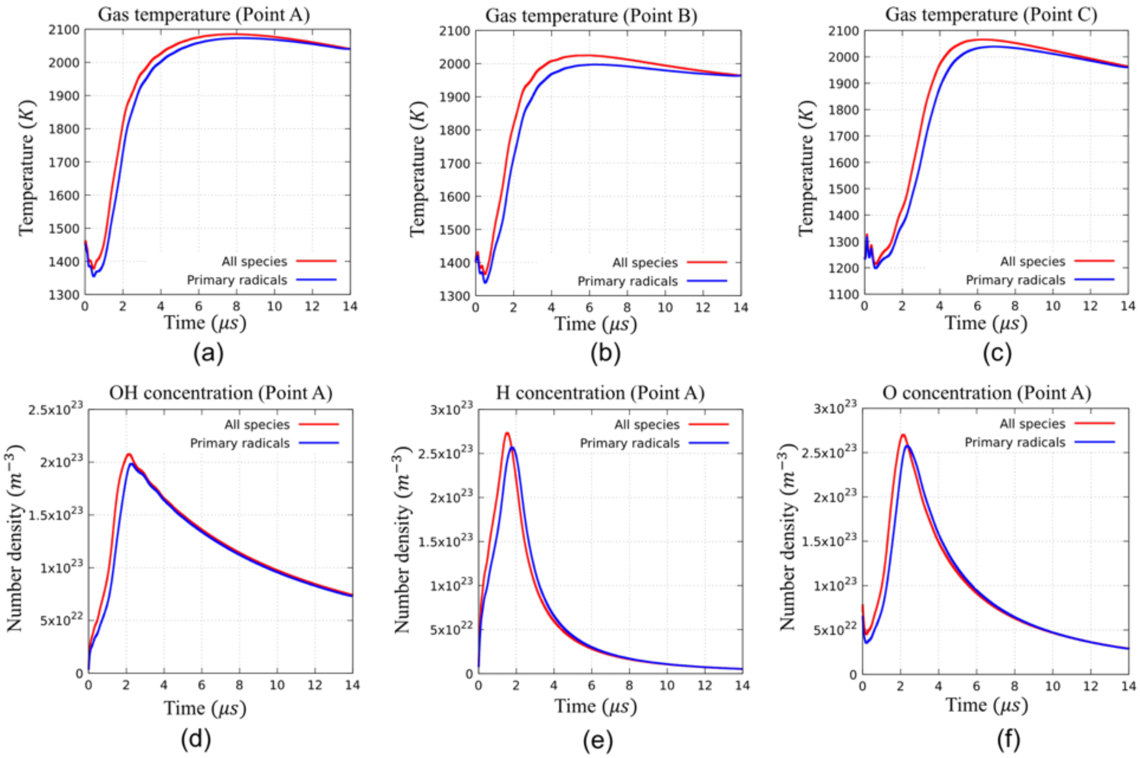

Figure 6.21: Top panel: comparison of time variation of gas temperature at (a) Point A (b) Point B and (c) Point C bottom panel: comparison of (d) H (e) OH and (f) O concentrations at point A between the case where all plasma species (red) and only primary radicals (blue) are interpolated from the discharge.

6.5 Conclusions

A coupled multi-dimensional study of nanosecond pulsed plasma assisted combustion provided several insights into the various mechanisms through which plasma discharges enhance ignition. A zero-dimensional study demonstrated the kinetic pathways via which trace concentration of primary combustion radicals generated by a nanosecond pulsed discharge significantly reduced ignition delays in H_2-O_2 fuel-oxidizer mixtures. This effect was found to be especially true at higher operating pressures. To investigate this combustion enhancing effect in further detail, coupled multi-dimensional simulations were performed. Two-dimensional axisymmetric simulations of a plasma discharge ignited in an interelectrode gap indicated large volumetric heating of the fuel-air mixture with an average temperature rise of approximately 400 K achieved within a relatively short timescale of few nanoseconds. The activation of metastable quenching reactions during the pulse ramp down phase was found be responsible for the majority of this ultra-fast gas heating. Also produced in the nanosecond timescales were desired concentrations of primary combustion radicals that were shown to lower ignition delay.

A multi-scale coupling framework and a centroid based interpolation scheme allowed the plasma generated solution variables to be incorporated into the initial conditions of the combustion simulations that was then used to study the spatio-temporal evolution of a flame kernel. The plasma generated heating effect produced two major temperature hotspots, a higher temperature low volume cathode kernel and relatively lower temperature higher volume anode kernel. From an ignitability perspective, the volumetric extent of a hotspot was found to be more important as the mixture first ignited within the anode hotspot. The inclusion of combustion enhancing radicals resulted in a further fifteen-fold decrease in ignition delay compared to the case where only plasma based gas-heating effects were considered, underlining the crucial role played by these active species. The primary combustion radicals, also found in high concentrations at the temperature hotspots, initiated ignition as soon as the nanosecond plasma pulse was switched off. Although the cathode kernel had higher radical densities, the anode kernel that exhibited a comparatively lower density but distributed over a larger volume was the location of ignition, again suggesting the importance of volumetric activation. The addition of plasma generated metastable species resulted in a further decrease in ignition delay by approximately 10%. However, the dominant ignition enhancing effects were found to arise from gas heating and primary combustion radicals, with high gas temperatures from the plasma kernel playing a critical role in nanosecond pulsed plasma-assisted combustion ignition phenomena.

Chapter 7

Conclusions and contribution

7.1 Summary

A fully coupled computational model for simulations of non-equilibrium plasmas and combustion is presented. Computational studies are conducted for multiphysics applications ranging from plasma based combustion ignition, surface streamer induced large gap thermal breakdown to electric discharge in liquids for reforming and biomedical applications.

The non-equilibrium plasma model is based on a multi-species, multi-temperature continuum description with finite-rate chemistry. The governing equations are derived by taking the moments of the species Boltzmann equation, with the first three moments yielding the continuity, momentum and energy conservation equations respectively. The details of the non-equilibrium plasma model are provided in chapter 2. The combustion process in the present work is modeled using reactive compressible Euler equations. The equation system consists of separate continuity equations for the densities of individual species and a global system of conservation equation for density, velocity and gas temperature. The details of the non-equilibrium plasma model are provided in chapter 2. Both plasma and combustion models use the same underlying mesh infrastructure and can be used in a standalone fashion or a fully coupled manner based on the application. The plasma and the combustion models are coupled self-consistently to model nanosecond pulsed plasma induced combustion ignition. Details of the coupling framework are discussed in the final section of chapter 2.

The non-equilibrium plasma governing equations are discretized in space using the finite volume method and integrated in time using the implicit backward Euler method. The governing equations in the combustion model are discretized in space using finite volume methods. For time-integration in the combustion model, the individual species continuity equations use implicit backward Euler scheme while the global conservation equations for mass, momentum and energy (solved as a single system) use explicit forward Euler scheme. Details of the numerical model for plasma and combustion processes are discussed in chapter 3.

The discretized governing equations in plasma and combustion model are non-dimensionalized before the solving them. The sparse linear system for each plasma governing equation is solved using GMRES algorithm from PETSc [124] with relevant preconditioners. In the combustion model, the explicit global conservation system forms a set of algebraic equations which are solved directly to update the conservation variables at each time step. On the other hand, the implicit species density equations (in the combustion model), form a sparse linear system for each equation and solved using GMRES algorithm with relevant preconditioners. Details regarding the linear solver and preconditioners used in the present work are discussed in chapter 3.

In chapter 4, argon surface streamers are modeled as low-voltage mechanism for thermal breakdown in large interelectrode gaps. The study also investigates the effect of impurities (molecular oxygen) on the development of continuous surface streamer channels under atmospheric-pressure conditions. In pure argon, a continuous conductive streamer successfully bridges the gap between two electrodes indicating high probability of transition to arc. Small amounts of oxygen impurities ($< 5\%$) are found to be conducive to the streamer evolution as they reduce the threshold voltage of surface streamers, eliminate unwanted streamer branching while maintaining a high probability of surface streamer transition to arcs. Higher oxygen impurities $> 5\%$ significantly deteriorate the streamer channel conductivity and greatly reduces its probability for transition to thermal plasma. A dimensional reduction algorithm is formulated using Recursive Principal Component Analysis (RPCA) and validated for $Ar-O_2$ chemistry. The recursive framework (RPCA) is devised to dynamically update the principal components during the transient simulation which is vital to resolve the influence of the highly non-linear reaction coefficients associated with the charged species in the plasma.

In chapter 5, computational studies of atmospheric pressure nanosecond streamer discharges generated in helium bubbles immersed in distilled water is presented. Two parameters namely a) trigger voltage polarity and b) the presence of multiple bubbles, are found to significantly influence the dynamic characteristics of the streamers. The polarity of the trigger voltages substantially changes the dynamic characteristics of the discharge. For a positive trigger voltage, the discharge progresses through a single cathode-directed streamer. However, for a negative trigger voltage of the pin electrode, the discharge evolves via multiple streamers originating along the axis and near the anode. A comparison between active species generated for the negative and positive trigger voltage showed larger number densities of active species in the latter case but more uniform distribution of active species in the former case. It is found that, the presence of multiple bubbles reduces the breakdown voltage and results in thicker and more uniform streamers compared to single bubble configuration which is highly desirable for liquid reforming applications. We also find that the streamer hops from one bubble to another to bridge the gap between the electrode at voltages above the breakdown voltage. It was observed that the presence of water vapor in the bubble leads to water complex ions dominating the concentration of negative ions and OH radicals dominating the concentration of excited neutrals. Thus streamer discharge through multiple bubbles is not-only feasible but also results in thicker discharge and more uniform generation of active species inside the gas bubble. From 1D preliminary multi-phase studies, it is found that a double layer is formed in the liquid medium over nanosecond timescales. It is also observed that an electrostatic debye layer is formed at the interface with a net negative polarity which shields the transport of negatively charged species into the liquid medium

In chapter 6, nanosecond pulse plasma induced flame ignition and combustion is simulated for a lean premixed H_2-air mixture in a high pressure environment. A coupled multi-dimensional study of nanosecond pulsed plasma assisted combustion provided several insights into the various mechanisms through which plasma discharges enhance ignition. A zero-dimensional study demonstrated the kinetic pathways via which trace concentration of primary combustion radicals (generated by a nanosecond pulsed discharge) significantly reduced ignition delays in H_2-O_2 fuel-oxidizer mixtures under lean high pressure conditions. The plasma is accompanied by fast gas heating due to N_2 metastable quenching that results in uniform volumetric heating in the interelectrode gap. A multi-scale coupling framework and a centroid based interpolation scheme allowed the plasma generated solution variables to be incorporated into the initial conditions of the combustion simulations that was then used to study the spatio-temporal evolution of a flame kernel. From an ignitability perspective, the volumetric extent of a hotspot was found to be more important. The inclusion of combustion enhancing radicals resulted in a further fifteen-fold decrease in ignition delay compared to the case where only plasma based gas-heating effects were considered, underlining the crucial role played by these active species. The addition of plasma generated metastable species resulted in a further decrease in ignition delay by approximately 10%. However, the dominant ignition enhancing effects were found to arise from gas heating and primary combustion radicals, with high gas temperatures from the plasma kernel playing a critical role in nanosecond pulsed plasma-assisted combustion ignition phenomena.

7.2 Contributions

The primary objective of the present work is to use and develop computational models to obtain physical insight into the discharge structure, chemical kinetics and spatio-temporal dynamics of high pressure nanosecond pulsed plasmas for multiphysics applications ranging from plasma assisted combustion ignition, large gap thermal breakdown to electric discharge in liquids for fuel reforming and biomedical applications.

The principle contributions of the present work are:

1. A coupled multi-dimensional computational model for modeling nanosecond pulsed plasma assisted combustion ignition.

   - Development of a standalone combustion solver as a part of the present work by integrating a plasma solver [108] and a compressible flow solver [111] on an common unstructured mesh infrastructure. The combustion solver adds significant new capability to the computational tool set that our group possesses.

   - Significant modifications and additions to the in-house plasma solver to improve convergence, performance and multiphysics coupling.

   - Development of a framework for coupling the combustion model alongside the non-equilibrium plasma model to resolve plasma formation, combustion ignition, and flame development stages self-consistently.

2. High fidelity simulations of nanosecond pulsed plasma assisted combustion ignition for a lean H_2-air mixture in a high pressure environment

- Simulations of nanosecond pulsed plasma assisted combustion ignition using the developed plasma-combustion computational framework for modeling plasma and combustion stages self-consistently.

- Formulation and validation of plasma and combustion chemistries for H_2-air mixtures for high pressure conditions.

- Investigation of the influence of three main parameters of non-equilibrium plasma kernel on the combustion kernel dynamics, namely a) gas temperature, b) primary combustion radicals $O, OH \text{ and } H$ and c) other plasma species such as ions and electronically excited radicals.

3. High fidelity simulations of non-equilibrium plasmas generated in Helium bubbles suspended in liquid water

   - Formulation and validation of gas plasma chemistries for $He-H_2O$, H_2O-air mixtures and liquid plasma chemistry for H_2O-air mixture for high pressure conditions.

   - Investigation of the effects of voltage polarity and the presence of multiple bubbles on the kinetics and dynamics of the active species generation inside the gas bubbles.

   - Development of a multi-phase plasma fluid model for modeling plasma evolution in both gas and liquid mediums. Integration of the multiphase plasma fluid model with the in-house plasma solver to extend its capability towards resolving active species transport and kinetics in liquid medium.

- Preliminary 1D simulations using the multi-phase plasma fluid model to resolve the formation of active liquid layer and electrostatic debye layer in the liquid medium.

4. High fidelity simulations of argon surface streamers in the presence of oxygen impurities for their use as a low-voltage mechanism for thermal breakdown in large interelectrode gaps.

   - Formulation and validation of gas plasma chemistries for $Ar-O_2$ mixture for high pressure conditions to account for a wide range of concentration of O_2 impurity (1-10%).

   - Investigation of the effect of the oxygen impurities on the dynamic characteristics of the discharge, primarily their effect on streamer branching and streamer channel conductivity.

   - Implementation of a Recursive Principal component analysis (RPCA) algorithm for dimensional reduction of chemical kinetics for complex chemistries. Integration of the dimensional reduction framework into the in-house plasma solver, adding chemistry reduction capability to the existing set of computational tools in our group.

   - Validation, testing and optimization of the dimensional reduction algorithm for $Ar-O_2$ gas chemistry.

5. Development and testing of a range of chemical kinetic mechanisms for modeling gas plasmas ($Ar-O_2$, $He-H_2O$, H_2-air, H_2O-air), liquid plas-

mas (H_2O−air) and combustion(H_2−air) phenomenon in high pressure regimes.

- Identification of dominant species, dominant reaction pathways and their relevant collision cross-sections from literature.

- Computation of reaction rate coefficients and transport coefficients or precompilation of reaction rates using existing literature.

7.3 Publications

1. A. Sharma, D. Levko, and L. L. Raja, "Effect of oxygen impurities on atmospheric-pressure surface streamer discharge in argon for large gap arc breakdown," Physics of Plasmas, vol. 23, no. 10, p. 103501, 2016.
2. A. Sharma, D. Levko, L. L. Raja, and M. S. Cha, "Kinetics and dynamics of nanosecond streamer discharge in atmospheric-pressure gas bubble suspended in distilled water under saturated vapor pressure conditions," Journal of Physics D: Applied Physics, vol. 49, no. 39, p. 395205, 2016.
3. A. Sharma, V. Subramaniam, E. Solmaz, and L. Raja, "Fully coupled modeling of nanosecond pulsed plasma assisted combustion ignition", 2019, Journal of Physics D: Applied Physics, Vol. 52, no. 9, p.095204
4. D. Levko, A. Sharma, and L. L. Raja, "Non-thermal plasma ethanol reforming in bubbles immersed in liquids," Journal of Physics D: Applied Physics, vol. 50, no. 8, p. 085202, 2017.

5. D. Levko, A. Sharma, and L. L. Raja, “Microwave plasmas generated in bubbles immersed in liquids for hydrocarbons reforming,” Journal of Physics D: Applied Physics, vol. 49, no. 22, p. 22LT01, 2016.
6. D. Levko, A. Sharma, and L. L. Raja, “Plasmas generated in bubbles immersed in liquids: direct current streamers versus microwave plasma,” Journal of Physics D: Applied Physics, vol. 49, no. 28, p. 285205, 2016.
7. D. Levko, A. Sharma, and L. L. Raja, “Kinetic modeling of streamer penetration into de-ionized water,” Physics of Plasmas, vol. 25, no. 3, p. 033515, 2018.
8. A. Sharma, D. Levko, and L. L. Raja, “Computational studies of positive and negative streamers in bubbles suspended in distilled water,” in 55th AIAA Aerospace Sciences Meeting, p. 1970, 2017.
9. A. Sharma and L. L. Raja, “Numerical Investigations of Cathode Surface Streamer Discharges for High-Pressure Large Gap Arc Breakdown,” in 53rd AIAA Aerospace Sciences Meeting, p. 1619, 2015.
10. A. Sharma, V. Subramaniam, E. Solmaz, and L. Raja, ”Coupled computational studies of non-thermal plasma based combustion ignition ”, 57th AIAA Aerospace Sciences Meeting, 2019.

7.4 Recommendations for future research

1. A natural extension to the work on the combustion solver is to paral-

lelize the combustion module. The MPI parallel paradigm is an appropriate choice because both the plasma and combustion modules use the same underlying mesh infrastructure and the plasma module uses this paradigm. In terms of development, the mesh data structures are already parallelized by the pre-processing routines in plasma module. The mesh data structures used in the combustion module are analogous to the plasma module and hence no additional work is needed in parallelizing these lower level infrastructure of the code. The individual species density equations in the combustion module following the same framework as the species density equations in the plasma module and can be parallelized using the same approach as followed for these equations in the plasma module. Mesh partitioning and domain decomposition in the combustion module can implemented using METIS based graph partitioning approach which is compatible with the MPI distributed memory paradigm. The global system of compressible Euler equations in the combustion module are currently solved using explicit forward Euler scheme and can be parallelized relatively easily as they don't involve solving a linear system at each time step. The residual vector of cell elements in each domain partition can be updated by the MPI processor using vectorized axpy operations from BLAS for optimum performance. Parallelizing the centroid based interpolation scheme which interpolates the variables from the plasma to the combustion module is non-trivial and will require certain efforts, as it involves searching operations and communicating information between different meshes.

2. As an extension to plasma assisted combustion ignition studies, we are currently working on modeling nanosecond pulsed plasma induced combustion ignition in lean methane-air mixtures under high-pressure conditions. The studies are a first step in gaining insight into the applicability of non-equilibrium plasmas for ignition tunability and combustion enhancement in practical fuels involving hydrocarbons used in IC engines and most combustion applications. The work involves devising chemical kinetic mechanisms for simulating plasma and combustion stages in CH_4-air and identifying the governing parameters in the plasma that influence flame ignition and propagation in hydrocarbons.

3. In this current work, we conducted preliminary 1D studies for plasma evolution into the liquid over nanometer length scales and nanosecond timescales using a multi-phase plasma fluid model developed. The next step towards understanding plasma-liquid interactions which are of interest in fuel reforming and biomedical applications is to perform multi-dimensional simulations for evolution of plasma discharges in liquids and hydrocarbons over much longer millisecond timescales associated with plasma evolution in liquid medium. This is computationally challenging due to highly disparate length scales across the gas and the liquid medium as well as extremely slow diffusion timescales in the liquid medium. One approach to get around this is to make use of the double

layer formation inside the liquid medium and use extremely fine mesh elements in the interface layer/active liquid layer (in the immediate vicinity of the gas-liquid interface) with coarse mesh elements in the bulk layer. Detailed chemical kinetics in the liquid phase will also necessitate efforts towards identifying the dominant pathways for reactions in the liquid medium, determining collision cross-sections for reaction pathways and deriving the constitutive relations for transport of species in the liquid hydrocarbons.

4. In the current work, a Recursive PCA algorithm was devised in order to reduce the chemical complexity of a global plasma model. The next step is to extend the approach to 1D and higher dimensions. Due to inclusion of spatial flux terms, this problem will involve finding the dominant principal components in the spatial domain, which is a challenging problem as different regions of the computational domain will have different set of dominant principal components. In addition, in the current approach, the lower dimensional basis in the current work was assumed to be governed only by the species number density, and the source terms were directly projected on this lower dimensional basis. This approximation will not be valid anymore with the involvement of the flux terms, and the training data will need to include information about the flux and source terms too while identifying the lower dimensional basis. Lastly, while solving the linear system of different equations, if the principal components are different at different spatial points, constructing the $AX = b$

at each point becomes non-trivial. This is because X which is the vector of principal components being updated, is different at different points, and hence the principal components being solved for across two adjacent points are not identical and computation of flux terms involving these two points is not straightforward. A couple of approaches followed in the combustion community involve the use of non-linear PCA [146], kernel PCA [147] and other non-linear reduction approaches, have shown success and can be referred [148],[149].

Appendices

Appendix A

Ar$-$O$_2$ high pressure plasma chemistry

Table A.1: Ar$-$O$_2$ high pressure plasma chemistry

#	Reactions	A	B	C	Ref.
$G1$	$e^- + Ar \rightarrow e + Ar^*$		BOLSIG+		[114]
$G2$	$e^- + Ar^* \rightarrow e + Ar$		BOLSIG+		[114]
$G3$	$e^- + Ar \rightarrow 2e + Ar^+$		BOLSIG+		[114]
$G4$	$e^- + Ar^* \rightarrow 2e + Ar^+$		BOLSIG+		[114]
$G5$	$e^- + Ar_2^* \rightarrow 2e + Ar_2^+$	1.285E-10	0.7	-4.247E+4	[150]
$G6$	$e^- + Ar_2^* \rightarrow e + 2Ar$	1.0E-10			[151]
$G7$	$e^- + Ar^+ \rightarrow Ar^*$	4.3E-11	-0.5		[151]
$G8$	$e^- + Ar_2^+ \rightarrow Ar + Ar^*$	2.590E-5	-0.66		[152]
$G9$	$2e^- + Ar^+ \rightarrow e + Ar^*$	9.79E-9	-4.5		[151]
$G10$	$e^- + O_2 \rightarrow e + O_2$		BOLSIG+		[114]
$G11$	$e^- + O_2 \rightarrow e + O_2$		BOLSIG+		[114]
$G12$	$e^- + O_2 \rightarrow e + O_2$		BOLSIG+		[114]
$G13$	$e^- + O_2 \rightarrow e + O_2$		BOLSIG+		[114]
$G14$	$e^- + O_2 \rightarrow e + O_2$		BOLSIG+		[114]
$G15$	$e^- + O_2 \rightarrow 2e + O_2^+$		BOLSIG+		[114]
$G16$	$e^- + O_2 \rightarrow 2e + O^+ + O$		BOLSIG+		[114]
$G17$	$e^- + O_2 \rightarrow O^- + O$		BOLSIG+		[114]
$G18$	$e^- + Ar + O^+ \rightarrow O + Ar$	3.11E-23	-1.5		[153]
$G19$	$e^- + O_2 + Ar \rightarrow O_2^- + Ar$	5.89E-27	-1	-7.08E+2	[12]
$G20$	$e^- + O_2 + O_2 \rightarrow O_2^- + O_2$	1.0E-31			[153]
$G21$	$e^- + O_2 \rightarrow e^- + 2O$		BOLSIG+		[114]
$G22$	$e^- + O_2^+ \rightarrow 2O$	2.36E-6	-0.5		[12]
$G23$	$2e^- + O^+ \rightarrow e^- + O$	1.439E-8	-4.5		[153, 12]
$G24$	$2e^- + O_2^+ \rightarrow e^- + O_2$	1.439E-8	-4.5		[153, 12]

#	Reactions	A	B	C	Ref.
$G25$	$e^- + O_2 \rightarrow O^- + O^+ + O$	6.59E-13	0.5	-1.97E+5	[12]
$G26$	$e^- + Ar + O_2^+ \rightarrow O_2 + Ar$	3.11E-23	-1.5		[153]
$G27$	$O^- + O \rightarrow O_2 + e^-$	5.0E-10			[153]
$G28$	$O_2^- + O \rightarrow O^- + O_2$	3.3E-10			[153]
$G29$	$Ar^* + O_2 \rightarrow Ar + 2O$	2.1E-10			[154]
$G30$	$Ar^+ + O \rightarrow Ar + O^+$	4.6E-11			[155]
$G31$	$Ar^+ + O_2 \rightarrow Ar + O_2^+$	4.6E-11			[155]
$G32$	$Ar_2^+ + O_2 \rightarrow 2Ar + O_2^+$	1.0E-10			[154]
$G33$	$Ar + O_2^+ \rightarrow Ar^+ + O_2$	5.5E-11			[155]
$G34$	$Ar_2^* + O_2 \rightarrow 2Ar + O_2$	4.6E-11			[154]
$G35$	$Ar_2^+ + O^- \rightarrow 2Ar + O$	1.0E-7			[154]
$G36$	$Ar_2^+ + O_2^- \rightarrow 2Ar + O_2$	1.0E-7			[154]
$G37$	$Ar_2^+ + O_2^- \rightarrow 2Ar + 2O$	1.0E-7			[154]
$G38$	$Ar + 2O \rightarrow Ar + O_2$	5.21E-35			[154]
$G39$	$Ar^+ + O^- \rightarrow Ar + O$	2.8E-7			[155]
$G40$	$Ar + O + O^+ \rightarrow Ar + O_2^+$	1.0E-29			[153]
$G41$	$Ar^* + 2Ar \rightarrow Ar_2^* + Ar$	1.14E-32			[152]
$G42$	$Ar^* + Ar^* \rightarrow e^- + Ar + Ar^+$	5.0E-10			[152]
$G43$	$Ar_2^* + Ar_2^* \rightarrow e^- + 2Ar + Ar_2^+$	5.0E-10			[152]
$G44$	$Ar^+ + 2Ar \rightarrow Ar_2^+ + Ar$	2.5E-31			[152]
$G45$	$Ar_2^* \rightarrow 2Ar$	6.0E+7			[152]
$G46$	$Ar_2^* + Ar \rightarrow 2Ar + Ar$	5.0E-15			[127]

The reaction rate coefficients are given in Arrhenius form $k = AT^B exp(-C/T)$.
Units for k are $cm^3 s{-}1$ for 2-body and $cm^6 s{-}1$ for 3-body reactions,T is in Kelvin.
BOLSIG+ refers to a pre-computation of the reaction rate coefficients from the electron energy distribution function that is solved for using the Boltzmann equation [114].

Appendix B

He$-$H$_2$O high pressure plasma chemistry

Table B.1: He$-$H$_2$O high pressure plasma chemistry

#	Reactions	A	B	C	Ref.
	Electron impact ionization				
$G1$	$e + He \rightarrow 2e + He^+$		BOLSIG+		[114]
$G2$	$e + He^* \rightarrow 2e + He^+$		BOLSIG+		[114]
$G3$	$e + H_2O \rightarrow 2e + H_2O^+$		BOLSIG+		[114]
$G4$	$e + H \rightarrow 2e + H^+$	5.08E-9	0.6	-13.6	[133]
$G5$	$e + H_2^* \rightarrow 2e + H_2^+$	9.1E-9	0.5	-15.4	[133]
$G6$	$e + O \rightarrow 2e + O^+$	9.1E-9	0.7	-13.6	[133]
$G7$	$e + O_2 \rightarrow 2e + O_2^+$	9.0E-10	2	-12.6	[133]
$G8$	$e + O_2(a) \rightarrow 2e + O_2^+$	9.0E-10	2.0	-11.6	[133]
$G9$	$e + OH \rightarrow 2e + OH^+$	2.0E-10	1.78	-13.8	[133]
	Electron impact excitation				
$G10$	$e + He \rightarrow e + He^*$		BOLSIG+		[114]
$G11$	$e + H_2O \rightarrow e + H + OH$		BOLSIG+		[114]
$G12$	$e + H_2O \rightarrow e + H_2 + O^1D$		BOLSIG+		[114]
$G13$	$e + H_2O \rightarrow e + H + OH(A)$		BOLSIG+		[114]
$G14$	$e + H_2 \rightarrow e + 2H$	8.73E-8	0.5	-11.7	[133]
$G15$	$e + O \rightarrow e + O^1D$	4.5E-9		-2.29	[133]
$G16$	$e + O_2 \rightarrow e + 2O$	7.1E-9		-8.6	[133]
$G17$	$e + O_2 \rightarrow e + O + O^1D$	4.0E-8		-8.4	[133]
$G18$	$e + O_2 \rightarrow e + O_2(b)$	3.24E-10		-2.218	[133]
$G19$	$e + O_2 \rightarrow e + O_2(a)$	1.7E-9		-3.1	[133]
$G20$	$e + O_2(a) \rightarrow e + O_2$	5.6E-9		-2.2	[133]
$G21$	$e + O_2(b) \rightarrow e + O + O^1D$	3.49E-8		-4.29	[133]
$G22$	$e + OH \rightarrow e + O + H$	2.08E-7	-0.76	-6.9	[133]

#	Reactions	A	B	C	Ref.
$G23$	$e + HO_2 \rightarrow e + H + O_2$	3.1E-9			[133]
$G24$	$e + H_2O_2 \rightarrow e + 2OH$	2.36E-9			[133]
$G25$	$e + H_2O_2 \rightarrow e + H + HO_2$	3.1E-11			[133]
$G26$	$e + O_3 \rightarrow O + O_2 + e$	5.88E-9			[133]
	Attachment				
$G27$	$e + H_2O \rightarrow OH + H^-$		BOLSIG+		[114]
$G28$	$e + H_2O \rightarrow H_2 + O^-$		BOLSIG+		[114]
$G29$	$e + H_2O \rightarrow OH^- + H$		BOLSIG+		[114]
$G30$	$e + OH + He \rightarrow OH^- + He$	3.1E-31			[133]
$G31$	$e + H_2O_2 \rightarrow H_2O + O^-$	1.57E-10	-0.55		[133]
$G32$	$e + H_2O_2 \rightarrow OH + OH^-$	2.7E-10	-0.5		[133]
	Dissociative Recombination				
$G33$	$e + He^+ + He \rightarrow He^* + He$	6.6E-30	-2.0		[133]
$G34$	$e + He_2^+ + He \rightarrow He^* + 2He$	3.5E-27			[133]
$G35$	$e + H_5O_2^+ \rightarrow 2H_2O + H$	1.62E-6	-0.15		[133]
$G36$	$e + H_4O_2^+ \rightarrow H_2O + OH + H$	9.6E-7	-0.2		[133]
$G37$	$e + H_7O_3^+ \rightarrow 3H_2O + H$	2.24E-6	-0.08		[133]
$G38$	$e + H_9O_4^+ \rightarrow 4H_2O + H$	3.6E-6			[133]
$G39$	$e + H_11O_5^+ \rightarrow 5H_2O + H$	4.0E-6			[133]
$G40$	$e + H_13O_6^+ \rightarrow 6H_2O + H$	4.0E-6			[133]
	Dissociative Recombination				
$G41$	$H^- + He \rightarrow He + H + e$	8.0E-12			[133]
$G42$	$He^+ + 2He \rightarrow He_2^+ + He$	1.4E-31			[133]
$G43$	$He^+ + H_2O \rightarrow H^+ + OH + He$	2.04E-10			[133]
$G44$	$He^+ + H_2O \rightarrow H + OH^+ + He$	2.86E-10			[133]
$G45$	$He^+ + H_2O \rightarrow H_2O^+ + He^+$	6.05E-11			[133]
$G46$	$HeH^+ + H \rightarrow H_2^+ + He$	9.1E-10			[133]

#	Reactions	A	B	C	Ref.
$G47$	$HeH^+ + H_2O \rightarrow H_3O^+ + He$	4.3E-10			[133]
$G48$	$He_2^+ + H_2O \rightarrow HeH^+ + He + OH(A)$	1.3E-10			[133]
$G49$	$He_2^+ + H_2O \rightarrow O^+ + H_2 + 2He$	2.1E-10			[133]
$G50$	$He_2^+ + H_2O \rightarrow OH^+ + H + 2He$	2.1E-10			[133]
$G51$	$He_2^+ + H_2O \rightarrow H^+ + OH + 2He$	2.1E-10			[133]
$G52$	$He_2^+ + H_2O \rightarrow HeH^+ + OH + He$	2.1E-10			[133]
$G53$	$He_2^+ + H_2O \rightarrow H_2 + O + 2He$	2.1E-10			[133]
$G54$	$H^+ + H_2O \rightarrow H_2O^+ + H$	6.9E-11			[133]
$G55$	$H^- + H_2O \rightarrow OH^- + H_2$	3.8E-11			[133]
$G56$	$H_2^+ + He \rightarrow HeH^+ + H$	1.3E-10			[133]
$G57$	$H^+ + H_2O \rightarrow H_2O^+ + H_2$	3.9E-9			[133]
$G58$	$H_2^+ + H_2O \rightarrow H_3O^+ + H$	3.4E-9			[133]
$G59$	$O^+ + H_2O \rightarrow H_2O^+ + O$	2.6E-9			[133]
$G60$	$O^- + H_2O \rightarrow OH^- + OH$	1.4E-9			[133]
$G61$	$OH^+ + O \rightarrow O_2^+ + H$	7.1E-10			[133]
$G62$	$OH^+ + H_2O \rightarrow H_2O^+ + OH$	1.5E-9			[133]
$G63$	$OH^+ + H_2O \rightarrow H_3O^+ + O$	1.3E-9			[133]
$G64$	$H_2O^+ + OH \rightarrow H_3O^+ + O$	6.9E-10			[133]
$G65$	$H_2O^+ + H_2O \rightarrow H_3O^+ + OH$	1.85E-10			[133]
$G66$	$O_2^+ + H_2O + M \rightarrow H_2O_3^+ + M$	2.6E-28			[133]
$G67$	$H_2O^+ + O_2 \rightarrow H_2O + O_2^+$	3.3E-10			[133]
$G68$	$H_2O_3^+ + H_2O \rightarrow H_4O_2^+ + O_2$	1.0E-9			[133]
$G69$	$H_2O_3^+ + H_2O \rightarrow H_3O^+ + OH + O_2$	3.0E-10			[133]

#	Reactions	A	B	C	Ref.
$G70$	$H_4O_2^+ + H_2O \rightarrow H_5O_2^+ + OH$	1.4E-9			[133]
$G71$	$H_3O^+ + H_2O + M \rightarrow H_5O_2^+ + M$	3.2E-27			[133]
$G72$	$H_5O_2^+ + H_2O + M \rightarrow H_7O_3^+ + M$	7.4E-27			[133]
$G73$	$H_7O_3^+ + H_2O + M \rightarrow H_9O_4^+ + M$	2.5E-27			[133]
$G74^g$	$H_9O_4^+ + M \rightarrow H_7O_3^+ + H_2O + M$	2.0E18	-8.1	-8360	[133]
$G75$	$H_9O_4^+ + H_2O + M \rightarrow H_1 1O_5^+ + M$	3.3E-28			[133]
$G76^g$	$H_1 1O_5^+ + M \rightarrow H_9O_4^+ + H_2O + M$	6.3E30	-14	-5750	[133]
$G77$	$H_1 1O_5^+ + H_2O + M \rightarrow H_1 3O_6^+ + M$	4.0E-29			[133]
$G78^g$	$H_1 3O_6^+ + M \rightarrow H_1 1O_5^+ + H_2O + M$	2.62E33	-15.3	-5000	[133]
$G79$	$O^- + H_2O + M \rightarrow H_2O_2^- + M$	1.3E-28			[133]
$G80$	$OH^- + H_2O + M \rightarrow H_3O_2^- + M$	2.5E-28			[133]
$G81$	$H_2O_2^- + H_2O \rightarrow H_3O_2^- + OH$	1.0E-11			[133]
$G82$	$H_3O_2^- + H_2O + M \rightarrow H_5O_3^- + M$	3.5E-28			[133]
$G83$	$He^+ + OH^- + M \rightarrow OH + He + M$	2.0E-25			[133]
$G84$	$He_2^+ + O^- + M \rightarrow O + 2He + M$	2.0E-25			[133]
$G85$	$He_2^+ + OH^- + M \rightarrow OH + 2He + M$	2.0E-25			[133]
$G86$	$He_2^+ + H_2O_2^- + M \rightarrow O + 2He + 2H_2O + M$	2.0E-25			[133]
$G87$	$He_2^+ + H_3O_2^- + M \rightarrow OH + 2He + H_2O + M$	2.0E-25			[133]
$G88$	$He_2^+ + H_5O_3^- + M \rightarrow OH + 2He + 2H_2O + M$	2.0E-25			[133]
$G89$	$OH^+ + O^- \rightarrow HO_2$	2.0E-7			[133]
$G90$	$OH^+ + H_2O_2^- + M \rightarrow O + OH + 2H_2O + M$	2.0E-25			[133]
$G91$	$OH^+ + H_5O_3^- + M \rightarrow 2OH + 2H_2O + M$	2.0E-25			[133]
$G92$	$H_2O^+ + OH^- + M \rightarrow OH + H_2O + M$	2.0E-25			[133]

#	Reactions	A	B	C	Ref.
$G93$	$H_2O^+ + O^- + M \rightarrow O + H_2O + M$	2.0E-25			[133]
$G94$	$H_2O^+ + H_2O_2^- + M \rightarrow O + 2H_2O + M$	2.0E-25			[133]
$G95$	$H_2O^+ + H_3O_2^- + M \rightarrow OH + 2H_2O + M$	2.0E-25			[133]
$G96$	$H_2O^+ + H_5O_3^- + M \rightarrow OH + 3H_2O + M$	2.0E-25			[133]
$G97$	$H_2O_3^+ + H_5O_3^- + M \rightarrow OH + 3H_2O + O_2 + M$	2.0E-25			[133]
$G98$	$H_9O_4^+ + H_2O_2^- + M \rightarrow OH + 5H_2O + M$	2.0E-25			[133]
$G99$	$H_9O_4^+ + H_5O_3^- + M \rightarrow 7H_2O + M$	2.0E-25			[133]
$G100$	$H_11O_5^+ + H_2O_2^- + M \rightarrow OH + 6H_2O + M$	2.0E-25			[133]
$G101$	$H_11O_5^+ + H_5O_3^- + M \rightarrow 8H_2O + M$	2.0E-25			[133]
$G102$	$H_13O_6^+ + H_2O_2^- + M \rightarrow OH + 7H_2O + M$	2.0E-25			[133]
$G103$	$H_13O_6^+ + H_5O_3^- + M \rightarrow 9H_2O + M$	2.0E-25			[133]
	Neutral reactions				
$G104$	$2He^* \rightarrow He_2^+ + e$	2.03E-9			[133]
$G105$	$2He^* \rightarrow He^+ + He + e$	8.7E-10			[133]
$G106$	$He^* + He_2^* \rightarrow He^+ + 2He + e$	5.0E-10			[133]
$G107$	$He^* + He_2^* \rightarrow He_2^+ + He + e$	2.0E-9			[133]
$G108$	$He^* + H \rightarrow H^+ + He + e$	1.1E-9			[133]
$G109$	$He^* + H_2 \rightarrow H_2^+ + He + e$	2.9E-11			[133]
$G110$	$He^* + O \rightarrow O^+ + He + e$	3.9E-10			[133]
$G111$	$He^* + O_2 \rightarrow O_2^+ + He + e$	2.54E-10			[133]
$G112$	$He^* + OH \rightarrow OH^+ + He + e$	7.8E-10			[133]
$G113$	$He^* + H_2O \rightarrow H_2O^+ + He + e$	6.6E-10			[133]
$G114$	$He^* + H_2O \rightarrow OH^+ + He + H + e$	1.5E-10			[133]
$G115$	$He^* + H_2O \rightarrow OH + He + H^+ + e$	2.6E-10			[133]

#	Reactions	A	B	C	Ref.
$G116$	$He^* + H_2O \rightarrow OH + HeH^+ + e$	8.5E-22			[133]
$G117$	$He^* + H_2O_2 \rightarrow He + OH^+ + OH + e$	7.5E-10			[133]
$G118$	$He_2^* + H_2 \rightarrow H_2^+ + 2He + e$	2.2E-10			[133]
$G119$	$He_2^* + OH \rightarrow OH^+ + 2He + e$	6E-10			[133]
$G120$	$He_2^* + H_2O \rightarrow H_2O^+ + 2He + e$	6E-10			[133]
$G121$	$He^* + 2He \rightarrow He_2^* + He$	2.0E-34			[133]
$G122$	$He_2^* + M \rightarrow 2He + M$	1.5E-15			[133]
$G123$	$He + O^1D \rightarrow O + He$	1.0E-13			[133]
$G124$	$He + OH(A) \rightarrow OH + He$	1.5E-14			[133]
$G125$	$He + H + O_2 \rightarrow He + HO_2$	2.0E-32			[133]
$G126$	$He + H + OH \rightarrow He + H_2O$	1.56E-31			[133]
$G127$	$He + OH + O_2 \rightarrow He + O_3$	3.4E-34			[133]
$G128$	$H + O_3 \rightarrow OH + O_2$	2.71E-11			[133]
$G129^g$	$H + HO_2 \rightarrow O_2 + H_2$	1.1E-12	0.56	-346	[133]
$G130$	$H + HO_2 \rightarrow 2OH$	2.25E-10			[133]
$G131$	$O^1D + O_2 \rightarrow O + O_2(b)$	2.56E-11			[133]
$G132^g$	$O + OH \rightarrow O_2 + H$	6.0E-11	-0.186	-154	[133]
$G133$	$O + HO_2 \rightarrow OH + O_2$	2.9E-11			[133]
$G134$	$O^1D + H_2O_2 \rightarrow H_2O + O_2$	5.2E-10			[133]
$G135$	$O^1D + H_2O_2 \rightarrow H_2O + O_2$	1.6E-12			[133]
$G136$	$O^1D + H_2O \rightarrow H_2O + O$	1.2E-11			[133]
$G137$	$O_2(b) + H_2O \rightarrow H_2O + O_2(a)$	4.52E-12			[133]
$G138^g$	$2OH \rightarrow H_2O + O$	2.52E-15	1.14	-50	[133]
$G139$	$2OH \rightarrow H_2O_2$	1.5E-11			[133]
$G140$	$OH + HO_2 \rightarrow O_2 + H_2O$	4.38E-11			[133]
$G141$	$OH + H_2O_2 \rightarrow HO_2 + H_2O$	4.53E-12			[133]
$G142$	$OH(A) + H_2O \rightarrow OH + H_2O$	4.9E-10			[133]
$G143$	$OH(A) + H_2O_2 \rightarrow HO_2 + H_2O$	2.93E-10			[133]

The reaction rate coefficients are given in Arrhenius form $k = AT_e^B exp(-C/T_e)$.

T_e is in eV.

Units for k are cm^3s^{-1} for 2-body and cm^6s^{-1} for 3-body reactions.

^{g} reactions depend on T_g where T_g and C are in Kelvin i.e. $k = AT_g^B exp(-C/T_g)$.

BOLSIG+ refers to a pre-computation of the reaction rate coefficients from the electron energy distribution function that is solved for using the Boltzmann equation [114].

Appendix C

H_2−air high pressure plasma chemistry

Table C.1: H_2−air high pressure plasma chemistry

#	Reactions	A	B	C	Ref.
		Electron impact excitation reactions			
$G1$	$e + O_2 \rightarrow e + O_2a1$		BOLSIG+		[114]
$G2$	$e + O_2 \rightarrow e + O_2b1$		BOLSIG+		[114]
$G3$	$e + O_2a1 \rightarrow e + O_2b1$		BOLSIG+		[114]
$G4$	$e + O_2 \rightarrow e + O_2$		BOLSIG+		[114]
$G5$	$e + O_2 \rightarrow e + O_2$		BOLSIG+		[114]
$G6$	$e + O_2 \rightarrow e + O_2^*$		BOLSIG+		[114]
$G7$	$e + O_2 \rightarrow e + O_2$		BOLSIG+		[114]
$G8$	$e + O_2 \rightarrow e + O_2$		BOLSIG+		[114]
$G9$	$e + O_2 \rightarrow e + O_2$		BOLSIG+		[114]
$G10$	$e + N_2 \rightarrow e + N_2$		BOLSIG+		[114]
$G11$	$e + N_2 \rightarrow e + N_2$		BOLSIG+		[114]
$G12$	$e + N_2 \rightarrow e + N_2A$		BOLSIG+		[114]
$G13$	$e + N_2 \rightarrow e + N_2B$		BOLSIG+		[114]
$G14$	$e + N_2 \rightarrow e + N_2B$		BOLSIG+		[114]
$G15$	$e + N_2 \rightarrow e + N_2B$		BOLSIG+		[114]
$G16$	$e + N_2 \rightarrow e + N_2a1$		BOLSIG+		[114]
$G17$	$e + N_2 \rightarrow e + N_2a1$		BOLSIG+		[114]
$G18$	$e + N_2 \rightarrow e + N_2a1$		BOLSIG+		[114]
$G19$	$e + N_2 \rightarrow e + N_2C$		BOLSIG+		[114]
$G20$	$e + N_2 \rightarrow e + N_2$		BOLSIG+		[114]
$G21$	$e + N_2 \rightarrow e + N_2$		BOLSIG+		[114]
$G22$	$e + N_2 \rightarrow e + N_2$		BOLSIG+		[114]

#	Reactions	A	B	C	Ref.
	Electron impact dissociative excitation				
$G23$	$e + O_2 \rightarrow e + O + O^1D$		BOLSIG+		[114]
$G24$	$e + O_2a1 \rightarrow e + O + O^1D$		BOLSIG+		[114]
$G25$	$e + O_2b1 \rightarrow e + O + O^1D$	1.8E-13		2.12E+5	[43]
$G26$	$e + O_2b1 \rightarrow e + O + O^1D$	1.8E-13		2.12E+5	[43]
	e impact ionization				
$G27$	$e + N_2 \rightarrow 2e + N_2^+$		BOLSIG+		[114]
$G28$	$e + O_2 \rightarrow 2e + O_2^+$		BOLSIG+		[114]
$G29$	$e + O_2a1 \rightarrow 2e + O_2^+$	9E-16	2.0	1.34E+5	[43]
$G30$	$e + O_2b1 \rightarrow 2e + O_2^+$	9E-16		1.46E+5	[43]
$G31^e$	$e + H_2 \rightarrow 2e + H_2^+$	9.1E-9	0.5	15.4	[43]
	e impact dissociative ionization				
$G32$	$e + O_2 \rightarrow 2e + O^+ + O$	4.49E-11	0.5	2.61E+5	[43]
$G33$	$e + O_2 \rightarrow e + O^+ + O^-$	7.1E-17	0.5	1.972E+5	[43]
$G34$	$e + O_2b1 \rightarrow 2e + O^+ + O$	5.3E-16	0.9	2.3E+5	[43]
	e impact dissociation				
$G35$	$e + O_2 \rightarrow e + 2O$		BOLSIG+		[114]
$G36$	$e + O_2a1 \rightarrow e + 2O$	4.2E-15		5.3E+4	[43]
$G37$	$e + O_2b1 \rightarrow e + 2O$	7.1E-15		9.97E+4	[43]
$G38^e$	$e + H_2 \rightarrow e + 2H$	8.73E-8	-0.5	11.7	[133]
	metastable de-excitation				
$G38$	$e + O_2a1 \rightarrow e + O_2$	5.6E-15	-0.5	2.55E+4	[43]
$G39$	$e + O_2b1 \rightarrow e + O_2$	5.6E-15	-0.5	2.55E+4	[43]
	Attachment				
$G40$	$e + O_2 \rightarrow O^- + O$		BOLSIG+		[114]
$G41$	$e + O_2a1 \rightarrow O^- + O$		BOLSIG+		[114]
$G42$	$e + O_2b1 \rightarrow O^- + O$		BOLSIG+		[114]
$G43$	$e + 2O_2 \rightarrow O_2^- + O_2$	6.0E-39	-1.0		[108]

#	Reactions	A	B	C	Ref.
$G43$	$e + O_2 + O \rightarrow O_2^- + O$	1.0E-43			[43]
	electron ion recombination				
$G44$	$e + O_2^+ \rightarrow 2O$		BOLSIG+		[114]
$G44$	$e + O_2^+ \rightarrow O + O^1D$	3.65E-12	-0.7		[43]
$G45$	$e + H_2^+ \rightarrow 2H$	5.19E-7	-0.5		[133]
$G46$	$e + O_4^+ \rightarrow 2O_2$		BOLSIG+		[114]
	ion ion impact				
$G47$	$e + O^- \rightarrow N_4^+ + M$	2.16E-16	0.5	3.94E4 [43]	
$G48$	$N_2^+ + N_2 + M \rightarrow O + 2e$	5.0E-41		0	[108]
$G49$	$N_4^+ + O_2 \rightarrow O_2^+ + 2N_2$	2.5E-16			[108]
$G50$	$N_2^+ + O_2 \rightarrow O_2^+ + N_2$	1.04E-15	-0.5		[108]
$G51$	$O_2^+ + 2N_2 \rightarrow O_2 + N_2 + N_2$	8.1E-38	-2.0		[108]
$G52$	$O_2 + N_2 + N_2 \rightarrow O_2+ + 2N_2$	14.8	-5.3	2357	[108]
$G53$	$O_2 + N_2 + O_2 \rightarrow O_2+ + 2N_2$	1E-15			[108]
$G54$	$O_2^+ + O_2 + M \rightarrow O_4+ + M$	2.03E-34	-3.2		[43]
	ion ion recombination				
$G55$	$O_2^- + O_4^+ \rightarrow 3O_2$	1.0E-13			[108]
$G56$	$O_2^- + O_4^+ + M \rightarrow 3O_2 + M$	3.12E-31	-2.5		[108]
$G57$	$O_2^- + O_2^+ + M \rightarrow 2O_2 + M$	3.12E-31	-2.5		[108]
$G58$	$O^- + O_2^+ + M \rightarrow O + O_2$	3.46E-12	-0.5		[108]
$G59$	$O^- + O^+ \rightarrow 2O$	4.67E-12	-0.5		[43]
$G60$	$O^- + O^+ \rightarrow O + O^1D$	8.48E-15	-0.5		[43]
$G61$	$O_2^+ + O^- \rightarrow O + O_2$	3.46E-12	-0.5		[43]
	Nitrogen metastable quenching				
$G62^c$	$N_2A + O_2 \rightarrow N_2 + 2O$	1.7E-12			[96]
$G63^c$	$N_2A + H_2 \rightarrow N_2 + 2H$	4.4E-10		3500	[94]

#	Reactions	A	B	C	Ref.
$G64^c$	$N_2A + O_2 \rightarrow N_2 + O_2b1$	7.5E-13			[96]
$G65^c$	$2N_2A \rightarrow N_2 + N_2B$	7.7E-11			[96]
$G66^c$	$2N_2A \rightarrow N_2 + N_2C$	1.6E-10			[96]
$G67^c$	$N_2A + N_2 \rightarrow N_2 + N_2B$	1.0E-10		1500	[96]
$G68^c$	$N_2A + O \rightarrow N_2 + O$	3.0E-11			[96]
$G69^c$	$N_2B + O_2 \rightarrow N_2 + 2O$	3.0E-10			[96]
$G70^c$	$N_2B + N_2 \rightarrow N_2A + N_2$	1.0E-11			[96]
$G71^c$	$N_2a1 + O_2 \rightarrow N_2 + 2O$	2.8E-11			[96]
$G72^c$	$N_2a1 + N_2 \rightarrow N_2 + N_2$	2.0E-13			[96]
$G73^c$	$N_2C + O_2 \rightarrow N_2 + 2O$	3.0E-10			[96]
$G74^c$	$N_2C + H_2 \rightarrow N_2 + 2H$	3.0E-10			[94]
$G75^c$	$N_2C + N_2 \rightarrow N_2a1 + N_2$	1.0E-11			[96]
$G76^c$	$N_2C \rightarrow N_2B$	3.0E+7			[96]
	Oxygen metastable quenching				
$G77^c$	$O_2^* + O_2 \rightarrow O_2a1 + O_2$	1.86E-13			[96]
$G78^c$	$O_2^* + O_2 \rightarrow O_2b1 + O_2$	8.1E-14			[96]
$G79^c$	$O_2^* + O_2 \rightarrow O_2 + O_2$	2.3E-14			[96]
$G80^c$	$O_2^* + O \rightarrow O_2 + O$	5.0E-12			[96]
$G81^c$	$O_2^* + O \rightarrow O_2a1 + O$	2.7E-12			[96]
$G82^c$	$O_2^* + O \rightarrow O_2b1 + O$	1.35E-12			[96]
$G83$	$O_2a1 + O_2a1 \rightarrow O_2b1 + O_2$	6.99E-35	3.8	-700	[43]
$G84$	$O_2a1 + O_2 \rightarrow O_2 + O_2$	1.69E-24			[43]
$G85$	$O_2a1 + H_2 \rightarrow O_2 + H_2$	4.48E-24			[43]
$G86$	$O_2a1 + O \rightarrow O_2 + O$	6.97E-22			[43]

#	Reactions	A	B	C	Ref.
$G86$	$O_2a1 + H \rightarrow O_2 + H$	6.97E-22			[43]
$G87$	$O_2b1 + O_2 \rightarrow O_2a1 + O_2$	4.58E-23			[43]
$G88$	$O_2b1 + H_2 \rightarrow O_2a1 + H_2$	8.17E-19			[43]
$G89$	$O_2b1 + O \rightarrow O_2a1 + O$	7.97E-20			[43]
$G90$	$O_2b1 + H \rightarrow O_2a1 + H$	7.97E-20			[43]
$G91$	$O_2b1 + O_2 \rightarrow O_2 + O_2$	1.0E-24			[43]
$G92$	$O_2b1 + O \rightarrow O_2 + O$	8.0E-20			[43]
$G93$	$O_2 + O^1D \rightarrow O_2a1 + O$	6.31E-18		-67	[43]
$G94$	$O_2 + O^1D \rightarrow O_2b1 + O$	2.55E-17		-67	[43]
$G95$	$O_2a1 + O^1D \rightarrow O_2b1 + O$	4.98E-17			[43]
$G96$	$O^1D + H_2 \rightarrow O + H_2$	5.48E-18			[43]
$G97$	$O^1D + O_2 \rightarrow O + O_2$	3.18E-17		-67	[43]
$G98$	$O^1D + N_2 \rightarrow O + N_2$	1.8E-11		-107	[94]
$G99$	$O^1D + H_2 \rightarrow H + OH$	1.1E-10			[94]
$G100$	$O_2a1 + H \rightarrow O + OH$	6.5E-11		2530	[94]
$G101$	$O_2a1 + H_2 \rightarrow OH + OH$	2.8E-9		17900	[94]
	Ion neutral reactions				
$G102$	$O^- + O \rightarrow O_2 + e$	1.4E-16		-107	[43]
$G103$	$O_2^- + O \rightarrow O_2 + O^-$	5.73E-15		-0.5	[43]
$G104$	$O^+ + O_2 \rightarrow O_2^+ + O$	5.73E-15		-0.5	[43]
	Ion metastable reactions				
$G105$	$O_2a1 + O^- \rightarrow O_2^- + O$	1.9E-16		-0.5	[43]
$G106$	$O_2a1 + O_2^- \rightarrow 2O_2 + e$	4.67E-16		-0.5	[43]

The reaction rate coefficients are given in Arrhenius form $k = AT_e^B exp(-C/T_e)$.

T_e is in Kelvins.

Units for k are m^3s^{-1} for two body and m^6s^{-1} for three body reactions.

[c] Units for k are cm^3s^{-1} for 2-body and cm^6s^{-1} for 3-body reactions.

[e] Units for T_e is eV BOLSIG+ refers to a pre-computation of the reaction rate coefficients from the electron energy distribution function that is solved for using the Boltzmann equation [114].

Appendix D

H_2−air high pressure combustion chemistry

Table D.1: H_2−air high pressure combustion chemistry

#	Reactions	A	B	C	Ref.
	Plasma reactions				From Appendix C
	Combustion reactions				
$G1$	$2O + M \leftrightarrow O_2 + M$	1.2E+17	-1.0		[143]
$G2$	$O + H + M \leftrightarrow OH + M$	5.0E+17	-1.0		[143]
$G3$	$O + H_2 \leftrightarrow H + OH$	3.87E+4	2.7	6260	[143]
$G4$	$O + HO_2 \leftrightarrow OH + O_2$	2.0E+13			[143]
$G5$	$O + H_2O_2 \leftrightarrow OH + HO_2$	9.63E+6	2.0	4000	[143]
$G6$	$H + O_2 + M \leftrightarrow HO_2 + M$	2.8E+18	-0.862		[143]
$G7$	$H + 2O_2 \leftrightarrow HO_2 + O_2$	2.8E+19	-1.24		[143]
$G8$	$H + O_2 + H_2O \leftrightarrow HO_2 + H_2O$	11.26E+18	-0.76		[143]
$G9$	$H + O_2 + N_2 \leftrightarrow HO_2 + N_2$	2.6E+19	-1.24		[143]
$G10$	$H + O_2 \leftrightarrow HO + O$	2.65E+16	-0.67	17041	[143]
$G11$	$2H + M \leftrightarrow H_2 + M$	1.0E+18	-1.0		[143]
$G12$	$2H + H_2 \leftrightarrow 2H_2$	9.0E+16	-0.6		[143]
$G13$	$2H + H_2O \leftrightarrow H_2 + H_2O$	6.0E+19	-1.25		[143]
$G14$	$H + OH + M \leftrightarrow H_2O + M$	2.2E+22	-2.00		[143]
$G15$	$H + HO_2 \leftrightarrow H_2O + O$	3.97E+12		671	[143]
$G16$	$H + HO_2 \leftrightarrow OH + OH$	0.84E+14		635	[143]
$G17$	$H + H_2O_2 \leftrightarrow HO_2 + H_2$	1.21E+07	2.0	5200	[143]
$G18$	$H + H_2O_2 \leftrightarrow OH + H_2O$	1.0E+13		3600	[143]

#	Reactions	A	B	C	Ref.
$G19$	$OH + H_2 \leftrightarrow H + H_2O$	2.16E+08	1.510	3430	[143]
$G20$	$2OH + M \leftrightarrow H_2O_2 + M$	7.4E+13	-0.371		[143]
$G21$	$2OH \leftrightarrow H_2O + O$	3.57E+04	2.4	-2100	[143]
$G22$	$OH + HO_2 \leftrightarrow H_2O + O_2$	1.45E+13		-500	[143]
$G23$	$OH + H_2O_2 \leftrightarrow H_2O + HO_2$	2.0E+12		427	[143]
$G24$	$OH + H_2O_2 \leftrightarrow H_2O + HO_2$	1.7E+18		29410	[143]
$G25$	$HO_2 + HO_2 \leftrightarrow O_2 + H_2O_2$	1.3E+11		-1630	[143]
$G26$	$HO_2 + HO_2 \leftrightarrow O_2 + H_2O_2$	4.2E+14		12000	[143]
$G27$	$OH + HO_2 \leftrightarrow O_2 + H_2O$	0.5E+16		17330	[143]

The reaction rate coefficients are given in Arrhenius form $k = AT_g^B exp(-C/T_g)$.

T_g is in Kelvins.

Units for k are $cm^3 mol^{-1} s^{-1}$ for 2-body and $cm^6 mol^{-2} s^{-1}$ for 3-body reactions.

Bibliography

[1] M. V. Pachuilo, F. Stefani, L. L. Raja, R. D. Bengtson, G. A. Henkelman, A. C. Tas, W. M. Kriven, and K. S. Suraj, "Development of a gas-fed plasma source for pulsed high-density plasma/material interaction studies," *IEEE Transactions on Plasma Science*, vol. 42, no. 10, pp. 3245–3252, 2014.

[2] R. Miotk, B. Hrycak, D. Czylkowski, M. Dors, M. Jasinski, and J. Mizeraczyk, "Liquid fuel reforming using microwave plasma at atmospheric pressure," *Plasma Sources Science and Technology*, vol. 25, no. 3, p. 035022, 2016.

[3] A. M. Hirst, F. M. Frame, M. Arya, N. J. Maitland, and D. O'Connell, "Low temperature plasmas as emerging cancer therapeutics: the state of play and thoughts for the future," *Tumor Biology*, vol. 37, no. 6, pp. 7021–7031, 2016.

[4] KAUST, "Reactive flow modeling lab," 2008.

[5] A. Nikipelov, A. Rakitin, I. Popov, G. Correale, and A. Starikovskii, "Plasmatrons Powered By Pulsed High-Voltage Nanosecond Discharge For Ultra-Lean Flames Stabilization," in *49th AIAA Aerospace Sciences*

Meeting including the New Horizons Forum and Aerospace Exposition, p. 1214, 2011.

[6] S. B. Leonov and D. A. Yarantsev, "Plasma-induced ignition and plasma-assisted combustion in high-speed flow," *Plasma Sources Science and Technology*, vol. 16, no. 1, p. 132, 2006.

[7] W. Kim, H. Do, M. Mungal, and M. Cappelli, "Flame stabilization enhancement and NOx production using ultra short repetitively pulsed plasma discharges," in *44th AIAA Aerospace Sciences Meeting and Exhibit*, p. 560, 2006.

[8] A. Hamdan and M. S. Cha, "Ignition modes of nanosecond discharge with bubbles in distilled water," *Journal of Physics D: Applied Physics*, vol. 48, no. 40, p. 405206, 2015.

[9] A. Sharma, V. Subramaniam, E. Solmaz, and L. L. Raja, "Fully coupled modeling of nanosecond pulsed plasma assisted combustion ignition," *Journal of Physics D: Applied Physics*, vol. 52, no. 9, p. 095204, 2019.

[10] V. Y. Chernyak, S. V. Olszewski, V. V. Yukhymenko, E. V. Solomenko, I. V. Prysiazhnevych, V. V. Naumov, D. S. Levko, A. I. Shchedrin, A. V. Ryabtsev, V. P. Demchina, *et al.*, "Plasma-assisted reforming of ethanol in dynamic plasma-liquid system: experiments and modeling," *IEEE Transactions on plasma science*, vol. 36, no. 6, pp. 2933–2939, 2008.

[11] S. Starikovskaia, “Plasma assisted ignition and combustion,” *Journal of Physics D: Applied Physics*, vol. 39, no. 16, p. R265, 2006.

[12] M. A. Lieberman and A. J. Lichtenberg, *Principles of plasma discharges and materials processing*. John Wiley & Sons, 2005.

[13] U. Kogelschatz, “Dielectric-barrier discharges: their history, discharge physics, and industrial applications,” *Plasma chemistry and plasma processing*, vol. 23, no. 1, pp. 1–46, 2003.

[14] X. Lu, G. Naidis, M. Laroussi, S. Reuter, D. Graves, and K. Ostrikov, “Reactive species in non-equilibrium atmospheric-pressure plasmas: Generation, transport, and biological effects,” *Physics Reports*, vol. 630, pp. 1–84, 2016.

[15] T. Belmonte, A. Hamdan, F. Kosior, C. Noël, and G. Henrion, “Interaction of discharges with electrode surfaces in dielectric liquids: application to nanoparticle synthesis,” *Journal of Physics D: Applied Physics*, vol. 47, no. 22, p. 224016, 2014.

[16] Q. Chen, J. Li, and Y. Li, “A review of plasma–liquid interactions for nanomaterial synthesis,” *Journal of Physics D: Applied Physics*, vol. 48, no. 42, p. 424005, 2015.

[17] B. Jiang, J. Zheng, S. Qiu, M. Wu, Q. Zhang, Z. Yan, and Q. Xue, “Review on electrical discharge plasma technology for wastewater remediation,” *Chemical Engineering Journal*, vol. 236, pp. 348–368, 2014.

[18] A. Sharma, D. Levko, and L. L. Raja, "Effect of oxygen impurities on atmospheric-pressure surface streamer discharge in argon for large gap arc breakdown," *Physics of Plasmas*, vol. 23, no. 10, p. 103501, 2016.

[19] G. G. Hudson and L. B. Loeb, "Streamer mechanism and main stroke in the filamentary spark breakdown in air as revealed by photomultipliers and fast oscilloscopic techniques," *Physical Review*, vol. 123, no. 1, p. 29, 1961.

[20] L. Loeb, "Encyclopedia of Physics," 1956.

[21] E. Nasser, "Die zeitliche Entwicklung positiver Entladungskanäle längs der Oberfläche von Isolierfilmen," *Archiv für Elektrotechnik*, vol. 44, no. 7, pp. 455–462, 1960.

[22] T. Suzuki, "Transition from the Primary Streamer to the Arc in Positive Point-to-Plane Corona," *Journal of Applied Physics*, vol. 42, no. 10, pp. 3766–3777, 1971.

[23] E. Marode, "The mechanism of spark breakdown in air at atmospheric pressure between a positive point and a plane. I. Experimental: Nature of the streamer track," *Journal of Applied Physics*, vol. 46, no. 5, pp. 2005–2015, 1975.

[24] S. Ganesh, A. Rajabooshanam, and S. Dhali, "Numerical studies of streamer to arc transition," *Journal of applied physics*, vol. 72, no. 9, pp. 3957–3965, 1992.

[25] M. Boussaton, S. Coquillat, S. Chauzy, and J. Georgis, “Influence of water conductivity on micro-discharges from raindrops in strong electric fields,” *Atmospheric research*, vol. 76, no. 1-4, pp. 330–345, 2005.

[26] X. Zhang and M. S. Cha, “Tailored reforming of n-dodecane in an aqueous discharge reactor,” *Journal of Physics D: Applied Physics*, vol. 49, no. 17, p. 175201, 2016.

[27] P. Lukes and B. R. Locke, “Plasmachemical oxidation processes in a hybrid gas–liquid electrical discharge reactor,” *Journal of Physics D: Applied Physics*, vol. 38, no. 22, p. 4074, 2005.

[28] J. Yan, C. M. Du, X. Li, B. Cheron, M. Ni, and K. Cen, “Degradation of phenol in aqueous solutions by gas–liquid gliding arc discharges,” *Plasma Chemistry and Plasma Processing*, vol. 26, no. 1, pp. 31–41, 2006.

[29] A. Demirbas, “Political, economic and environmental impacts of biofuels: A review,” *Applied energy*, vol. 86, pp. S108–S117, 2009.

[30] Z. C. Yan, C. Li, and W. H. Lin, “Hydrogen generation by glow discharge plasma electrolysis of methanol solutions,” *International Journal of Hydrogen Energy*, vol. 34, no. 1, pp. 48–55, 2009.

[31] B. Yan, P. Xu, X. Li, C. Y. Guo, Y. Jin, and Y. Cheng, “Experimental study of liquid hydrocarbons pyrolysis to acetylene in H 2/Ar plasma,” *Plasma Chemistry and Plasma Processing*, vol. 32, no. 6, pp. 1203–1214, 2012.

[32] D. Levko, A. Shchedrin, V. Chernyak, S. Olszewski, and O. Nedybaliuk, "Plasma kinetics in ethanol/water/air mixture in a 'tornado'-type electrical discharge," *Journal of Physics D: Applied Physics*, vol. 44, no. 14, p. 145206, 2011.

[33] D. Levko, A. Sharma, and L. L. Raja, "Non-thermal plasma ethanol reforming in bubbles immersed in liquids," *Journal of Physics D: Applied Physics*, vol. 50, no. 8, p. 085202, 2017.

[34] J. Kolb, R. Joshi, S. Xiao, and K. Schoenbach, "Streamers in water and other dielectric liquids," *Journal of Physics D: Applied Physics*, vol. 41, no. 23, p. 234007, 2008.

[35] A. Starikovskiy and N. Aleksandrov, "Plasma-assisted ignition and combustion," *Progress in Energy and Combustion Science*, vol. 39, no. 1, pp. 61–110, 2013.

[36] Y. Ju and W. Sun, "Plasma assisted combustion: Dynamics and chemistry," *Progress in Energy and Combustion Science*, vol. 48, pp. 21–83, 2015.

[37] Y. P. Raizer, "Gas discharge physics," 1991.

[38] J. Boeuf and L. Pitchford, "Electrohydrodynamic force and aerodynamic flow acceleration in surface dielectric barrier discharge," *Journal of Applied Physics*, vol. 97, no. 10, p. 103307, 2005.

[39] W. Shyy, B. Jayaraman, and A. Andersson, “Modeling of glow discharge-induced fluid dynamics,” *Journal of applied physics*, vol. 92, no. 11, pp. 6434–6443, 2002.

[40] J. R. Roth, “Aerodynamic flow acceleration using paraelectric and peristaltic electrohydrodynamic effects of a one atmosphere uniform glow discharge plasma,” *Physics of plasmas*, vol. 10, no. 5, pp. 2117–2126, 2003.

[41] S. El-Khabiry and G. Colver, “Drag reduction by dc corona discharge along an electrically conductive flat plate for small Reynolds number flow,” *Physics of fluids*, vol. 9, no. 3, pp. 587–599, 1997.

[42] S. O. Macheret, M. N. Shneider, and R. B. Miles, “Scramjet inlet control by off-body energy addition: a virtual cowl,” *AIAA journal*, vol. 42, no. 11, pp. 2294–2302, 2004.

[43] D. Breden and L. Raja, “Simulations of nanosecond pulsed plasmas in supersonic flows for combustion applications,” *AIAA journal*, vol. 50, no. 3, pp. 647–658, 2012.

[44] C. D. Cathey, T. Tang, T. Shiraishi, T. Urushihara, A. Kuthi, and M. A. Gundersen, “Nanosecond plasma ignition for improved performance of an internal combustion engine,” *IEEE Transactions on Plasma Science*, vol. 35, no. 6, pp. 1664–1668, 2007.

[45] E. Moreau, "Airflow control by non-thermal plasma actuators," *Journal of physics D: applied physics*, vol. 40, no. 3, p. 605, 2007.

[46] G. Naidis, "Dynamics of streamer breakdown of short non-uniform air gaps," *Journal of Physics D: Applied Physics*, vol. 38, no. 21, p. 3889, 2005.

[47] M. R. Khani, A. Khosravi, E. Dezhbangooy, B. M. Hosseini, and B. Shokri, "Study on the Feasibility of Plasma (DBD Reactor) Cracking of Different Hydrocarbons (*n*-Hexadecane, Lubricating Oil, and Heavy Oil)," *IEEE Transactions on Plasma Science*, vol. 42, no. 9, pp. 2213–2220, 2014.

[48] A. Fridman, *Plasma chemistry.* Cambridge university press, 2008.

[49] P. Bruggeman and C. Leys, "Non-thermal plasmas in and in contact with liquids," *Journal of Physics D: Applied Physics*, vol. 42, no. 5, p. 053001, 2009.

[50] A. Starikovskiy, Y. Yang, Y. I. Cho, and A. Fridman, "Non-equilibrium plasma in liquid water: dynamics of generation and quenching," *Plasma Sources Science and Technology*, vol. 20, no. 2, p. 024003, 2011.

[51] S. Gershman, O. Mozgina, A. Belkind, K. Becker, and E. Kunhardt, "Pulsed electrical discharge in bubbled water," *Contributions to Plasma Physics*, vol. 47, no. 1-2, pp. 19–25, 2007.

[52] M. Witzke, P. Rumbach, D. B. Go, and R. M. Sankaran, "Evidence for the electrolysis of water by atmospheric-pressure plasmas formed at the

surface of aqueous solutions," *Journal of Physics D: Applied Physics*, vol. 45, no. 44, p. 442001, 2012.

[53] R. M. Roberts, J. A. Cook, R. L. Rogers, A. M. Gleeson, and T. A. Griffy, "The energy partition of underwater sparks," *The Journal of the Acoustical Society of America*, vol. 99, no. 6, pp. 3465–3475, 1996.

[54] X. Lu, Y. Pan, K. Liu, M. Liu, and H. Zhang, "Spark model of pulsed discharge in water," *Journal of applied physics*, vol. 91, no. 1, pp. 24–31, 2002.

[55] X. Zhang and M. S. Cha, "The reformation of liquid hydrocarbons in an aqueous discharge reactor," *Journal of Physics D: Applied Physics*, vol. 48, no. 21, p. 215201, 2015.

[56] D. Levko, A. Sharma, and L. L. Raja, "Plasmas generated in bubbles immersed in liquids: direct current streamers versus microwave plasma," *Journal of Physics D: Applied Physics*, vol. 49, no. 28, p. 285205, 2016.

[57] A. Sharma, D. Levko, and L. L. Raja, "Computational studies of positive and negative streamers in bubbles suspended in distilled water," in *55th AIAA Aerospace Sciences Meeting*, p. 1970, 2017.

[58] D. Levko, A. Sharma, and L. L. Raja, "Microwave plasmas generated in bubbles immersed in liquids for hydrocarbons reforming," *Journal of Physics D: Applied Physics*, vol. 49, no. 22, p. 22LT01, 2016.

[59] B. Sommers and J. Foster, "Nonlinear oscillations of gas bubbles submerged in water: implications for plasma breakdown," *Journal of Physics D: Applied Physics*, vol. 45, no. 41, p. 415203, 2012.

[60] B. Sommers and J. Foster, "Plasma formation in underwater gas bubbles," *Plasma Sources Science and Technology*, vol. 23, no. 1, p. 015020, 2014.

[61] K. Tachibana, Y. Takekata, Y. Mizumoto, H. Motomura, and M. Jinno, "Analysis of a pulsed discharge within single bubbles in water under synchronized conditions," *Plasma Sources Science and Technology*, vol. 20, no. 3, p. 034005, 2011.

[62] A. Hamdan and M. S. Cha, "The effects of gaseous bubble composition and gap distance on the characteristics of nanosecond discharges in distilled water," *Journal of Physics D: Applied Physics*, vol. 49, no. 24, p. 245203, 2016.

[63] N. Y. Babaeva and M. J. Kushner, "Structure of positive streamers inside gaseous bubbles immersed in liquids," *Journal of Physics D: Applied Physics*, vol. 42, no. 13, p. 132003, 2009.

[64] N. Y. Babaeva and M. J. Kushner, "Effect of inhomogeneities on streamer propagation: I. Intersection with isolated bubbles and particles," *Plasma Sources Science and Technology*, vol. 18, no. 3, p. 035009, 2009.

[65] N. Y. Babaeva and M. J. Kushner, "Effect of inhomogeneities on streamer propagation: II. Streamer dynamics in high pressure humid air with bubbles," *Plasma Sources Science and Technology*, vol. 18, no. 3, p. 035010, 2009.

[66] N. Y. Babaeva, D. V. Tereshonok, and G. V. Naidis, "Initiation of breakdown in bubbles immersed in liquids: pre-existed charges versus bubble size," *Journal of Physics D: Applied Physics*, vol. 48, no. 35, p. 355201, 2015.

[67] N. Y. Babaeva, D. V. Tereshonok, G. V. Naidis, and B. M. Smirnov, "Initiation of breakdown in strings of bubbles immersed in transformer oil and water: String orientation and proximity of bubbles," *Journal of Physics D: Applied Physics*, vol. 49, no. 2, p. 025202, 2015.

[68] W. Tian and M. J. Kushner, "Atmospheric pressure dielectric barrier discharges interacting with liquid covered tissue," *Journal of Physics D: Applied Physics*, vol. 47, no. 16, p. 165201, 2014.

[69] W. Tian, K. Tachibana, and M. J. Kushner, "Plasmas sustained in bubbles in water: optical emission and excitation mechanisms," *Journal of Physics D: Applied Physics*, vol. 47, no. 5, p. 055202, 2013.

[70] J. E. Dec, "Advanced compression-ignition engines—understanding the in-cylinder processes," *Proceedings of the combustion institute*, vol. 32, no. 2, pp. 2727–2742, 2009.

[71] K.-Y. Hsu, L. Goss, and W. Roquemore, “Characteristics of a trapped-vortex combustor,” *Journal of Propulsion and Power*, vol. 14, no. 1, pp. 57–65, 1998.

[72] Y. Gong and F. Xuejun, “Supersonic combustion and hypersonic propulsion,” *Advanced Mechanical Systems*, vol. 43, no. 5, pp. 449–471, 2013.

[73] J. Santner, F. L. Dryer, and Y. Ju, “The effects of water dilution on hydrogen, syngas, and ethylene flames at elevated pressure,” *Proceedings of the Combustion Institute*, vol. 34, no. 1, pp. 719–726, 2013.

[74] G. Lou, A. Bao, M. Nishihara, S. Keshav, Y. G. Utkin, J. W. Rich, W. R. Lempert, and I. V. Adamovich, “Ignition of premixed hydrocarbon–air flows by repetitively pulsed, nanosecond pulse duration plasma,” *Proceedings of the Combustion Institute*, vol. 31, no. 2, pp. 3327–3334, 2007.

[75] W. Kim, M. G. Mungal, and M. A. Cappelli, “The role of in situ reforming in plasma enhanced ultra lean premixed methane/air flames,” *Combustion and Flame*, vol. 157, no. 2, pp. 374–383, 2010.

[76] D. Singleton, S. Pendleton, and M. Gundersen, “The role of non-thermal transient plasma for enhanced flame ignition in C2H4–air,” *Journal of Physics D: Applied Physics*, vol. 44, no. 2, p. 022001, 2010.

[77] G. Pilla, D. Galley, D. A. Lacoste, F. Lacas, D. Veynante, and C. O. Laux, “Stabilization of a turbulent premixed flame using a nanosec-

ond repetitively pulsed plasma," *IEEE Transactions on Plasma Science*, vol. 34, no. 6, pp. 2471–2477, 2006.

[78] A. Starikovskiy, N. Aleksandrov, and A. Rakitin, "Plasma-assisted ignition and deflagration-to-detonation transition," *Phil. Trans. R. Soc. A*, vol. 370, no. 1960, pp. 740–773, 2012.

[79] A. E. Rakitin and A. Y. Starikovskii, "Mechanisms of deflagration-to-detonation transition under initiation by high-voltage nanosecond discharges," *Combustion and Flame*, vol. 155, no. 1-2, pp. 343–355, 2008.

[80] K. Busby, J. Corrigan, S.-T. Yu, S. Williams, C. Carter, F. Schauer, J. Hoke, C. Cathey, and M. Gundersen, "Effects of corona, spark and surface discharges on ignition delay and deflagration-to-detonation times in pulsed detonation engines," in *45th AIAA Aerospace Sciences Meeting and Exhibit*, p. 1028, 2007.

[81] I. Kimura, H. Aoki, and M. Kato, "The use of a plasma jet for flame stabilization and promotion of combustion in supersonic air flows," *Combustion and Flame*, vol. 42, pp. 297–305, 1981.

[82] H. Do, S.-k. Im, M. A. Cappelli, and M. G. Mungal, "Plasma assisted flame ignition of supersonic flows over a flat wall," *Combustion and Flame*, vol. 157, no. 12, pp. 2298–2305, 2010.

[83] F. Wang, J. Liu, J. Sinibaldi, C. Brophy, A. Kuthi, C. Jiang, P. Ronney, and M. A. Gundersen, "Transient plasma ignition of quiescent and flow-

ing air/fuel mixtures," *IEEE Transactions on Plasma Science*, vol. 33, no. 2, pp. 844–849, 2005.

[84] T. Shiraishi, T. Urushihara, and M. Gundersen, "A trial of ignition innovation of gasoline engine by nanosecond pulsed low temperature plasma ignition," *Journal of Physics D: Applied Physics*, vol. 42, no. 13, p. 135208, 2009.

[85] B. Penetrante, R. Brusasco, B. Merritt, W. Pitz, G. Vogtlin, M. Kung, H. H. Kung, C. Wan, and K. Voss, "Plasma-assisted catalytic reduction of NO x," *SAE transactions*, pp. 1222–1231, 1998.

[86] H. Kim, K. Takashima, S. Katsura, and A. Mizuno, "Low-temperature NOx reduction processes using combined systems of pulsed corona discharge and catalysts," *Journal of Physics D: Applied Physics*, vol. 34, no. 4, p. 604, 2001.

[87] T. Oda, "Reduction of NOx from combustion flue gases by superimposed barrier discharge plasma reactor," *IEEE Trans, Industr. Applic*, vol. 33, no. 4, pp. 879–886, 1997.

[88] M. Higashi, S. Uchida, N. Suzuki, and K. Fujii, "Soot elimination and NO/sub x/and SO/sub x/reduction in diesel-engine exhaust by a combination of discharge plasma and oil dynamics," *IEEE transactions on plasma science*, vol. 20, no. 1, pp. 1–12, 1992.

[89] M. Uddi, N. Jiang, E. Mintusov, I. V. Adamovich, and W. R. Lempert, "Atomic oxygen measurements in air and air/fuel nanosecond pulse discharges by two photon laser induced fluorescence," *Proceedings of the Combustion Institute*, vol. 32, no. 1, pp. 929–936, 2009.

[90] W. Sun, M. Uddi, T. Ombrello, S. H. Won, C. Carter, and Y. Ju, "Effects of non-equilibrium plasma discharge on counterflow diffusion flame extinction," *Proceedings of the Combustion Institute*, vol. 33, no. 2, pp. 3211–3218, 2011.

[91] Z. Yin, I. Adamovich, and W. Lempert, "OH radical and temperature measurements during ignition of H2-air mixtures excited by a repetitively pulsed nanosecond discharge," *Proceedings of the Combustion Institute*, vol. 34, no. 2, pp. 3249–3258, 2013.

[92] A. Sharma, D. Levko, L. L. Raja, and M. S. Cha, "Kinetics and dynamics of nanosecond streamer discharge in atmospheric-pressure gas bubble suspended in distilled water under saturated vapor pressure conditions," *Journal of Physics D: Applied Physics*, vol. 49, no. 39, p. 395205, 2016.

[93] D. Breden, L. L. Raja, C. A. Idicheria, P. M. Najt, and S. Mahadevan, "A numerical study of high-pressure non-equilibrium streamers for combustion ignition application," *Journal of Applied Physics*, vol. 114, no. 8, p. 083302, 2013.

[94] S. Kobayashi, Z. Bonaventura, F. Tholin, N. A. Popov, and A. Bourdon, "Study of nanosecond discharges in H2–air mixtures at atmospheric

pressure for plasma assisted combustion applications," *Plasma Sources Science and Technology*, vol. 26, no. 7, p. 075004, 2017.

[95] N. L. Aleksandrov, S. V. Kindysheva, I. N. Kosarev, S. M. Starikovskaia, and A. Y. Starikovskii, "Mechanism of ignition by non-equilibrium plasma," *Proceedings of the Combustion Institute*, vol. 32, no. 1, pp. 205–212, 2009.

[96] N. Aleksandrov, S. Kindysheva, E. Kukaev, S. Starikovskaya, and A. Y. Starikovskii, "Simulation of the ignition of a methane-air mixture by a high-voltage nanosecond discharge," *Plasma physics reports*, vol. 35, no. 10, p. 867, 2009.

[97] N. A. Popov, "The effect of nonequilibrium excitation on the ignition of hydrogen-oxygen mixtures," *High Temperature*, vol. 45, no. 2, pp. 261–279, 2007.

[98] S. Yang, S. Nagaraja, W. Sun, and V. Yang, "Multiscale modeling and general theory of non-equilibrium plasma-assisted ignition and combustion," *Journal of Physics D: Applied Physics*, vol. 50, no. 43, p. 433001, 2017.

[99] L. Massa and J. B. Freund, "Plasma-combustion coupling in a dielectric-barrier discharge actuated fuel jet," *Combustion and Flame*, vol. 184, pp. 208–232, 2017.

[100] S. Nagaraja, W. Sun, and V. Yang, "Effect of non-equilibrium plasma

on two-stage ignition of n-heptane," *Proceedings of the Combustion Institute*, vol. 35, no. 3, pp. 3497–3504, 2015.

[101] S. Nagaraja and V. Yang, "A 'frozen electric-field'approach to simulate repetitively pulsed nanosecond plasma discharges and ignition of hydrogen–air mixtures," *Journal of Physics D: Applied Physics*, vol. 47, no. 38, p. 385201, 2014.

[102] F. Tholin and A. Bourdon, "Simulation of the hydrodynamic expansion following a nanosecond pulsed spark discharge in air at atmospheric pressure," *Journal of Physics D: Applied Physics*, vol. 46, no. 36, p. 365205, 2013.

[103] F. Tholin, D. A. Lacoste, and A. Bourdon, "Influence of fast-heating processes and O atom production by a nanosecond spark discharge on the ignition of a lean H2–air premixed flame," *Combustion and Flame*, vol. 161, no. 5, pp. 1235–1246, 2014.

[104] X. Yuan, *One-dimensional simulation study of atmospheric-pressure glow discharges*. Ph.D. Dissertation, The University of Texas at Austin, 2005.

[105] P. Kothnur, *Simulation of Direct Current Microdischarges for Microthruster Applications*. Ph.D. Dissertation, The University of Texas at Austin, 2006.

[106] J. Shin, *A study of direct-current surface discharge plasma for Mach 3 supersonic flow actuation*. Ph.D. Dissertation, The University of Texas

at Austin, 2007.

[107] T. Deconinck, *Simulation studies of direct-current microdischarges for electric propulsion.* Ph.D. Dissertation, The University of Texas at Austin, 2008.

[108] S. Mahadevan, *Simulation of Direct-Current Surface Plasma Discharges in Air for Supersonic Flow Control.* Ph.D. Dissertation, The University of Texas at Austin, 2010.

[109] D. Breden, *Simulations of atmospheric pressure plasma discharges.* Ph.D. Dissertation, The University of Texas at Austin, 2013.

[110] P. Chelvam and P. Kumar, *Computational modeling of electromagnetic waves and their interactions with microplasmas.* Ph.D. Dissertation, 2017.

[111] S. Vivek, *Multi-physics computational modeling of electromagnetic acceleration devices.* Ph.D. Dissertation, 2018.

[112] G. Hagelaar and G. Kroesen, "A Monte Carlo modelling study of the electrons in the microdischarges in plasma addressed liquid crystal displays," *Plasma Sources and Sciences Technology*, vol. 9, no. 605, 2000.

[113] P. K. Panneer Chelvam and L. L. Raja, "Computational modeling of the effect of external electron injection into a direct-current microdischarge," *Journal of Applied Physics*, vol. 118, no. 24, p. 243301, 2015.

[114] G. Hagelaar and L. Pitchford, “Solving the Boltzmann equation to obtain electron transport coefficients and rate coefficients for fluid models,” *Plasma Sources Science and Technology*, vol. 14, no. 4, p. 722, 2005.

[115] D. B. Graves and K. F. Jensen, “A continuum model of DC and RF discharges,” *IEEE Transactions on plasma science*, vol. 14, no. 2, pp. 78–91, 1986.

[116] S. T. Surzhikov and J. S. Shang, “Two-component plasma model for two-dimensional glow discharge in magnetic field,” *Journal of Computational Physics*, vol. 199, no. 2, pp. 437–464, 2004.

[117] A. Bourdon, V. Pasko, N. Liu, S. Célestin, P. Ségur, and E. Marode, “Efficient models for photoionization produced by non-thermal gas discharges in air based on radiative transfer and the Helmholtz equations,” *Plasma Sources Science and Technology*, vol. 16, no. 3, p. 656, 2007.

[118] M. Zheleznyak, A. Mnatsakanian, and S. Sizykh, “Photoionization of mixtures of nitrogen and oxygen by gas discharge radiation,” *Teplofiz. Vys. Temp*, vol. 20, pp. 423–8, 1982.

[119] C. K. Law, *Combustion physics.* Cambridge university press, 2010.

[120] D. L. Scharfetter and H. K. Gummel, “Large-signal analysis of a silicon read diode oscillator,” *IEEE Transactions on electron devices*, vol. 16, no. 1, pp. 64–77, 1969.

[121] S. Patankar, *Numerical heat transfer and fluid flow.* CRC press, 1980.

[122] T. Deconinck, S. Mahadevan, and L. Raja, “Discretization of the Joule heating term for plasma discharge fluid models in unstructured meshes,” *Journal of computational physics*, vol. 228, no. 12, pp. 4435–4443, 2009.

[123] G. Karypis and V. Kumar, “METIS A software package for partitioning unstructured graphs, partitioning meshes, and computing fill-reducing orderings of sparse matrices,” 1998. `http://glaros.dtc.umn.edu/gkhome/metis/metis/overview`.

[124] S. Balay, S. Abhyankar, M. F. Adams, J. Brown, P. Brune, K. Buschelman, L. Dalcin, V. Eijkhout, W. D. Gropp, D. Kaushik, M. G. Knepley, L. C. McInnes, K. Rupp, B. F. Smith, S. Zampini, H. Zhang, and H. Zhang, “PETSc Users Manual,” 2016. `http://www.mcs.anl.gov/petsc`.

[125] R. J. LeVeque, *Finite volume methods for hyperbolic problems*, vol. 31. Cambridge university press, 2002.

[126] A. Sharma and L. L. Raja, “Numerical Investigations of Cathode Surface Streamer Discharges for High-Pressure Large Gap Arc Breakdown,” in *53rd AIAA Aerospace Sciences Meeting*, p. 1619, 2015.

[127] Y. Itikawa, “Cross sections for electron collisions with oxygen molecules,” *Journal of Physical and Chemical Reference Data*, vol. 38, no. 1, pp. 1–20, 2009.

[128] A. Phelps, C. H. Greene, and J. Burke Jr, “Collision cross sections for argon atoms with argon atoms for energies from 0.01 eV to 10 keV,” *Journal of Physics B: Atomic, Molecular and Optical Physics*, vol. 33, no. 16, p. 2965, 2000.

[129] E. Technologies, “Users Manual,” 2016. `http://esgeetech.com/products/vizmesh-mesh-generator-software`.

[130] A. Parente, J. C. Sutherland, L. Tognotti, and P. J. Smith, “Identification of low-dimensional manifolds in turbulent flames,” *Proceedings of the Combustion Institute*, vol. 32, no. 1, pp. 1579–1586, 2009.

[131] A. Biglari and J. C. Sutherland, “A filter-independent model identification technique for turbulent combustion modeling,” *Combustion and Flame*, vol. 159, no. 5, pp. 1960–1970, 2012.

[132] K. Peerenboom, A. Parente, T. Kozák, A. Bogaerts, and G. Degrez, “Dimension reduction of non-equilibrium plasma kinetic models using principal component analysis,” *Plasma Sources Science and Technology*, vol. 24, no. 2, p. 025004, 2015.

[133] D.-X. Liu, P. Bruggeman, F. Iza, M.-Z. Rong, and M. G. Kong, “Global model of low-temperature atmospheric-pressure He+ H2O plasmas,” *Plasma Sources Science and Technology*, vol. 19, no. 2, p. 025018, 2010.

[134] I. Kikoin, “Tables of physical quantities,” *Atomizdat, Moscow*, vol. 1008, 1976.

[135] S. Tabata, "A simple but accurate formula for the saturation vapor pressure over liquid water," *Journal of Applied Meteorology*, vol. 12, no. 8, pp. 1410–1411, 1973.

[136] L. M. Chanin and G. Rork, "Experimental determinations of the first Townsend ionization coefficient in helium," *Physical Review*, vol. 133, no. 4A, p. 1005, 1964.

[137] D. K. Davies, F. L. Jones, and C. Morgan, "Primary ionization coefficient of helium," *Proceedings of the Physical Society*, vol. 80, no. 4, p. 898, 1962.

[138] D. Levko, A. Sharma, and L. L. Raja, "Kinetic modeling of streamer penetration into de-ionized water," *Physics of Plasmas*, vol. 25, no. 3, p. 033515, 2018.

[139] A. D. Lindsay, D. B. Graves, and S. C. Shannon, "Fully coupled simulation of the plasma liquid interface and interfacial coefficient effects," *Journal of Physics D: Applied Physics*, vol. 49, no. 23, p. 235204, 2016.

[140] P. Rumbach, D. M. Bartels, R. M. Sankaran, and D. B. Go, "The solvation of electrons by an atmospheric-pressure plasma," *Nature communications*, vol. 6, p. 7248, 2015.

[141] A. Sharma, D. Levko, and L. L. Raja, "Coupled computational studies of non-thermal plasma based combustion ignition," in *57th AIAA Aerospace Sciences Meeting*, 2019.

[142] S. Pancheshnyi, M. Nudnova, and A. Starikovskii, “Development of a cathode-directed streamer discharge in air at different pressures: experiment and comparison with direct numerical simulation,” *Physical Review E*, vol. 71, no. 1, p. 016407, 2005.

[143] G. Smith, D. Golden, M. Frenklach, N. Moriarty, B. Eiteneer, M. Goldenberg, C. Bowman, R. Hanson, S. Song, W. Gardiner Jr, *et al.*, “GRI-Mech 3.0, Chemical Kinetic Mechanism,” 1999. `http://combustion.berkeley.edu/gri-mech/version30/text30.html`.

[144] E. Technologies, “Users Manual,” 2018. `http://esgeetech.com/products/chemzone-simulation-software`.

[145] M. Slack and A. Grillo, “Investigation of hydrogen-air ignition sensitized by nitric oxide and by nitrogen dioxide,” 1977.

[146] M. R. Malik, B. J. Isaac, A. Coussement, P. J. Smith, and A. Parente, “Principal component analysis coupled with nonlinear regression for chemistry reduction,” *Combustion and Flame*, vol. 187, pp. 30–41, 2018.

[147] H. Mirgolbabaei and T. Echekki, “Nonlinear reduction of combustion composition space with kernel principal component analysis,” *Combustion and Flame*, vol. 161, no. 1, pp. 118–126, 2014.

[148] B. J. Isaac, A. Coussement, O. Gicquel, P. J. Smith, and A. Parente, “Reduced-order PCA models for chemical reacting flows,” *Combustion*

and flame, vol. 161, no. 11, pp. 2785–2800, 2014.

[149] H. Mirgolbabaei and T. Echekki, “A novel principal component analysis-based acceleration scheme for LES–ODT: An a priori study,” *Combustion and Flame*, vol. 160, no. 5, pp. 898–908, 2013.

[150] T. Deconinck and L. L. Raja, “Modeling of mode transition behavior in argon microhollow cathode discharges,” *Plasma processes and polymers*, vol. 6, no. 5, pp. 335–346, 2009.

[151] B. Lay, R. S. Moss, S. Rauf, and M. J. Kushner, “Breakdown processes in metal halide lamps,” *Plasma Sources Science and Technology*, vol. 12, no. 1, p. 8, 2002.

[152] F. Kannari, M. Obara, and T. Fujioka, “An advanced kinetic model of electron-beam-excited KrF lasers including the vibrational relaxation in KrF*(B) and collisional mixing of KrF*(B, C),” *Journal of applied physics*, vol. 57, no. 9, pp. 4309–4322, 1985.

[153] I. Kossyi, A. Y. Kostinsky, A. Matveyev, and V. Silakov, “Kinetic scheme of the non-equilibrium discharge in nitrogen-oxygen mixtures,” *Plasma Sources Science and Technology*, vol. 1, no. 3, p. 207, 1992.

[154] W. Van Gaens and A. Bogaerts, “Kinetic modelling for an atmospheric pressure argon plasma jet in humid air,” *Journal of Physics D: Applied Physics*, vol. 46, no. 27, p. 275201, 2013.

[155] E. Meeks, R. S. Larson, P. Ho, C. Apblett, S. M. Han, E. Edelberg, and E. S. Aydil, “Modeling of SiO 2 deposition in high density plasma reactors and comparisons of model predictions with experimental measurements,” *Journal of Vacuum Science & Technology A: Vacuum, Surfaces, and Films*, vol. 16, no. 2, pp. 544–563, 1998.

[156] P. S. Kothnur and L. L. Raja, “Two-dimensional simulation of a direct-current microhollow cathode discharge,” *Journal of Applied Physics*, vol. 97, no. 4, p. 043305, 2005.

Vita

Ashish Sharma was born in Mumbai, India on 20th January 1990, the son of Sitaram Sharma and Kaushalya Sharma. He received the Bachelor of Technology degree in Mechanical Engineering from the Indian Institute of Technology Guwahati in August 2011. In August 2013, he entered the graduate school in the Department of Aerospace Engineering and Engineering Mechanics at The University of Texas at Austin and obtained the degree of Master of Science in Aerospace Engineering in July 2015.

Permanent address: ashsha990@utexas.edu

This dissertation was typeset with LaTeX[†] by the author.

[†] LaTeX is a document preparation system developed by Leslie Lamport as a special version of Donald Knuth's TeX Program.